ISSN 2782-2192 (Print)
ISSN 2782-2206 (Online)

Journal of Advanced Materials and Technologies

J·A·M·T

Vol.11, No. 1.
2026

TSTU Publishing

ISSN 2782-2192 (Print)
ISSN 2782-2206 (Online)
DOI: 10.17277/jamt

Journal of Advanced Materials and Technologies

Vol. 11, No. 2.
2026

Том 11, № 2.
2026

16+

Journal of Advanced Materials and Technologies

Scientific Journal

"Journal of Advanced Materials and Technologies" is a peer-reviewed scientific journal of research in materials science and related issues in materials physics and mechanics.

"Journal of Advanced Materials and Technologies" publishes original articles, reviews, short reports written by both renowned scientists and young researchers that contribute to the development of modern materials science.

The journal promotes research and exchange of information in the field of theoretical and practical research into materials science, modeling of processes involved in the creation of new materials, including nanomaterials, their properties and application.

The journal papers and metadata abstracted and indexed in CAS (American Chemical Society), Google Scholar, Research4life, Dimensions, ROAD, OpenAlex, Scilit.

ISSN 2782-2192 (Print), ISSN 2782-2206 (Online)

Rename information	Advanced materials & technologies (2016-2021) Print ISSN 2414-4606, Online ISSN 2541-8513
The journal was founded	2016
Publication frequency	Quarterly
Founders	Tambov State Technical University (TSTU), Merzhanov Institute of Structural Macrokinetics and Materials Sciences of Russian Academy of Sciences (ISMAN)
Postal address	TSTU: Bld. 2, 106/5, Sovetskaya St., Tambov, 392000 ISMAN: 8, Academician Osipyan St., Moscow region, Chernogolovka, 142432
Editorial office address	Bld. 2, 106/5, Sovetskaya St., Tambov, 392000
Contacts	Phone + 7 4752 63 03 91; amt.journal@yandex.ru
Printing House	TSTU Publishing, 112A, Michurinskaya St., Tambov, 392032 Phone + 7 4752 63 03 91; + 7 4752 63 07 46
Website ***E-mail*** ***Phone***	http://amt.tstu.ru/ amt.journal@yandex.ru +7 4752 63 92 93
Subscription	The electronic version of the Journal is freely available on the journal's website, as well as in open access databases.
Editor-in-Chief	Mikhail I. Alymov, D. Sc. (Engineering), Professor, Corresponding Member of the Russian Academy of Sciences

Journal of Advanced Materials and Technologies

Научный журнал

«Journal of Advanced Materials and Technologies» – научный рецензируемый журнал, посвященный исследованиям в области материаловедения и примыкающих вопросов физики и механики материалов.

Журнал «Journal of Advanced Materials and Technologies» публикует оригинальные статьи, обзоры, краткие сообщения, содействующие развитию современной науки о материалах, подготовленные как известными учеными, так и молодыми специалистами.

Миссия журнала – обмен актуальной научной информацией в области теоретических и практических исследований и моделирования процессов, связанных с получением, определением свойств новых материалов, в том числе наноразмерных, и их применения.

Средство массовой информации периодическое печатное издание, журнал «Journal of Advanced Materials and Technologies» зарегистрировано Федеральной службой по надзору в сфере связи, информационных технологий и массовых коммуникаций. Регистрационный номер СМИ ПИ № ФС 77-74804 от 25.01.2019.

Журнал входит в перечень рецензируемых научных изданий (перечень ВАК Минобрнауки РФ) от 16 декабря 2021 г. по научным специальностям: 1.4.15 – Химия твердого тела; 2.6.6 – Нанотехнологии и наноматериалы; 2.6.13 – Процессы и аппараты химических технологий; 2.6.17 – Материаловедение.

Журнал индексируется в РИНЦ, ЕГПНИ (Белый список 2.0), RSCI, CAS (American Chemical Society), Google Scholar, Research4life, Dimensions, ROAD, OpenAlex, Scilit.

ISSN 2782-2192 (Print), ISSN 2782-2206 (Online)

Сведения о переименовании	«Advanced materials & technologies» (2016–2021) Print ISSN 2414-4606, Online ISSN 2541-8513
Журнал основан	2016 г.
Периодичность	4 раза в год
Учредители	Федеральное государственное бюджетное образовательное учреждение высшего образования «Тамбовский государственный технический университет» (ФГБОУ ВО «ТГТУ»), Федеральное государственное бюджетное учреждение науки Институт структурной макрокинетики и проблем материаловедения им. А. Г. Мержанова Российской академии наук (ИСМАН)
Адреса учредителей	ФГБОУ ВО «ТГТУ»: 392000, Тамбовская область, г.о. город Тамбов, г. Тамбов, ул. Советская, д. 106/5, помещ. 2, ИСМАН: 142432, Московская область, г. Черноголовка, ул. Академика Осипьяна, д. 8
Адрес издателя	ФГБОУ ВО «ТГТУ»: 392000, Тамбовская область, г.о. город Тамбов, г. Тамбов, ул. Советская, д. 106/5, помещ. 2
Адрес редакции	392000, Тамбовская область, г.о. город Тамбов, г. Тамбов, ул. Советская, д. 106/5, помещ. 2
Контакты	Тел.: + 7 4752 63 03 91; amt.journal@yandex.ru
Адрес типографии	392032, Тамбовская обл., г. Тамбов, ул. Мичуринская, д. 112А Тел.: + 7 4752 63 03 91; + 7 4752 63 07 46
Сайт	http://amt.tstu.ru/
E-mail	amt.journal@yandex.ru
Телефон	+7 4752 63 92 93
Подписка	Электронная версия журнала находится в свободном доступе на сайте журнала, а также в базах данных открытого доступа
Главный редактор	Алымов Михаил Иванович, д. т. н., профессор, член-корреспондент РАН

EDITORIAL BOARD

СОВЕТ РЕДАКТОРОВ

CONTENTS

Short communications

Nobelistics

Original papers

Advanced structural materials, materials for extreme conditions

Materials for energy and environment, next-generation photovoltaics, and green technologies

Reviews

Nanostructured, nanoscale materials and nanodevices

СОДЕРЖАНИЕ

Short communications
Nobelistics

УДК 06.068+544.5+539.175 DOI: 10.17277/jamt-2026-11-02-098-103

Chain reactions in chemistry and physics: 130th anniversary of Nikolai Nikolaevich Semenov

© Viacheslav M. Tyutyunnik [a]✉

[a] *Tambov State Technical University, Bld. 2, 106/5, Sovetskaya St., Tambov, 392000, Russian Federation, International Nobel Information Centre, 30-6, Pervomaiskaya Sq., Tambov, 392002, Russian Federation*

✉ vmtyutyunnik@gmail.com

Abstract. On the occasion of the 130th anniversary of the outstanding Russian scientist Nikolai Nikolaevich Semenov, the winner of the Nobel Prize in Chemistry in 1956, the main milestones of his biography are described and the main scientific achievements are shown. N.N. Semenov is the discoverer of chain reactions in chemistry, the creator of the theory of chain processes, the theory of branched chain reactions, and the law of the increase in the concentration of active centers over time. From 1931, N.N. Semenov created and continuously led the Institute of Chemical Physics for 55 years; now the institute bears his name. The research and administration work of N.N. Semenov and his personal qualities are described. The paper presents materials about N. N. Semenov preserved at the International Nobel Information Center, which has been honoring the scientist's memory for half a century. It also provides detailed information about Semenov's nomination for the Nobel Prize in Chemistry, as well as the people he himself nominated for the award.

Keywords: Nikolai Nikolaevich Semenov; chain reactions; physics; chemistry; Nobel Prize in Chemistry in 1956.

For citation: Tyutyunnik VM. Chain reactions in chemistry and physics: 130th anniversary of Nikolai Nikolaevich Semenov. *Journal of Advanced Materials and Technologies*. 2026;11(2):098-103. DOI: 10.17277/jamt-2026-11-02-098-103

Цепные реакции в химии и физике: 130 лет со дня рождения Николая Николаевича Семёнова

© В. М. Тютюнник [a]✉

[a] *Тамбовский государственный технический университет, ул. Советская, 106/5, пом. 2, Тамбов, 392000, Российская Федерация, Международный Информационный Нобелевский Центр, Первомайская площадь, 30-6, Тамбов, 392002, Российская Федерация*

✉ vmtyutyunnik@gmail.com

Аннотация. К 130-летию выдающегося отечественного ученого Николая Николаевича Семёнова, лауреата Нобелевской премии по химии 1956 года, описаны основные вехи его биографии и показаны главные научные достижения. Н. Н. Семёнов – первооткрыватель цепных реакций в химии, создатель теории цепных процессов, теории разветвленных цепных реакций, закона роста концентрации активных центров со временем. С 1931 г. Н. Н. Семёнов создал и бессменно руководил Институтом химической физики в течение 55 лет; ныне институт носит его имя. Описана научно-организационная деятельность Н. Н. Семёнова, его личные качества. Показаны материалы о Н. Н. Семёнове в Международном Информационном Нобелевском Центре, который полвека хранит память об ученом. Детально раскрыты сведения о номинировании Н. Н. Семёнова на Нобелевскую премию по химии, а также сведения о том, кого он сам выдвигал на эту премию.

Ключевые слова: Николай Николаевич Семёнов; цепные реакции; физика; химия; Нобелевская премия по химии 1956 года.

Для цитирования: Tyutyunnik VM. Chain reactions in chemistry and physics: 130th anniversary of Nikolai Nikolaevich Semenov. *Journal of Advanced Materials and Technologies*. 2026;11(2):098-103. DOI: 10.17277/jamt-2026-11-02-098-103

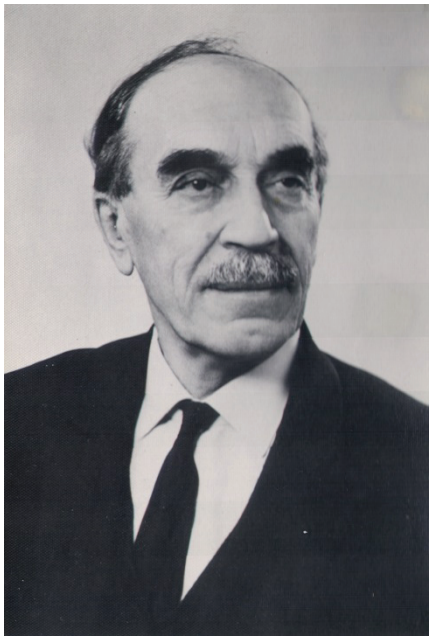

Fig. 1. N.N. Semenov.
A gift from N.N. Semenov to the author of the article in 1975

Fate gifted the author with the immense joy of communicating with legendary Nikolai Nikolaevich Semenov (Fig. 1), whom he met repeatedly, first in 1975, when Academician I.L. Knunyants introduced us. The great scientist, founder of a new branch of science - chemical physics - twice Hero of Socialist Labor, Nobel Prize laureate, holder of the Lenin and State Prizes, and Academician Nikolai Nikolaevich Semenov turns 130 on April 15.

Nikolai Nikolaevich Semenov was born on April 3(15), 1896, in Saratov. After leaving school in 1913, he enrolled in the physics department of the physics-mathematics faculty at St. Petersburg University, where he studied under the renowned Russian physicist Abram Fedorovich Ioffe (1880–1960). After graduating from Petrograd University in 1917, Semenov worked as an assistant at the physics faculty of Tomsk Technological Institute and the university from 1918 to 1920. In 1920, he returned to Petrograd, where he was appointed head of the laboratory of electronic phenomena, and from 1922 to 1927 served as deputy director of the State Physico-Technical X-ray Institute (SPTXI). In 1926, he was sent to Germany, England, and France to familiarize himself with the leading physics laboratories, and in 1927 he became the head of the physico-chemical sector of SPTXI, on the basis of which the Leningrad Research Institute of Chemical Physics of the USSR Academy of Sciences (LRICP) was established on October 15, 1931. N.N. Semenov was appointed director of the institute, holding the position for 55 years (in 1943, the Institute of Chemical Physics (ICP) of the USSR Academy of Sciences – ICP - relocated to Moscow, settling on Vorobyovy Gory, where it continues to operate today). In 1972, N.N. Semenov revived the institute laboratory of chain processes and personally headed it.

N.N. Semenov's entire life in science was connected with the Academy of Sciences. When he was elected a full member of the USSR Academy of Sciences, he was only 36 years old! N.N. Semenov was a member of the Bureau (1946–1957) and Academician-Secretary (1957–1963) of the Chemical Sciences Division of the USSR Academy of Sciences, and Vice President of the Academy from 1963–1971. For nearly 30 years (from 1957 until his death), N.N. Semenov served on the Presidium of the USSR Academy of Sciences, working on many of the Academy's councils, sections, and commissions, including those on free radicals, macromolecular compounds, philosophical issues of modern natural science, the physicochemical foundations of producing new heat-resistant inorganic materials, chemical engineering, and biological sciences, among others.

N.N. Semenov completed his first two scientific papers, “On the Collisions of Slow Electrons with Molecules” and “On the Theory of the Passage of Electricity through Gases”, under the supervision of A.F. Ioffe and published them in 1916 in the Journal of the Russian Physical-Chemical Society. After 1922, the young scientist's publications began to appear regularly in Soviet and foreign journals. N.N. Semenov's (1921–1926) physical research focused on three areas: electric fields, molecular physics, and electronic phenomena. To explain phenomena observed in experiments on the oxidation of phosphorus vapor with oxygen, which were incomprehensible from the standpoint of classical concepts of transformation mechanisms, N.N. Semenov in 1926–1927 proposed the theory of branched chain reactions: if the number of chain branches exceeds the number of terminations, the reaction accelerates sharply, leading to ignition of the mixture of reactants, i.e., a “chain explosion”. The scientist developed a rigorous theory of chain termination on the walls and in the volume of a reaction vessel, establishing that the reaction rate is proportional to the square of the vessel diameter or the first power of the pressure within it. He then discovered limiting phenomena in the oxidation of sulfur, hydrogen, carbon monoxide, carbon disulfide, and other vapors, demonstrating the prevalence of chain reactions in inorganic chemistry. Based on experimental results, he developed a general theory

of chain chemical reactions and discovered the law of increasing concentration of active centers over time.

In 1934, N.N. Semenov's fundamental monograph, “Chain Reactions”, was published, in which he described his discoveries in detail (Fig. 2). From that time on, chemical physics emerged [1–6]. In 1956, N.N. Semenov, the first Soviet scientist, was awarded the Nobel Prize in Chemistry (which he shared with the English scientist S.N. Hinshelwood) "for his research into the mechanism of chemical reactions." Speaking in Stockholm after receiving the Nobel Prize, N.N. Semenov said: “Natural phenomena know nothing about the fact that we have divided our knowledge into sciences... Only a comprehensive examination of phenomena from the point of view of physics, chemistry, mechanics, and sometimes biology will allow us to recognize their essence and apply them in practice...” [7].

In 1951, N.N. Semenov proposed a chain mechanism for processes occurring on the surface of solid catalysts. Since 1955, problems of controlling homogeneous and heterogeneous catalysis of chain reactions have played a significant role in his work. However, within two decades, this area of research gave way to the kinetics of combustion and explosions. From 1958, N.N. Semenov intensively pursued research in molecular biology and biochemistry, particularly the kinetics of biological processes. In 1967, he was the first in the world to clearly formulate and substantiate the problem of preserving, protecting, and improving the quality of natural waters as one of the most important in modern science. In the 1970s, on N.N. Semenov's initiative, the Institute of Chemical Physics (ICP) began research on chemical bionics (an idea conceived in 1960) – applying the principles of enzymatic catalysis to carry out new catalytic reactions (photosynthesis, nitrogen fixation, etc.) using solar energy.

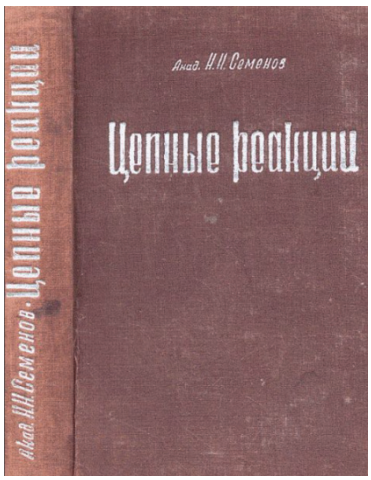

Fig. 2. Cover of N.N.Semenov's monograph, 1934

From 1944 until the last years of his life, N.N. Semenov headed the Department of Chemical Kinetics at the Faculty of Chemistry at Moscow State University. From 1951 to 1957, he simultaneously headed the department at the Moscow Engineering Physics Institute, and from 1957 to 1959, he was a professor in that department. His talent as a teacher, scientific advisor, and director is widely recognized. He created the largest, world-renowned scientific school in chemical physics and trained a whole galaxy of Soviet kineticists, including academicians, corresponding members, doctors, and candidates of science.

In December 1960, at the regular Pugwash Conference in Moscow, N.N. Semenov delivered a brilliant report, clearly and unambiguously entitled: *Eliminating Wars from the Lives of Nations*. Using simple mathematical equations, he clearly demonstrated that the longer the time between the start and end of disarmament, the greater the danger of war. N.N. Semenov's participation in the Pugwash movement of scientists was only one aspect of his work aimed at averting the threat of nuclear war from humanity.

Even in the last years of his life, N.N. Semenov remained a scientific enthusiast, a creative individual distinguished by boundless energy. He was tall and lean, enjoyed hunting and gardening, and was passionate about architecture, theater, music, and painting. He was kind, sympathetic, easy to talk to, and accessible to anyone who needed his advice, as the author of this article repeatedly witnessed during visits to his office at the Institute of Chemical Physics or to his home. A scientist must always remember that neither rank, nor age, nor scientific merit should have any significance in their scientific communication with students, no matter how young they may be. When I think of Nikolai Nikolaevich Semyonov, the same thought always comes to mind: the most important thing in a scientist's personality is not so much what he accomplished himself (after all, others would have made the discoveries), but what he gave to others – students, colleagues, friends, and simply ordinary people (Fig. 3).

In April 1986, during the celebration of the great scientist's 90th birthday, we spent four hours talking at his home on Frunzenskaya Naberezhnaya. Nikolai Nikolaevich talked at length about his life, the difficulties of developing chemical physics, his involvement in the Soviet atomic project, and his meetings with scientists. Ashtrays were scattered throughout his office, as N.N. Semenov smoked almost nonstop, lighting one Novost cigarette after another. When the author of the article dared to

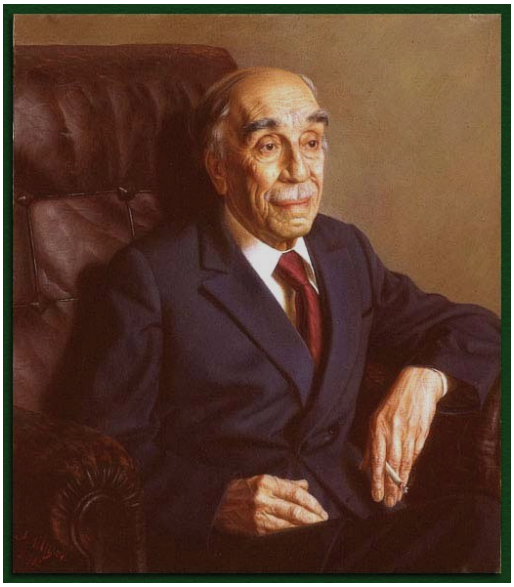

Fig. 3. Portrait of N.N. Semenov by the artist A.M. Shilov

say: “Nikolai Nikolaevich, you smoke a lot. You know that carcinogenic substances form at the phase boundary in a cigarette; it's a classic chain reaction...” The great scientist listened calmly and then sternly replied: “You, son, first live to be 90, and then you can talk about the dangers of smoking!” This phrase stuck with me for life. Nikolai Nikolaevich Semenov died on September 25, 1986, in Moscow at the age of 90. He is buried at the Navodevichy Cemetery (Fig. 4).

Fig. 4. N.N. Semyonov's grave at Novodevichy Cemetery. Photo by the author in April 2006

The International Nobel Information Center (INIC) has been preserving the memory of our great scientist for half a century. The Nobel Scientific Library, the Nobel Museum, and the INC archives contain a vast amount of material on the life and work of N.N. Semenov (Figs. 5, 6) [8–11]. It is significant that Nikolai Nikolaevich read, corrected, and personally endorsed the author's first anniversary article about him in April 1976 [8]. Numerous books and articles have been written about him [9–16].

From the now-declassified materials of the Nobel Committee in Chemistry for 1901–1974: It became known that N.N. Semenov was nominated for the Nobel Prize seven times: in 1946 by the English physical chemist S.N. Hinshelwood; in 1947 and 1948 by the Swedish physical chemist T. Svedberg, winner of the 1926 Nobel Prize in Chemistry; in 1950 by S.N. Hinshelwood again; in 1955 and 1956 by the Swedish professor L.G. Sillen. The only nomination from the USSR, from Academician A.P. Vinogradov, arrived in Stockholm late and was therefore only taken into account in 1957, when N.N. Semenov had already become a Nobel Prize laureate after six nominations!

It is interesting that N.N. Semenov himself nominated 13 Nobel Prizes by 1974: twice in physics (1957 – P.L. Kapitsa; 1964 – E.K. Zavoisky and K.Ya. Gorter from the Netherlands), 11 times in chemistry (1964 – A.P. Vinogradov and A. Holmes from Great Britain, then A.N. Frumkin, and M. Volmer from Germany; 1965 – A.N. Frumkin and M. Volmer, then A.P. Vinogradov and A. Holmes; 1967 – A.N. Frumkin; 1968 – A.N. Frumkin, American B. Lewis and Ya.B. Zeldovich; 1970 – N.M. Emanuel; 1971 – N.M. Emanuel; 1972 – A.E. Shilov and M.E. Volpin; 1973 – N.M. Emanuel; 1974 – N.M. Emanuel, A.E. Shilov and M.E. Volpin).

Funding

The present study did not receive any external funding.

Финансирование

Настоящее исследование не получило внешнего финансирования.

Acknowledgements

The author is grateful to the family of N.N. Semenov for their long-standing friendship and for providing materials, some of which formed the basis for this article.

Fig. 5. A stand made by the MINC and donated to the N.N. Semenov Museum in Chernogolovka

Fig. 6. Books about N.N. Semenov, donated by his wife L.G. Shcherbakova-Semyonova

Благодарности

Автор выражает благодарность семье Н. Н. Семенова за многолетнюю дружбу и предоставление материалов, часть из которых легла в основу данной статьи.

Conflict of interests

The authors declare no conflict of interest.

Конфликт интересов

Авторы заявляют об отсутствии конфликта интересов.

References

1. Semenov NN. *Chain reactions*. Leningrad: Goskhimizdat; 1934. 556 p; 2nd ed., rev. and additional – Moscow: Nauka; 1986. 536 p. (In Russ.)
2. Semenov NN. *Chain reactions*. Moscow: Nauka; 2004, Vol. 1(1). 392 p. (In Russ.)
3. Semenov NN. *Chain reactions*. Moscow: Nauka, 2004, Vol. 1(2). 603 p. (In Russ.)
4. Semenov NN. *Combustion and explosion*. Moscow: Nauka; 2005, Vol. 2. 704 p. (In Russ.)
5. Semenov NN. *On some problems of chemical kinetics and reactivity*. Moscow: Nauka; 2004, Vol. 3. 499 p. (In Russ.)
6. Semenov NN. *About time and myself*. Moscow: Nauka; 2006, Vol. 4. 610 p. (In Russ.)
7. Tyutyunnik VM, Soboleva AA, Korskova IS. *Materials about N.N. Semenov in the International Nobel Information Center: to the 115th anniversary of the birth of N.N. Semenov and the 55th anniversary of the first and only Nobel Prize in Chemistry awarded to a Russian scientist.* Tambov; Moscow; Saint Petersburg; Baku; Vein; Hamburg: Mining and Metallurgical Center "Nobelistika" Publ. House; 2011. 112 p. (In Russ.)

8. Tyutyunnik VM. Nikolai Nikolaevich Semenov. *Chemists – Lenin Prize Laureates*. Moscow: 1978. p. 53-61. (In Russ.)

9. Tyutyunnik VM. Meetings of Nobel Laureates in Lindau: (on the 30th Anniversary of the Nobel Conf. in Lindau (Bavaria, Germany). *Zhurnal vsesoyuznogo khimicheskogo obshchestva im. D.I. Mendeleyeva.* 1980;25(2):221-225. (In Russ.)

10. Tyutyunnik VM, Fedotova TA. *Gold Medals and Prizes of the USSR Academy of Sciences: bibliographic index*. Tambov: Tambov State Institute of Culture Publ. House; 1988, pp. 21, 48. (In Russ.)

11. Karikova EV, Korskova IS, Bobyakova OE, Tyutyunnik VM. Materials about N.N.Semyonov in the collections of the International Nobel Information Center. *Istoriya nauki i tekhniki*. 2006;4:45-64. (In Russ.)

12. Chernyshev AK. *Nikolai Nikolaevich Semenov – an outstanding scientist and organizer of the USSR atomic project*. Sarov: All-Russian Research Institute of Experimental Physics Publ. House; 2012. 80 p.; 2nd ed. 2016. (In Russ.)

13. Anikin VM. *Nikolai Nikolaevich Semenov: fragments of scientific biography*. Saratov: Saratov University Publ. House; 2017. 80 p. (In Russ.)

14. *Memories of Academician Nikolai Nikolaevich Semenov*. ed. Academician A.E. Shilov. Moscow: Nauka; 1993. 302 p. (In Russ.)

15. Goldansky VI. A Word about Semenov. *Priroda*. 1996;3-4:4-10. (In Russ.)

16. Shcherbakova-Semyonova LG. *Write about us... (preface by E. Shubina)*. Moscow: Boslen; 2022. 410 p. (In Russ.)

Information about the authors / Информация об авторах

Vyacheslav M. Tyutyunnik, D. Sc. (Eng.), Professor, Tambov State Technical University; Director General, International Nobel Information Centre, Tambov, Russian Federation; ORCID 0000-0003-2099-5730; e-mail: vmtyutyunnik@gmail.com

Тютюнник Вячеслав Михайлович, доктор технических наук, профессор, Тамбовский государственный технический университет; генеральный директор, Международный Информационный Нобелевский Центр, Тамбов, Российская Федерация; ORCID 0000-0003-2099-5730; e-mail: vmtyutyunnik@gmail.com

Received 20 April 2026; Revised 22 May 2026; Accepted 25 May 2026

Original papers
Advanced structural materials, materials for extreme conditions

УДК 621.791.13 DOI: 10.17277/jamt-2026-11-02-104-117

Study of evolution and phase formation at the 08Cr18Ni10Ti–AlMg6 weld interface after explosive welding and heat treatment via layer-by-layer XRD analysis

© Andrey Yu. Malakhov[a], Dmitry Yu. Kovalev[a], Stepan A. Seropyan[a]✉, Nemat N. Niyozbekov[a], Igor V. Denisov[a], Gulnaz R. Saikova[a]

[a] *Merzhanov Institute of Structural Macrokinetics and Materials Science, Russian Academy of Science, 8, Academician Osipyan St., Chernogolovka, 142432, Russian Federation*

✉ stepan.seropyan@yandex.ru

Abstract. The phase evolution in the joint zone of the 08Cr18Ni10Ti–AlMg6 bimetal obtained by explosive welding followed by isothermal annealing at 500–550 °C was investigated using the method of layer-by-layer XRD analysis. It was established that after explosive welding, a metastable quasicrystalline phase, $Al_{86}Fe_{14}$, forms in the near-surface layers. This phase decomposes during isothermal annealing, leading to the formation of equilibrium intermetallic compounds Al_5Fe_2 and $Al_{13}Fe_4$. Additionally, after annealing, the formation of a ternary phase, $Cr_2Mg_3Al_{18}$, is detected, indicating the activation of diffusion interaction between the components of the steel and the aluminium alloy. Thus, a sequential evolution of the phase composition in the joint zone after explosive welding and thermal exposure is demonstrated. The results obtained expand the understanding of the mechanisms of phase formation and diffusion processes at the joint interface in the 08Cr18Ni10Ti–AlMg6 bimetal during explosive welding, as well as the influence of thermal exposure on phase evolution.

Keywords: explosive welding; phase transformation; 08Cr18Ni10Ti steel; AlMg6 alloy; layer-by-layer XRD; recrystallization.

For citation: Malakhov AYu, Kovalev DYu, Seropyan SA, Niyozbekov NN, Denisov IV, Saikova GR. Study of evolution and phase formation at the 08Cr18Ni10Ti–AlMg6 weld interface after explosive welding and heat treatment via layer-by-layer XRD analysis. *Journal of Advanced Materials and Technologies*. 2026;11(2):104-117. DOI: 10.17277/jamt-2026-11-02-104-117

Исследование эволюции и фазообразования на границе раздела сварного соединения 08Х18Н10Т–АМг6 после сварки взрывом и термической обработки с помощью послойного рентгеноструктурного анализа

© А. Ю. Малахов[a], Д. Ю. Ковалев[a], С. А. Серопян[a]✉, И. В. Денисов[a], Н. Н. Ниезбеков[a], Г. Р. Сайкова[a]

[a] *Институт структурной макрокинетики и проблем материаловедения им. А. Г. Мержанова РАН, ул. Академика Осипьяна, 8, Черноголовка, 142432, Российская Федерация*

✉ stepan.seropyan@yandex.ru

Аннотация. Методом послойного рентгеноструктурного анализа (РФА) исследована фазовая эволюция в зоне соединения биметалла сталь 08Х18Н10Т–АМг6, полученного сваркой взрывом, с последующим изотермическим отжигом при 500–550 °С. Установлено, что после сварки взрывом в приповерхностных слоях формируется метастабильная квазикристаллическая фаза $Al_{86}Fe_{14}$, которая распадается при изотермическом отжиге с образованием равновесных интерметаллических соединений Al_5Fe_2 и $Al_{13}Fe_4$. Также после отжига фиксируется формирование тройной фазы $Cr_2Mg_3Al_{18}$, что свидетельствует об активизации диффузионного взаимодействия

компонентов стали и алюминиевого сплава. Таким образом, показана последовательная эволюция фазового состава в зоне соединения после сварки взрывом и термического воздействия. Полученные результаты расширяют представления о механизмах фазообразования и диффузионных процессов на границе соединения в биметалле сталь 08Х18Н10Т–АМг6 при сварке взрывом, а также о влиянии термического воздействия на эволюцию фаз.

Ключевые слова: сварка взрывом; фазовое изменение; сталь 08Х18Н10Т; сплав АМг6; послойный РФА; рекристаллизация.

Для цитирования: Malakhov AYu, Kovalev DYu, Seropyan SA, Niyozbekov NN, Denisov IV, Saikova GR. Study of evolution and phase formation at the 08Cr18Ni10Ti–AlMg6 weld interface after explosive welding and heat treatment via layer-by-layer XRD analysis. *Journal of Advanced Materials and Technologies*. 2026;11(2):104-117. DOI: 10.17277/jamt-2026-11-02-104-117

1. Introduction

Aluminium alloys are widely used in aircraft, mechanical engineering, marine construction and the chemical industry [1]. For example, aluminium-magnesium (Al–Mg) alloys are used due to their high corrosion resistance, low density and high strength [2–4]. At present, bimetallic transition joints consisting of Al–Mg alloy and stainless steel enable weight reduction in various structures [5, 6]. The bimetallic transitions have significant potential for transport equipment and large-scale chemical vessel production [7, 8]. These transitions are produced by using friction stir welding [9], cold rolling [10], gas tungsten arc welding [11], spot welding [12], diffusion welding [13], explosive welding (EW) [14], and magnetic pulse welding [15]. In contrast to other methods, EW enables the joining of large-area plates without requiring complex high-cost equipment [16, 17]. Welding Al–Mg alloys to steels presents many challenges, inherent in all welding methods. Primarily, there is a significant difference in thermophysical properties between the Al–Mg alloys and steels [18].

Furthermore, the formation of a strong joint is complicated by: 1) the accumulation of Mg near the weld interface, 2) the presence of MgO on the Al–Mg alloy surface [19], and 3) the formation of brittle Fe–Al intermetallic compounds resulting from the low solubility of Mg atoms in Fe [20–22]. These factors are important to consider when plastic deformation occurs in EW [16, 23]. There are numerous scientific works that have investigated phase formation between Fe and Al [25–27]. These works show that Al_3Fe and Al_5Fe_2 are the dominant phases.

One of the methods for reducing Fe–Al intermetallic compounds at the weld interface involves using interlayers (e.g., Ti, Cu, Al, Ta) [24]. However, using interlayers may not prevent the formation of brittle Fe–Al intermetallic compounds during service [16].

Chemical composition of the intermetallic compounds at the weld interface is primarily analyzed on cross-sectional planes [19]. However, isolated particles and intermetallic compounds with low concentrations cannot be detected by this method.

This study investigates phase formation at the AlMg6 alloy–08Cr18Ni10Ti steel weld interface via layer-by-layer X-ray diffraction (XRD) analysis with sequential layer removal. Thus, this study enabled high-accuracy detection of low-concentration intermetallic compounds at significant distances from the weld interface.

2. Materials and Methods

2.1. Materials

Initial materials included aluminium-magnesium alloy AlMg6 sheet (4×200×300 mm) and 08Cr18Ni10Ti stainless steel sheet (3×200×300 mm). Their chemical compositions are given in Table 1.

2.2. The basic setup for the EW experiment

Prior to the start of the experiment, the initial sheets were cleaned from the oxide films and rusts. Figure 1 shows the basic setup for the EW experiment. The explosive used is a mixture of microporous ammonium nitrate and diesel oil (ANFO) at the ratio 96:4. The detonation velocity was 2500 $m \cdot s^{-1}$. The distance between the flyer and base sheets was 6 mm. For other details of the EW experiments, see [28]. The EW parameters were calculated using the formulas in [29].

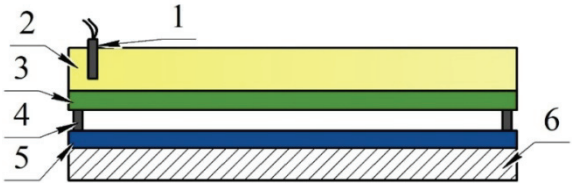

Fig. 1. Basic setup for explosive welding: *1* – detonator; *2* – explosive; *3* – flyer sheet (08Cr18Ni10Ti steel); *4* – support; *5* – base sheet (AlMg6 alloy); *6* – anvil (low carbon steel)

Table 1. Chemical compositions (wt. %) of initial materials

Material	Element (wt. %)									
	Fe	Si	C	Ti	Al	Mg	Cu	Cr	Ni	Mn
AlMg6 (Russian Standard 4784-2019)	0.4	0.4	–	0.1	Base	5.8–6.8	0.1	–	–	0.5–0.8
08Cr18Ni10Ti (Russian Standard 5632-2014)	Base	0.8	0.08	1.0	–	–	0.3	17–19	9–11	2.0

2.3. XRD analysis

Specimens for XRD analysis were prepared following the methodology illustrated in Fig. 2*a*. The wire cutting machine DK7725 was used to cut the specimens. Specimens were heat-treated in air at 500 and 550 °C for holding times of 60, 90, and 120 min, respectively. The specimens were split after EW and heat treatment (Fig. 2*b*). The surfaces of the split specimens were analyzed using XRD analysis.

The XRD analysis of the specimens was performed before and after the EW. On an automated LAP-1000 grinding/polishing machine, a layer of (30 ± 5) μm was removed from the analysis surface of AlMg6 and 08Cr18Ni10Ti in two stages, with approximately (15 ± 5) μm removed per stage, followed by XRD analysis (Fig. 3). Heat treated specimens underwent the same procedure: grinding (15 ± 5) μm → XRD → repeat → total removal: (30 ± 5) μm.

3. Results and Discussion

3.1. Analysis of initial materials before explosive welding

The diffraction pattern from the initial surface (pre-explosive welding) of 08Cr18Ni10Ti steel reveals two phases – austenite and ferrite (Fig. 4). A pronounced {220} austenite texture is observed, evidently resulting from prior rolling. The microstructure further indicates highly elongated grains.

The diffraction pattern from the initial surface of the AlMg6 alloy (Fig. 5) reveals that the primary phase is an aluminium-based FCC solid solution

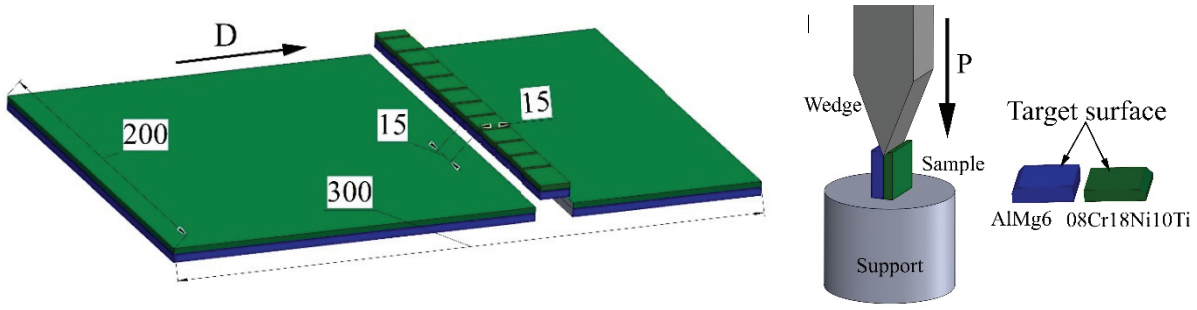

Fig. 2. Specimen preparation:
a – specimen extraction; *b* – layer separation method; *D* – detonation direction; *P* – applied pressure direction

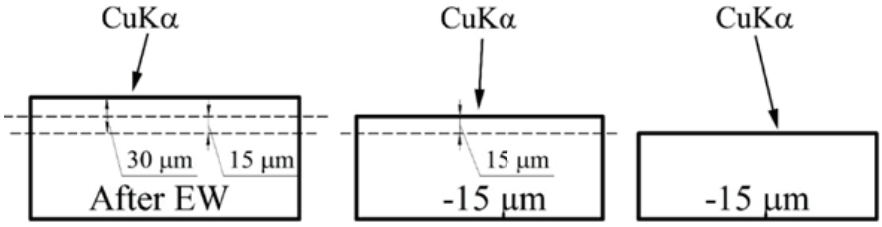

Fig. 3. Schematic of stepwise layer removal

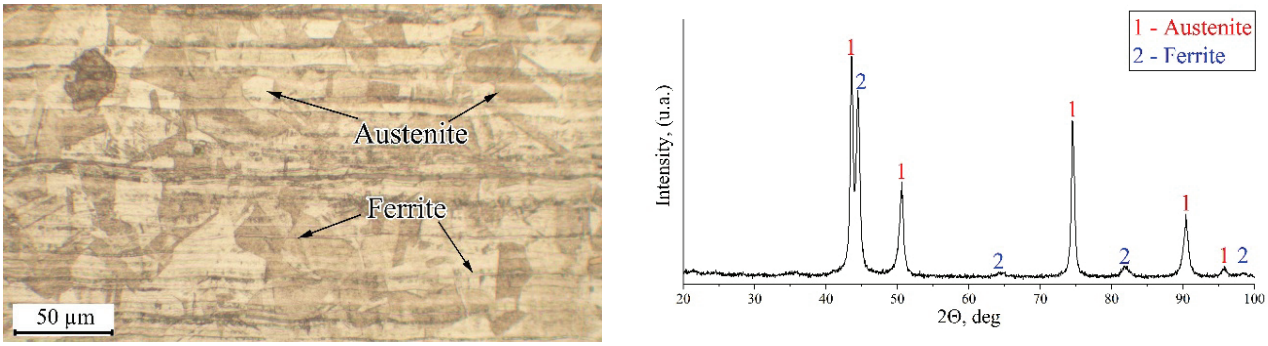

(a) *(b)*

Fig. 4. Microstructure of 08Cr18Ni10Ti steel with XRD pattern

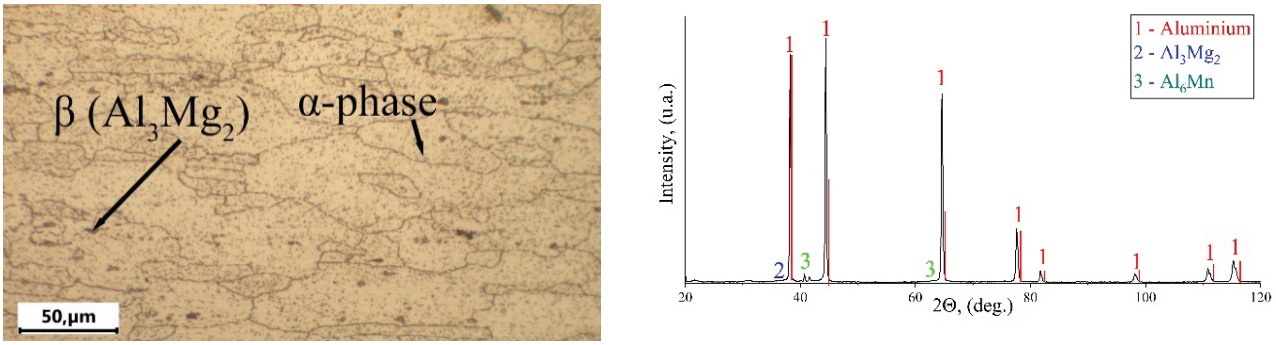

(a) *(b)*

Fig. 5. Microstructure of AlMg6 alloy with XRD pattern

(α-phase). Reflections of the solid solution are shifted relative to pure aluminium angular positions, indicating dissolution of alloying elements – principally Mg and Mn, per chemical analysis. A strong {200} texture in the solid solution is observed, consistent with elongated α-phase grains and attributable to sheet processing via rolling. The diffraction pattern also shows weak, near-background reflections of secondary Al_3Mg_2 (β-phase) and Al_6Mn phases, present as dispersed inclusions at grain boundaries and within α-phase grains.

3.2 Analysis of the 08Cr18Ni10Ti–AlMg6 weld interface after explosive welding

As a result of EW, a transition layer forms at the AlMg6–08Cr18Ni10Ti weld interface (Fig. 6). The layer thickness varies between 5 and 20 μm. Due to the limited cross-sectional area of the transition layer, the diffraction pattern shows only reflections from the parent phases: the aluminium-based solid solution (α-phase), austenite, and ferrite.

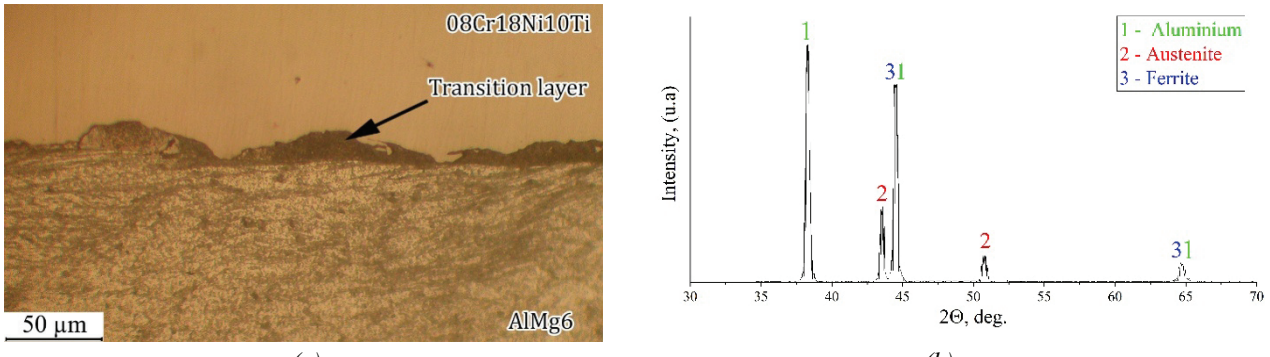

(a) *(b)*

Fig. 6. Explosively welded AlMg6–08Cr18Ni10Ti interface:
a – Transition layer morphology; *b* – XRD pattern showing parent phases only (α-Al, γ-Fe, δ-Fe)

3.2.1. Analysis of the 08Cr18Ni10Ti fracture surface after explosive welding

The diffraction patterns of the 08Cr18Ni10Ti steel specimen after EW shows austenite reflections (Fig. 7). The intensity of the strongest δ-ferrite (110) peak decreases to near-background levels compared to the initial 08Cr18Ni10Ti steel. No new phases were detected at the steel-side weld interface within the detection limits of XRD.

It should be noted that the preferred {220} grain orientation in austenite – initially induced by rolling – is significantly reduced. The relative intensity of the austenite (220) reflection at the welded surface decreases by nearly half (2 times). This indicates recrystallization of austenitic grains in the weld interface region, likely induced by heat exposure and severe plastic deformation during EW. The heat exposure is caused by both plastic deformation and the impact of shock-compressed gas in the welding gap [30]. After removing a ~15 μm surface layer, the intensity of the austenite (220) reflection increases, demonstrating that recrystallization is localized to areas affected by shock loading.

The angular positions of austenite reflections remain identical before and after EW, indicating no change in its lattice parameter. This demonstrates the absence of significant dissolved aluminium in the austenitic phase within the 08Cr18Ni10Ti-side transition layer. It suggests that either no solid solution of Al forms in austenite, or its concentration is insufficient to alter the austenite lattice parameter. Notably, α-phase reflections (FCC Al-based solid solution) appear after removing a 15 μm layer from the 08Cr18Ni10Ti surface, despite this phase being absent at the immediate weld interface. Furthermore, a weak reflection of the $Al_{86}Fe_{14}$ quasi-crystalline phase emerges after the first layer removal – a phase later identified in the surface layer of the AlMg6 alloy post-welding.

The appearance of aluminium-based phases suggests material transfer of AlMg6 alloy grains into the 08Cr18Ni10Ti steel subsurface layer. It should be noted that the angular positions of several diffraction peaks for the α-phase (FCC structure) and ferrite (BCC structure) nearly coincide. Consequently, based on the obtained data, the presence of ferrite in the 08Cr18Ni10Ti surface layer after explosive welding cannot be confirmed. Thus, the primary phase in the steel's surface layer remains austenite, alongside phases transferred from the AlMg6 alloy during shock loading.

3.2.2. Analysis of the AlMg6 alloy fracture surfaces after explosive welding

Thus, this study demonstrates substantial phase transformation in the AlMg6 surface layer following EW. The diffraction patterns (Fig. 8) reveal not only reflections from the original α-phase but also two new phases: an FCC iron-based solid solution (γ-phase) and metastable icosahedral $Al_{86}Fe_{14}$. Removal of a 15 μm layer does not significantly reduce the intensity of these phases. The angular positions of γ-phase reflections match those of 08Cr18Ni10Ti steel's austenite, confirming austenite grain transfer into the AlMg6 surface during welding.

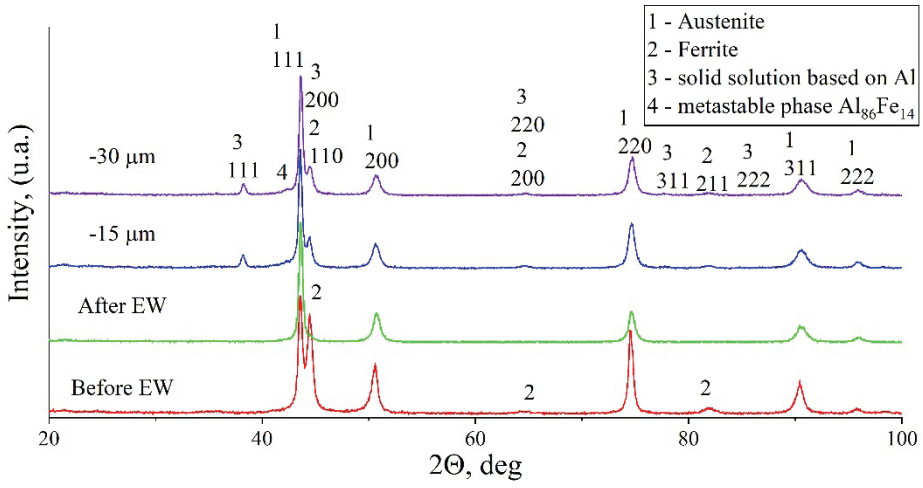

Fig. 7. XRD patterns of the 08Cr18Ni10Ti steel before and after explosive welding

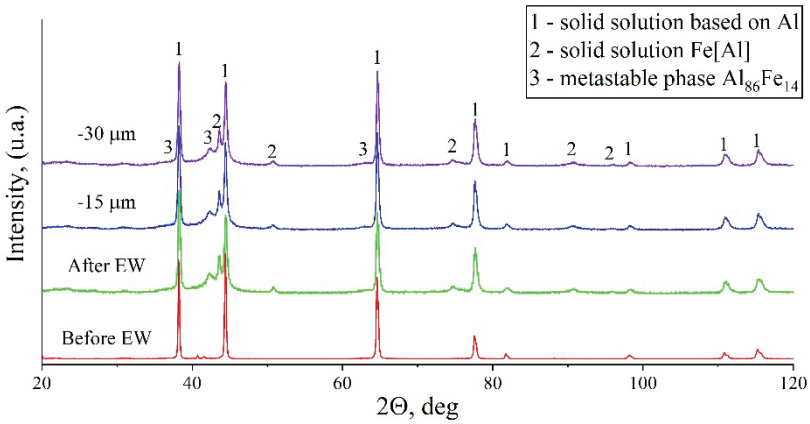

Fig. 8. XRD patterns of the AlMg6 surface before and after explosive welding

The metastable $Al_{86}Fe_{14}$ phase – previously reported by [31] – forms through rapid solidification ($2 \cdot 10^6$ K·s^{-1}) of Fe–Al melt. It features an icosahedral quasicrystalline structure lacking Bravais lattice periodicity. Notably, its diffraction peaks exhibit significant broadening, indicating nanocrystalline grain size (< 50 nm).

Heating would inevitably decompose the metastable $Al_{86}Fe_{14}$ phase. The differential thermal analysis in [31] demonstrated decomposition at 400 °C via $Al_{86}Fe_{14} \rightarrow Al_6Fe + Al$, followed by further transformation $Al_6Fe \rightarrow Al_3Fe + Al$ at ~530 °C. Thus, the altered phase composition in the AlMg6 surface layer results directly from shock-induced iron transfer from 08Cr18Ni10Ti steel during EW.

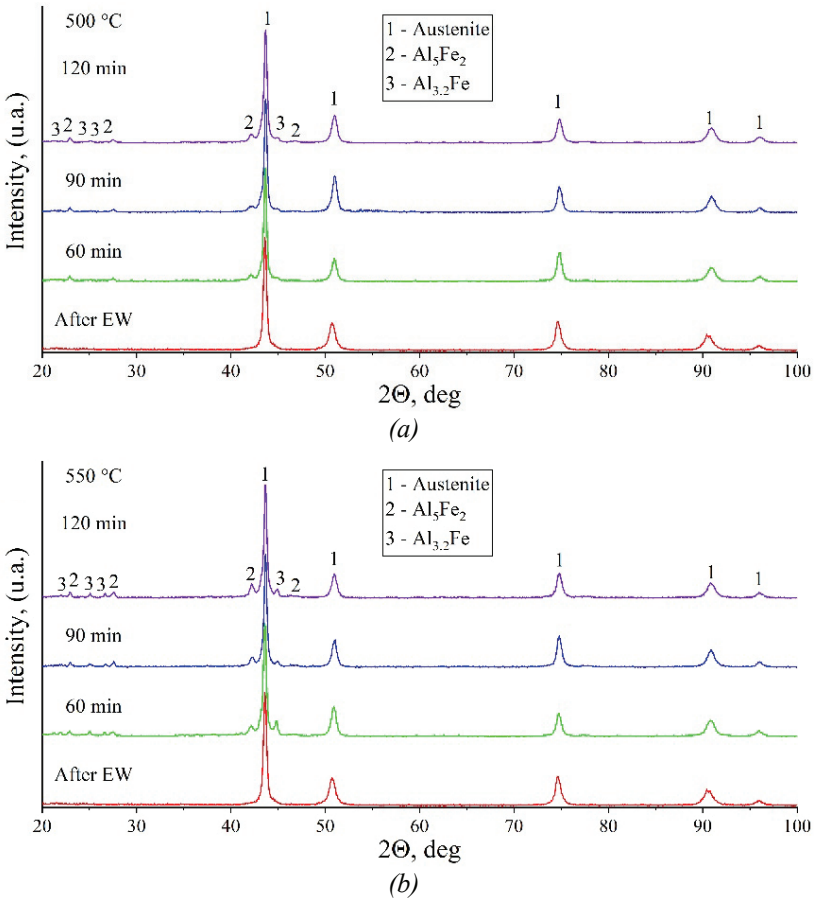

Fig. 9. XRD patterns of the 08Cr18Ni10Ti steel surface after explosive welding and isothermal annealing: *a* – 500 °C; *b* – 550 °C

3.3. Analysis of specimens after explosive welding and isothermal annealing at 500 and 550 °C

3.3.1. Analysis of the 08Cr18Ni10Ti steel surfaces after explosive welding and isothermal annealing at 500 and 550 °C for 60, 90, and 120 minutes

Isothermal annealing of explosively welded AlMg6–08Cr18Ni10Ti specimens at 500–550 °C for 60–120 min alters the phase composition in the steel interfacial region adjacent to AlMg6. Diffraction patterns (Figs. 9*a*, 9*b*) reveal reflections of two iron aluminides – Al_5Fe_2 and $Al_{3.2}Fe$ – alongside the dominant austenite phase. Intermetallic peak intensities increase with higher temperatures and longer durations. Given the absence of new phases at the steel interface in the as-welded state, these transformations confirm post-heating aluminium diffusion into the steel substrate and subsequent formation of iron aluminides upon cooling.

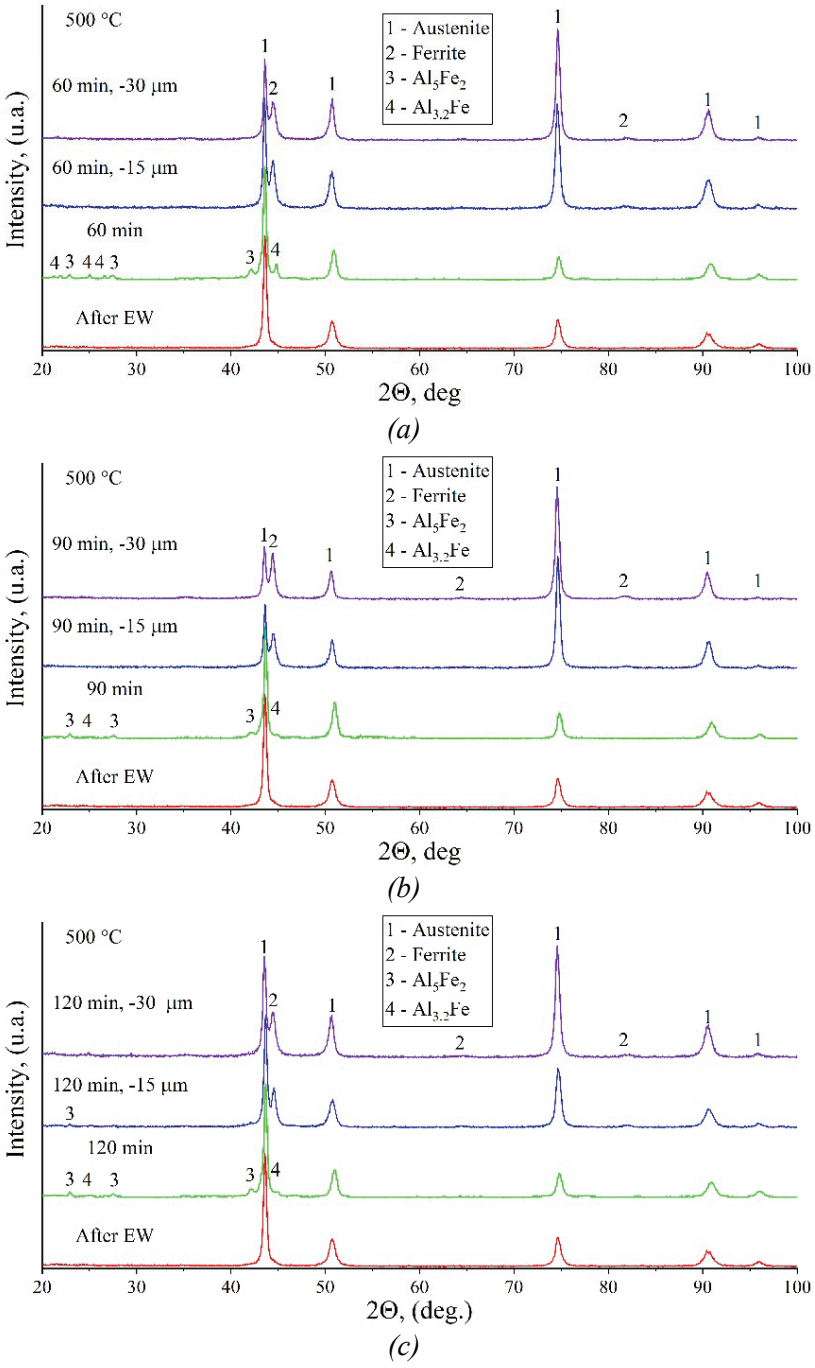

Fig. 10. XRD patterns of the 08Cr18Ni10Ti steel surface after explosive welding, isothermal annealing (at 500 °C), and surface layer removal for: *a* – 60 min; *b* – 90 min; *c* – 120 min

The layer-by-layer XRD analysis of the 08Cr18Ni10Ti steel surface confirms that removing a 15 μm layer eliminates reflections from iron aluminides formed during 500 °C annealing for 60–90 min (Figs. 10*a*, 10*b*). Reflections of α-phase (Al-based) and $Al_{86}Fe_{14}$ – previously detected in the steel subsurface after EW – also disappear. Critically, post-anneal diffraction patterns after 15 μm removal lack the characteristic α-phase (111) reflection at $2\theta \approx 38.5°$, which was prominent in the as-welded subsurface layer. This demonstrates that annealing dissolves aluminide phases through aluminium diffusion into austenite and ferrite solid solutions. For 120-minute treatments, aluminium penetration depth increases significantly: iron aluminide reflections persist until removal of a second steel layer (Fig. 10*c*).

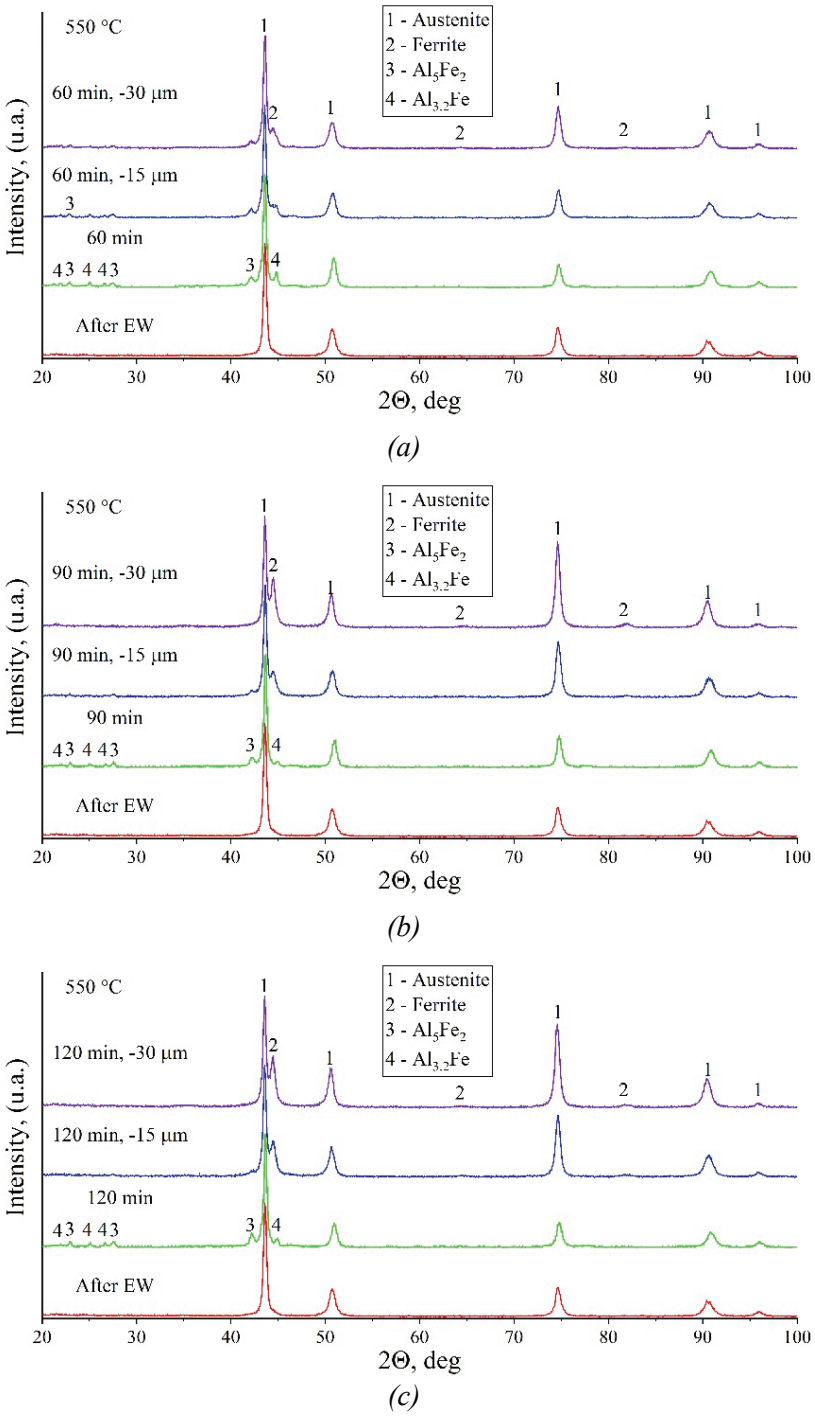

Fig. 11. XRD patterns of the 08Cr18Ni10Ti steel surface after explosive welding, isothermal annealing (at 550 °C), and surface layer removal for: *a* – 60 min; *b* – 90 min; *c* – 120 min

An identical trend occurs at 550 °C heat treatment (Figs. 11*a*, 11*b*). Iron aluminide reflections virtually disappear after 30μm layer removal for both 60- and 90-minute annealed samples. Layer-by-layer analysis further reveals that material removal progressively increases ferrite reflection intensity. After grinding away 30 μm, the intensity matches the pre-welding state of 08Cr18Ni10Ti steel (Fig. 11*c*). The preferred {220} grain orientation in the bulk 08Cr18Ni10Ti steel persists after 500 and 550 °C heat treatments. Consistent with this, removing 30 μm of material increases the intensity of the austenite (220) reflection (Figs. 10 and 11).

Thus, recrystallization of austenitic grains occurs exclusively at the weld interface region, driven by localized heating to high temperatures at the contact zone between 08Cr18Ni10Ti steel and AlMg6 alloy sheets following shock loading.

3.3.2. Analysis of AlMg6 alloy surfaces after explosive welding and isothermal annealing at 500 and 550 °C for 60, 90, and 120 minutes

Isothermal annealing of explosively welded AlMg6–08Cr18Ni10Ti samples at 500–550 °C for 60–120 min alters the phase composition in the AlMg6 interfacial region adjacent to the steel. Diffraction patterns (Fig. 12) reveal reflections of intermetallic phases Al_5Fe_2 and $Al_{13}Fe_4$ – previously identified in the steel interfacial layer after annealing- alongside the primary α-phase (FCC Al-based solid solution). Additionally, reflections of the ternary phase $Cr_2Mg_3Al_{18}$ are observed. This confirms that heating to 500 °C decomposes the metastable quasicrystalline $Al_{86}Fe_{14}$ phase formed in the AlMg6 surface layer during EW, resulting in crystalline iron aluminides Al_5Fe_2 and $Al_{13}Fe_4$. This transformation aligns with prior differential thermal analysis (DTA) study [1], where $Al_{86}Fe_{14}$ (produced by rapid Fe-Al melt quenching) decomposed at ~530 °C. Formation of the $Cr_2Mg_3Al_{18}$ ternary phase during annealing indicates chromium diffusion – a primary alloying element in 08Cr18Ni10Ti steel – into the AlMg6 surface layer, where it reacts with β-phase (Al_3Mg_2) present in the alloy. Intermetallic peak intensities increase with higher temperatures and longer durations.

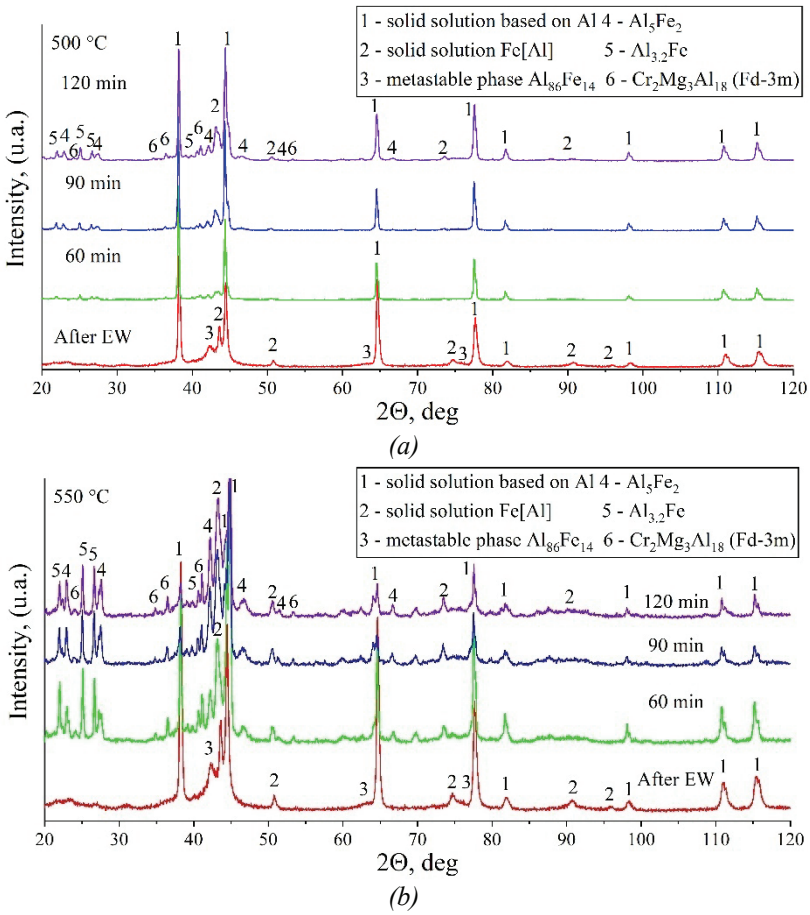

Fig. 12. XRD patterns of the AlMg6 alloy surface after explosive welding and isothermal annealing for 60, 90, and 120 min at: *a* – 500 °C; *b* – 550 °C

The layer-by-layer XRD analysis of the AlMg6 alloy surface reveals that removing 14–42 μm of material does not fully eliminate intermetallic reflections formed during 500 °C (Fig. 13) and 550 °C (Fig. 14) annealing for 60–120 min. The thickness of the aluminide-containing layer increases with prolonged annealing. Consequently, even after grinding away two layers (~30 μm) from the AlMg6 surface, reflections from Al_5Fe_2, $Al_{13}Fe_4$, and $Cr_2Mg_3Al_{18}$ retain significant intensity.

Thus, the explosive-welding-modified layer depth is greater in AlMg6 alloy than in 08Cr18Ni10Ti steel, attributable to localized melting of the AlMg6 surface. The presence of a liquid phase – where bulk diffusion coefficients exceed solid-state values by 4–5 orders of magnitude – enables dissolution of iron and alloying elements from the steel into the molten AlMg6 layer, followed by formation of aluminium-based intermetallic phases (Fig. 14).

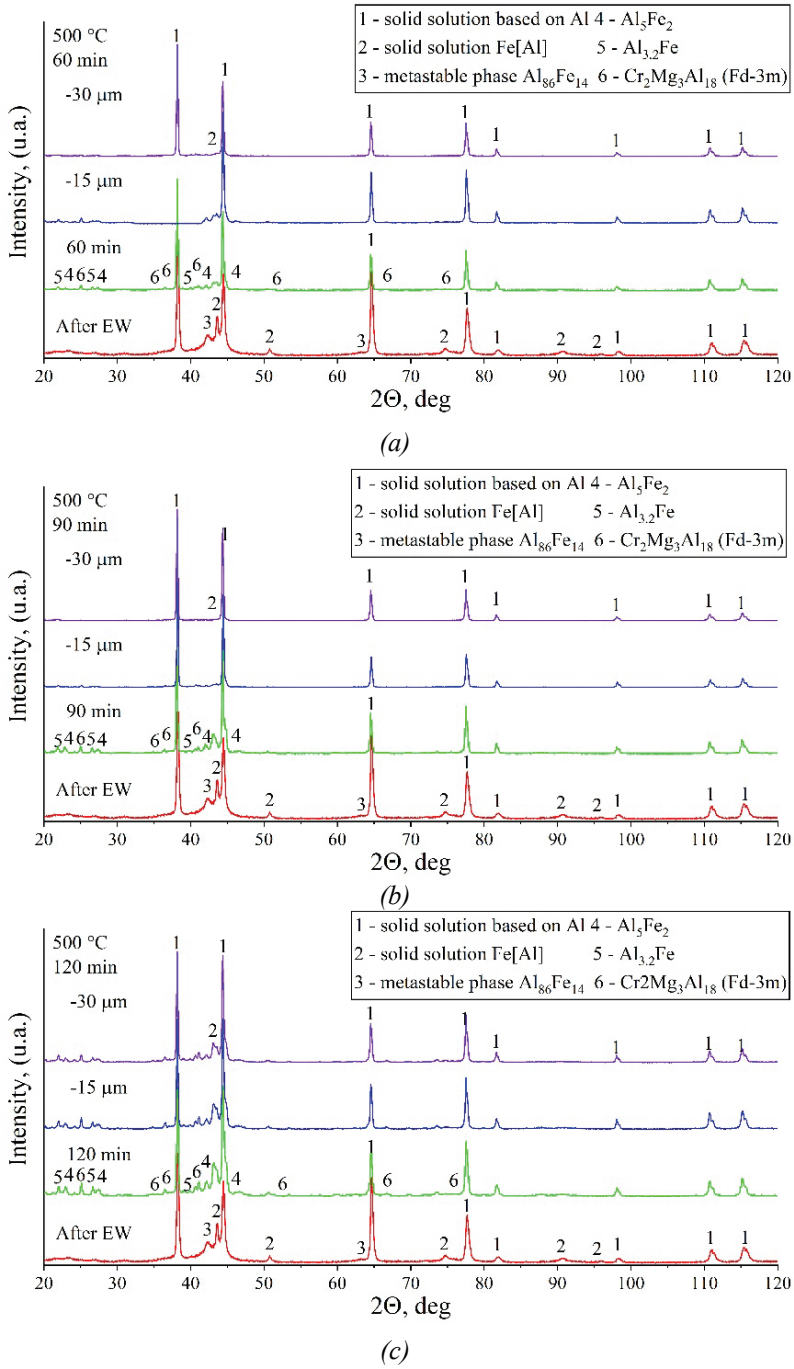

Fig. 13. XRD patterns of the AlMg6 surface after explosive welding, isothermal annealing (at 500 °C), and surface layer removal for: *a* – 60 min; *b* – 90 min; *c* – 120 min

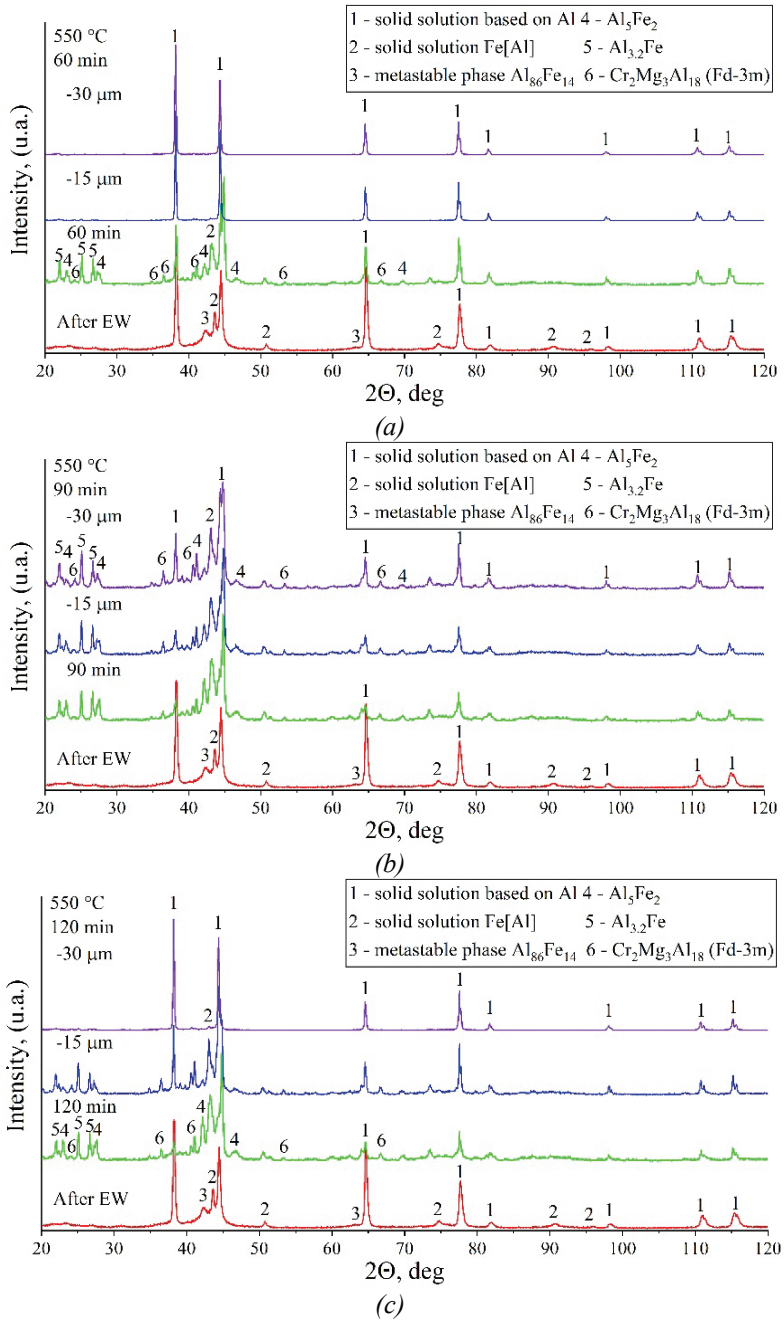

Fig. 14. XRD patterns of the AlMg6 surface after explosive welding, isothermal annealing (at 550 °C), and surface layer removal for: *a* – 60 min; *b* – 90 min; *c* – 120 min

4. Conclusion

The observed recrystallization of austenitic grains in 08Cr18Ni10Ti steel near the weld interface is determined by the combined effect of plastic deformation and localized heating during explosive welding. The presence of the α-phase and the quasicrystalline $Al_{86}Fe_{14}$ phase in the subsurface layer of 08Cr18Ni10Ti steel after removing a 15 μm-thick layer indicates the transfer of aluminium from the AlMg6 alloy. This process likely occurs due to mechanical mixing and localized melting, promoting the formation of new phases. In the surface layer of the AlMg6 alloy after explosive welding, changes in the phase composition are observed, associated with the transfer of iron from 08Cr18Ni10Ti steel. This leads to the formation of an FCC iron-based solid solution (γ-phase) and the metastable icosahedral $Al_{86}Fe_{14}$ phase.

Isothermal annealing of the bimetallic sample results in the diffusion of aluminium deeper into the steel and the subsequent formation of iron aluminides upon cooling. It is evident that annealing leads to the dissolution of aluminide phases, forming solid

solutions of aluminium in austenite and ferrite. Thus, it is clear that the recrystallization of austenitic grains occurs only in the weld interface region and is associated with localized heating to high temperatures in the contact zone of 08Cr18Ni10Ti steel and AlMg6 alloy plates after exposure to plastic deformation and shock-compressed gas. The layer-by-layer XRD analysis revealed that the removal of material layers leads to an increase in the intensity of ferrite reflections. After removing a 30 μm-thick layer, the reflection intensity reaches values characteristic of the material's initial state before explosive welding. This indicates that the top layer, subjected to the most intense impact during welding, contains structural changes that can be eliminated by removing a thin surface layer. The restoration of the initial ferrite characteristics after removing 30 μm confirms that these changes are localized in the surface zone and do not affect the deeper material layers. The findings extend the current understanding of the mechanisms governing phase formation and diffusion processes during explosive welding, and also shed light on the effect of thermal exposure on phase evolution.

5. Funding

This work was supported by Russian Science Foundation No. 23-19-00446, https://rscf.ru/project/23-19-00446/

Финансирование

Исследование выполнено за счет средств гранта Российского научного фонда № 23-19-00446, https://rscf.ru/project/23-19-00446/

6. Acknowledgements

This research was performed by using the set of modern scientific instruments available for multiple accesses at the ISMAN Center of Shared Services.

Благодарности

Данное исследование было проведено с применением комплекса современных научных приборов на базе Центра коллективного пользования ИСМАН.

7. Conflict of interests

The authors declare no conflict of interest.

Конфликт интересов

Авторы заявляют об отсутствии конфликта интересов.

References

1. Starke EA, Rashed HMMA. Alloys: aluminum. In: *Reference Module in Materials Science and Materials Engineering*. Elsevier; 2017. DOI:10.1016/B978-0-12-803581-8.09210-9

2. Pesin AM, Pustovoytov DO, Steblyanko VL, Fedoseev SA. Physical and computer simulation of severe plastic deformations on shear-compression testing of AMg6 (AMr6) aluminium alloy. *Non-Ferrous Metals*. 2017;42(1):17-21. DOI:10.17580/nfm.2017.01.04

3. Wahid MA, Siddiquee AN, Khan ZA. Aluminum alloys in marine construction: characteristics, application, and problems from a fabrication viewpoint. *Marine Systems & Ocean Technology*. 2020;15(1):70-80. DOI:10.1007/s40868-019-00069-w

4. Yang J, Li Y long, Zhang H. Microstructure and mechanical properties of pulsed laser welded Al/steel dissimilar joint. *Transactions of Nonferrous Metals Society of China*. 2016;26(4):994-1002. DOI:10.1016/S1003-6326(16)64196-1

5. Moreno-Blanco J, Petitpas G, Espinosa-Loza F, Elizalde-Blancas F, et al. The fill density of automotive cryo-compressed hydrogen vessels. *International Journal of Hydrogen Energy*. 2019;44(2):1010-1020. DOI:10.1016/j.ijhydene.2018.10.227

6. Agudo L, Eyidi D, Schmaranzer CH, Arenholz E, et al. Intermetallic Fe_xAl_y-phases in a steel/Al-alloy fusion weld. *Journal of Materials Science*. 2007;42(12):4205-4214. DOI:10.1007/s10853-006-0644-0

7. Rathod MJ, Kutsuna M. Joining of aluminum Alloy 5052 and low-carbon steel by laser roll welding. *Welding Journal*. 2004;83(1):16-26.

8. Shubhavardhan RN, Surendran S. Friction welding to join stainless steel and aluminum materials. *International Journal of Metallurgical & Materials Science and Engineering*. 2012;2:53-73.

9. Tsujino J, Hidai K, Hasegawa A, Kanai R, et al. Ultrasonic butt welding of aluminum, aluminum alloy and stainlesssteel plate specimens. *Ultrasonics*. 2002;40(1-8):371-374. DOI:10.1016/S0041-624X(02)00124-5

10. Acarer M, Demir B. An investigation of mechanical and metallurgical properties of explosive welded aluminum-dual phase steel. *Materials Letters*. 2008;62(25):4158-4160. DOI:10.1016/j.matlet.2008.05.060

11. Sierra G, Peyre P, Deschaux-Beaume F, Stuart D, et al. Steel to aluminium key-hole laser welding. *Materials Science and Engineering: A*. 2007;447(1-2):197-208. DOI:10.1016/j.msea.2006.10.106

12. Bugajska M, Maj L, Jarzebska A, Terlicka S, et al. Variety of aluminum/steel interface microstructures formed in explosively welded clads followed by the weld's thermal expansion response. *Journal of Materials Engineering and Performance*. 2022;31(9):7088-7097. DOI:10.1007/s11665-022-07027-5

13. He P, Yue X, Zhang JH. Hot pressing diffusion bonding of a titanium alloy to a stainless steel with an aluminum alloy interlayer. *Materials Science and*

Engineering: A. 2008;486(1-2):171-176. DOI:10.1016/j.msea.2007.08.076

14. Giudice F, Missori S, Scolaro C, Sili A. A review on metallurgical issues in the production and welding processes of clad steels. *Materials*. 2024;17(17):4420. DOI:10.3390/ma17174420

15. Schubert E, Klassen M, Zerner I, Walz C, et al. Light-weight structures produced by laser beam joining for future applications in automobile and aerospace industry. *Journal of Materials Processing Technology*. 2001;115(1): 2-8. DOI:10.1016/S0924-0136(01)00756-7

16. Chen X, Inao D, Tanaka S, Mori A, et al. Explosive welding of Al alloys and high strength duplex stainless steel by controlling energetic conditions. *Journal of Manufacturing Processes*. 2020;58:1318-1333. DOI:10.1016/j.jmapro.2020.09.037

17. Potesser M, Schoeberl T, Antrekowitsch H, Bruckner J. The characterization of the intermetallic Fe–Al layer of steel-aluminum weldings. In: *EPD Congress 2006*, Howard SM et al (eds). TMS; 2016. p. 167-176.

18. Gąsior W, Dębski A, Moser Z. Formation enthalpy of intermetallic phases from Al–Fe system measured with solution calorimetric method. *Intermetallics.* 2012;24:99-105. DOI:10.1016/j.intermet.2012.02.001

19. Shirzadi AA, Zhang C, Mughal MZ, Xia P. Challenges and latest developments in diffusion bonding of high-magnesium aluminium alloy (Al-5056/Al-5A06) to stainless steels. *Metals*. 2022;12(7):1193. DOI:10.3390/met12071193

20. Li B, Han S, Ao W, Yang Y, et al. Investigation on microstructure and mechanical properties of the dissimilar lap welding of Al alloy to steel with different filler materials and laser powers. *The International Journal of Advanced Manufacturing Technology*. 2024;134(1-2): 935-948. DOI:10.1007/s00170-024-14185-4

21. Atabaki MM, Nikodinovski M, Chenier P, Ma J, et al. Welding of aluminum alloys to steels: an overview. *Journal for Manufacturing Science and Production*. 2014;14(2):59-78. DOI:10.1515/jmsp-2014-0007

22. Beygi R, Galvão I, Akhavan-Safar A, Pouraliakbar H, et al. Effect of alloying elements on intermetallic formation during friction stir welding of dissimilar metals: a critical review on aluminum/steel. *Metals*. 2023;13(4):768. DOI:10.3390/met13040768

23. Rahman SAA, Mamat S, Ahmad MI, Mungkung N, et al. Study on intermetallic compound (IMC) in dissimilar joining of steel and aluminum (Fe-Al) – a review paper. *Welding in the World*. 2024;68(9):2351-2376. DOI:10.1007/s40194-024-01784-8

24. Aceves SM, Espinosa-Loza F, Elmer JW, Huber R. Comparison of Cu, Ti and Ta interlayer explosively fabricated aluminum to stainless steel transition joints for cryogenic pressurized hydrogen storage. *International Journal of Hydrogen Energy*. 2015; 40(3):1490-1503. DOI:10.1016/j.ijhydene.2014.11.038

25. Aizawa Y, Nishiwaki J, Harada Y, Muraishi S, et al. Experimental and numerical analysis of the formation behavior of intermediate layers at explosive welded Al/Fe joint interfaces. *Journal of Manufacturing Processes*. 2016;24:100-106. DOI:10.1016/j.jmapro.2016.08.002

26. Sherpa BB, Rani R. Advancements in explosive welding process for bimetallic material joining: A review. *Journal of Alloys and Metallurgical Systems*. 2024; 6:100078. DOI:10.1016/j.jalmes.2024.100078

27. Haidara F, Record MC, Duployer B, Mangelinck D. Phase formation in Al–Fe thin film systems. *Intermetallics*. 2012;23:143-147. DOI:10.1016/j.intermet.2011.11.017

28. Malakhov AY, Saikov IV, Denisov IV, Niyezbekov NN. AlMg6 to titanium and AlMg6 to stainless steel weld interface properties after explosive welding. *Metals*. 2020;10(11):1500. DOI:10.3390/met10111500

29. Lysak VI, Kuzmin SV. Energy balance during explosive welding. *Journal of Materials Processing Technology*. 2015;222:356-364. DOI:10.1016/j.jmatprotec.2015.03.024

30. Malakhov A, Denisov I, Niyozbekov N, Saikov I, et al. Theoretical and experimental studies of the shock-compressed gas parameters in the welding gap. *Materials*. 2024;17(1):265. DOI:10.3390/ma17010265

31. Dunlap RA, Dini K. Formation, structure, and crystallization of metastable quasi-crystalline Al-transition metal alloys prepared by rapid solidification. *Canadian Journal of Physics*. 1985;63(10):1267-1269. DOI:10.1139/p85-208

Information about the authors / Информация об авторах

Andrey Yu. Malakhov, Cand. Sc. (Eng.), Senior Researcher, Merzhanov Institute of Structural Macrokinetics and Materials Science RAS (ISMAN), Chernogolovka, Russian Federation; ORCID 0000-0002-0567-7307; e-mail: sir.malahov2009@yandex.ru

Малахов Андрей Юрьевич, кандидат технических наук, старший научный сотрудник, Институт структурной макрокинетики и проблем материаловедения им. А. Г. Мержанова РАН (ИСМАН), Черноголовка, Российская Федерация; ORCID 0000-0002-0567-7307; e-mail: sir.malahov2009@yandex.ru

Dmitry Yu. Kovalev, D. Sc. (Phys. and Math.), Chief Research, ISMAN, Chernogolovka, Russian Federation; ORCID 0000-0002-8285-5656; e-mail: kovalev@ism.ac.ru

Ковалев Дмитрий Юрьевич, доктор физико-математических наук, главный научный сотрудник, ИСМАН, Черноголовка, Российская Федерация; ORCID 0000-0002-8285-5656; e-mail: kovalev@ism.ac.ru

Stepan A. Seropyan, Junior Research, ISMAN, Chernogolovka, Russian Federation; ORCID 0000-0002-3714-3983; e-mail: stepan.seropyan@yandex.ru

Nemat N. Niyozbekov, Junior Research, ISMAN, Chernogolovka, Russian Federation; ORCID 0000-0003-1812-2930; e-mail: nemat199595@mail.ru

Igor V. Denisov, Cand. Sc. (Eng.), Senior Researcher, ISMAN, Chernogolovka, Russian Federation; ORCID 0000-0002-1065-3318; e-mail: denisov@ism.ac.ru

Gulnaz R. Saikova, Cand. Sc. (Eng.), Senior Researcher, ISMAN, Chernogolovka, Russian Federation; ORCID 0000-0002-6542-7123; e-mail: gulnaz-84@mail.ru

Серопян Степан Арутюнович, младший научный сотрудник, ИСМАН, Черноголовка, Российская Федерация; ORCID 0000-0002-3714-3983; e-mail: stepan.seropyan@yandex.ru

Ниёзбеков Неъмат Ниёзбекович, младший научный сотрудник, ИСМАН, Черноголовка, Российская Федерация; ORCID 0000-0003-1812-2930; e-mail: nemat199595@mail.ru

Денисов Игорь Владимирович, кандидат технических наук, старший научный сотрудник, ИСМАН, Черноголовка, Российская Федерация; ORCID 0000-0002-1065-3318; e-mail: denisov@ism.ac.ru

Сайкова Гульназ Рафиковна, кандидат технических наук, старший научный сотрудник, ИСМАН, Черноголовка, Российская Федерация; ORCID 0000-0002-6542-7123; e-mail: gulnaz-84@mail.ru

Received 29 October 2025; Revised 28 November 2025; Accepted 03 December 2025

Original papers
Advanced structural materials, materials for extreme conditions

УДК 620.3 DOI: 10.17277/jamt-2026-11-02-118-128

The influence of graphene oxide additives on the structure of graphite/boron nitride filler and tribological characteristics of anti-friction material

© Roman D. Balabanov[a]✉, Tatyana P. Dyachkova[a], Irina V. Gutnik[a], Nikolay A. Chapaksov[a], Elena A. Burakova[a]

[a] *Tambov State Technical University, Bld. 2, 106/5, Sovetskaya St., Tambov, 392000, Russian Federation*

✉ balabanoff98@gmail.com

Abstract. The influence of graphene oxide (GO) additives on the structure of the graphite/hexagonal boron nitride hybrid filler and the tribotechnical characteristics of anti-friction composites obtained on its basis was assessed. The nanocomposite preparation method included obtaining the filler (mixture) through mechanical activation of the components, hot mixing the mixture with high-temperature coal tar pitch, pressing, and high-temperature firing. To ensure hermetic sealing, the products were finally impregnated with a furfuryl alcohol solution, followed by polymerization at 300°C. Mixture samples were analysed using thermogravimetry and X-ray diffraction analysis. It was found that with an increase in GO content to 2.80 wt.%, the thermal stability of the mixture increased, after which it began to decline. The dependence of the crystal structure parameters of the filler components (L_c and N) on the GO concentration also exhibited an extreme behaviour. A sample of the charge containing 1.64 wt. % graphene oxide is characterized by maximum L_c and N values for boron nitride and minimum values for the graphite component. Furthermore, the filler of this composition demonstrates maximum sorption capacity for pitch, which contributes to the formation of a high-density and durable material. The finished nanocomposite demonstrates gas permeability of less than 1×10^{-5} $cm^2 \cdot s^{-1}$ and compressive strength equal to 197.5 MPa, which is 1.5 times higher than that of an analogue (NIGRAN-V). Bench tests showed that due to the introduction of graphene oxide into the filler composition, wear intensity is reduced by 16 times compared to a sample based on an unmodified charge. The nanocomposite of the optimal composition remains hermetically sealed under extreme operating conditions and can serve as the basis for the creation of high-density and ultra-strong anti-friction materials suitable for use in sealed friction units of pump and compressor systems.

Keywords: graphene oxide; graphite; boron nitride; nanocomposite; sealed anti-friction material.

For citation: Balabanov RD, Dyachkova TP, Gutnik IV, Chapaksov NA, Burakova EA. The influence of graphene oxide additives on the structure of graphite/boron nitride filler and tribological characteristics of anti-friction material. *Journal of Advanced Materials and Technologies*. 2026;11(2):118-128. DOI: 10.17277/jamt-2026-11-02-118-128

Влияние добавок оксида графена на структуру наполнителя графит/нитрид бора и триботехнические характеристики антифрикционного материала

© Р. Д. Балабанов[a]✉, Т. П. Дьячкова[a], И. В. Гутник[a], Н. А. Чапаксов[a], Е. А. Буракова[a]

[a] *Тамбовский государственный технический университет, ул. Советская, 106/5, пом. 2, Тамбов, 392000, Российская Федерация*

✉ balabanoff98@gmail.com

Аннотация. Проведена оценка влияния добавок оксида графена (ОГ) на структуру гибридного наполнителя графит/гексагональный нитрид бора и триботехнические характеристики антифрикционных композитов, полученных на его основе. Методика приготовления нанокомпозитов включала получение наполнителя (шихты)

посредством механической активации компонентов, горячее смешивание шихты с высокотемпературным каменноугольным пеком, прессование и высокотемпературный обжиг. Для придания герметичности на финальной стадии изделия подвергались пропитке раствором фурфурилового спирта с последующей полимеризацией при 300 °C. Образцы шихты изучали методами термогравиметрии и рентгенофазового анализа. Установлено, что при увеличении содержания ОГ до 2,80 мас. % термическая стабильность шихты росла, а после снижалась. Зависимость параметров кристаллической структуры компонентов наполнителя (L_c и N) от концентрации ОГ также имела экстремальный характер. Образец шихты, содержащей 1,64 мас. % оксида графена, характеризовался максимальными значениями L_c и N для нитрида бора и минимальными – для графитового компонента. Кроме того, наполнитель данного состава демонстрировал максимальную сорбционную емкость по пеку, что способствует формированию высокоплотного и прочного материала. Готовый нанокомпозит демонстрировал газопроницаемость менее 1×10^{-5} см^2/с и прочность при сжатии, равную 197,5 МПа, что в 1,5 раза выше, чем у аналога (НИГРАН-В). В результате стендовых испытаний установлено, что за счет введения в состав наполнителя оксида графена интенсивность износа снижается в 16 раз по сравнению с образцом на основе немодифицированной шихты. Нанокомпозит оптимального состава остается герметичным в экстремальных условиях эксплуатации и может являться основой для создания высокоплотных и сверхпрочных антифрикционных материалов, пригодных для использования в герметичных узлах трения насосных и компрессорных систем.

Ключевые слова: оксид графена; графит; нитрид бора; нанокомпозит; герметичный антифрикционный материал.

Для цитирования: Balabanov RD, Dyachkova TP, Gutnik IV, Chapaksov NA, Burakova EA. The influence of graphene oxide additives on the structure of graphite/boron nitride filler and tribological characteristics of anti-friction material. *Journal of Advanced Materials and Technologies*. 2026;11(2):118-128. DOI: 10.17277/jamt-2026-11-02-118-128

1. Introduction

Ensuring high ductility of the anti-friction layer in dry friction units while simultaneously maintaining the material's structural density is an extremely difficult task [1, 2]. Typically, when producing self-lubricating composites, hermetic sealing is sacrificed for a low friction coefficient, making such materials unsuitable for use in modern high-pressure pump and compressor systems [3, 4]. Therefore, the development of composites with increased hermetic seal is critical for the reliable operation of sealing elements that prevent leaks in pumping units and compressors of modern technical devices.

The challenge of achieving high sealing performance combined with low friction remains unresolved, as traditional graphite materials often exhibit porosity that reduces their barrier properties [5], and the incorporation of conventional fillers does not always allow for the desired balance of mechanical and tribological characteristics to be achieved [6].

The advent of graphene and the subsequent development of methodologies for producing diverse nanostructures based on it have catalyzed research endeavors aimed at utilizing such materials in the field of tribology [7]. As demonstrated in studies [8, 9], there is considerable potential for the utilization of graphene oxide (GO) in anti-friction composites. The presence of oxygen-containing functional groups on GO facilitates chemical interaction with matrices and fillers, thereby ensuring uniform distribution of components throughout the composite volume and, consequently, enhancing the adhesive strength of the resultant material [10–12]. The utilization of GO additives in anti-friction materials has been demonstrated to reduce the coefficient of friction by forming a thin transfer film on the counterface, thereby significantly enhancing their sealing properties [13–14]. The low gas permeability of the resulting composites is ensured by the "labyrinth effect," which is effectively realized when the GO is uniformly distributed throughout the volume [15–17].

At the same time, according to [18], using graphene oxide alone as a filler generally fails to provide the required load-bearing capacity and thermal conductivity of the composite in the contact zone. To achieve a synergistic effect, combinations of GO with traditional solid lubricants – graphite [19] and hexagonal boron nitride (h-BN) [20–21] – can be used. Graphite provides high thermal conductivity and excellent lubricity in a wet environment, while boron nitride demonstrates high thermal stability and chemical inertness, performing well in conditions where graphite begins to oxidize [22–23]. The use of a mixture of fillers allows for the production of materials suitable for a wide range of operating conditions [24].

Most of the known studies concentrate on binary systems (graphene oxide–graphite or graphene oxide–boron nitride). However, combining graphite, boron nitride, and graphene oxide within a singular compositional system may help achieve maximum

effects [25]. The primary challenge in the formation of such materials stems from the agglomeration of dissimilar particles and the non-uniform distribution of nanoscale GO between graphite microparticles and h-BN [26–27]. The lack of fundamental knowledge regarding the mechanisms of interphase interaction in the "graphene oxide–boron nitride–graphite" ternary systems hinder the creation of materials with predictable tribotechnical properties [28–29]. Studies generally overlook the influence of filler morphology and orientation on the formation of tribolayers and structural integrity, despite the fact that these factors determine the sealing ability of the composite [30–33]. The objective of this research is to establish the patterns through which graphene additives influence the structure of "graphite–boron nitride" hybrid fillers and the tribological characteristics of the final composites.

2. Materials and Methods

2.1. Initial components

The starting components used to prepare the filler were MPG-7 synthetic graphite (apparent density 1.8 g·cm^{-3}) and hexagonal boron nitride (particle size less than 30 μm). A 1% aqueous suspension of graphene oxide (NanoTechCenter, Tambov) was used as a modifying additive. High-temperature coal tar pitch (softening point 148 °C) was used to form the composite matrix. The impregnating agent was a 95 % solution of furfuryl alcohol (Pallav Chemicals).

2.2. Sample preparation method

The sample preparation procedure included a mechanical activation step, carried out in a high-speed pulverizing machine (RT-N06SF, Rong Tsong Precision Technology, Taiwan), to ensure a homogeneous distribution of graphite throughout the charge. First, the graphite was ground into two fractions: one with particle sizes up to 30 μm and another ranging from 30 to 63 μm. Boron nitride and fine-fraction synthetic graphite (< 30 μm) were then loaded into the pulverizing machine at a mass ratio of 59:100. The nanomodifier content was varied between 0 and 3.66 wt. %. Mixing was performed at a blade rotation speed of 25,000 rpm for 30 s.

The resulting batch was subsequently combined with artificial graphite (particle size 30-63 μm) and pitch at a mass ratio of 1:2:2. This mixture was placed in a Z-blade mixer, heated to 230 °C, and processed for 30 min. After unloading and cooling, the mixture was ground in the pulverizing machine until a powder with particle sizes below 90 μm was obtained. The powder was then pressed in a 40-mm-diameter mold at 200 MPa using an AUTO M-PL 3890 (Carver, USA) press. The resulting cylindrical compacts (Fig. 1*a*) were finally fired at 900 °C.

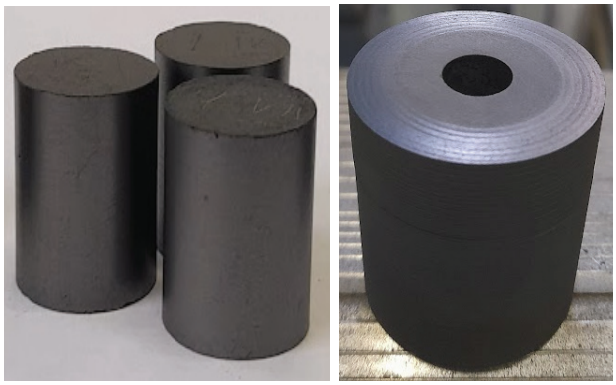

(a) *(b)*

Fig. 1. Photographs of cylindrical compacts (*a*) and a finished sample (*b*)

To ensure tight seal, the samples were additionally impregnated with a furfuryl alcohol solution, followed by polymerization at 300 °C. A photo of the finished sample is shown in Fig. 1*b*.

2.3 Evaluation of mixture adsorption capacity toward the binder and tribotechnical testing

The adsorption capacity of the mixture with respect to the pitch was determined by the difference in the optical density (OD) of the pitch solution in toluene before (D_0) and after (D_1) contact with the adsorbent, as measured on a UNICO 1201 (Unico, USA) photometric colorimeter using a 540 nm filter. Using a calibration curve, the concentrations (mg·mL^{-1}) of pitch C_0 and C_1 corresponding to the optical densities D_0 and D_1 were determined. The adsorption capacity of the filler (A_s, mg·m^{-2}) was calculated using the formula:

$$A_s = \frac{(C_0 - C_1)V}{mS_{\text{BET}}},$$

where m is the mass of the batch sample, g; V is the volume of the pitch solution in toluene, mL; and S_{BET} is the specific surface area of the material according to the BET method, m^2·g^{-1}.

Tribological testing and verification of the sealing performance of the finished nanocomposite samples were conducted on a high-pressure test bench designed to simulate the operation of a centrifugal pump's mechanical seal. The "graphite composite–anti-friction bronze" contact pair was

tested at a constant rotational speed of 2000 rpm in a water-alcohol mixture with a viscosity equivalent to that of the sealed liquid. To assess the material's leak tightness in the friction zone, an overpressure of 29.4 MPa was maintained, which corresponds to the extreme operating conditions of mainline equipment.

Seal tightness was assessed using a manometric method based on pressure drop in the system and detection of leaks through the seal joint. The wear rate J was calculated as a dimensionless criterion determined by the ratio of the linear wear of the sample (I_l, m), recorded by the micrometric method after running-in and reaching a steady-state friction regime, to the total sliding distance (L, m):

$$J = \frac{I_l}{L}.$$

For illustrative purposes, the characteristics of the experimental nanocomposite samples were compared with those of the most widely used sealing anti-friction material, NIGRAN-V [34].

2.4. Analytical methods

X-ray diffraction patterns of the mixture samples were recorded using an ARL Equinox 1000 diffractometer (CuKα radiation, $\lambda = 1.5406$ Å). To determine the center and half-width of the reflections, peak deconvolution was performed using OriginPro software (calculation error $\chi < 10^{-6}$). The formulas used to determine the crystal structure parameters of the samples, based on X-ray phase analysis data with references to sources, are presented in Table 1.

Table 1. Processing of the X-ray phase analysis results

Parameter	Formula	Reference
D-space, d_{002}	$d_{002} = \frac{\lambda}{2\sin\theta}$	[35]
Cohesive scattering area, L_c	$L_c = \frac{K\lambda}{\beta\cos\theta}$, where $K = 0.89$, β – half-width of a reflection	[36]
Number of layers, N	$N = \frac{L_c}{d_{002}} + 1$	[36]

The TG-DSC curves of the filler were recorded on a STA 449 F3 Jupiter (Netzsch, Germany) simultaneous thermal analyzer in air at a heating rate of 10°C/min. Mechanical compression tests were performed on an Allround Line Z250 SR Materials Testing Machine (Zwick/Roell Group). The density and open porosity of the composite samples were determined by hydrostatic weighing in isooctane ($\rho = 0.696$ g·cm^{-3}) according to the standard method (Russian Standard 2409-2014). The specific surface area (S_{BET}) was measured based on nitrogen adsorption at 77 K using an ASAP 2020 analyzer (Micromeritics, USA) via the BET method. Images of the tribocontacting surfaces of anti-friction nanocomposite products were obtained using an Axiovert metallographic microscope (Zeiss, Germany) at 20× magnification.

3. Results and Discussion

X-ray diffraction patterns of charge samples with varying graphene oxide content, compared with graphite and hexagonal boron nitride, are shown in Fig. 2.

The X-ray diffraction pattern of graphite shows a distinct reflection of the (002) crystallographic plane at $2\theta = 26.3°$. Peaks of the (100) plane at 42.7°, (101) at 44.3°, (004) at 54.2°, (112) at 83°, and (006) at 87° are also identified but are less intense.

The X-ray diffraction pattern of the boron nitride sample has a typical appearance. It shows an intense reflection from the (002) basal plane at $2\theta = 26.4°$. Peaks for the (100) plane at 41.2°, (101) at 43.4°, (102) at 49.6°, (004) at 54.6°, (110) at 76°, and (006) at 88° are also present.

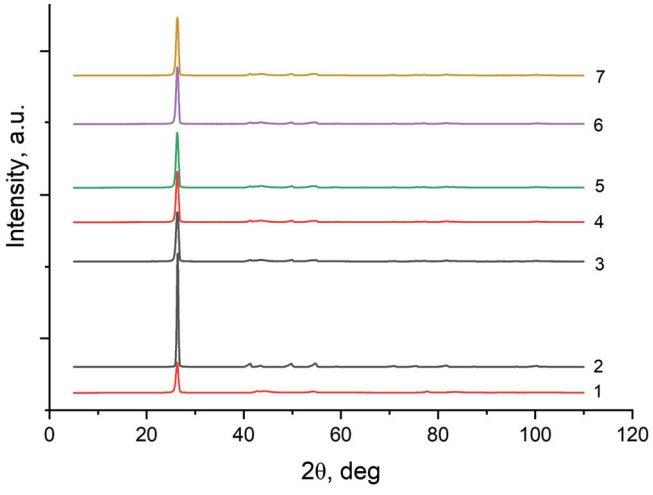

Fig. 2. X-ray diffraction patterns of graphite (*1*), hexagonal boron nitride (*2*) and charge samples containing 0 (*3*), 0.50 (*4*), 1.64 (*5*), 2.80 (*6*) and 3.66 (*7*) wt. % of graphene oxide

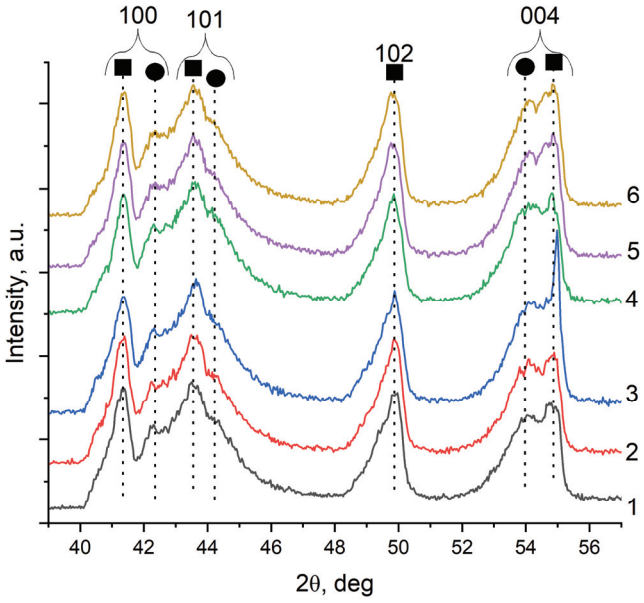

Fig. 3. Fragment of the X-ray diffraction patterns of experimental samples for the batch containing 0 (*1*), 0.50 (*2*), 1.64 (*3*), 2.80 (*4*) and 3.66 (*5*) wt. % of graphene oxide. Additional designations: ■ – boronnitride; ● – graphite

Thus, the most intense peaks on the diffraction patterns of graphite and h-BN appear virtually identical. The most distinct differences are observed in the 2θ range from 40 to 56°, which is why this specific section of the patterns of the charge samples was analyzed in greater detail (Fig. 3).

Analysis of the diffraction peaks of the experimental samples confirms that the hexagonal layered structure of the graphite and boron nitride phases is preserved during mechanical mixing in a pulverizing machine. Structural changes are most clearly observed in the second-order reflections from the (004) planes in the 54–55° range. The calculated crystal structure parameters of the experimental samples are presented in Table 2.

According to the obtained data, the introduction of GO exerts a nonlinear influence on the calculated crystallite parameters of the filler components following the cold mixing stage. The concentration dependence of both L_c and N on GO content exhibits an extremal character. At a GO content of 1.64 wt. %, the maximum values of L_c and N are observed for h-BN crystallites, suggesting ordered aggregation of this phase. In contrast, the graphite component shows the opposite trend: at the same GO concentration, its L_c and N values reach a minimum. Notably, the magnitude of these changes is substantially more pronounced for h-BN than for graphite.

It can therefore be assumed that, up to certain concentrations, GO acts as a “binding agent” for boron nitride particles, facilitating the formation of larger and more oriented stacks of h-BN layers under mechanical stress.

The decrease in the L_c and N parameters at graphene oxide concentrations above 1.64 wt. % is likely due to the fact that graphene oxide begins to act as a “dry lubricant” between the particles of the macrocomponents. As a result, the efficiency of mechanical energy transfer during grinding decreases, leading to layer disorientation and local disorder in the particle structure of the charge. The constancy of the interplanar spacing values (d_{002}) for both components suggests that during the mechanical activation process, GO does not penetrate the interlayer spaces of graphite and boron nitride, and its influence on the filler structure is due solely to surface effects.

Table 2. Results of X-ray phase analysis of the experimental samples

Component	Parameter	Values for the pure component	Values for the experimental sample with graphene oxide content, wt. %				
			0	0.5	1.64	2.8	3.66
Graphite	2θ, °	54.2	54.0	54.0	54.0	54.1	54.1
	d_{002}, Å	3.38	3.39	3.39	3.39	3.39	3.39
	L_c, Å	57.49	59.44	57.53	57.16	59.46	60.26
	N, units	18	19	18	18	19	19
Boron nitride	2θ, °	54.6	54.8	54.9	54.8	54.9	54.9
	d_{002}, Å	3.36	3.35	3.34	3.35	3.34	3.34
	L_c, Å	111.00	168.82	213.10	218.29	194.57	190.43
	N, units	34	51	65	66	59	58

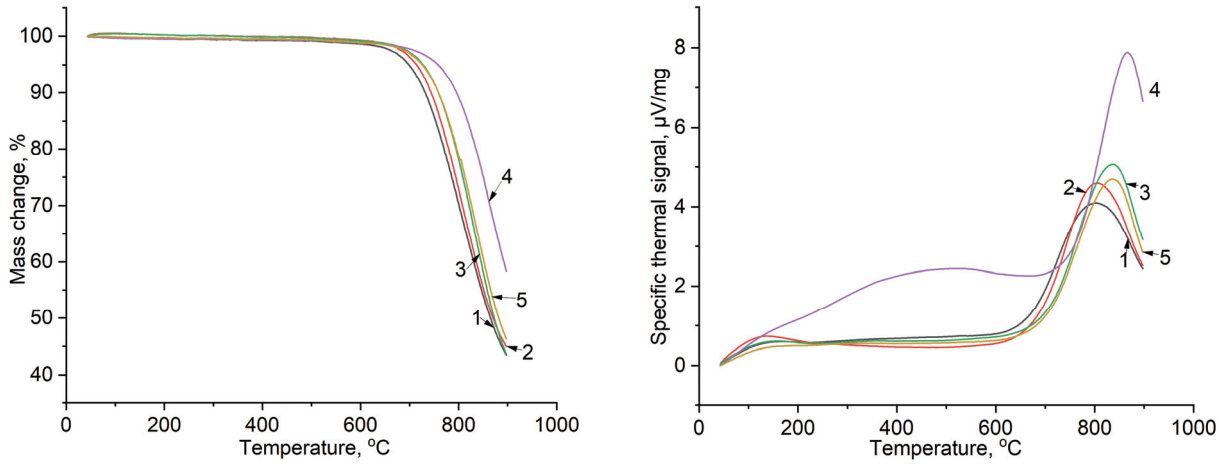

Fig. 4. TG (*a*) and DSC (b) curves of experimental samples of the batch containing 0 (*1*), 0.50 (*2*), 1.64 (*3*), 2.80 (*4*) and 3.66 (*5*) wt. % of graphene oxide

Figure 4 presents the results of simultaneous thermal analysis of the unmodified mixture and samples with different GO contents.

All studied samples remain thermally stable up to 600–650 °C, after which an intensive stage of oxidative destruction of the carbon phase begins. The effect of graphene oxide concentration on the thermal stability of the mixture is nonlinear. The sample containing 2.80 wt. % GO exhibits the highest stability, with the onset of decomposition shifted to 750 °C, whereas at other GO concentrations, decomposition begins at considerably lower temperatures. These differences in the onset temperature of thermal oxidation are likely attributable to the barrier effect of boron nitride particles, which hinder oxygen diffusion toward the graphite particles.

The DSC curves show distinct exothermic peaks in the 750–850 °C range, which corresponds to intense heat release during the oxidation of the carbon phase and confirms the thermogravimetric data on the material's decomposition. The nature of the curves suggests that the introduction of a nanomodifier affects the kinetics of the thermal oxidation process: for the sample with a content of 2.80 wt. %, the maximum heat release is shifted most to the high-temperature region. The presence of less pronounced exothermic peaks in the 100–600 °C range may be due to processes of structural rearrangement of graphene oxide or the removal of functional groups.

The properties of the final composite are significantly influenced not only by the structural but also by the textural characteristics of the filler. In this regard, as part of this work, the specific surface area (S_{BET}) values of the experimental charge samples and their adsorption capacity relative to carbon black (A_s) were determined and are presented in Table 3.

The S_{BET} dependence on GO concentration is minimal for the sample containing 1.64 % graphene oxide. Typically, materials with low specific surface areas exhibit low sorption activity. However, in this case, the sample with 1.64 % GO exhibits the maximum A_s value. Such an effect can occur only if the sorption of the pitch is specific in nature and takes place not over the entire surface of the filler, but only at active sites of a particular composition and structure. Oxygen-containing groups of graphene oxide can act as such active sites. At the optimal GO content, a filler structure is formed with the maximum number of functional groups available for the pitch sorption (Fig. 5). As the concentration of the nanomodifier (GO) increases, the filler structure is being rearranged, which contributes to a decrease in the number of active sites available for the adsorbate. This assumption is generally confirmed by the X-ray phase analysis data.

Table 3. Values of specific surface area and adsorption capacity of the filler samples

Graphene oxide content, %	S_{BET}, $m^2 \cdot g^{-1}$	A_s, $mg \cdot m^{-2}$
0	9.6	3.8
0.50	9.0	3.9
1.64	8.7	4.3
2.80	9.3	2.7
3.66	9.5	2.3

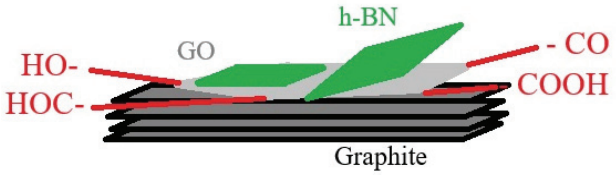

Fig. 5. Formation of a nanomodified boron nitride-graphite-graphene oxide filler

From the perspective of the composite manufacturing process, maximizing the A_s value ensures optimal wetting of the filler by the pitch binder during the hot mixing stage, which should contribute to the formation of a dense anti-friction material structure with minimal porosity.

During the next stage, the effect of the graphene oxide content in the mixture on the most important physical and mechanical properties of the experimental composite samples after the firing at 900 °C was evaluated. According to the data presented in Fig. 6, materials with a filler containing 1.64 wt. % of GO have minimum porosity and maximum compressive strength.

Thus, there is a correlation between the change in the filler structure upon modification with graphene oxide, its sorption capacity relative to the pitch, and the strength characteristics of the composite.

The best sample after firing had a porosity of 12.7 %, which is insufficient to ensure the required material impermeability. To reduce the porosity of the fired specimens, they were subjected to single and double impregnation with a furfuryl alcohol solution using the method described above, with subsequent polymerization at 300 °C.

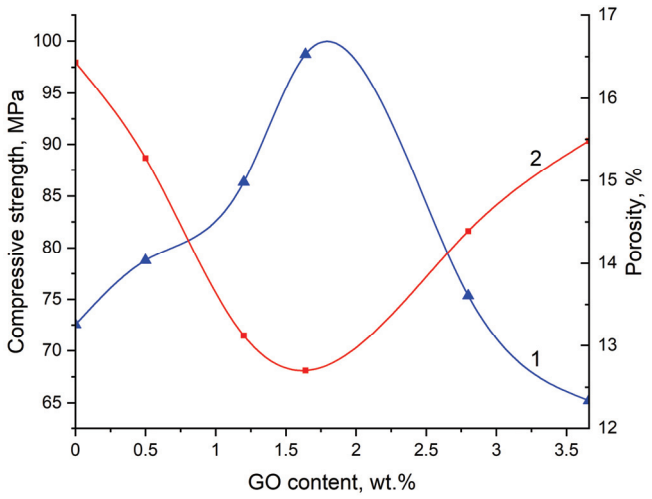

Fig. 6. The influence of graphene oxide content in the filler on the compressive strength (*1*) and porosity (*2*) of nanocomposite samples after firing at 900 °C

Table 4. Physical and mechanical properties of the finished samples of anti-friction nanocomposite in comparison with an analogous material

Number of impregnations with furfuryl alcohol solution	1	2	Analogue (NIGRAN-V)
Density, $g \cdot cm^{-3}$	1.79	1.82	1.80
Porosity, %	3.89	1.01	–
Compressive strength, MPa	–	197.5	130
Gas permeability, 10^{-5} $cm^2 \cdot s^{-1}$	107	<1	5

Thus, experimental samples of the final composite based on filler with a GO content of 1.64 wt. % were obtained. Their most important physical and mechanical properties are presented in Table 4.

After a single impregnation, the material's porosity decreases to 3.89 %, but it remains sufficiently gas-permeable. Double impregnation results in the formation of a sealed anti-friction composite that matches the density of its analogue (NIGRAN-V), has a lower gas permeability, yet its compressive strength of 197.5 MPa is 1.5 times higher than that of NIGRAN-V.

Thus, the use of GO as a charge modifier leads to the formation of a high-density and exceptionally durable material. An additional advantage lies in the relative simplicity of the nanocomposite production process. In contrast, conventionally used methods involve further processing of fired samples – comprising a product of mechanical treatment of synthetic fine-grained graphite and boron nitride bonded with pitch coke – by impregnation with coal tar pitch (softening point 65–110 °C), followed by high-temperature treatment at 1500–2050 °C and subsequent impregnation with a furfuryl alcohol solution [37].

To evaluate the developed anti-friction composite for use in sealed friction assemblies, tribotechnical bench tests were conducted on experimental samples based on both unmodified and graphene oxide-modified mixtures.

Figure 7 presents photographs of the tribologically mated surfaces of the disassembled friction assembly after testing the composites.

Following bench testing, the surface of the unmodified sample showed unacceptable defects in the form of flaking and the initiation of cracks concentric with the diameter. The observed morphological changes are indicative of fatigue failure processes occurring in the surface layer.

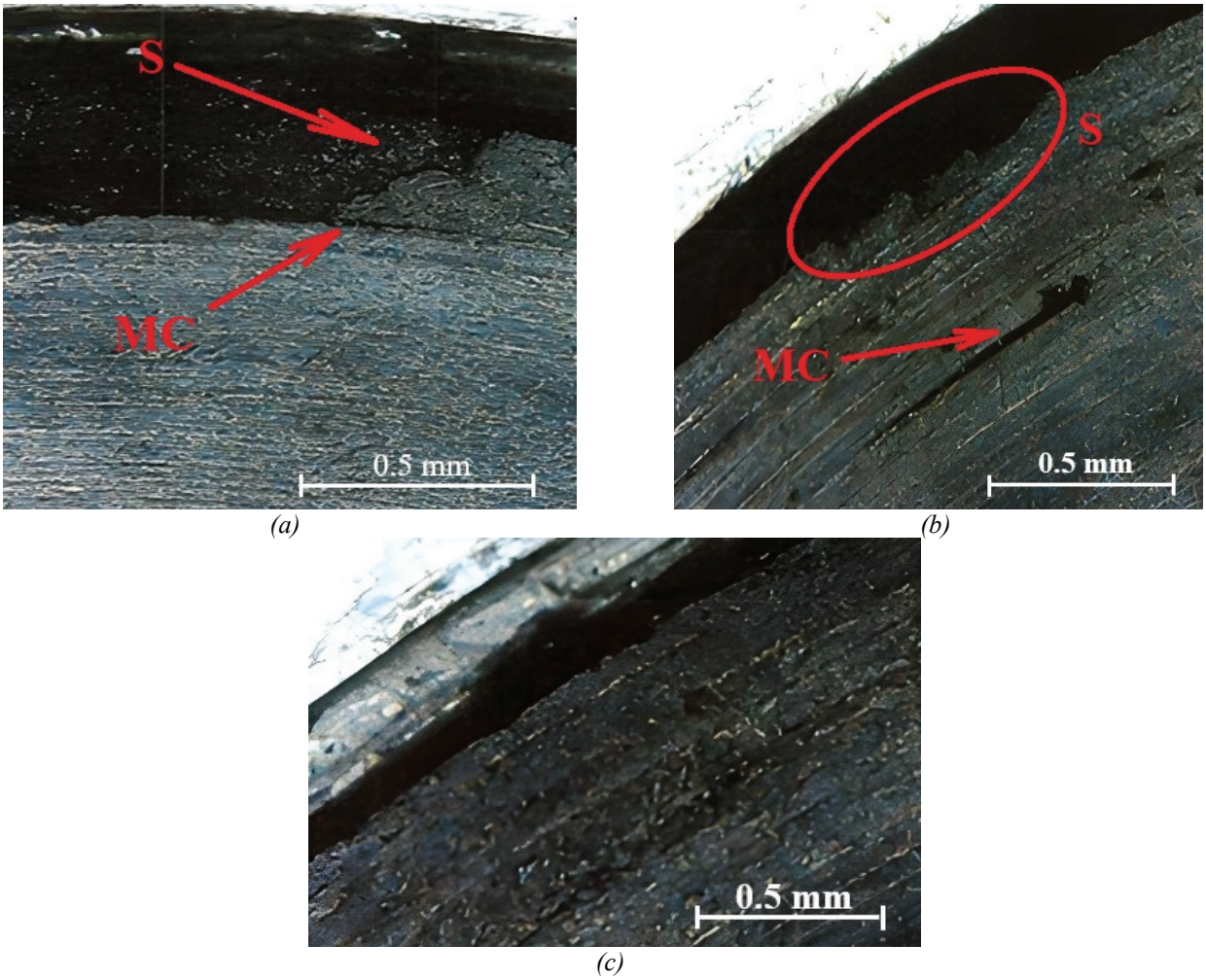

Fig. 7. Photographs of tribologically mated surfaces after testing samples of nanocomposites based on unmodified (*a*, *b*) and graphene oxide-modified (*c*) mixtures. Arrows indicate the presence of microcracks (MC) and spalling (S)

The sample based on a graphene oxide-modified mixture shows virtually no wear. Presumably, GO contributes to strengthening the bond between the filler and the binder, which is confirmed by a qualitative change in morphology after impregnation and polymerization of furfuryl alcohol (Fig. 7*c*), whereas in the control (unmodified) sample, there is a local concentration of stresses in the micropore zones (Fig. 7*a*, *b*). Under cyclic loading, these stresses trigger microcrack initiation and coalescence. The resulting crack network causes material spalling and rapid surface degradation.

Table 5. Bench test results

Graphene oxide content, wt. %	Wear rate, 10^{-9}	Seal tightness
0	59	Inleakage is observed
1.64	3.7	sealed

The data presented in Table 5 confirm the effectiveness of using GO in the composition of an anti-friction self-lubricating composite. By modifying the filler mixture, it is possible to increase the material's wear resistance by a factor of 16. Additionally, the composite retains its sealing properties even under extreme operating conditions.

4. Conclusion

This study identified key patterns in how graphene oxide influences both the formation of the matrix structure – comprising synthetic graphite and hexagonal boron nitride – and the performance properties of the resulting anti-friction composites. An addition of 1.64 wt. % graphene oxide proved critical for achieving an optimal balance of properties. At this concentration, the mixture exhibits maximum adsorption capacity for pitch, ensuring adequate wetting of the filler by the binder, which in turn facilitates the formation of a high-density matrix

with minimal open porosity. The effect of graphene oxide modification is already evident at the primary framework formation stage. Specifically, the ultimate strength of unfired samples containing 25 % graphene oxide is 25 % higher than that of the base formulation, thereby providing a structural foundation for subsequent densification. Furthermore, modifying the filler with graphene oxide, followed by impregnation with furfuryl alcohol, yielded exceptional strength characteristics due to a synergistic effect. The compressive strength reached 197.5 MPa – more than 1.5 times higher than that of the best comparable material (NIGRAN-V).

The results of tribological tests on the test bench confirmed the high effectiveness of the developed formulation. The modified composite demonstrated a nearly 16-fold reduction in wear rate compared to the base formulation, while maintaining complete sealing integrity under extreme conditions at a pressure of 29.4 MPa. Unlike unmodified samples, which are prone to fatigue spalling and the formation of main cracks, the developed material retains its structural integrity due to the strengthening effect of graphene oxide at the phase boundary. By modifying the mixture with graphene oxide, it is not only possible to obtain materials for friction components with significantly improved service life characteristics, but also to substantially simplify the manufacturing process for anti-friction composites by eliminating the stages of repeated high-temperature pitch impregnation.

5. Funding

The present study did not receive any external funding.

Финансирование

Настоящее исследование не получило внешнего финансирования.

6. Acknowledgements

This work has been done using the facilities of the shared access center “Production and Application of Multifunctional Nanomaterials” (Tambov State Technical University, Russia).

Благодарности

Работа выполнена с использованием оборудования центра коллективного пользования «Получение и применение полифункциональных наноматериалов» (Тамбовский государственный технический университет, Россия).

7. Conflict of interests

The authors declare no conflict of interest.

Конфликт интересов

Авторы заявляют об отсутствии конфликта интересов.

References

1. Chen F, Yan K, Hong J, Song J. Synergistic effect of graphene and β-Si_3N_4 whisker enables Si_3N_4 ceramic composites to obtain ultra-low friction coefficient. *Tribology International*. 2023;178:108045. DOI:10.1016/j.triboint.2022.108045

2. Nayak UP,Mücklich F, Guitar MA. Interplay between the microstructure and tribological performance of a destabilized 26 wt. % Cr HCCI: the influence of temperature and heating rate. *Tribology International.* 2023;185:108532. DOI:10.1016/j.triboint.2023.108532

3. Liu SH, Liang TH, Wang WG, Zhang BJ, et al. Tribological properties of graphene-reinforced graphite in high-temperature and high-pressure water. *Wear*. 2025;568-569:205967. DOI:10.1016/j.wear.2025.205967

4. Gong X, Chen H, Zhang F, Zhu W, et al. Degradation of tensile mechanical properties of two $Al_xCoCrFeNi$ ($x = 0.3$ and 0.4) high-entropy alloys exposed to liquid lead-bismuth eutectic at 350 and 500 °C. *Journal of Nuclear Materials*. 2022;558:153364. DOI:10.1016/j.jnucmat.2021.153364

5. Liang G, Zhang J, An S, Tang J, et al. Phase change material filled hybrid 2D/3D graphene structure with ultra-high thermal effusivity for effective thermal management. *Carbon.* 2021;176:11-20. DOI:10.1016/j.carbon.2020.12.046

6. Tofighy MA, Mohammadi T. Barrier, diffusion, and transport properties of rubber nanocomposites containing carbon nanofillers. In: *Carbon-Based Nanofillers and Their Rubber Nanocomposites*. Elsevier; 2019. p. 253-285. DOI:10.1016/B978-0-12-817342-8.00009-3

7. Wang R, Zhang F, Yang K, Xiong Y, et al. Review of two-dimensional nanomaterials in tribology: recent developments, challenges and prospects. *Advances in Colloid and Interface Science*. 2023;321:103004. DOI:10.1016/j.cis.2023.103004

8. Baiti A, Aldavud S, Algurabi A, Salhi H, et al. Modification of lubricants with graphite nanoplates. *Journal of Advanced Materials and Technologies*. 2023; 8(2):157-169. DOI:10.17277/jamt.2023.02.pp.157-169

9. Gao Q, Liu S, Hou K, Li Z, et al. Graphene-based nanomaterials as lubricant additives: a review. *Lubricants*. 2022;10(10):273. DOI:10.3390/lubricants10100273

10. Yu H, He Y, Xiao G, Fan Y, et al. The roles of oxygen-containing functional groups in modulating water purification performance of graphene oxide-based membrane. *Chemical Engineering Journal*. 2020;389:124375. DOI:10.1016/j.cej.2020.124375

11. Moazzami Gudarzi M, Sharif F. Enhancement of dispersion and bonding of graphene-polymer through wet transfer of functionalized graphene oxide. *Express Polymer*

Letters. 2012;6(12):1017-1031. DOI:10.3144/expresspolymlett.2012.107

12. Kukielski M, Kasprzak A, Zurowski R, Tanska J, et al. Functionalization of graphene oxide surface by conjugation with glucosamine and analysis of interactions occurring in nanoceramic-graphene heterostructures. *Powder Technology*. 2024;431:119089. DOI:10.1016/j.powtec.2023.119089

13. Wakchaure MB, Menezes PL. Advances in the tribological performance of graphene oxide and its composites. *Materials.* 2025;18(15):3587. DOI:10.3390/ma18153587

14. Sun J, Du S. Application of graphene derivatives and their nanocomposites in tribology and lubrication: a review. *RSC Advances*. 2019;9(69):40642-40661. DOI:10.1039/C9RA05679C

15. Ashfaq J, Channa IA, Memon AG, Chandio IA, et al. Enhancement of thermal and gas barrier properties of graphene-based nanocomposite films. *ACS Omega*. 2023;8(44):4105441063. DOI:10.1021/acsomega.3c02885

16. Bilisik K, Akter M. Polymer nanocomposites based on graphite nanoplatelets (GNPs): a review on thermal-electrical conductivity, mechanical and barrier properties. *Journal of Materials Science*. 2022;57(15):7425-7480. DOI:10.1007/s10853-022-07092-0

17. Zhao L, Peng R, Gao J, Li Y, et al. Strengthening mechanism of tribological properties of graphene oxide/multiwalled carbon nanotubes hybrid nanofluids: Molecular dynamics and experimental validation. *Journal of Colloid and Interface Science*. 2025;689:137154. DOI:10.1016/j.jcis.2025.02.162

18. Yang K, Xiong Y, Wu G, Lin H, et al. Multi-dimensional nano-additives for their superlubricity: tribological behaviors and lubrication mechanisms. *Advanced Materials Interfaces*. 2025;12(9):2400796. DOI:10.1002/admi.202400796

19. Balabanov R, Dyachkova T, Fedyushkina A, Gutnik I, et al. Influence of graphene oxide additives on the filler structure and the physical and mechanical properties of carbon-graphite nanocomposite. *Journal of Advanced Materials and Technologies.* 2025;10(1):19-31. DOI:10.17277/jamt-2025-10-01-019-031

20. Samanta S, Sahoo RR. Covalently linked hexagonal boron nitride-graphene oxide nanocomposites as high-performance oil-dispersible lubricant additives. *ACS Applied Nano Materials*. 2020;3(11):10941-10953. DOI:10.1021/acsanm.0c02193

21. Uz Zaman A, Abdul Karim MR, Hussain A, Khan MA, et al. Graphite and white graphite (h-BN) reinforced metal matrix composites and cermets: a review of processing and properties. *Advances in Materials and Processing Technologies*. 2026;12(1):222-247. DOI:10.1080/2374068X.2025.2594440

22. Yu J, Zhao W, Wu Y, Wang D, et al. Tribological properties of epoxy composite coatings reinforced with functionalized C-BN and H-BN nanofillers. *Applied Surface Science*. 2018;434:1311-1320. DOI:10.1016/j.apsusc.2017.11.204

23. Liu Y, Wang K, Xu Q, Zhang J, et al. Superlubricity between graphite layers in ultrahigh vacuum. *ACS Applied Materials & Interfaces*. 2020;12(38):43167-43172. DOI:10.1021/acsami.0c05422

24. Ouyang JH, Li YF, Zhang YZ, Wang YM, et al. High-temperature solid lubricants and self-lubricating composites: a critical review. *Lubricants*. 2022;10(8):177. DOI:10.3390/lubricants10080177

25. Srivyas PD, Charoo MS. Nano lubrication behaviour of graphite, h-BN and graphene nano platelets for reducing friction and wear. *Materials Today: Proceedings*. 2021;44:7-11. DOI:10.1016/j.matpr.2020.04.785

26. Eswaran MK, Riyas ZM, Asaithambi T. Exploring the synergistic effect of two-dimensional (2D) layered MoS2/GO/h-BN ternary nanocomposite as an electrode material for asymmetric supercapacitor application. *Journal of Materials Science: Materials in Electronics.* 2025;36(14):850. DOI:10.1007/s10854-025-14883-z

27. Zhang N, Zhang Y, Li S, Guo L, et al. 3D structurally advanced graphene oxide/h-BN hybrid for solid self-lubrication with enhanced thermal conductivity. *Tribology International*. 2022;176:107918. DOI:10.1016/j.triboint.2022.107918

28. Gupta MK, Bijwe J. Combination of nanoparticles of graphite and hexagonal boron nitride as anti-wear and extreme-pressure additives- On exploring the possibility of synergism. *Surface Topography: Metrology and Properties*. 2020;8(2):025025. DOI:10.1088/2051-672X/ab958d

29. Chen B, Dong W, Shi W, Li X, et al. Enhanced mechanical and tribological performance of epoxy nanocomposite coating by non-covalent bonded h-BN nanosheets/graphene oxide. *Progress in Organic Coatings*. 2024;197:108826. DOI:10.1016/j.porgcoat.2024.108826

30. Yang W, Luo R, Hou Z. Effect of interface modified by graphene on the mechanical and frictional properties of carbon/graphene/carbon composites. *Materials*. 2016;9(6):492. DOI:10.3390/ma9060492

31. Dhairiyasamy R, Bassi W, Algethami AA, Saleh B, et al. Advanced epoxy composites for tribological applications: investigating the role of hybrid ceramic and lubricant fillers. *Polymer Testing*. 2025;150:108932. DOI:10.1016/j.polymertesting.2025.108932

32. Li B, Zhou X, Huang J, Huang Q, et al. Investigation of multi-scale fillers on tribological properties of UHMWPE composites for water-lubricated bearings. *Tribology International*. 2025;212:110961. DOI:10.1016/j.triboint.2025.110961

33. Fan S, Zhang L, Xu Y, Cheng L, et al. Microstructure and tribological properties of advanced carbon/silicon carbide aircraft brake materials. *Composites Science and Technology*. 2008;68(14):3002-3009. DOI:10.1016/j.compscitech.2008.06.013

34. Eliseev YS, Skvortsov MA, Efremov AA, Sankin AE, Vasiliev YN. *Method for producing graphitized material*. Russian Federation patent 2,374,174 C2. 27 November 2009. (In Russ.)

35. Samoilov VM, Samsonova VB, Nakhodnova AV, Verbets DB, et al. Raman spectroscopy and crystalline structure of polyacrylonitrile-based carbon fibres. *Advanced Materials & Technologies*. 2019;3(15):008-015. DOI:10.17277/amt.2019.03.pp.008-015

36. Memetova A, Tyagi I, Rao Karri R, Suhas, et al. High-density nanoporous carbon materials as storage material for methane: A value-added solution. *Chemical Engineering Journal*. 2022;433:134608. DOI:10.1016/j.cej.2022.134608

37. Pankov MI, Kulakov VV, Lavruhin SP, Luchkin MS. *Method for producing self-lubricating material based on artificial finegrained graphite*. Russian Federation patent 2,748,329 C1. 24 May 2021. (In Russ.)

Information about the authors / Информация об авторах

Roman D. Balabanov, Postgraduate Student, Tambov State Technical University (TSTU), Tambov, Russian Federation; ORCID 0009-0001-2946-3119; e-mail: balabanoff98@gmail.com

Tatyana P. Dyachkova, D. Sc. (Chem.), Professor, TSTU, Tambov, Russian Federation; ORCID 0000-0002-4884-5171; e-mail: dyachkova_tp@mail.ru

Irina V. Gutnik, Cand. Sc. (Eng.), Associate Professor, TSTU, Tambov, Russian Federation; ORCID 0000-0003-1236-7187; e-mail: i.v.gutnik@yandex.ru

Nikolay A. Chapaksov, Cand. Sc. (Eng.), Associate Scientist, TSTU, Tambov, Russian Federation; ORCID 0000-0001-9076-9400; e-mail: tchapaxov.nikolaj@yandex.ru

Elena A. Burakova, D. Sc. (Eng.), Associate Professor, TSTU, Tambov, Russian Federation; ORCID 0000-0001-8927-7433; e-mail: elenburakova@yandex.ru

Балабанов Роман Дмитриевич, аспирант, Тамбовский государственный технический университет (ТГТУ), Тамбов, Российская Федерация; ORCID 0009-0001-2946-3119; e-mail: balabanoff98@gmail.com

Дьячкова Татьяна Петровна, доктор химических наук, профессор, ТГТУ, Тамбов, Российская Федерация; ORCID 0000-0002-4884-5171; e-mail: dyachkova_tp@mail.ru

Гутник Ирина Владимировна, кандидат технических наук, доцент, ТГТУ, Тамбов, Российская Федерация; ORCID 0000-0003-1236-7187; e-mail: i.v.gutnik@yandex.ru

Чапаксов Николай Андреевич, кандидат технических наук, младший научный сотрудник, ТГТУ, Тамбов, Российская Федерация; ORCID 0000-0001-9076-9400; e-mail: tchapaxov.nikolaj@yandex.ru

Буракова Елена Анатольевна, доктор технических наук, доцент, ТГТУ, Тамбов, Российская Федерация; ORCID 0000-0001-8927-7433; e-mail: elenburakova@yandex.ru

Received 19 March 2026; Revised 24 April 2026; Accepted 28 April 2026

Original papers
Advanced structural materials, materials for extreme conditions

УДК 621.762+544.463 DOI: 10.17277/jamt-2026-11-02-129-138

Mechanochemical synthesis of niobium silicides: the effect of ball diameter and activation time on niobium and silicon mechanical activation

© Nikita E. Belyaev[a], Olga A. Shkoda[b]✉, Evgeniy D. Golovin[a]

[a] *Novosibirsk State Technical University, 20, K. Marksa Av., Novosibirsk, 630073, Russian Federation,*
[b] *Tomsk Scientific Center of the Siberian Branch of the Russian Academy of Sciences, 10/4, Akademicheskij Av., Tomsk, 634055, Russian Federation*

✉ O.Shkoda@dsm.tsc.ru

Abstract. The paper investigated the regularities of mechanochemical formation of niobium silicides utilizing industrial waste (niobium turnings and silicon wafers) as feedstock. The influence of the milling ball diameter and the duration of mechanical activation on the mass fraction of formed niobium silicides was identified. X-ray phase analysis and scanning electron microscopy methods revealed that morphological changes are closely related to the formation of new phases such as $NbSi_2$, Nb_5Si_3, Nb_3Si. A high degree of comminution and particle deformation is required for successful mechanochemical synthesis, with activation time being a key factor. Maximum structural disordering and refinement are achieved in intermediate activation regimes (10–15 min). The use of larger balls (8 mm) intensifies deformation and disordering processes, leading to a sharper increase in microstrain and faster formation of nanoscale silicides. The total mass fraction of niobium silicides reached 46 wt. % when using 8 mm balls, compared to 38 wt. % when using 5 mm balls after 30 minutes of MA. The utilization of secondary waste as raw materials is suitable for niobium silicide production.

Keywords: niobium; silicon; niobium silicides; mechanical activation; morphology; mechanochemical synthesis; X-ray phase analysis; technological processing, industrial waste.

For citation: Belyaev NE, Shkoda OA, Golovin ED. Mechanochemical synthesis of niobium silicides: the effect of ball diameter and activation time on niobium and silicon mechanical activation. *Journal of Advanced Materials and Technologies*. 2026;11(2):129-138. DOI: 10.17277/jamt-2026-11-02-129-138

Механическая активация ниобия и кремния: роль диаметра шаров и времени в механохимическом синтезе силицидов ниобия

© Н. Е. Беляев[a], О. А. Шкода[b]✉, Е. Н. Головин[a]

[a] *Новосибирский государственный технический университет, пр. К. Маркса, 20, Новосибирск, 630073, Российская Федерация,*
[b] *Томский научный центр Сибирского отделения Российской академии наук, пр. Академический, 10/4, Томск, 634055, Российская Федерация*

✉ O.Shkoda@dsm.tsc.ru

Аннотация. Исследованы закономерности механохимического формирования силицидов ниобия с использованием техногенных отходов (стружка ниобия и пластины кремния) в качестве исходных материалов. Выявлены роль диаметра мелющих шаров и времени механической активации на изменения массовой доли образованных силицидов ниобия. Методами рентгенофазового анализа и растровой электронной микроскопии изучено и показано, что морфологические изменения тесно связаны с образованием таких новых фаз как $NbSi_2$, Nb_5Si_3, Nb_3Si. Высокая степень измельчения и деформации частиц является предпосылкой для успешного механохимического синтеза. Время механической активации является ключевым фактором в процессе механохимического синтеза силицидов ниобия. Максимальное разупорядочение и измельчение структуры,

достигается в промежуточных режимах активации (10…15 мин). Использование более крупных шаров (8 мм) интенсифицирует процессы деформации и разупорядочения, приводя к более резкому увеличению микроискажений и к более быстрому образованию наноразмерных силицидов. Массовая суммарная доля силицидов ниобия составила 46 мас. % при использовании шаров 8 мм против 38 мас. % при использовании шаров 5 мм после 30-минутной механической активации. Использование вторичных отходов в качестве исходных материалов пригодно для получения силицидов ниобия.

Ключевые слова: ниобий; кремний; силициды ниобия; механическая активация; морфология; механохимический синтез; рентгенофазовый анализ; технологическая обработка, техногенные отходы.

Для цитирования: Belyaev NE, Shkoda OA, Golovin ED. Mechanochemical synthesis of niobium silicides: the effect of ball diameter and activation time on niobium and silicon mechanical activation. *Journal of Advanced Materials and Technologies*. 2026;11(2):129-138. DOI: 10.17277/jamt-2026-11-02-129-138

1. Introduction

Transition-metal silicides, including niobium silicides, are promising for many applications owing to their high melting points, chemical stability in aggressive environments, high hardness, and thermal resilience. They exhibit excellent high-temperature performance, good oxidation resistance and retention of properties at elevated temperatures, as well as favorable electrical conductivity and chemical compatibility. These attributes enable their use in heat-resistant materials and as components of wear-prone high-temperature alloys, and in heat-resistant coatings [1–4]. Such properties also make them attractive for aerospace applications, heating elements, and protective coatings operating under extreme conditions, and they are considered potential substitutes for nickel-based alloys in heat-loaded components exposed to high temperatures [5]. Given their superior operational characteristics, research on the synthesis of these materials is of considerable scientific and practical importance. Mechanical activation (MA) is a widely used method, applied both for direct synthesis and as an effective preliminary treatment of materials [6–8].

Methods for synthesizing niobium silicides often require high temperatures and prolonged reaction times [9], which limits their applicability. In this context, mechanical activation (MA) for mechanochemical synthesis of niobium silicides appears promising. Single-phase Nb_5Si_3 has been successfully produced by high-energy impact loading and by self-propagating high-temperature synthesis following preliminary MA [10, 11], whereas formation of amorphous $Nb_{50}Si_{50}$ in a planetary mill required an extended milling time (150 h) [12]. A distinctive feature of mechanical activation is the simultaneous operation and interaction of many controllable process parameters. These parameters and their combined effects determine the evolution of the powder mixture and the subsequent phase-structural transformations of the material.

In the present work, technogenic waste – niobium metal turnings and silicon plates – were used as feedstock. The use of secondary resources addresses environmental and resource-saving goals, reduces raw-material costs, and minimizes waste, thereby promoting rational use of natural resources. International experience supports the effectiveness of using niobium and silicon wastes as raw-material sources [13, 21].

Under certain conditions, mechanochemical synthesis and mechanical alloying with formation of new phases occur during mechanical activation (MA). Interaction of powder particles with milling media (balls) and the drum walls produces heating, deformation, mixing, and comminution of the starting powder particles, the formation of layered agglomerates, an increase in interfacial area, welding, and the emergence of new phases and alloy particles [8, 14–17]. The feasibility of mechanochemical reactions and alloying depends on the characteristics of the mill, the selected mode, and the chosen operating parameters [18, 19]. Reaction progression in the contact zones is driven by the energy stored there, and the reaction yield is proportional to the total contact area between reagent particles, which depends on the number and diameter of the balls used [20]. The present study investigates the influence of MA time and ball diameter on the mechanochemical synthesis of niobium silicides.

The objective of the study is to determine the effect of milling ball diameter and MA time on the formation of niobium silicides during mechanochemical synthesis using technogenic waste as starting materials. To achieve this objective, the following tasks have been set: to perform mechanical activation of niobium and silicon while varying MA time and ball diameter; to investigate the morphology, phase composition, and structural state of the mechanically activated mixtures using X-ray phase analysis, X-ray structural analysis, and scanning electron microscopy.

2. Materials and Methods

2.1. Method for obtaining niobium silicides

Niobium powder was produced by processing turnings of commercially pure niobium. The turnings were sheared with guillotine shears into platelets of approximately 5 × 5 × 2 mm, which were then milled in a ball mill ("Activator 2SL") for 10 min. Silicon powder was prepared from technical-grade silicon plates sized 100 × 100 × 5 mm. The plates were comminuted using a laboratory disintegrator (Desi 11).

A planetary mill "Activator 2SL" with water cooling was used for the mechanochemical synthesis of niobium silicides. MA conditions were as follows: drum/disc radius ratio 1.57, planetary radius 103 mm, drum volume (WC-Co, VK8) 200 mL. The disk and drum rotation speeds were 1000 and 1500 min^{-1}, respectively. WC-Co balls of 5 mm and 8 mm diameter were used as grinding media. A 100 g powder mixture of niobium and silicon, prepared to the stoichiometry of Nb_5Si_3, was activated for 5, 10, 15, and 30 minutes with a ball-to-powder mass ratio of 6.3 : 1.

2.2. Analytic methods

The mechanically activated powders were analyzed by X-ray phase analysis (XRD-6000, Cu Kα radiation, PDF-4+ and POWDER CELL 2.4 databases) and by scanning electron microscopy (Quanta 200 3D). Crystallite sizes were estimated using the Scherrer equation. Rietveld refinement was applied to the X-ray diffraction patterns to separate contributions from crystallite size and microstrain and to assess their uncertainties; this refinement accounted for both instrumental broadening (via instrument parameters) and physical broadening (related to crystallite size and microstrain). Statistical uncertainties for the refined parameters (including crystallite size and microstrain) ranged from 3.4 to 6.2 %. Specific surface area was measured by nitrogen thermal desorption using the four-point BET method on a SORBI-M instrument, with nitrogen as the adsorbate. Prior to measurement, powders were degassed by thermal treatment for 1 hour at 200 °C.

3. Results and Discussion

Figure 1 shows a scanning electron microscope (SEM) image of a niobium-silicon powder mixture obtained after 5 minutes of mechanical activation (Fig. 1*a*). The image demonstrates particle morphology indicating the initial stages of intense particle crushing and agglomeration. The dominant structural element is large agglomerates, reaching sizes comparable to 50 μm. These agglomerates have a non-uniform, lumpy surface, indicating their formation from smaller particles under the influence of shock-shear loads. The surface of the agglomerates bears traces of intense mechanical action: roughness and the presence of small particles adhering to larger ones. A significant number of small particles are visible between the large agglomerates. Some of these small particles appear more angular, while others are smoothed, which may reflect different stages of mechanical processing. During this time interval (5 min MA) the destruction of the original particles occurs and the simultaneous formation of new, smaller ones, which begin to agglomerate, sticking to each other.

A SEM-image of a niobium-silicon powder mixture after 15 min of MA (Fig. 1*b*) demonstrates differences from the morphology observed after 5 minutes of MA, where large agglomerates with a non-uniform surface predominated. After 15 min, a finer grinding was observed. The number of small, freely distributed particles increased. The main agglomerates appear smaller and consist of even smaller components. The total volume of the powder mixture now consists of a larger number of small particles. This indicates that the grinding process, crushing both the original particles and the previously formed agglomerates, continued during the additional 10 minutes of MA (from 5 to 15 min). While after 5 min of MA, the agglomerates had a more "sculpted" shape with clear signs of clumping, after 15 min they appear "loose", consisting of smaller particles. The increased degree of dispersion and the increase in the interphase surface of the agglomerates create favorable conditions for the occurrence of mechanochemical reactions, and promote diffusion processes and the formation of silicide phases.

A comparative analysis (5 min MA *vs*. 15 min MA) shows that after 15 minutes of MA, a decrease in the average particle size and an increase in the proportion of fine particles were observed compared to 5 minutes of MA. Increased crushing and agglomeration processes created the preconditions for the formation of layered agglomerates and an increase in the interfacial surface area, creating conditions for the mechanochemical synthesis of niobium silicides. These changes indicate that increasing the MA time prepares the material for the formation of the target phases.

Figure 1*c* shows the SEM-image of a niobium-silicon powder mixture after 30 min of MA, where

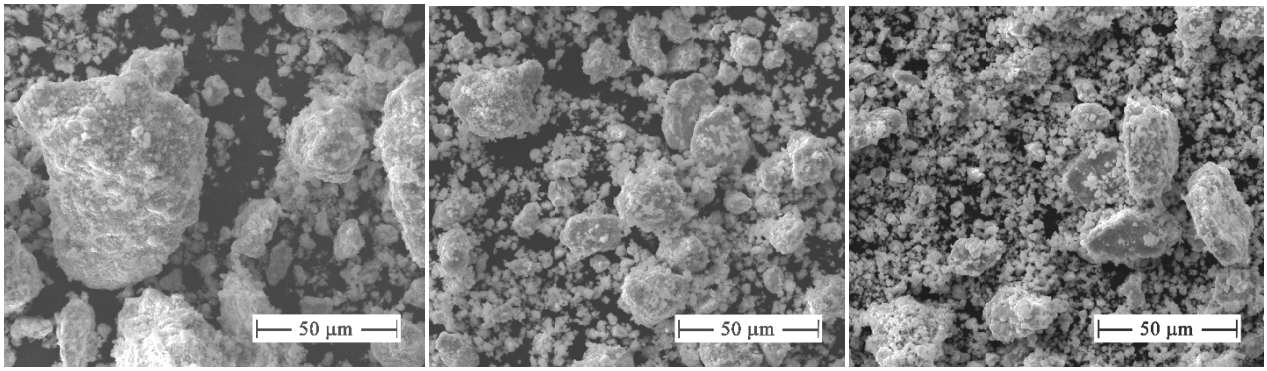

(a) *(b)* *(c)*

Fig. 1. SEM-images of the silicon-niobium powder mixture after: *a* – 5 min MA; *b* – 15 min MA; *c* – 30 min MA using 5 mm balls

further changes in morphology were visible and the finest grinding was observed. Most of the particles were smaller than in previous stages. Fine material was formed, with micron and submicron particles predominating. This indicates an intensive crushing process that continued throughout the entire MA period. While large agglomerates predominated after 5 minutes of MA, and became looser after 15 min, after 30 min large agglomerates were virtually absent. Clusters of very small particles were observed, which began to form new, smaller and looser aggregates that lacked the distinct structure of the primary, large agglomerates. This structure facilitates more efficient mechanochemical reactions. A morphology characterized by strong comminution and a high degree of particle deformation often correlates with the onset of amorphous or nanostructured phase formation [8, 11, 14, 19]. The analysis of the powder mixture after 30 min of MA demonstrated a transition to a highly dispersed state with a predominance of very small particles.

Thus, analyzing the samples after 5, 15, and 30 min of mechanical activation, we see that after 5 min of mechanical activation, large agglomerates with pronounced traces of impact-shear action predominated. Small particles were relatively few. After 15 minutes of mechanical activation, the agglomerate size decreased, the proportion of small particles increased, with looser aggregates formed. The grinding process continued actively. After 30 minutes of mechanical activation, a high degree of dispersion was observed. Very small particles predominated, with virtually no large agglomerates. An increase in the specific surface area was observed, creating optimal conditions for mechanochemical synthesis.

Thus, the morphological changes in the niobium-silicon powder mixture observed with increasing mechanical activation time indicate progressive degradation of the starting materials and the preparation of the powder structure for the formation of new compounds.

Figure 2 shows the changes in the specific surface area of the powder mixture depending on the MA time using grinding balls with diameters of 5 and 8 mm. The specific surface area for the 5 mm diameter (square) initially increased sharply from the initial state (presumably up to 5 min of MA, where it is about 2.4 $m^2 \cdot g^{-1}$), then decreased by 15 min (about 1.1 $m^2 \cdot g^{-1}$), and again increases slightly by 30 min (about 1.4 $m^2 \cdot g^{-1}$). The specific surface area for the 8 mm diameter (circle) also initially decreased from the initial value (about 1.9 $m^2 \cdot g^{-1}$ at 5 min of MA), reached a minimum at 15 minutes (about 1.3 $m^2 \cdot g^{-1}$), and then increased slightly by 30 minutes (about 1.4 $m^2 \cdot g^{-1}$). The analysis of the effect of grinding ball size (5 mm *vs*. 8 mm) shows that using 8 mm balls resulted in a lower specific surface area at early stages (5 and 10 min of MA), but by 15 and

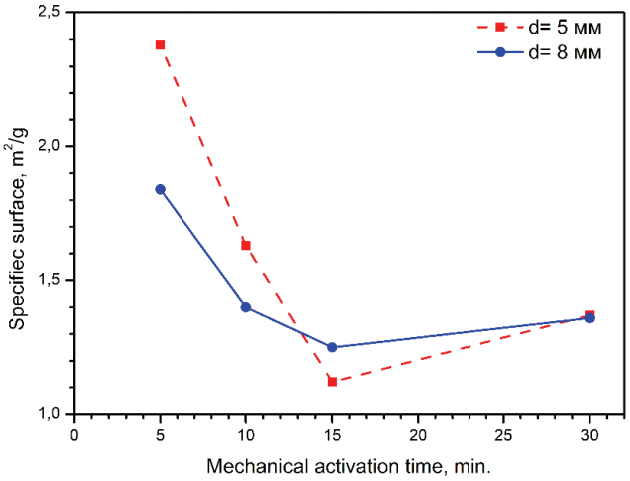

Fig. 2. Specific surface area as a function of mechanical activation time using 5 mm diameter balls (■) and 8 mm diameter balls (●)

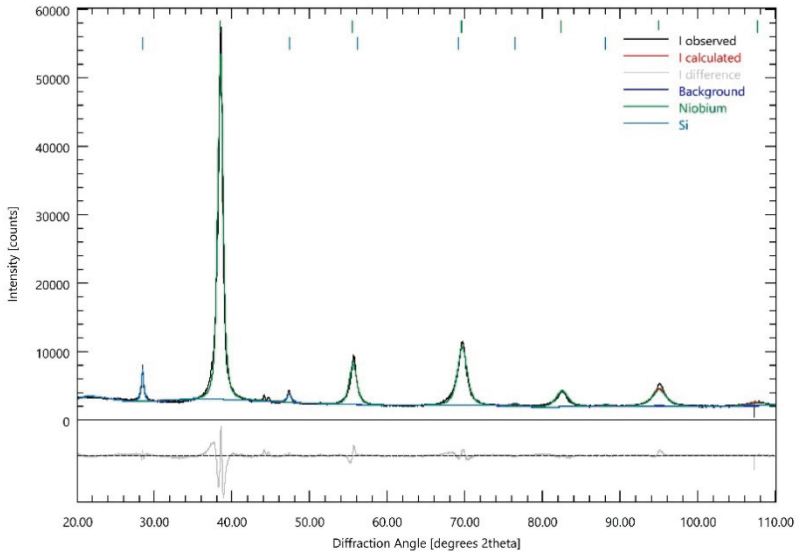

(a)

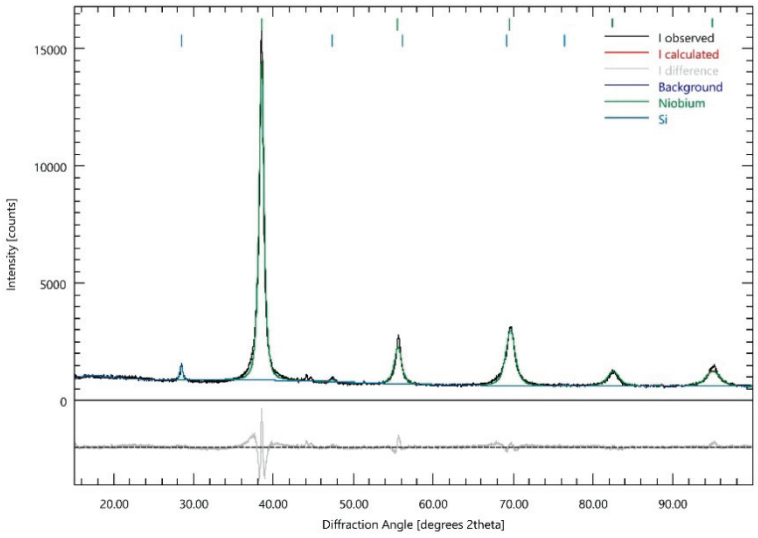

(b)

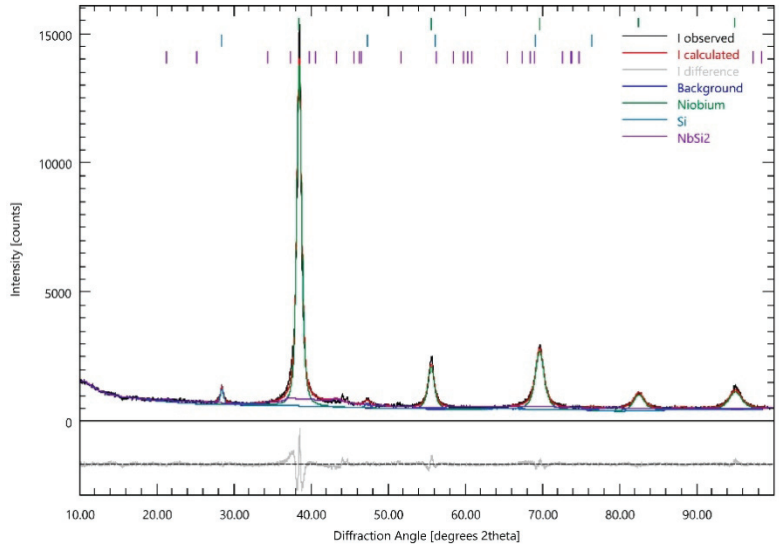

(c)

Fig. 3. Powder mixture diffractogram fragments: *a* – initial mixture, after 5 min MA, obtained using ball diameters: *b* – 5 mm; *c* – 8 mm. Nb (#01-077-3017), Si (#00-026-1481), NbSi2 (#01-0746870)

30 min of MA, the values became similar. This is consistent with the assumption that 8 mm balls provide higher MA intensity but lead to more rapid agglomeration and powder compaction, which is reflected in the specific surface area curve.

Figure 3 shows fragments of the diffraction patterns after 5 min of MA for ball diameters of 5 (Fig. 3*a*) and 8 mm (Fig. 3*b*). The diffraction patterns in Fig. 3*a* show intense peaks corresponding to Nb and Si, while Figure 3b also shows the initial Nb and Si, but with noticeable peaks related to the $NbSi_2$ phase. This indicates that using larger balls (8 mm) at the same MA time (5 min) results in a slightly more active reaction onset.

Figure 4 shows fragments of the diffraction patterns after 30 min of MA for balls with diameters of 5 and 8 mm. When using 5 mm balls, the appearance of the diffraction pattern differed significantly from the case of 5 min of MA. Now there are pronounced peaks corresponding to niobium silicides: $NbSi_2$ (marked as "1") and Nb_5Si_3 ("2"). The peaks of Nb and Si were also preserved, but their intensity decreased. When using 8 mm balls (Fig. 4*b*), a fragment of the diffraction pattern also shows the presence of silicides, but here, in addition to $NbSi_2$ ("1") and Nb_5Si_3 ("2"), peaks of Nb_3Si ("3") were observed. The intensity of the niobium silicide peaks, especially $NbSi_2$ and Nb_5Si_3, was significantly higher here than for 5 mm balls at the same MA time (30 min). The intensity of the initial niobium was lower than for 5 mm balls.

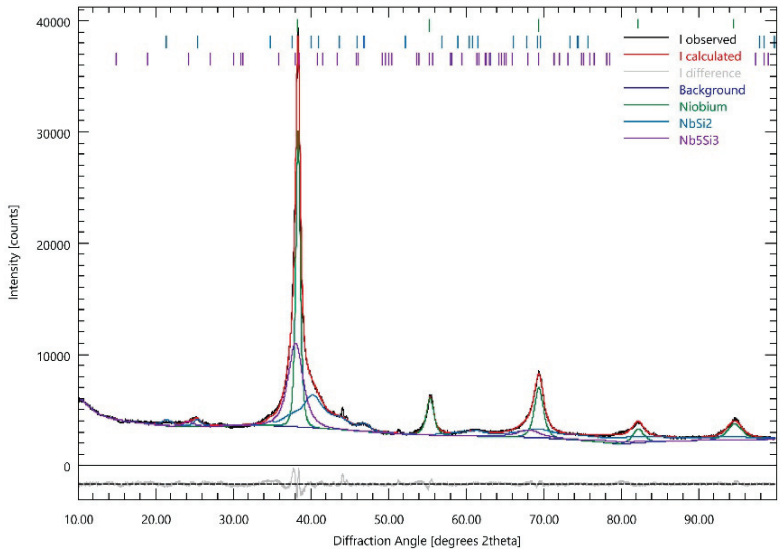

(a)

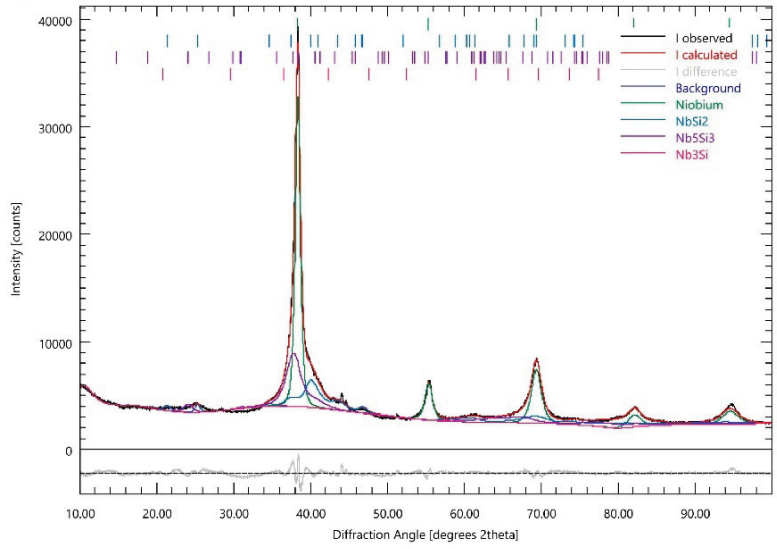

(b)

Fig. 4. Powder mixture diffractogram fragments after 30 min MA, obtained using ball diameters: *a* – 5 mm; *b* – 8 mm

The SEM-image after 30 min of MA (Fig. 1*c*) shows a high degree of grinding and dispersion, which is completely consistent with the diffraction data. It is precisely at this fine grinding that the intensive formation of new phases (niobium silicides) occurs. The higher intensity of the silicide peaks for 8 mm balls at 30 min of MA, compared to 5 mm balls, may be due to more effective mechanical alloying and/or the higher temperature generated during impacts with the larger balls, which facilitates the reactions.

Figure 5 shows the dependence of the change in the mass fraction of the initial components and the formed silicides on the MA time, as determined by X-ray diffraction data. The graph provides a quantitative assessment of the phase composition as a function of MA time and sphere size.

The proportion of initial niobium (curve *1*, squares) decreased with MA time, especially noticeably after 15 minutes of MA. This confirms that Nb actively participates in silicide formation reactions. The proportion of initial silicon (curve *2*, circles) also decreased, but less dramatically than the proportion of Nb. This is due to the fact that it was used in smaller quantities (based on the stoichiometry of Nb_5Si_3). The proportion of mechanochemically formed niobium silicides (curve *3*, triangles) increased with MA time.

The analysis of the influence of the ball size (5 mm *vs*. 8 mm) according to XRD shows that after 5 min of MA: when using 8 mm balls (Fig. 3*b*, and curve *3* in Fig. 5*b*) a higher proportion of silicides was observed than with 5 mm balls (Fig. 3*a*, and curve *3* in Fig. 5*a*). This confirms that larger balls contribute to a faster reaction start. After 30 min of MA for 5 mm balls (Fig. 4*a*, Fig. 5*a*) the proportion of silicides reached approximately 38 % and for 8 mm balls (Fig. 4*b*, Fig. 5*b*) the proportion of silicides was about 46 %, and a greater variety of phases was present (Nb_2Si, Nb_5Si_3, Nb_3Si). Figure 5*b*, curve *3*, also shows an increase in the proportion of silicides, comparable to that in Fig. 5*a*. After 30 min of the MA process for 5 mm balls, the predominant silicide was $NbSi_2$ (30 wt. %), with Nb5Si3 accounting for 8 wt%. For 8 mm balls, with the same MA time, the $NbSi_2$ content was also 30 wt. %, Nb_5Si_3 – 1 wt. %, and Nb_3Si (15 wt. %) was added.

Thus, using 8 mm balls accelerates the silicide formation process and can facilitate the formation of a more diverse set of phases.

Figure 6 shows the dependences of changes in coherent scattering areas (CSA) on the MA time. CSA (crystallite size) is the average size of regions within the material where the crystalline structure remains continuous. During MA, the crystals were crushed, and the CSA decreased. When using 5 mm balls, (Fig. 6*a*) the CSA size for Nb (*1*) remained relatively stable within 10–20 nm, with a noticeable decrease at 15 min of MA. The CSA size for Si (*2*) initially increased slightly (up to 10 min of MA) and then decreased. The CSA size for niobium silicide Nb_5Si_3 (*3*), which began to form, initially decreases (up to 10 min) and then increased. This may be due to the initial formation of nanoparticles, which then began to agglomerate or enlarge. When using 8 mm balls, (Fig. 6*b*) The CSR size for Nb (*1*) also decreased with MA time, remaining within 10-20 nm.

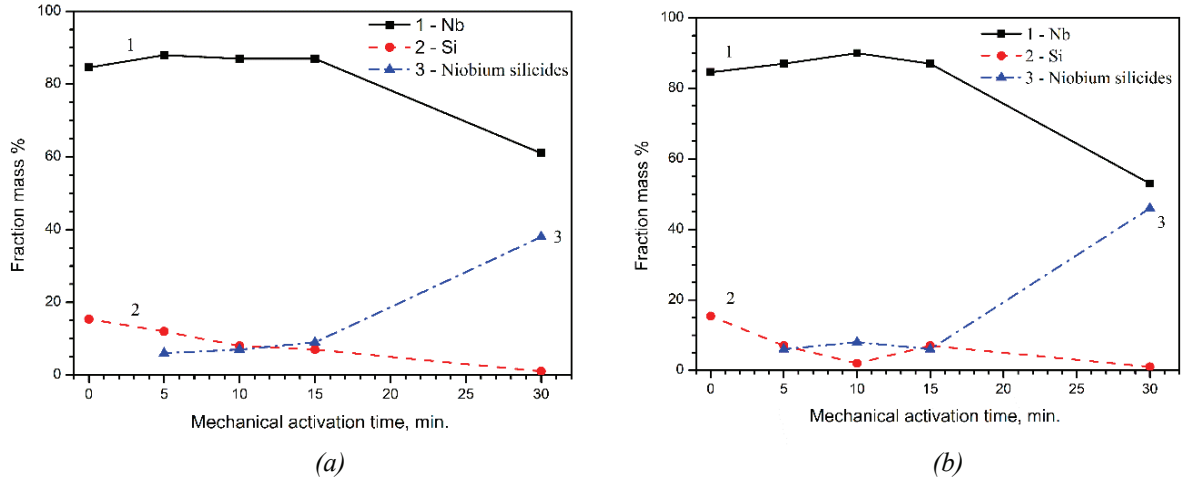

Fig. 5. XRD-based mass fraction changes of initial components and mechanochemically formed silicides, using ball diameters: *a* – 5 mm; *b* – 8 mm

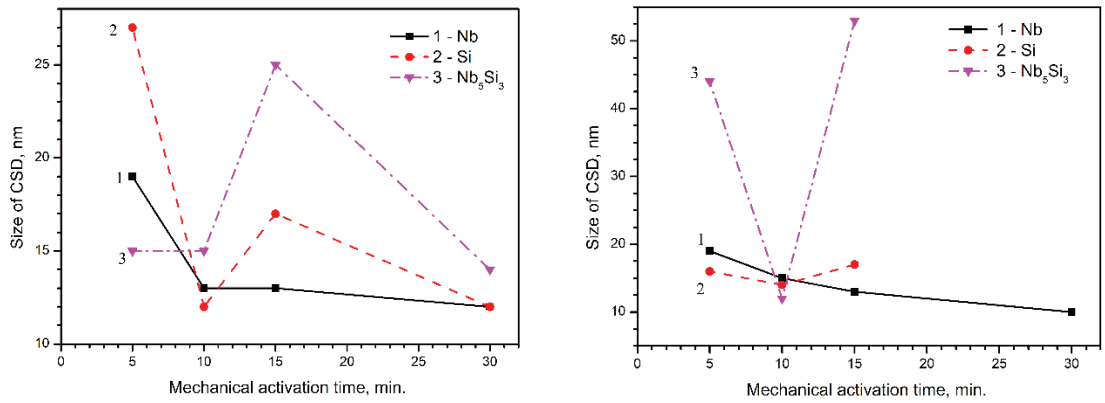

(a) *(b)*

Fig. 6. Evolution of crystallite size (coherent scattering domain size) for initial components and mechanochemically formed niobium silicides as a function of mechanical activation time, with ball diameters: *a* – 5 mm; *b* – 8 mm

The CSR size for Si (*2*) remained relatively low and stable. The CSR size for niobium silicide Nb_5Si_3 (*3*) behaved similarly to that for 5 mm spheres, with a sharp increase after 15 min of MA and then a decrease. However, after 5 minutes of MA, the CSR of the silicide was already significantly smaller than that for 5 mm spheres, which may indicate more rapid formation of nanoscale regions.

The decrease in the CSR for the initial components during MA indicates their refinement and disordering of the crystalline structure. This is consistent with SEM-images, which showed progressive particle refinement. The increase and subsequent decrease in the CSR for silicides may reflect the process of their formation and refinement of already formed phases.

Figure 7 shows the dependence of changes in crystal lattice microdistortions ($\Delta d/d$) on the MA time. Microdistortions (or deformations) of the crystal lattice are a violation of the ideal periodicity of the crystal structure. MA causes deformations and the accumulation of vacancies and dislocations, leading to an increase in microdistortions. For 5 mm spheres, microdistortions for Nb (*1*) and Si (*2*) initially increased (up to 15 min of MA), reaching a maximum, and then began to decrease. Microdistortions for Nb_5Si_3 (*3*) tended to increase over time, reaching their maximum at 15 min of MA and then decreasing. This may be due to relaxation processes and some annealing with increasing temperature.

For 8 mm spheres, microdistortions for Nb (*1*) initially increased, reaching a maximum at 10 min of MA, and then decreased, while for Si (*2*) they remained relatively low and stable. For 8 mm balls, the peak microdistortions for Nb and Nb_5Si_3 were reached earlier (around 10 min) and were more pronounced. This indicates a more intense and rapid accumulation of defects when using larger balls. The peak microdistortions for Nb_5Si_3 for 8 mm balls after 10 min of MA were very high (more than $7 \cdot 10^{-3}$), indicating significant disordering of its crystal lattice. This may be due to the more active formation of nanoscale or amorphous regions under more intense mechanical activation.

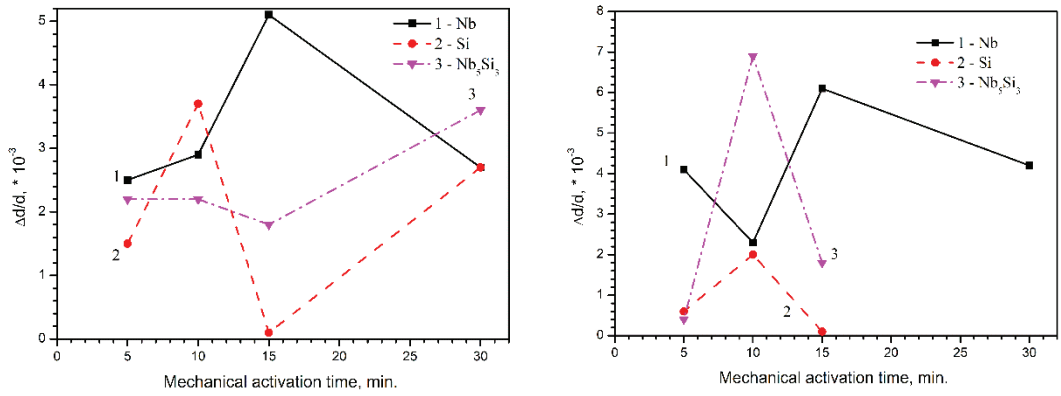

(a) *(b)*

Fig. 7. Evolution of lattice microstrain in initial components (*1* – niobium, *2* – silicon) and mechanochemically formed niobium silicides (*3* – Nb_5Si_3) as a function of mechanical activation time, with ball diameters: *a* – 5 mm; *b* – 8 mm

An increase in microdistortions with increasing MA time indicates the accumulation of defects in the crystal lattice of the starting components and the forming silicides. A decrease in the coherent scattering area and an increase in microdistortions occur in parallel, reflecting the intensity of deformation processes. High microdistortion values and low coherent scattering area values (especially at 15 min of MA) correlate with the high degree of dispersion observed in SEM-images.

Thus, the use of larger grinding balls (8 mm), all other things being equal, accelerates the MA and synthesis process, leading to more rapid formation of silicides and the formation of a more complete set of silicide phases.

4. Conclusion

It was found that with increasing MA time, particle refinement occurred, their specific surface area increased, and, consequently, the proportion of formed silicide phases increased. According to X-ray diffraction data, maximum disordering and structure refinement were achieved in intermediate activation modes (10–15 min), which correlates with the specific surface area and morphology data. Using larger balls (8 mm) intensified the deformation and disordering processes, leading to a sharper increase in microdistortions and faster formation of nanoscale silicides. The total mass fraction of niobium silicides was 46 % when using 8 mm balls versus 38 % when using 5 mm balls after 30 minutes of mechanical activation.

The use of secondary waste as starting materials is suitable for producing niobium silicides. With increasing MA time, particle refinement occurred, their specific surface area increased, and, consequently, the proportion of formed silicide phases increased. Mechanical activation leads to crystallite refinement (reduction in CSR) and defect accumulation (increased microdistortions) in the starting components and the resulting silicides. According to X-ray diffraction data, maximum disordering and structure refinement were achieved in intermediate activation modes (10–15 min), which correlates with the specific surface area and morphology data. The use of larger balls (8 mm) intensified the deformation and disordering processes, leading to a sharper increase in microdistortions and faster formation of nanoscale silicides. The total mass fraction of niobium silicides was 46 wt. % when using 8 mm balls versus 38 wt. % when using 5 mm balls after 30 minutes of mechanical activation. The use of secondary waste as starting materials is suitable for producing niobium silicides.

5. Funding

The research was carried out as part of the TSC SB RAS state assignment (project No. FWRF-2024-0009) and with the support of project FSUN-2024-0005.

Финансирование

Работа выполнена в рамках государственного задания ТНЦ СО РАН (проект № FWRF-2024-0009) и при поддержке проекта FSUN-2024-0005.

6. Acknowledgements

The authors are grateful to the Tomsk Regional Center for Collective Use and the Center for Collective Use "Structure, Mechanical, and Physical Properties of Materials" at NSTU.

The authors express their gratitude to Sharif M. Sharafeev for assistance with interpreting and visualizing X-ray phase analysis data.

Благодарности

Авторы благодарят Томский региональный центр коллективного пользования и Центр коллективного пользования «Структура, механические и физические свойства материалов» НГТУ.

Авторы выражают благодарность Шарифу М. Шарафееву за помощь в интерпретации и визуализации данных рентгенофазового анализа.

7. Conflict of interests

The authors declare no conflict of interest.

Конфликт интересов

Авторы заявляют об отсутствии конфликта интересов.

Reference

1. Sankar M, Satya Prasad VV, Baligidad RG, Alam MdZ, et al. Microstructure, oxidation resistance and tensile properties of silicide coated Nb-alloy C-103. *Materials Science and Engineering: A*. 2015;645:339-346. DOI:10.1016/j.msea.2015.07.063

2. Shkoda OA, Terekhova OG. SHS in the Nb–Si system: Influence of mechanical alloying. *International Journal of Self-Propagating High-Temperature Synthesis*. 2016;25(1):14-16. DOI:10.3103/S106138621601012X

3. Shkoda OA. Thermal explosion in Nb–Si mixtures: influence of mechanical activation. *International Journal of Self-Propagating High-Temperature Synthesis*. 2018;27(1):60-63. DOI:10.3103/S1061386218010089

4. Knittel S, Mathieu S, Portebois L, Drawin S, et al. Development of silicide coatings to ensure the protection of Nb and silicide composites against high temperature oxidation. *Surface and Coatings Technology*. 2013;235:401-406. DOI:10.1016/j.surfcoat.2013.07.053

5. Shchetanov BV, Graschenkov DV, Efimochkin IU, Paegle SV, et al. Investigation of a high-temperature Nb-based composite material mechanically doped with Si. *Inorganic Materials: Applied Research*. 2019;10(5):1033-1038. DOI:10.1134/S2075113319050290

6. Zhang YH, Wu LR, Ma J, Cui G. Nanotechnology in solid state batteries, what's next? *Next Nanotechnology*. 2023;2:100011. DOI:10.1016/j.nxnano.2023.100011

7. Cardozo EP, D'Oliveira ASCM. Niobium silicide multilayers processed by in situ synthesis during deposition of powder mixtures. *Journal of Materials Engineering and Performance*. 2022;31(5):3998-4005. DOI:10.1007/s11665-021-06460-2

8. Kovalevskaya ZhG, Khimich MA, Korchagin MA, Sharkee YuP. Special aspects of formation of Ti-Nb system β-alloys by the mechanical alloying in a high-energy ball mill. *Vektor nauki Tol'yattinskogo gosudarstvennogo universiteta*. 2017;3(41):65-69. DOI: 10.18323/2073-5073-2017-3-65-69 (In Russ.)

9. Goncharov IS, Hisamova LV, Saubanova LYu, Polozov IA, et al. Synthesis of the *In Situ* Nb-Si composites by binder jetting additive manufacturing technology. *Key Engineering Materials*. 2019;822:311-319. DOI:10.4028/www.scientific.net/KEM.822.311

10. Ling X, Liu F, Zhang M, Liu Q. Shock synthesis of niobium silicide (Nb_5Si_3) via the flyer plate impact technique with high impact velocities. *Journal of Alloys and Compounds*. 2018;740:1032-1036. DOI:10.1016/j.jallcom.2017.12.089

11. Shkoda OA. Effect of mechanical activation on the synthesis of pentaniobium trisilicide. *Izvestiya vuzov. Fizika.* 2025;68(8):73-79. DOI: 10.17223/00213411/68/8/9 (In Russ.)

12. Li B, Liu L, Ma XM, Dong YD. Amorphization in the Nb–Si system by mechanical alloying. *Journal of Alloys and Compounds*. 1993;202(1-2):161-163. DOI: 10.1016/0925-8388(93)90535-U

13. Shin J, Park J, Park N. A method to recycle silicon wafer from end-of-life photovoltaic module and solar panels by using recycled silicon wafers. *Solar Energy Materials and Solar Cells*. 2017;162:1-6. DOI:10.1016/j.solmat.2016.12.038

14. Boldyrev VV. Mechanochemistry and mechanical activation of solids. *Russian Chemical Reviews.* 2006;75(3):177-189. DOI:10.1070/RC2006v075n03ABEH001205

15. Kuzmich YuV, Kolesnikova IT, Serba VI, Freidin BM. *Mechanical alloying*. Moscow: Nauka; 2005. 213 p. (In Russ.)

16. Suryanarayana C. Mechanical alloying and milling. *Progress in Materials Science.* 2001;46:1-184.

17. Butyagin PY. Problems in mechanochemistry and prospects for its development. *Russian Chemical Reviews*. 1994;63(12):965-976. DOI:10.1070/RC1994v063n12ABEH000129

18. Trevino R, Maguregui E, Perez F, Shafirovich E. Mechanically activated SHS of Nb5Si3 and Nb_5Si_3/Nb composites. *Journal of Alloys and Compounds*. 2020;826:154228. DOI:10.1016/j.jallcom.2020.154228

19. Shkoda OA, Terekhova OG. Combustion of Nb–Si powder blends: interrupted mechanical activation. *International Journal of Self-Propagating High-Temperature Synthesis.* 2011;20(4):224-228. DOI: 10.3103/S1061386211040121

20. Thiessen P-A, Meyer K, Heinicke G. *Grundlagen der Tribochemie*. Berlin: Akademie-Verlag; 1967. 194 p.

21. Kolobov GA, Panov VS, Rakova NN. Processes of secondary refractory rare metals (Review). *Izvestiya. Non-Ferrous Metallurgy*. 2014;1:41-48. DOI:10.17073/0021-3438-2014-1-41-48 (In Russ.)

Information about the authors / Информация об авторах

Nikita E. Belyaev, Postgraduate Student, Novosibirsk State Technical University (NSTU), Novosibirsk, Russian Federation; ORCID 0000-0002-7371-7905; e-mail: N.E.Belyaev@yandex.ru

Olga A. Shkoda, Cand. Sc. (Eng.), Senior Researcher, Tomsk Scientific Center of the Siberian Branch of the Russian Academy of Sciences, Tomsk, Russian Federation; ORCID 0000-0002-6068-4817; e-mail: O.Shkoda@dsm.tsc.ru

Evgeniy D. Golovin, Cand. Sc. (Eng.), Senior Researcher, Associate Professor, Head of the Department, NSTU, Novosibirsk, Russian Federation; ORCID 0000-0001-7634-1045; e-mail: golovin@corp.nstu.ru

Беляев Никита Евгеньевич, аспирант, Новосибирский государственный технический университет (НГТУ), Новосибирск, Российская Федерация; ORCID 0000-0002-7371-7905; e-mail: N.E.Belyaev@yandex.ru

Шкода Ольга Александровна, кандидат технических наук, старший научный сотрудник, Томский научный центр Сибирского отделения Российской академии наук, Томск, Российская Федерация; ORCID 0000-0002-6068-4817; e-mail: O.Shkoda@dsm.tsc.ru

Головин Евгений Дмитриевич, кандидат технических наук, старший научный сотрудник, доцент, зав. кафедрой, НГТУ, Новосибирск, Российская Федерация; ORCID 0000-0001-7634-1045; e-mail: golovin@corp.nstu.ru

Received 22 January 2026; Revised 11 May 2026; Accepted 13 May 2026

Original papers
Materials for energy and environment, next-generation photovoltaics, and green technologies

УДК 544.6.076+544.6.018.47-039.7+544.636/.638 DOI: 10.17277/jamt-2026-11-02-139-151

Supercapacitors based on graphene nanoflakes and redox-active ferrocene-containing ionic liquids

© Mikhail M. Levin[a]✉, Ekaterina A. Arkhipova[a], Anton S. Ivanov[a], Konstantin I. Maslakov[a], Serguei V. Savilov[a]

[a] *Lomonosov Moscow State University, Faculty of Chemistry, Leninskie gory, Bld. 3, 1, Moscow, 119234, Russian Federation*
✉ mikhail.levin@chemistry.msu.ru

Abstract. A series of ferrocene-containing ionic liquids (Fc-ILs) (bis(trifluoromethylsulfonyl)imides ofN-methyl-N-(ferrocenylmethyl)pyrrolidinium, N-methyl-N-(ferrocenylmethyl)piperidinium and N-ethyl-N-(ferrocenylmethyl) pyrrolidinium) were tested as redox-active additives for supercapacitor (SC)ionic liquid electrolytes. Undoped and nitrogen-dopedgraphene nanoflakes (GNFs) were used as an electrode material. The electrochemical characteristics of SCs were analyzed bycyclic voltammetry (CV), galvanostatic charge-discharge (GCD) and electrochemical impedance spectroscopy. Self-discharge of SCs was measured at open-circuit potential. The specific capacitance, energy density, Coulombic efficiency and self-discharge of the SCs depended on the textural parameters of the electrode material and type and content of the additive to the electrolyte. The increase in the Fc-IL fraction in the 0.5 M [EMIm][NTf_2]/ acetonitrile supporting electrolyte enhanced the specific capacitance of the GNF-based electrode from 85 to 126 $F \cdot g^{-1}$ at a scan rate of 5 $mV \cdot s^{-1}$ due to additional pseudocapacitive contribution from reversible electron transfer in Fe^{2+}/Fe^{3+}. Moreover, the redox-active additives provided the increase in energy density of the SC up to 21.7 $Wh \cdot kg^{-1}$. Nitrogen doping of GNF accelerated the self-discharge due to the interaction between redox-active species and nitrogen groups on the electrode surface.

Keywords: supercapacitors; graphene nanoflakes; redox-active electrolytes; ferrocene; ionic liquids.

For citation: Levin MM, Arkhipova EA, Ivanov AS, Maslakov KI, Savilov SV. Supercapacitors based on graphene nanoflakes and redox-active ferrocene-containing ionic liquids. *Journal of Advanced Materials and Technologies*. 2026;11(2):139-151. DOI: 10.17277/jamt-2026-11-02-139-151

Суперконденсаторы на основе малослойных графитовых фрагментов и редокс-активных ферроценсодержащих ионных жидкостей

© М. М. Левин[a]✉, Е. А. Архипова[a], А. С. Иванов[a], К. И. Маслаков[a], С. В. Савилов[a]

[a] *Московский государственный университет им. М. В. Ломоносова, Химический факультет, ул. Ленинские горы, 1, стр. 3, Москва, 119234, Российская Федерация*

✉ mikhail.levin@chemistry.msu.ru

Аннотация. Ферроценсодержащие ионные жидкости (Fc-ИЖ) (бис(трифторметилсульфонил)имиды N-метил-N-(ферроценилметил)пирролидиния, N-метил-N-(ферроценилметил)пиперидиния и N-этил-N-(ферроценилметил) пирролидиния) испытаны в качестве окислительно-восстановительных добавок для электролитов суперконденсаторов (СК). В качестве электродного материала изучены малослойные графитовые фрагменты (МГФ), в том числе азотзамещённые (N-МГФ). Анализ электрохимических характеристик СК проведен с помощью методов циклической вольтамперометрии, гальваностатического заряда-разряда и спектроскопии электрохимического импеданса. Саморазряд СК измерен при потенциале холостого хода. Показано, что пористые параметры электродного материала, тип и содержание редокс-добавки в электролите определяют удельную ёмкость, плотность энергии, кулоновскую эффективность и величину саморазряда СК. Установлено, что увеличение доли Fc-ИЖ в фоновом электролите 0,5 М [EMIm][NTf_2]/ацетонитрил приводит к увеличению удельной емкости электрода на основе МГФ с 85 до 126 Ф/г при скорости развертки потенциала 5 мВ/с за счет дополнительного псевдоемкостного вклада, обусловленного обратимым переносом электронов в ходе редокс-

процесса Fe^{2+}/Fe^{3+}, а также способствует росту удельной энергии СК до 21,7 Вт/кг. В отличие от МГФ, легирование азотом оказывает негативное влияние на электрохимические характеристики СК, приводя к ускорению саморазряда вследствие взаимодействия редокс-активных частиц с азотными группами на поверхности электрода.

Ключевые слова: суперконденсаторы; малослойные графитовые фрагменты; редокс-активные электролиты; ферроцен; ионные жидкости.

Для цитирования: Levin MM, Arkhipova EA, Ivanov AS, Maslakov KI, Savilov SV. Supercapacitors based on graphene nanoflakes and redox-active ferrocene-containing ionic liquids. *Journal of Advanced Materials and Technologies*. 2026;11(2):139-151. DOI: 10.17277/jamt-2026-11-02-139-151

1. Introduction

The rapid expansion of the global economy leads to depletion of fossil fuels and accelerates anomalous climate change. This makes the development of clean renewable energy solutions the key task of modern industries. Nowadays, different energy storage technologies, such as supercapacitors (SCs), metal-ion batteries and fuel cells have been rapidly growing. Among them SCs stand out by fast charge/discharge rates, cycling stability, high-power density and low cost [1, 2]. However, compared to Li-ion batteries the commercially available SCs release lower specific energy density that is about 5–15 $Wh \cdot kg^{-1}$ [3]. The increase in the specific capacitance C and potential range V allows enhancing the SC energy density calculated as $E_{SC} = 0.5CV^2$ [4]. The use of redox-active electrode materials or electrolytes is a successful strategy to improve the specific capacitance of SCs due to additional pseudocapacitive contribution caused by reversible Faradaic reactions [5, 6].

Over a decade, different metal oxides [7, 8], conducting polymers (polyaniline, polythiophene, polypyrrole, etc.) [9], and modified carbon nanomaterials [10] have been applied as electrode materials of SCs. Carbon-based nanomaterials are of particular interest due to their chemical stability, developed porosity and low cost. The introduction of heteroatoms, such as nitrogen, sulfur, oxygen, phosphorus and boron, into graphene layers changes their electronic structure, magnetic, optical and electrochemical properties [11]. In particular, N-doping enhances electrochemical activity of the electrode material because higher electronegativity of nitrogen atoms and their additional lone electron pairs improve its electrical conductivity [11] and enable efficient charge storage [12]. Sliwak et al. [12] showed that pseudocapacitance contribution increased the specific capacitance of reduced graphene oxide from 142 up to 209 $F \cdot g^{-1}$ at a current density of 20 $F \cdot g^{-1}$ in 6 M KOH. Similarly, a 300-fold enhancement in specific capacitance of pristine graphite in 1 M KOH was reported after doping of the electrode material with nitrogen.

The choice of electrolyte is crucial for the electrochemical performance of the SC. Currently, various aqueous and organic systems are widely used in SCs because of their high ionic conductivities and good interface wettability. Several redox-active electrolyte additives such as $K_3Fe(CN)_6$ [13–15], $K_4Fe(CN)_6$ [16], KI [17, 18], KBr [19, 20], $VOSO_4$ [17, 21], hydroquinone (HQ) [22, 23] have been reported. These additives provide extra redox pairs that boost charge storage via electron exchange. In contrast to electrode material engineering, tuning the electrolyte offers a more facile and cost-effective route to high pseudocapacitance. However, the potential operating window of SCs based on aqueous electrolytes is thermodynamically limited (< 1.23 V) by water decomposition [24]. Furthermore, freezing of aqueous electrolytes limits their applicability at extremely low temperatures. Replacement of aqueous solutions with ionic liquids (ILs) helps to overcome these limitations.

ILs are salts composed of organic cations and organic or inorganic anions. They are distinguished by negligible flammability and volatility, high thermal stability, and a wide operational temperature range [25, 26]. Moreover, a wide electrochemical stability window of ILs (up to 5–6 V [26]) enables higher energy densities of SCs. In recent years, a few redox-active ILs including 1-butyl-3-methylimidazolium iodide (BMIMI) [27], 1-butyl-3-methylimidazolium bromide (BMIMBr) [28, 29], N-butyl-N-methylpyrrolidinium bromide ($Pyr_{14}Br$) [30], dimethyl-1,1’-bis(N-butylimidazolium)ferrocene chloride [31], 1-ethyl-3-methylimidazolium ferrocenylsulfonyl-(trifluoromethylsulfonyl)-imide ([Emim][FcNTf]) [32], N-6-ferrocenehexyl-N’-methylimidazolium bis(trifluoromethanesulfon)imide [33], N-2-ethylhexyl-N′-isopentyl-4,4′-bipyridinium bis(di(trifluoromethanesulfon)imide) [33] and 1-methyl-3-(3-((2,2,6,6-tetramethylpiperidin-4-yl)oxy) propyl)-1H-imidazol-3-ium

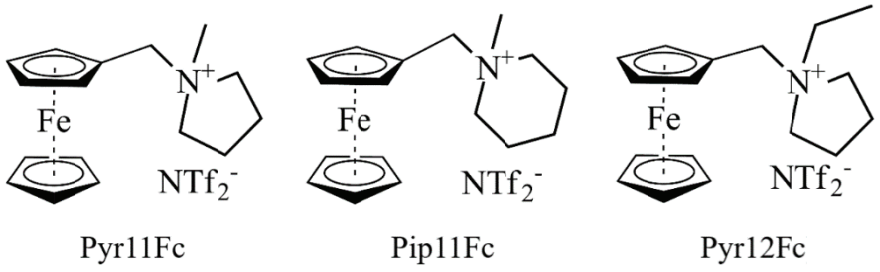

Fig. 1. Fc-ILs used as redox-active electrolyte additives

bis(trifluoromethanesulfon)imide [33] have been tested as SC electrolytes. Fan et al. [28] found that a pseudocapacitance contribution from a Br^-/Br_3^-. Faradaic reaction at the electrode/electrolyte interface increased the specific capacitance from 65.3 to 392 $F \cdot g^{-1}$ at 0.25 $A \cdot g^{-1}$, and enhanced the energy density of the quasi-solid-state SC from 7.1 to 43.1 $Wh \cdot kg^{-1}$ [28]. Similarly, replacing the poly(vinyl alcohol) (PVA)/Li_2SO_4/BMIMCl electrolyte with a PVA/Li_2SO_4/BMIMI-based one increased the specific capacitance from 139.1 to 384.1 $F \cdot g^{-1}$ at a current density of 0.25 $A \cdot g^{-1}$ [27]. 80 wt. % solution of [Emim][FcNTf] in acetonitrile demonstrated higher specific energy of the SC (up to 13.2 $Wh \cdot kg^{-1}$) in the potential range of 2 V than the same solution of [Emim][NTf_2] (7.2 $Wh \cdot kg^{-1}$) [32]. Among redox-active ILs, ferrocene-based ILs (Fc-ILs) are considered as promising electroactive electrolytes due to the good solubility, high chemical and electrochemical stability, wide availability, and low cost of ferroceneprecursor [34]. The redox behavior of Fc-ILs originates from the reversible electron transfer in the Fe^{2+}/Fe^{3+} couple during charge/discharge cycles that provides pseudocapacitance.

Herein, the earlier synthesized Fc-ILs [35] (N-methyl-N-(ferrocenylmethyl)pyrrolidinium bis(trifluoromethylsulfonyl)imide (Pyr11Fc), N-methyl-N-(ferrocenylmethyl)piperidinium bis(trifluoromethylsulfonyl)imide (Pip11Fc), N-ethyl-N-(ferrocenylmethyl)pyrrolidinium bis(trifluoromethylsulfonyl)imide (Pyr12Fc)) (Fig. 1) were tested in SCs as redox-active electrolyte additives to enhance their electrochemical performance.

The aim of this study was to evaluate the effect of redox-active additives combined with graphene nanoflakes (GNFs) and nitrogen-doped GNFs electrodes on specific capacitance, self-discharge, energy and power densities of SCs.

2. Materials and Methods

The synthesis and characterization of Pyr11Fc, Pyr12Fc and Pip11Fc are described in detail in [35]. Redox-active solutions containing 0.01, 0.03 and 0.05 M Fc-ILs with a 0.5 M [EMIm][NTf_2] supporting electrolyte in acetonitrile (AN) (Sigma-Aldrich, ≥ 99.9 %) were prepared in an argon-filled glove box (water content < 0.1 ppm). A blank 0.5 M [EMIm][NTf_2] solution in AN was used as a reference additive-free electrolyte. GNFs (S_{BET} = = 1720 $m^2 \cdot g^{-1}$) [36] and N-GNFs ($[N]_{XPS}$ = 8.8 at. %, S_{BET} = 1180 $m^2 \cdot g^{-1}$) [37] were used as electrode materials. To prepare the slurry, 160 mg of the electrode material, 20 mg of conductive carbon black (Super C65, MTI Corporation) and 33 mg of a 60 wt. % polytetrafluoroethylene (PTFE) aqueous dispersion (MTI Corporation) were thoroughly mixed in ethanol using an agate mortar with a pestle. Then, a homogeneous paste was passed through a roller press and coated onto a nickel foam disk (d = 1 cm, porosity 98 %, MTI Corporation) used as a current collector. Afterwards, the electrodes were dried at a vacuum oven at 60 °C for 24 hours to remove moisture impurities. The coated paste area was 0.785 cm^2 with a mass loading of active material of ~7 $mg \cdot cm^{-2}$ (GNFs) and ~16 $mg \cdot cm^{-2}$ (N-GNFs).

Electrochemical measurements were carried out on a Biologic VSP potentiostat-galvanostat (Bio-Logic Science Instruments SAS, France). The SC was assembled in a 2032 coin-cell configuration with two identical electrodes separated by a glass microfiber filter (Whatman). Electrolyte volume corresponded to 140 μL. Cyclic voltammetry (CV) curves were recorded at a scan rate v of 5, 10, 20, 50, 100 and 200 $mV \cdot s^{-1}$ in the potential range of 0–2.5 V that corresponded the electrochemical stability windows of individual components of the electrolytes [35, 38]. Galvanostatic charge/discharge cycling was conducted at a current density i of 1, 1.5, 2, 2.5 $A \cdot g^{-1}$. The specific capacitances of the single electrode C_{CV} and C_{GCD} ($F \cdot g^{-1}$) and the SC cell C_{SC} were calculated from a discharge curve as [39]:

$$C_{CV} = \frac{4}{2m\Delta V v}\int_0^t IdV(t); \quad (1)$$

$$C_{GCD} = 4C_{SC} = 4\frac{2i\int Vdt}{(\Delta V)^2}, \quad (2)$$

where V is potential, V; I is current, A; and m is mass of active electrode material, g. The energy E_{SC} (Wh·kg^{-1}) and power P_{SC} (kW·kg^{-1}) densities were determined as:

$$E_{SC} = \frac{C_{GCD}\,\Delta V^2}{8\times 3.6}; \quad (3)$$

$$P_{SC} = \frac{E_{SC}}{t/3.6}, \quad (4)$$

where t is the discharge time, s.

The SCs were studied by electrochemical impedance spectroscopy in the frequency range from 10 MHz to 1 MHz with a potential amplitude of 10 mV around the open circuit potential of the discharged state.

To evaluate self-discharge of the SCs, the cells were charged up to 2.5 V at a scan rate of 10 mV·s^{-1} and kept at this potential for 60 s. Then, the open-circuit voltage was recorded for 5 h.

3. Results and Discussion

Figure 2 shows the CV curves recorded at a scan rate of 50 mV·s^{-1} for different concentrations of Fc-ILs in 0.5 M [EMIm][NTf$_2$]. The CV curves for the SCs with the blank electrolyte exhibit nearly rectangular response attributed to the charge accumulation through the electrochemical double-layer formation under adsorption of charge carriers at the electrode/electrolyte interface. In contrast, addition of the Fc-ILs to the electrolytes results in the appearance of reversible oxidation/reduction peaks attributing to the Fe^{3+}/Fe^{2+} redox reaction. The redox peaks became more pronounced with increasing the Fc-IL concentration (Fig. 2*b*) indicating the enhanced pseudocapacitance contribution.

For each Fc-IL additive the CV curve for 0.05 M Fc-IL electrolyte exhibited the highest current density. At a scan rate of 5 mV·s^{-1} the specific capacitances of GNF-electrodes in the electrolytes with additives were 126 (Pyr11Fc), 123 (Pyr12Fc) and 122 (Pip11Fc) F·g^{-1}, which were well above 85 F·g^{-1} observed for the blank electrolyte (Table 1). Even at a scan rate of 200 mV·s^{-1} the specific capacitance retained high values of 101 (Pyr11Fc), 99 (Pyr12Fc) and 97 (Pip11Fc) F·g^{-1} compared to 73 F·g^{-1} for the blank electrolyte. The decrease in the capacitance with increasing the scan rate is caused by the kinetic limitations due to the lack of time for charge carriers to penetrate into the porous electrode structure [40, 41].

N-GNFs showed similar to GNFs specific capacitances of 120 (0.05 MPyr11Fc), 118 (0.05 MPyr12Fc), 125 (0.05 MPip11Fc) and 101 (blank electrolyte) F·g^{-1} at 5 mV·s^{-1}. However, the increase in the scan rate resulted in a more pronounced dropin the specific capacitances of N-GNFs (Table 1). At 50 mV·s^{-1} the contribution of redox peaks to the CV area for N-GNFs electrodes is lower (Fig. 2*c*), which may be attributed to their significantly different porosity. The GNFs specific surface area of 1720 m^2·g^{-1} and mesopore volume of 2.38 cm^3·g^{-1} [36] are significantly higher than those of N-GNFs (1180 m^2·g^{-1} and 1.16 cm^3·g^{-1} [37]). The abundant mesopores in the electrode material should shorten the ion diffusion pathways and facilitate smooth and high-rate ion mobility [42]. Therefore, higher free pore volume of GNFs provided by mesopores reduces the kinetic limitations for charge carriers during charging/discharging processes. In contrast, lower fraction of mesopores and a high content of micropores (0.54 cm^3·g^{-1}) in N-GNFs can impede migration of bulk solvated ions of Fc-ILs into the porous electrode structure. These limitations become more pronounced at higher scan rates. Thus, the difference in the GNFs and N-GNFs porosity was expected to result in their different electrochemical performances in SCs. Nevertheless, the similar values of specific capacitances of these electrodes at low scan rates suggest that lower double layer capacitance of N-GNFs because of their lower specific surface area is compensated by extra pseudocapacitive contribution provided by reversible redox reactions that involve nitrogen species in N-GNF. However, this compensation effect diminishes at higher scan rates. At 200 mV·s^{-1} the specific capacitances of N-GNFs were lower than those of GNFs:76 (Pyr11Fc), 72 (Pyr12Fc), 81 (Pip11Fc) and 74 (blank electrolyte) F·g^{-1}.

The non-linearity of the GCD curves recorded for Fc-ILs-electrolytes confirms the Faradaic behavior of redox-active electrolytes (Figs. 2*d–f*). The GCD results demonstrate that the GNFs-based electrodes combined with redox-additives of the electrolytes provide higher capacitances than the N-GNFs electrodes (Table 2), which agrees with the CV data (Table 1).

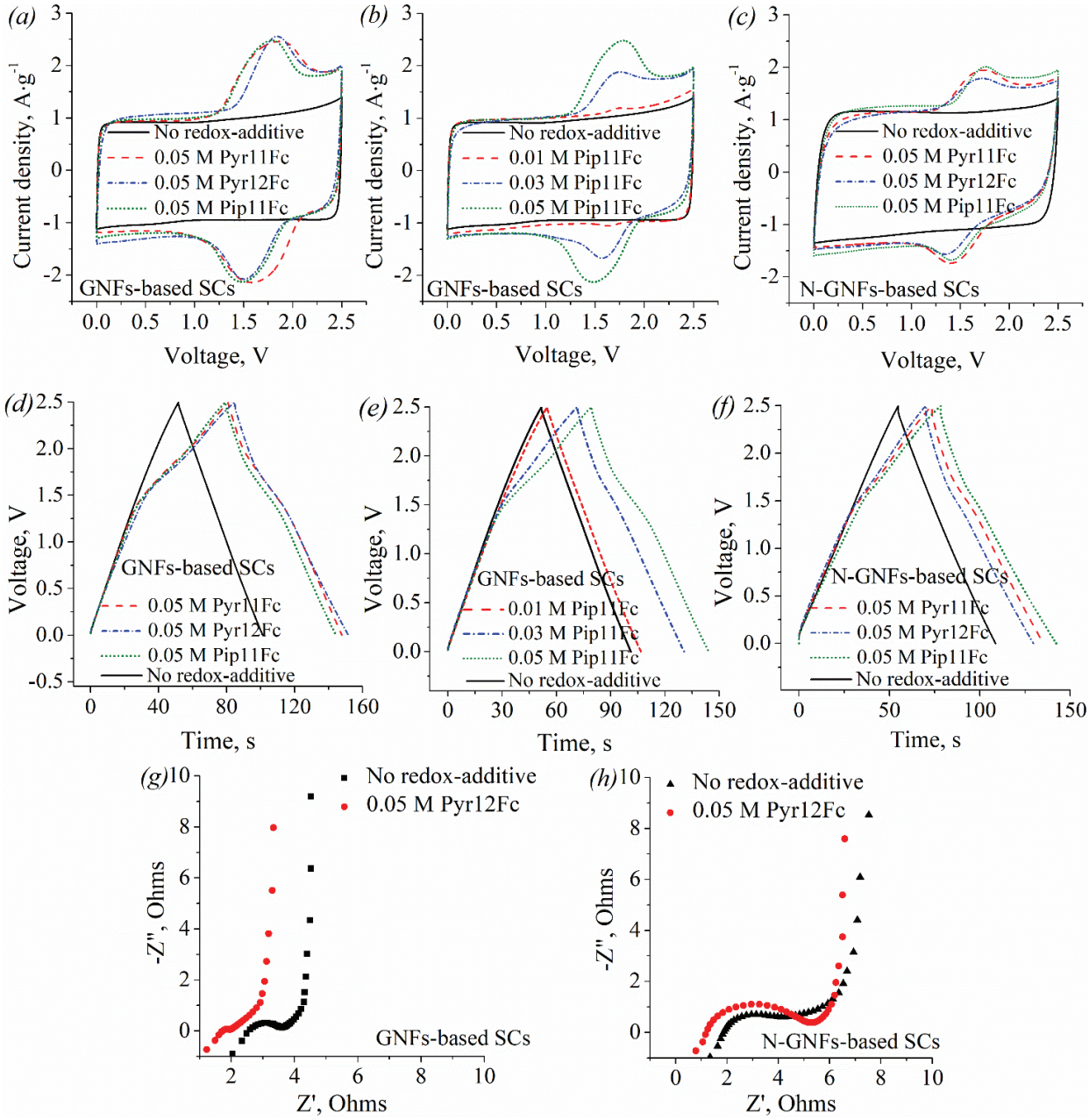

Fig. 2. CV (*a* – *c*) and GCD (*d* – *f*) curves of GNFs- (*a*, *b*, *d*, *e*) and N-GNFs- (*c*, *f*) based SCs recorded at scan rate of 50 mV·s^{-1} and current density of 1 A·g^{-1} (Potential range = 0 – 2.5 V, T = 298 K). Nyquist plots for GNFs- (*g*) and N-GNFs-based SCs (*h*) with 0.5 M [EMIm][NTf_2]/AN + 0.05 M Pyr12Fc

However, in the blank electrolyte the specific capacitance of N-GNFs (90.1 F·g^{-1} at 1 A·g^{-1}) exceeded this value for GNFs (79.6 F·g^{-1} at 1 A·g^{-1}). These results point to specific interactions between surface nitrogen-species and redox-active additives that reduce electrochemical performance of the SC. In particular, nitrogen groups may enhance the adsorption of products forming in a Faradaic process on the carbon electrode and increase self-discharge. The 0.05M Pyr11Fc additive to supporting electrolyte 0.5 M [EMIm][NTf_2]/AN provided slightly higher specific capacitance of GNFs (108.3 F·g^{-1} at 1 A·g^{-1}) than 0.05M Pyr12Fc(107.3 F·g^{-1}) and 0.05M Pip11Fc (104.6 F·g^{-1}) ones. The unit cell volume of the crystals increases in the series Pyr11Fc (1156.96(14) Å^3) < Pyr12Fc (2407.1(3) Å^3) < Pip11Fc (4771.6(5) Å^3) [35]. The lowest volume of Pyr11Fc is favorable for ions migration inside the smallest inner pores of the electrode. Indeed, the ionic conductivity of Fc-ILs in AN with a molar fraction of $x_{Fc\text{-IL}}$ = = 0.05 at 298.15 K follows the decreasing order: Pyr11Fc ((26.25 ± 0.28) mS·cm^{-1}) > Pyr12Fc ((25.79 ± ± 0.31) mS·cm^{-1}) > Pip11Fc ((23.94 ± 0.30) mS·cm^{-1}) [35].

Table 1. Effect of redox-active additives on specific capacitances ($F \cdot g^{-1}$) of GNF- and N-GNF-based electrodes at different scan rates

v, $mV \cdot s^{-1}$	GNFs						N-GNFs					
	5	10	20	50	100	200	5	10	20	50	100	200
No additive	85	83	81	78	76	73	101	97	93	88	83	74
0.01M Pyr11Fc	99	97	93	88	84	80	111	106	101	94	86	74
0.03M Pyr11Fc	112	109	106	101	96	90	116	110	104	94	89	64
0.05M Pyr11Fc	126	121	117	112	107	101	120	114	109	100	90	76
0.01M Pyr12Fc	93	91	89	85	82	78	105	99	95	88	81	71
0.03M Pyr12Fc	119	117	114	109	105	99	114	107	102	94	85	72
0.05M Pyr12Fc	123	119	115	109	102	93	118	113	106	95	85	71
0.01M Pip11Fc	93	91	88	84	81	78	104	97	92	84	76	65
0.03M Pip11Fc	110	107	103	97	90	83	117	112	105	92	80	65
0.05M Pip11Fc	122	119	115	109	104	97	125	119	113	104	95	81

Table 2. Effect of redox-active additives on specific capacitances ($F \cdot g^{-1}$) of GNF- and N-GNF-based electrodes at different current densities

i, $A \cdot g^{-1}$	GNFs				N-GNFs			
	1	1.5	2	2.5	1	1.5	2	2.5
No additive	79.6	74.6	78.2	72.4	90.1	88.2	86.5	85.0
0.01M Pyr11Fc	90.5	80.5	88.1	78.0	95.4	93.0	90.7	88.6
0.03M Pyr11Fc	92.6	89.2	91.8	87.3	95.9	92.5	88.7	85.1
0.05M Pyr11Fc	108.3	106.2	106.7	104.2	100.4	98.1	95.6	93.1
0.01M Pyr12Fc	86.6	79.5	84.3	76.8	89.4	86.9	84.8	82.8
0.03M Pyr12Fc	103.6	97.5	103.5	96.0	94.4	92.2	89.8	87.5
0.05M Pyr12Fc	107.3	98.5	106.6	95.0	84.7	85.0	89.1	91.4
0.01M Pip11Fc	83.3	77.2	81.8	75.0	85.4	82.5	80.0	77.6
0.03M Pip11Fc	95.1	86.5	92.5	83.2	92.3	90.7	88.0	85.0
0.05M Pip11Fc	104.6	99.6	103.4	97.3	103.9	101.8	99.5	97.2

This trend correlates with the mobility of the cations: the diffusion coefficients determined for 0.01 M Fc-IL solutions in AN were $5.06 \cdot 10^{-6}$ $cm^2 \cdot s^{-1}$ ($Pyr11Fc^+$), $4.76 \cdot 10^{-6}$ $cm^2 \cdot s^{-1}$ ($Pyr12Fc^+$), and $4.51 \cdot 10^{-6}$ $cm^2 \cdot s^{-1}$ ($Pip11Fc^+$) [35].

The results are consistent with the electrochemical impedance spectroscopy data (Fig. 2*g*, *h*). The charge transfer resistance (R_{ct}), defined by the diameter of the semicircle, is the smallest for GNFs-based SCs. In contrast, N-GNFs-based SCs demonstrate a higher R_{ct} value, which is attributed to diffusion limitations caused by ion migration within the porous electrode structure during charge storage.

GCD curves were also used to study the effect of self-discharge due to the so-called "shuttle effect" – diffusion of the redox component to the opposite electrode immediately after oxidation/reduction [43]. Because of this effect the charge capacity exceeds the discharge capacity. The ratio of discharge to charge capacities is the Coulomb efficiency that characterizes the excess energy required to charge the device. This excess energy is dissipated as heat. Therefore, high Coulomb efficiency, close to 100 % is desirable for any electrochemical device. Table 3 summarizes the Coulomb efficiencies of the ILs-based SCs. For all the electrolytes, an increase in Coulomb efficiency was observed with increasing the current density. At high current densities of 1–2.5 $A \cdot g^{-1}$ the Coulomb efficiencies exceed 80 %, which are suitable for electrochemical application. At the same time, a low current density of 0.2 $A \cdot g^{-1}$

Table 3. The Coulomb efficiency (%) of GNF- and N-GNF-based SCs at different current densities *i*

i, A·g^{-1}	GNFs					N-GNFs				
	0.2	1	1.5	2	2.5	0.2	1	1.5	2	2.5
No additive	84.6	95.5	96.7	97.3	97.8	88.1	97.7	98.5	98.8	99.1
0.01M Pyr11Fc	69.4	85.8	90.4	92.3	93.9	83.1	91.1	89.7	93.9	96.1
0.03M Pyr11Fc	41.8	78.6	85.3	88.8	91.1	55.2	83.9	89.1	92.1	93.7
0.05M Pyr11Fc	26.8	81.9	87.8	90.7	92.7	23.3	60.0	72.8	79.1	83.0
0.01M Pyr12Fc	76.2	91.4	94.1	95.5	96.4	87.0	95.1	96.8	97.7	98.2
0.03M Pyr12Fc	37.9	80.1	86.2	89.7	91.7	43.5	86.4	90.8	93.0	94.4
0.05M Pyr12Fc	29.3	78.7	85.5	89.2	91.5	27.5	84.7	85.0	89.1	91.4
0.01M Pip11Fc	83.2	93.9	95.7	96.7	97.3	83.1	94.6	96.5	97.4	98.0
0.03M Pip11Fc	43.1	82.3	87.6	90.8	92.6	51.2	87.8	89.4	89.5	86.3
0.05M Pip11Fc	35.4	81.6	87.0	90.4	92.2	42.4	81.7	87.6	90.6	92.4

led to significant drop in the Coulomb efficiencies of the Fc-ILs-based SCs down to 27 % probably because at low current density the rate of a potential leakage due to self-diffusion of the oxidized species to the anode was comparable with the rates of electric double layer accumulation and pseudo-capacitive processes. The similar result was reported by Bodin et al. [44] for the self-discharge of SCs based on 0.1 M of a 4-methylimidazolium-2,2,6,6-tetramethylpiperidine-1-oxyl bis(trifluoromethyl-sulfonyl)imide [TEMPOIm][NTf_2] redox-active IL in 1-butyl-3-methylimidazolium bis(trifluoromethyl-sulfonyl)imide [BMIm][NTf_2]. At a high current density of 0.5 A·g^{-1} the Coulomb efficiency of the SCs approached 100 %, while it significantly degraded at low current densities (< 0.1 A·g^{-1}).

The self-discharge rate is a crucial parameter for assessing performance and practical viability of SCs, as it directly impacts their energy retention capability. The self-discharge drop is usually described by several mechanisms [45–47]:

1) The self-discharge caused by redistribution of charge due to its non-uniform distribution on the surface and in the bulk of the electrode. In particular, after charging, ions gradually diffuse from the surface into the bulk material, decreasing the cell voltage.

2) The self-discharge controlled by a potential-dependent Faraday charge-transfer reaction (Fe^{2+}/Fe^{3+}):

$$E_t = E_0 - A\ln(t + t_0). \quad (5)$$

Here, A corresponds to Tafel slope constant, t is the time, t_0 is the integration constant, and E_0 is the initial cell potential.

3) The self-discharge determined by the semi-infinite diffusion of impurities within pores of the electrode material:

$$E_t = E_0 - 2zFSCc_0\sqrt{D\pi t}. \quad (6)$$

Here, D is the diffusion coefficient, S is the specific surface area of the porous electrode material, C is the cell capacitance.

4) The self-discharge caused by the leakage current flowing through a resistance between electrodes due to the imperfection of insulating materials used in the SC:

$$E_t = E_0 \exp\left(-\frac{t}{RC}\right). \quad (7)$$

Here, RC is the time constant of resistance.

In general, different mechanisms contribute to the self-discharge of SC. When the ohmic leakage is the main reason for self-discharge, a linear dependence between $\ln E_t$ and t is observed. In our case the $\ln E_t - t$ dependences are linear after discharging for approximately 10000 s (Fig. 3*a*). Also, experimental E_t versus $\ln(t)$ dependencies initially exhibit a plateau followed by a linear drop in the intermediate part of the self-discharge curves (Fig. 3*b*). When the self-discharge process is limited by diffusion in porous electrode, the voltage E_t should be proportional to the square root of the self-discharge time $t^{1/2}$. Such linear dependence is not observed for the Fc-ILs-based SCs (Fig. 3*c*), which excludes the significant effect of semi-infinite diffusion of impurities to a self-discharge. Therefore,

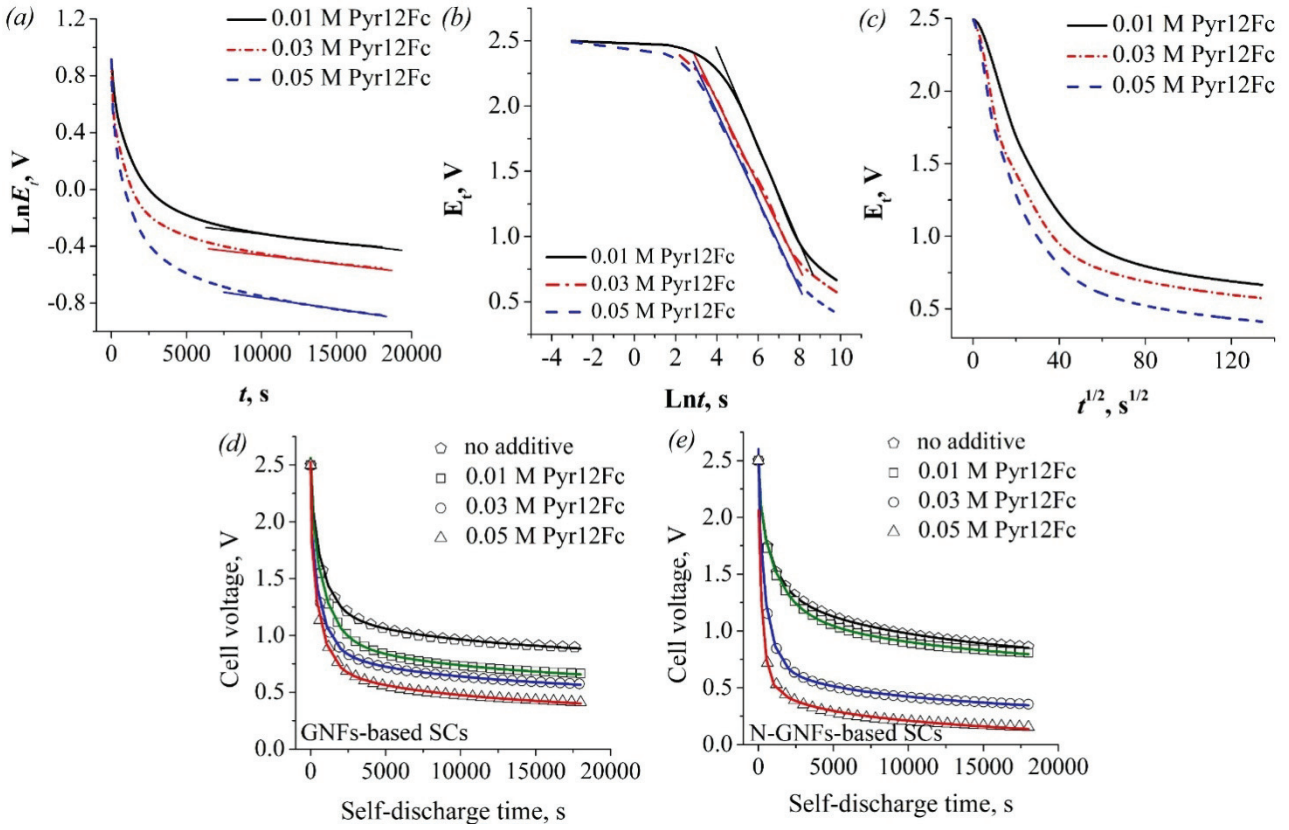

Fig. 3. Self-discharge profiles of SCs based GNFs and IL electrolyte with PyrFcEt additive as ln$E_t - t$ (*a*), E_t – ln$t$ (*b*) and $E_t - t^{1/2}$ (*c*), self-discharge profiles of GNF- (*d*) and N-GNF-based (*e*) SCs (Solid lines show the best-fit curves for hybrid model)

the initial drop in E_t after charging (Fig. 3*d*, *e*) attributed to the charge redistribution is followed by an activation-controlled process in the intermediate stage and, finally, by ohmic leakage, which agrees with data reported by Zhao et al. for all-solid-state SCs [48].

Faradaic redox processes and leakage-current mechanism mainly contribute to the self-discharge of the SCs. To account for the effects of both these mechanisms on self-discharge, the hybrid model was proposed:

$$E_t = A_0 - A_1 \ln(t + t_0) + A_2 \exp\left(-\frac{t}{RC}\right). \qquad (8)$$

Here, A_i is the fitting parameter. This model describes the experimental voltage drop versus time dependencies with high accuracy (coefficient of determination $R^2 > 0.997$) (Figs. 3*d*, *e*, Table 4).

In contrast to the SCs without redox-additives, the addition of Fc-ILs to the electrolyte enhances the rate of self-discharge due to the increased contribution of the "shuttle effect". Modification of the electrolytes with Fc-ILs leads to the formation of Fe^{3+} redox impurities. These species can migrate between two electrodes, where they are oxidized or reduced. The associated shuttle process causes a parasitic charge transfer, which lowers the SC voltage and increases its self-discharge rate. A similar trend was previously reported for the KOH/$K_3Fe(CN)_6$ [46] and Li_2SO_4/4-n-pentyl-4'-cyanobiphenyl [47] redox electrolytes.

The N-GNF-based SCs with the blank electrolyte showed a drop in the potential profile similar to that observed for GNFs-based SCs but with a higher self-discharge rate (Fig. 3*e*). Modification of carbon surface with nitrogen groups may facilitate adsorption of the oxidized species forming during Faradaic reactions. At the same time such products cannot quickly leave the electrode surface during self-discharge due to their strong interactions. In contrast to N-GNFs, adsorption of the oxidized species on the surface of undoped GNFs is weaker, which lowers their surface concentration and thus slows the self-discharge. Therefore, nitrogen-containing groups on the carbon surface don't facilitate self-discharge in the absence of redox impurities while redox-active electrolyte additives provide a shuttle of ferrocenyl-groups with their subsequent reduction on the cathode surface.

Table 4. Parameters of the best-fits to potential drop profiles with hybrid model (8)

Redox-electrolyte additive	$E_t = A_0 - A_1 \ln(t + t_0) + A_2 \exp\left(-\frac{t}{RC}\right)$					
	A_1, V	A_2, V	A_0, V	t_0, s	RC, s	R^2
			GNFs			
No additive	0.136 ± 0.001	0.708 ± 0.004	2.21 ± 0.01	14.7 ± 1.5	874 ± 7	0.9989
0.01M Pyr11Fc	0.124 ± 0.001	0.812 ± 0.008	1.85 ± 0.01	2.8 ± 0.5	495 ± 7	0.9979
0.03M Pyr11Fc	0.183 ± 0.001	0.404 ± 0.004	2.35 ± 0.01	2.9 ± 0.2	911 ± 11	0.9987
0.05M Pyr11Fc	0.129 ± 0.001	0.556 ± 0.008	1.92 ± 0.01	0.7 ± 0.1	503 ± 11	0.9970
0.01M Pyr12Fc	0.136 ± 0.001	0.821 ± 0.004	1.99 ± 0.01	6.4 ± 0.6	995 ± 6	0.9989
0.03M Pyr12Fc	0.123 ± 0.002	0.735 ± 0.009	1.77 ± 0.01	0.9 ± 0.2	720 ± 12	0.9972
0.05M Pyr12Fc	0.126 ± 0.001	0.800 ± 0.005	1.63 ± 0.01	0.5 ± 0.1	679 ± 6	0.9969
0.01M Pip11Fc	0.129 ± 0.001	0.834 ± 0.008	1.94 ± 0.01	6.2 ± 1.0	589 ± 8	0.9983
0.03M Pip11Fc	0.132 ± 0.001	0.794 ± 0.008	1.74 ± 0.01	1.1 ± 0.2	627 ± 9	0.9980
0.05M Pip11Fc	0.138 ± 0.001	0.684 ± 0.005	1.80 ± 0.01	0.6 ± 0.1	685 ± 8	0.9979
			N-GNFs			
No additive	0.184 ± 0.001	0.504 ± 0.002	2.60 ± 0.01	16.4 ± 0.6	1398 ± 6	0.9989
0.01M Pyr11Fc	0.153 ± 0.001	0.628 ± 0.003	2.12 ± 0.01	2.1 ± 0.2	626 ± 4	0.9963
0.03M Pyr11Fc	0.082 ± 0.001	1.373 ± 0.005	0.88 ± 0.01	0.04±0.01	211 ± 1	0.9911
0.05M Pyr11Fc	0.175 ± 0.001	0.398 ± 0.002	2.30 ± 0.01	1.4 ± 0.1	706 ± 6	0.9967
0.01M Pyr12Fc	0.215 ± 0.001	0.344 ± 0.001	2.96 ± 0.01	35.5 ± 0.6	963 ± 5	0.9995
0.03M Pyr12Fc	0.131 ± 0.001	1.031 ± 0.002	1.63 ± 0.01	1.6 ± 0.1	591 ± 1	0.9988
0.05M Pyr12Fc	0.125 ± 0.001	1.132 ± 0.004	1.37 ± 0.01	0.6 ± 0.1	282 ± 1	0.9945
0.01M Pip11Fc	0.239 ± 0.001	0.301 ± 0.001	3.19 ± 0.01	60.9 ± 0.5	1641 ± 5	0.9999
0.03M Pip11Fc	0.075 ± 0.001	1.371 ± 0.005	0.84 ± 0.01	0.02±0.01	176 ± 1	0.9896
0.05M Pip11Fc	0.129 ± 0.001	0.987 ± 0.002	1.56 ± 0.01	0.8 ± 0.1	471 ± 1	0.9988

Table 5. Energy ($Wh \cdot kg^{-1}$) [power ($kW \cdot kg^{-1}$)] densities of GNF- and N-GNF-based SCs

i, $A \cdot g^{-1}$	GNFs				N-GNFs			
	1	1.5	2	2.5	1	1.5	2	2.5
No additive	16.4 [1.1]	16.2 [1.7]	16.0 [2.4]	15.7 [2.9]	17.0 [1.1]	16.2 [1.7]	15.5 [2.2]	14.8 [2.7]
0.01M Pyr11Fc	17.7 [1.1]	17.5 [1.7]	17.0 [2.3]	16.9 [2.8]	18.0 [1.1]	17.1 [1.6]	16.3 [2.1]	15.5 [2.6]
0.03M Pyr11Fc	19.4 [1.1]	19.3 [1.7]	19.2 [2.3]	18.9 [2.9]	17.7 [0.9]	16.9 [1.4]	15.8 [1.9]	14.6 [2.3]
0.05M Pyr11Fc	23.1 [1.1]	23.0 [1.8]	22.9 [2.3]	22.6 [3.1]	18.8 [1.1]	18.0 [1.6]	17.1 [2.1]	16.3 [2.6]
0.01M Pyr12Fc	17.6 [1.2]	17.3 [1.7]	17.0 [2.5]	16.7 [2.9]	16.8 [1.1]	16.0 [1.6]	15.2 [2.1]	14.4 [2.6]
0.03M Pyr12Fc	21.2 [1.2]	21.2 [1.7]	21.1 [2.3]	20.8 [2.9]	17.2 [1.0]	16.4 [1.6]	15.59 [2.1]	14.8 [2.6]
0.05M Pyr12Fc	21.6 [1.1]	21.4 [1.7]	21.1 [2.4]	20.6 [2.9]	17.6 [1.1]	17.8 [1.5]	16.4 [2.0]	15.2 [2.4]
0.01M Pip11Fc	17.0 [1.1]	16.8 [1.8]	16.5 [2.4]	16.3 [2.9]	15.8 [1.1]	14.9 [1.6]	14.0 [2.1]	13.2 [2.5]
0.03M Pip11Fc	19.1 [1.2]	18.8 [1.7]	18.5 [2.4]	18.1 [2.9]	17.6 [0.9]	17.4 [1.4]	16.7 [1.9]	15.8 [2.4]
0.05M Pip11Fc	21.7 [1.1]	21.6 [1.8]	21.4 [2.4]	21.1 [2.9]	19.1 [1.1]	18.4 [1.6]	17.6 [2.1]	16.9 [2.6]

Specific energies and power densities were calculated from the GCD curves (Table 5). The highest E_{SC} values of 23.1, 21.6 and 21.7 Wh·kg^{-1} at P_{SC} of 1.2 kW·kg^{-1} were observed for the GNFs-based SCs with the supporting electrolyte 0.5 M [EMIm][NTf_2]/AN and 0.05 M Pyr11Fc, Pyr12Fc and Pip11Fc additives, respectively. For N-GNFs the energy densities were lower: 18.8 (0.05 M Pyr11Fc), 17.6 (0.05 M Pyr12Fc) and 19.1 (0.05 M Pip11Fc) Wh·kg^{-1}, which may be caused by higher impact of self-discharge. The specific energy densities of the Fc-ILs-based SCs were close to those previously reported for activated carbon in PVA/poly (vinyl pyrrolidone)/$EMIHSO_4$/HQ (24.3 Wh·kg^{-1} at ~1.5 kW·kg^{-1}) [5], PVA/Li_2SO_4/BMIMBr (38.0 Wh·kg^{-1} at 0.2 kW·kg^{-1}) [28], and PVA/Li_2SO_4/BMIMI (29.3 Wh·kg^{-1} at ~0.1 kW·kg^{-1}) [27], N-doped carbon in 2.5 M KBr + 2 M H_2SO_4 (14.3 Wh·kg^{-1} at 639.8 W·kg^{-1}) [20], reduced graphene oxide in H_2O/$K_4[Fe(CN)_6]$/K_2SO_4 (36.8 Wh·kg^{-1} at 1.2 kW·kg^{-1}) [16].

4. Conclusion

In summary, the ferrocene-containing ionic liquids were tested as new redox-additives to ILs electrolytes of non-aqueous supercapacitors with undoped and N-doped GNF electrodes. The electrochemical performance of the SCs was found to depend on the fraction of the redox-additive in 0.5 M [EMIm][NTf_2]/AN and the type of electrode material. Modification of 0.5 M [EMIm][NTf_2]/AN with 0.05 M Fc-ILs significantly improved the specific capacitance of the SCs due to reversible Faradaic reactions. Although nitrogen doping of GNFs was anticipated to enhance their pseudocapacitance, the results of our work demonstrate that changes in the textural parameter of GNFs under doping are the dominant factor affecting their specific capacitance in Fc-IL-based SCs. A self-discharge mechanism was analyzed using the hybrid model that accounts for contributions of charge redistribution, Faradaic redox processes and leakage-currents. In contrast to GNFs, N-GNFs negatively affected the SCs performance, increasing self-discharge due to the adsorption of redox-species on the electrode surface that was consistent with the decrease in Coulombic efficiencies (Table 3). Undoubtedly, this work demonstrates the promising performances of the Fc-ILs-based supercapacitors, however, a crucial role of the electrode material is highlighted.

5. Funding

This study was carried out with the financial support of the Russian Science Foundation (Project No. 24-23-00165).

Финансирование

Исследование выполнено за счет средств гранта Российского научного фонда № 24-23-00165.

6. Conflict of interests

The authors declare no conflict of interest.

Конфликт интересов

Авторы заявляют об отсутствии конфликта интересов.

References

1. Qin G, Liu Y, Zhang W, He W, et al. Integrated supercapacitor with self-healing, arbitrary deformability and anti-freezing based on gradient interface structure from electrode to electrolyte. *Journal of Colloid and Interface Science*. 2023;635:427-440. DOI:10.1016/j.jcis.2022.12.164

2. Hor AA, Yadav N, Hashmi SA. High energy density carbon supercapacitor with ionic liquid-based gel polymer electrolyte: role of redox-additive potassium iodide. *Journal of Energy Storage*. 2022;47:103608. DOI:10.1016/j.est.2021.103608

3. Arsha MS, Biju V. A 3.5 V supercapacitor with ultrahigh energy and power capabilities using thermally deoxygenated graphite oxide electrodes and water-in-salt electrolyte. *Energy & Fuels*. 2024;38(19):19076-19087. DOI:10.1021/acs.energyfuels.4c02984

4. Hao L, Shen L, Wang J, Xu Y, et al. Hollow $NiCo_2S_4$ nanotube arrays grown on carbon textile as a self-supported electrode for asymmetric supercapacitors. *RSC Advances*. 2016;6(12):9950-9957. DOI:10.1039/C5RA24068A

5. Yadav N, Yadav N, Hashmi SA. Ionic liquid incorporated, redox-active blend polymer electrolyte for high energy density quasi-solid-state carbon supercapacitor. *Journal of Power Sources*. 2020;451:227771. DOI:10.1016/j.jpowsour.2020.227771

6. Luo Y, Wang S, Xu Y, Liu N, et al. Exploring redox-active electrolytes to boost energy density of carbon-based supercapacitors. *Journal of Colloid and Interface Science*. 2025;684:729-734. DOI:10.1016/j.jcis.2025.01.082

7. Halder J, De P, Chandra A. Synergistic contribution of redox additive electrolytes to significantly increase the performances of hybrid supercapacitors. *Journal of Energy Storage*. 2024;104:114583. DOI:10.1016/j.est.2024.114583

8. Arkhipova EA, Ivanov AS, Isaikina OYa, Novotortsev RYu, et al. Application of MnO_2/MWCNT composite in supercapacitors. *Materials Today: Proceedings*. 2022;60:1008-1011. DOI:10.1016/j.matpr.2021.12.408

9. Shanmugavani A, Kaviselvi S, Sankar KV, Selvan RK. Enhanced electrochemical performances of PANI using redox additive of $K_4[Fe(CN)_6]$ in aqueous electrolyte for symmetric supercapacitors. *Materials Research Bulletin*. 2015;62:161-167. DOI:10.1016/j.materresbull.2014.10.075

10. Arkhipova EA, Ivanov AS, Maslakov KI, Savilov SV. Nitrogen-doped mesoporous graphene nanoflakes for high performance ionic liquid supercapacitors. *Electrochimica Acta*. 2020;353:136463. DOI:10.1016/j.electacta.2020.136463

11. Kumar R, Sahoo S, Joanni E, Singh RK, et al. Heteroatom doped graphene engineering for energy storage and conversion. *Materials Today*. 2020;39:47-65. DOI:10.1016/j.mattod.2020.04.010

12. Śliwak A, Grzyb B, Díez N, Gryglewicz G. Nitrogen-doped reduced graphene oxide as electrode material for high-rate supercapacitors. *Applied Surface Science*. 2017;399:265-271. DOI:10.1016/j.apsusc.2016.12.060

13. Chen Y, Huang J, Zhang X, Xu H. Fabrication of hybrid supercapacitor of RGO//PPyNTs/$Co(OH)_2$ based on $K_3Fe(CN)_6$ redox-active electrolyte. *Journal of Electroanalytical Chemistry*. 2021;884:115069. DOI:10.1016/j.jelechem.2021.115069

14. Akhtar MA, Chowdhury A, Chandra A. Addition of redox additives–synergic strategy for enhancing the electrochemical activity of spinel Co_3O_4 based supercapacitors. *Journal of Physics D: Applied Physics*. 2019;52(15):155501. DOI:10.1088/1361-6463/ab00d3

15. Oskin P, Lepikash R, Dyachkova T, Alferov S. Comparative evaluation of different methods for determining the specific surface area of carbon materials used in electrochemical systems. *Journal of Advanced Materials and Technologies*. 2024;9(3):167-176. DOI:10.17277/jamt.2024.03.pp.167-176

16. Sawant SA, Waikar MR, Chodankar GR, Gurav SR, et al. A redox additive electrolyte boosted supercapacitive energy density of wrinkled RGO sheets. *Journal of Energy Storage*. 2024;76:109739. DOI:10.1016/j.est.2023.109739

17. Raja TA, Vickraman P. Role of dual redox additives KI/ $VOSO_4$ in manganese ammonium phosphate at graphene quantum dots for supercapattery. *International Journal of Energy Research*. 2022;46(7):9097-9113. DOI:10.1002/er.7787

18. Yang W, Han Q, Li W, Wu M, et al. Suppressed shuttle effect and Self-Discharge of redox electrochemical capacitors using biphasic electrolyte with a Liquid-Liquid interface. *Chemical Engineering Journal*. 2022;448:137731. DOI:10.1016/j.cej.2022.137731

19. Fic K, Morimoto S, Frąckowiak E, Ishikawa M. Redox activity of bromides in carbon-based electrochemical capacitors. *Batteries & Supercaps*. 2020;3(10):1080-1090. DOI:10.1002/batt.202000061

20. Hwang B, Yang J, Kim D, Yun WC, et al. Redox enhanced membraneless electrochemical capacitor with CO_2-derived hierarchical porous carbon electrodes. *Electrochimica Acta*. 2023;442:141871. DOI:10.1016/j.electacta.2023.141871

21. Liu Y, Dai J, Xiao Y, Wang Y, et al. Novel zinc-ion hybrid supercapacitors with enhanced specific capacity by redox-active ions. *Journal of Energy Storage*. 2024;77:109834. DOI:10.1016/j.est.2023.109834

22. Huang X, Wang Q, Chen XY, Zhang ZJ. The effects of amine/nitro/hydroxyl groups on the benzene rings of redox additives on the electrochemical performance of carbon-based supercapacitors. *Physical Chemistry Chemical Physics*. 2016;18(15):10438-10452. DOI:10.1039/C6CP00211K

23. Manickavasakam K, Suresh Balaji S, Kaipannan S, Karthick Raj AG, et al. Electrochemical performance of Thespesia Populnea seeds derived activated carbon – supercapacitor and its improved specific energy in redox additive electrolytes. *Journal of Energy Storage*. 2020;32:101939. DOI:10.1016/j.est.2020.101939

24. Gebremariam GK, Jovanović AZ, Pašti IA. The effect of electrolytes on the kinetics of the hydrogen evolution reaction. *Hydrogen*. 2023;4(4):776-806. DOI:10.3390/hydrogen4040049

25. Warrington A, O'Dell LA, Hutt OE, Forsyth M, et al. Structure and interactions of novel ether-functionalised morpholinium and piperidinium ionic liquids with lithium salts. *Energy Advances*. 2023;2(4):530-546. DOI:10.1039/D2YA00348A

26. Ong SP, Andreussi O, Wu Y, Marzari N, et al. Electrochemical windows of room-temperature ionic liquids from molecular dynamics and density functional theory calculations. *Chemistry of Materials*. 2011;23(11):2979-2986. DOI:10.1021/cm200679y

27. Tu QM, Fan LQ, Pan F, Huang JL, et al. Design of a novel redox-active gel polymer electrolyte with a dual-role ionic liquid for flexible supercapacitors. *Electrochimica Acta*. 2018;268:562-568. DOI:10.1016/j.electacta.2018.02.008

28. Fan LQ, Tu QM, Geng CL, Huang JL, et al. High energy density and low self-discharge of a quasi-solid-state supercapacitor with carbon nanotubes incorporated redox-active ionic liquid-based gel polymer electrolyte. *Electrochimica Acta*. 2020;331:135425. DOI:10.1016/j.electacta.2019.135425

29. Lee KS, Jeong HT. Development and optimization of ionic liquid-based gel polymer electrolyte for all solid-state supercapacitor. *Journal of Energy Storage*. 2021;42:103001. DOI:10.1016/j.est.2021.103001

30. Geng CL, Fan LQ, Wang CY, Wang YL, et al. High energy density and high working voltage of a quasi-solid-state supercapacitor with a redox-active ionic liquid added gel polymer electrolyte. *New Journal of Chemistry*. 2019;43(47):18935-18942. DOI:10.1039/C9NJ04769G

31. Benjamin M, Manoj D, Karnan M, et al. Switching the solubility of electroactive ionic liquids for designing high energy supercapacitor and low potential biosensor. *Journal of Colloid and Interface Science*. 2021;588:221-231. DOI:10.1016/j.jcis.2020.12.033

32. Xie HJ, Gélinas B, Rochefort D. Redox-active electrolyte supercapacitors using electroactive ionic liquids. *Electrochemistry Communications*. 2016;66:42-45. DOI:10.1016/j.elecom.2016.02.019

33. Borchers PS, Gerlach P, Liu Y, Hager MD, et al. The influence of the nature of redox-active moieties on the properties of redox-active ionic liquids and on their use as electrolyte for supercapacitors. *Energies*. 2021;14(19): 6344. DOI:10.3390/en14196344

34. Gélinas B, Forgie JC, Rochefort D. Conductivity and electrochemistry of ferrocenyl-imidazolium redox ionic liquids with different alkyl chain lengths. *Journal of The Electrochemical Society*. 2014;161(4):H161-H165. DOI:10.1149/2.017404jes

35. Arkhipova EA, Levin MM, Ivanov AS, Zakharov MA, et al. Electroactive ferrocene-based ionic liquids: transport and electrochemical properties of their acetonitrile solutions. *Electrochimica Acta*. 2025;512:145443. DOI:10.1016/j.electacta.2024.145443

36. Arkhipova EA, Ivanov AS, Maslakov KI, Egorov AV, et al. Mesoporous graphene nanoflakes for high performance supercapacitors with ionic liquid electrolyte. *Microporous and Mesoporous Materials*. 2020;294:109851. DOI:10.1016/j.micromeso.2019.109851

37. Savilov SV, Arkhipova EA, Ivanov AS, Maslakov KI, et al. Pyrolytic synthesis and characterization of N-doped carbon nanoflakes for electrochemical applications. *Materials Research Bulletin*. 2015;69:7-12. DOI:10.1016/j.materresbull.2014.12.057

38. Klein JM, Panichi E, Gurkan B. Potential dependent capacitance of [EMIM][TFSI], [N_{1114}][TFSI] and [PYR_{13}][TFSI] ionic liquids on glassy carbon. *Physical Chemistry Chemical Physics*. 2019;21(7):3712-3720. DOI:10.1039/C8CP04631J

39. Choudhury BJ, Muigai HH, Kalita P, Moholkar VS. Biomass blend derived porous carbon for aqueous supercapacitors with commercial-level mass loadings and enhanced energy density in redox-active electrolyte. *Applied Surface Science*. 2022;601:154202. DOI:10.1016/j.apsusc.2022.154202

40. Ghosh K, Srivastava SK. Enhanced supercapacitor performance and electromagnetic interference shielding effectiveness of CuS quantum dots grown on reduced graphene oxide sheets. *ACS Omega*. 2021;6(7):4582-4596. DOI:10.1021/acsomega.0c05034

41. Duraisamy N, Arshid N, Kandiah K, Iqbal J, et al. Development of asymmetric device using $Co_3(PO_4)_2$ as a positive electrode for energy storage application. *Journal of Materials Science: Materials in Electronics*. 2019;30(8):7435-7446. DOI:10.1007/s10854-019-01057-x

42. Zhou D, Wang H, Mao N, Chen Y, et al. High energy supercapacitors based on interconnected porous carbon nanosheets with ionic liquid electrolyte. *Microporous and Mesoporous Materials*. 2017;241:202-209. DOI:10.1016/j.micromeso.2017.01.001

43. Lee J, Srimuk P, Fleischmann S, Su X, et al. Redox-electrolytes for non-flow electrochemical energy storage: a critical review and best practice. *Progress in Materials Science*. 2019;101:46-89. DOI:10.1016/j.pmatsci.2018.10.005

44. Bodin C, Sekhar Bongur C, Deschanels M, Catrouillet S, et al. Shuttle effect quantification for redox ionic liquid electrolyte correlated to the coulombic efficiency of supercapacitors. *Batteries & Supercaps*. 2020;3(11):1193-1200. DOI:10.1002/batt.202000084

45. Shang W, Yu W, Xiao X, Ma Y, et al. Insight into the self-discharge suppression of electrochemical capacitors: progress and challenges. *Advanced Powder Materials.* 2023;2(1):100075. DOI:10.1016/j.apmate.2022.100075

46. Chen H, Zhang Y, Yang H, Jia B, et al. Self-discharge of redox electrolyte enhanced supercapacitors based on nanosheet-like CoS_2. *Chemical Engineering Journal*. 2024;494:152910. DOI:10.1016/j.cej.2024.152910

47. Volfkovich YuM. Self-discharge of supercapacitors: a review. *Russian Journal of Electrochemistry*. 2023;59(1):24-36. DOI:10.1134/S1023193523010123

48. Zhao H, Zhang H, Wang Z, Jiang X, et al. Chain-Elongated ionic liquid electrolytes for low self-discharge all-solid-state supercapacitors at high temperature. *ChemSusChem*. 2021;14(18):3895-3903. DOI:10.1002/cssc.202101294

Information about the authors / Информация об авторах

Mikhail M. Levin, Technician, Lomonosov Moscow State University (MSU), Faculty of Chemistry, Moscow, Russian Federation; ORCID 0000-0003-1156-2159; e-mail: mikhail.levin@chemistry.msu.ru

Ekaterina A. Arkhipova, Cand. Sc. (Chem.), Senior Researcher, MSU, Faculty of Chemistry, Moscow, Russian Federation; ORCID 0000-0002-1710-2041; e-mail: ekaterina.a.arkhipova@gmail.com

Anton S. Ivanov, Cand. Sc. (Chem.), Senior Researcher, MSU, Faculty of Chemistry, Moscow, Russian Federation; ORCID 0000-0003-1719-0106; e-mail: anthon.s.ivanov@gmail.com

Левин Михаил Михайлович, техник, Московский государственный университет им. М. В. Ломоносова (МГУ), Химический факультет, Москва, Российская Федерация; ORCID 0000-0003-1156-2159; e-mail: mikhail.levin@chemistry.msu.ru

Архипова Екатерина Анатольевна, кандидат химических наук, старший научный сотрудник, МГУ, Химический факультет, Москва, Российская Федерация; ORCID 0000-0002-1710-2041; e-mail: ekaterina.a.arkhipova@gmail.com

Иванов Антон Сергеевич, кандидат химических наук, старший научный сотрудник, МГУ, Химический факультет, Москва, Российская Федерация; ORCID 0000-0003-1719-0106; e-mail: anthon.s.ivanov@gmail.com

Konstantin I. Maslakov, Cand. Sc. (Phys. and Math.), Senior Researcher, MSU, Faculty of Chemistry, Moscow, Russian Federation; ORCID 0000-0002-0672-2683; e-mail: nonvitas@gmail.com

Serguei V. Savilov, D. Sc. (Chem.), Associate Professor, Leading Researcher, MSU, Faculty of Chemistry, Moscow, Russian Federation; ORCID 0000-0002-5827-3912; e-mail: savilov@mail.ru

Маслаков Константин Игоревич, кандидат физико-математических наук, старший научный сотрудник, МГУ, Химический факультет, Москва, Российская Федерация; ORCID 0000-0002-0672-2683; e-mail: nonvitas@gmail.com

Савилов Сергей Вячеславович, доктор химических наук, доцент, ведущий научный сотрудник, МГУ, Химический факультет, Москва, Российская Федерация; ORCID 0000-0002-5827-3912; e-mail: savilov@mail.ru

Received 03 November 2025; Revised 08 December 2025; Accepted 09 December 2025

Original papers
Materials for energy and environment, next-generation photovoltaics, and green technologies

УДК 546.824; 665.7.035.8 DOI: 10.17277/jamt-2026-11-02-152-161

Influence of doping additives and fluxes on the electrical properties of ceramic materials based on hollandite-like solid solutions in the K_2O-MnO-Al_2O_3-Cr_2O_3-TiO_2 system

© Nikolay V. Gorshkov[a], Alexey R. Tsyaganov[a], Andrey V. Durakov[a], Alexey A. Makarov[a], Alexander V. Gorokhovsky[a]✉

[a] *Yuri Gagarin State Technical University of Saratov, 77, Polytekhnicheskaya St., Saratov, 410054, Russian Federation*

✉ algo54@mail.ru

Abstract. Intermediates to produce ceramic powders were synthesized using amorphous potassium polytitanate ($K_2O{\cdot}4TiO_2{\cdot}xH_2O$, PPT) modified in aqueous solutions of mixtures of manganese and aluminum sulfates, taken in a 2 : 1 molar ratio, and manganese, aluminum, and chromium sulfates, taken in a 2 : 1/2 : 1/2 molar ratio. It was shown that heat treatment of these intermediates enables the synthesis of single-phase powders of hollandite-like solid solutions $K_{1.70}Mn_{1.66}Al_{0.81}Ti_{5.52}O_{16}$ and $K_{1.76}Mn_{1.60}Al_{0.39}Cr_{0.45}Ti_{5.48}O_{16}$, respectively. Ceramic dielectrics were fabricated using compacted powders of the obtained products, which were sintered at 1080 °C/3 h. The electrical properties of the ceramic specimens produced were investigated by impedance spectroscopy methods. It was shown that partial replacement of Al with Cr in the intermediate composition increases the permittivity (from 820 to 1580) and reduces dielectric loss (tg(δ), from 0.89 to 0.22). Moreover, some justified doping additives (Nb_2O_5, 0.5 %; Nd_2O_3, 0.3 %; LiF, 0.8 %) and a flux (zinc borate, 2%) allow for a further increase in dielectric constant (up to 57,800 ± 600), decrease of tg(δ) (down to 0.084 ± 0.02) and significantly increase the temperature stability of permittivity for the obtained ceramics in the temperature range from –55 to +125 °C up to the level corresponding to a X7T category of dielectrics.

Keywords: titanates; hollandite-like solid solutions; ceramics; synthesis; permittivity; dielectric losses.

For citation: Gorshkov NV, Tsyaganov AR, Durakov AV, Makarov AA, Gorokhovsky AV. Influence of doping additives and fluxes on the electrical properties of ceramic materials based on hollandite-like solid solutions in the K_2O-MnO-Al_2O_3-Cr_2O_3-TiO_2 system. *Journal of Advanced Materials and Technologies*. 2026;11(2):152-161. DOI: 10.17277/jamt-2026-11-02-152-161

Влияние допирующих добавок на электрофизические свойства керамики на основе голландитоподобных твердых растворов системы K_2O-MnO-Al_2O_3-Cr_2O_3-TiO_2

© Н. В. Горшков[a], А. Р. Цыганов[a], А. В. Дураков[a], А. А. Макаров[a], А. В. Гороховский[a]✉

[a] *Саратовский государственный технический университет имени Гагарина Ю.А., ул. Политехническая, 77, Саратов, 410054, Российская Федерация*

✉ algo54@mail.ru

Аннотация. На основе аморфного полититаната калия ($K_2O{\cdot}4TiO_2{\cdot}xH_2O$, ПТК), модифицированного в водных растворах смеси сульфата марганца и сульфата алюминия, взятых в мольном соотношении 2 : 1, а также смеси сульфатов марганца, алюминия и хрома, взятых в мольном соотношении 2 : 1/2 : 1/2, синтезированы интермедиаты для получения керамических порошков. Показано, что термическая обработка этих интермедиатов при 850 °C/2 ч позволяет получить монофазные порошки голландитоподобных твердых растворов состава $K_{1,70}Mn_{1,66}Al_{0,81}Ti_{5,52}O_{16}$ и $K_{1,76}Mn_{1,60}Al_{0,39}Cr_{0,45}Ti_{5,48}O_{16}$ соответственно. На основе компактированных порошков полученных продуктов изготовлены керамические диэлектрики, спеченные при 1080 °C/3 ч.

Электрические свойства полученных образцов исследованы методами импедансной спектроскопии. Показано, что частичная замена Al на Cr в составе интермедиата увеличивает диэлектрическую проницаемость (от 820 до 1580) и снижает диэлектрические потери (от 0,89 до 0,22) на рабочей частоте 1 кГц. При этом введение обоснованной комбинации допантов (Nb_2O_5, 0,5 %; Nd_2O_3, 0,3 %; LiF, 0,8 %) и флюсообразующей добавки (борат цинка, 2 %) позволяет добиться существенного увеличения диэлектрической проницаемости (до 57800 ± 600) и снижения диэлектрических потерь (tg(δ), до $0{,}084 \pm 0{,}02$), а также увеличивает температурную стабильность диэлектрической проницаемости керамики в интервале от –55 до +125 °C до уровня требований к диэлектрикам категории X7T.

Ключевые слова: титанаты; голландитоподобные твердые растворы; керамика; синтез; диэлектрическая проницаемость, диэлектрические потери.

Для цитирования: Gorshkov NV, Tsyaganov AR, Durakov AV, Makarov AA, Gorokhovsky AV. Influence of doping additives and fluxes on the electrical properties of ceramic materials based on hollandite-like solid solutions in the K_2O-MnO-Al_2O_3-Cr_2O_3-TiO_2 system. *Journal of Advanced Materials and Technologies*. 2026;11(2):152-161. DOI: 10.17277/jamt-2026-11-02-152-161

1. Introduction

Developing electronic components requires searching for new types of functional ceramic materials that can expand product ranges, improve existing device performance, and reduce their size [1]. For ceramic capacitor structures, materials with an exceptionally high dielectric constant (CDC [2, 3]) are of the greatest interest. The most sought-after ceramic materials in the production of multilayer capacitor structures used in microelectronics correspond to the X7R category according to the international EIA-198-1 classification. These materials are characterized by a high dielectric constant and stability of this value over a wide temperature range with low dielectric losses [4, 5].

Our previous studies [6–8] have shown that hollandite-like solid solutions of the K_2O-Me_xO_y-TiO_2 system (where Me represents divalent and trivalent metals capable of isomorphously substituting titanium in the crystal structure of titanates) have good application prospects in this field. The high mobility of potassium ions in the solid solution structure results in the extremely high polarizability of these systems when an electric field is applied. This occurs because the ions can move with low energy costs through tunnels formed by paired titanium-oxygen octahedra in a 2×2 arrangement. Additionally, local inhomogeneities in the distribution of electron density arise from the substitution of titanium by transition metals. These factors result in an anomalously high dielectric constant [9–11]. Additionally, sintering of ceramics based on hollandite-like solid solutions of this system can be carried out at relatively low temperatures (1000–1100 °C), even without flux additives.

It was also noted that the difficulties associated with obtaining single-phase powders of hollandite-like solid solutions can be overcome by introducing both divalent and trivalent metal oxides into the K_2O-TiO_2 system simultaneously, for example, a combination of MnO-Me_2O_3 (where Me = Fe, Al, or Cr) [12]. However, ceramic materials obtained in this system based on potassium polytitanate ($K_2O{\cdot}4TiO_2{\cdot}xH_2O$), modified in aqueous solutions of mixtures of manganese sulfates and one of the listed trivalent metals, have sufficiently high dielectric permittivity values at the operating frequency of multilayer ceramic capacitors (1 kHz), and they are characterized by high dielectric losses ($\mathrm{tg}\,\delta > 1$), which creates problems for their use in industrial practice [7]. Traditional types of ceramic ferroelectrics with a perovskite structure can reduce dielectric losses by introducing doping additives and fluxes into their compositions [1, 4, 5]. However, this approach has not yet been used for dielectrics with a hollandite structure.

In this regard, the aim of this work was to investigate the possibility of increasing the dielectric permittivity and its temperature stability, as well as reducing dielectric losses in ceramics synthesized on the basis of potassium polytitanate, modified in aqueous solutions with a mixture of salts of one divalent (Mn^{2+}) and two trivalent (Al^{3+} and Cr^{3+}) metals. The objectives were to conduct a comparative study of the electrical properties using only Al^{3+} salts or an equimolar mixture of Al^{3+} and Cr^{3+} salts for modification, as well as to investigate the effect on the electrical properties of the synthesized ceramics of various combinations of doping additives and a standard flux (zinc borate).

2. Materials and Methods

2.1. Synthesis of hollandite-like solid solution powders

The synthesis of hollandite-like solid solutions was carried out using potassium polytitanate (PPT) powder grade 4 (TU 2146-021-96961827-2009) as an

intermediate, which had the chemical composition $K_2O{\cdot}4.1TiO_2{\cdot}2.1H_2O$. It was synthesized by reacting TiO_2, KOH, and KNO_3 in a 3 : 3 : 4 ratio at 500 °C for 2 h, and subsequently chemically modified in aqueous solutions of mixtures of manganese sulfates ($MnSO_4{\cdot}5H_2O$, Russian Standard 435-77), aluminum ($Al_2(SO_4)_3{\cdot}12H_2O$, Russian Standard 12966-85), and chromium ($Cr_2(SO_4)_3{\cdot}6H_2O$, Russian Standard 4472-78). Modification was carried out by adding PPT powder to aqueous solutions of mixtures of the above-mentioned salts. As a base for modification, 0.1 M solutions of mixtures of manganese and aluminum sulfates or manganese (Mn) sulfate and a mixture of trivalent metal sulfates (Al, Cr), taken in a molar ratio of 2 : 1, were used. Ceramics based on the intermediate obtained after modifying PPT in a solution of this composition were selected for the studies based on preliminary experiments, as they exhibited the highest dielectric constant values.

Two types of mixtures were prepared: 1) a mixture of manganese and aluminum sulfates, taken in amounts of 12.10 and 13.96 $g{\cdot}L^{-1}$, corresponding to a molar ratio of [manganese sulfate] : [aluminum sulfate] = 2 : 1; 2) a mixture of manganese, aluminum, and chromium sulfates in concentrations of 12.10, 6.98, and 6.25 $g{\cdot}L^{-1}$, respectively, corresponding to a molar ratio of $[MnSO_4] : [Al_2SO_4] : [Cr_2SO_4] = 2.0 : 0.5 : 0.5$.

The resulting solutions had the same molar concentration of metal ions (0.1 M), but contained, in the first case: 0.05 M manganese sulfate and 0.025 M aluminum sulfate; and in the second case: 0.05 M manganese sulfate, 0.0125 M aluminum sulfate, and 0.0125 M chromium sulfate. That is, both solutions used to modify the PPT had the same content of sulfates of divalent and trivalent metals (0.05 M and 0.25 M, respectively), but in the first case, the trivalent metal was aluminum, and in the second case, it was an equimolar mixture of aluminum and chromium. Given that the dissociation of trivalent metal sulfates from 1 mole of salt yields 2 moles of trivalent ions, the solutions used contained $[Mn^{2+}] : [R^{3+}]$ in a 1 : 1 ratio.

Modification of the PPT particles was carried out under constant stirring of the dispersion prepared at a ratio of 10 g of PPT powder to 200 mL of an aqueous salt solution at pH = 10 (in accordance with the recommendations in [7]). The pH value of the modifying solution was selected based on the fact that the optimal conditions for modification and obtaining a homogeneous distribution of transition metal oxide-hydroxide complexes forming on the surface of PPT particles correspond to the value of pH_{crit}, above which independent (without the participation of the PPT surface) sedimentation of the hydroxides of this metal begins. For single-component aqueous solutions of manganese salts, $pH_{crit} = 10$, and in the case of chromium salts, $pH_{crit} \sim 6$; however, according to the experimental data obtained, this value changes when salts of several metals are present in the solution. A detailed study of the behavior of such systems is planned for the future; in this work, a modification variant at pH = 10 was used, which showed the most stable result in modifying the chemical composition of the intermediate.

The homogenized dispersion was centrifuged after standing for 4 hours, the resulting product was washed with distilled water until SO_4^{2-} ions completely disappeared from the filtrate (tested using a $BaCl_2$ solution), dried at 50 °C (6 h), and used for the synthesis of a solid solution. The synthesis of the solid solution, in accordance with the recommendations of previous studies [7], was carried out by heat treatment at 850 °C for 2 h.

2.2. Production of ceramic samples

The resulting powder was used to prepare powder mixtures for the synthesis of ceramic disc samples. Two types of mixtures were used: 1) those containing only powders of hollandite-like solid solutions prepared from PPT/Mn, Al or PPT/Mn, Al, Cr intermediates; 2) containing mixtures of solid solution powder synthesized based on PPT/Mn, Al, Cr, as well as flux in the form of zinc borate grade H-207 (PRC) – 2 wt. %, and dopants: Nb_2O_5 – 0.5 wt. %, Nd_2O_3 – 0.3 wt. %, LiF – 0.8 wt. %. The selection of the flux and the combination of doping additives was carried out in accordance with the recommendations presented in the literature [13]. It was taken into account that upon the introduction of the Nb_2O_5 additive, niobium, as a representative of the 4*d* group of elements (*n*-type dopant), can occupy the titanium site and contribute to the formation of cation vacancies, as well as suppress the formation of oxygen vacancies on the dielectric surface, which should inhibit charge transport across grain boundaries and reduce dielectric losses [3, 14, 15]. Furthermore, it was hypothesized that the additional introduction of Li^+ and F^- ions in the form of LiF into the system would block cation and oxygen vacancies, respectively. At the same time, the addition of Nd_2O_3 would contribute to a reduction in the growth rate of solid solution crystal grains [16] and increase the dielectric

permittivity of the ceramic material [17]. Additionally, when Nd_2O_3 is introduced into the ceramic composition, a synergistic effect resulting from the co-doping effect may arise, positively influencing the electrical properties of the combination of two *p*-type dopants (Nd_2O_3 and Cr_2O_3, which is part of the PPT/Mn, Al, Cr intermediate), as well as the *n*-type dopant (Nb_2O_5) [16–18].

To test these hypotheses, which were formulated based on the trends observed in the literature for $BaTiO_3$-based ceramics, the aforementioned additives were introduced into the control samples in the following order: No. 2a – flux only; No. 2b – flux and Nb_2O_5; No. 2c – flux, Nb_2O_5, and Nd_2O_3; No. 2d – flux, Nb_2O_5, Nd_2O_3, and LiF; and No. 2e – Nb_2O_5, Nd_2O_3, and LiF without flux.

The process of preparing the ceramic mixture involved weighing out the appropriate components and grinding and homogenizing them together in a Pulverisette 6 ball mill (with a ZrO_2-based ceramic grinding set) for 30 min. Afterward, a 2 % solution of polyvinyl butyral (PVB grade P-1) in isopropyl alcohol was added to the resulting mixture at a ratio of 5 wt. % PVB to 95 wt. % of the powdered ceramic mixture (temporary binder), homogenized it by simple mixing, followed by drying in an air-circulating oven at 90 °C for 3 h. The dried ceramic mixture was ground manually using an agate mortar until a homogeneous consistency was achieved. The resulting powder was pressed at a pressure of 300 MPa in steel molds into tablets (discs) with a diameter of 12 mm and a thickness of (1.0 ± 0.1) mm.

The resulting tablets were sintered according to a temperature schedule that included: a temperature ramp at a rate of 180 °C·h^{-1} with intermediate holds at 400°C for 1 hour (dehydration and pyrolysis of the temporary polymer binder) and at 1000 °C for 2 h, as well as a final hold at a maximum temperature of 1080 °C for 3 h.

2.3. Study of the electrical properties of ceramics

The bases of the sintered tablets were ground, after which silver contact paste (grade K-13) was applied to them; the contacts were fired at a temperature of 690 °C in air for 1 hour. After cooling, the samples were examined using impedance spectroscopy with a Novocontrol impedance spectrometer in the 102–105 Hz range. The measurement accuracy of the dielectric loss tangent was 0.0001.

To verify the temperature stability of the dielectric properties of the synthesized ceramic samples, the capacitance of the resulting capacitor structures was measured using an MCE-15AM instrument at a measurement frequency of 1 kHz in the temperature range from –60 to +125 °C. The samples were cooled in a climatic chamber using liquid nitrogen to a temperature of –60 °C, after which the temperature and capacitance of the capacitor cell were measured simultaneously as the temperature was increased. Upon reaching room temperature, the heater was turned on, and measurements continued up to a temperature of +125 °C.

2.4. Investigation of the composition and structure of the samples

The phase composition of the ceramic materials was investigated using an ARL X'TRA X-ray diffractometer. Powders were obtained by grinding synthesized tablets, then grinding ceramic fragments to a particle size of d < 0.315 mm in a Pulverisette 6 ball mill with a ZrO_2-based ceramic grinding set for 30 minutes. An ASPEX Explorer scanning electron microscope equipped with an energy-dispersive X-ray spectrometer attachment was used to study the morphology of the ceramics and their chemical composition.

3. Results and Discussion

The elemental chemical composition of hollandite-like solid solutions synthesized based on PPT/Mn, Al and PPT/Mn, Al, Cr, according to X-ray fluorescence analysis, corresponds to the chemical formulas $K_{1.70}Mn_{1.66}Al_{0.81}Ti_{5.52}O_{16}$ and $K_{1.76}Mn_{1.60}Al_{0.39}Cr_{0.45}Ti_{5.48}O_{16}$, respectively. Thus, based on the molar ratio [Mn]/[Me^{3+}], the obtained solid solution compositions are similar.

Figure 1 shows electron micrographs of the polished surface of ceramic discs sintered using powders of hollandite-like solid solutions based on PPT/Mn,Al and PPT/Mn,Al,Cr intermediates.

In general, the structure of PPT/Mn, Al-based ceramics is similar to that of hollandite-like solid solution samples synthesized from other variants of PPT/Me intermediates [6, 7, 12]. However, the relatively large crystal grain size (20 μm and larger, Fig. 1*a*) is worth noting. At the same time, the PPT/Mn,Al,Cr-based ceramic has a very small (~1 μm) grain size (Fig. 1*d*). The introduction of dopants and flux does not change this effect but contributes to the formation of a more homogeneous grain boundary (Fig. 1*d* and 1*e*).

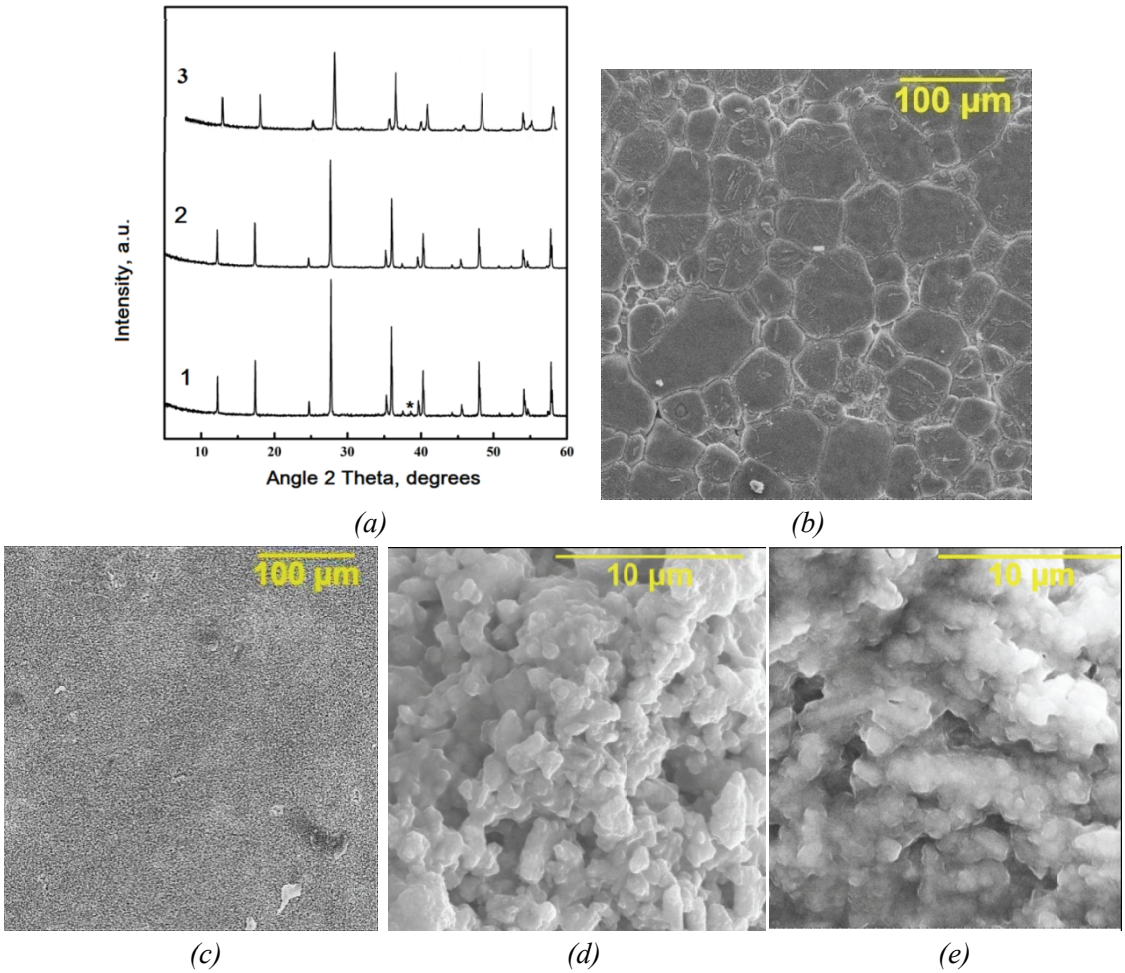

Fig. 1. X-ray diffractograms (*a*) of ceramics synthesized based on PPT/Mn, Al (*1*), PPT/Mn, Al, Cr without dopants and flux (*2*), and with a full set of dopants and flux (*3*); * – reflection corresponding to MnO_2; as well as electron micrographs of the structure of ceramic samples based on a solid solution obtained using PPT/Mn, Al (*b*), PPT/Mn, Al, Cr (*c*) and (*d*) powders: as well as PPT/Mn, Al, Cr with additions of Nb_2O_5, Nd_2O_3, LiF, and flux (*e*); (*b*) and (*c*) – polished surface; (*d*) and (*e*) – fracture

Thus, the presence of chromium in the composition of the PPT/Mn, Al, Cr intermediate inhibits the growth of solid solution crystal grains during the sintering of ceramic discs.

A comparison of the X-ray diffraction patterns of ceramic samples synthesized using PPT/Mn, Al and PPT/Mn, Al, Cr intermediate powders, Fig. 1*a*, shows that the simultaneous introduction of two trivalent metal oxides (Al and Cr) into the system also prevents the formation of secondary crystalline phases, although MnO_2 is present in the PPT/Mn, Al-based sample in an amount of less than 1 %.

Figure 2 shows the frequency dependence of the dielectric permittivity and dielectric loss for ceramic samples synthesized based on the PPT/Mn, Al and PPT/Mn, Al, Cr intermediates without the use of dopants or fluxes.

The results show that using a combination of Al and Cr salts to modify PPT, instead of Al alone, despite the approximately equal content of Al and Cr in the final product (solid solution), increases the dielectric permittivity of the ceramic at a frequency of 1 kHz (from 820 to 1580), and reduces its dielectric loss (tg δ decreases from 0.89 to 0.22). It is evident that chromium plays an active role in the formation of the intergranular boundaries of the ceramic, acting as a doping additive (by analogy with $BaTiO_3$-based ceramics [1, 4, 5, 16–18]). However, the electrical properties of the resulting material are still far from the characteristics typical of industrial samples of $BaTiO_3$-based capacitor ceramics (ε = 3000–4000, tg δ = 0.02–0.05 [19]).

In this regard, to improve the dielectric properties of the PPT/Mn, Al, Cr-based ceramic under study, doping additives and a flux were introduced into its composition. The results of the study of the obtained samples are presented in Fig. 3.

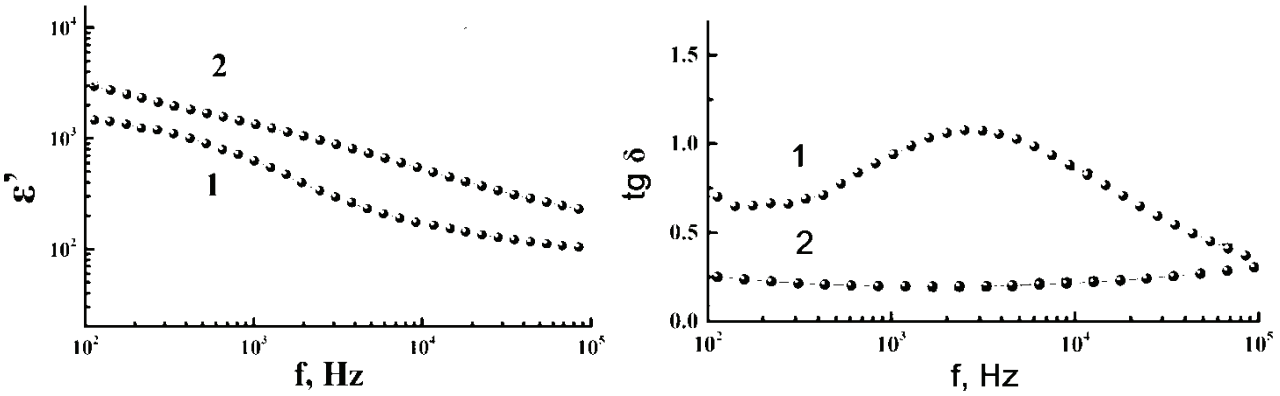

Fig. 2. Frequency dependencies of the dielectric permittivity (real part, ε′) and the tangent of the dielectric loss (tg δ), measured at room temperature for ceramic samples synthesized based on PPT/Mn, Al (*1*) and PPT/Mn, Al, Cr (*2*)

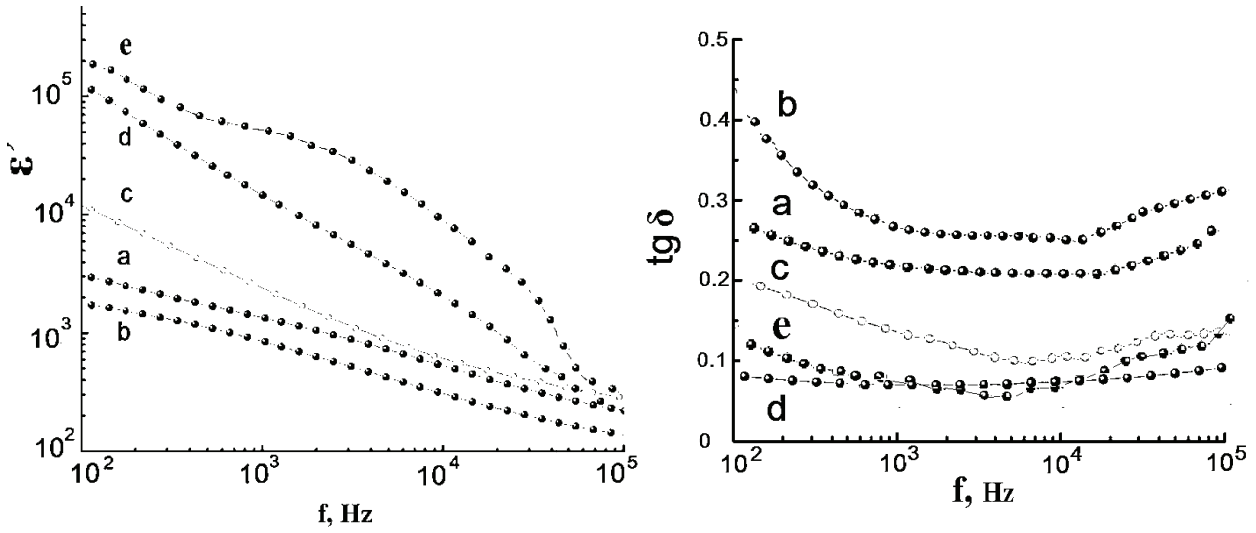

Fig. 3. Frequency dependencies of the dielectric permittivity (ε′) and the tangent of the loss angle (tgδ), measured at room temperature for ceramic samples synthesized based on the PPT/Mn, Al, Cr (*a*), with flux additive (*b*), with flux and Nb_2O_5 additives (*c*), with flux, Nb_2O_5, and Nd_2O_3 additives (*d*), and with flux, Nb_2O_5, Nd_2O_3, and LiF additives (*e*)

Analysis of the test results shows that the introduction of flux without doping additives slightly deteriorated the dielectric permittivity of the ceramics based on the studied hollandite-like solid solution. However, the combined introduction of flux and Nb_2O_5, flux and a combination of Nb_2O_5 and Nd_2O_3, as well as a combination of flux, Nb_2O_5, Nd_2O_3, and LiF led to a significant increase in the real part of the dielectric permittivity ε′ and a reduction in dielectric losses, most notably in the latter case (Fig. 3).

It should be noted that the ceramic samples tested at room temperature exhibit virtually identical electrical properties (ε, tg δ) within the margin of error, both in the presence and in the absence of flux. Nevertheless, the presence of flux is of fundamental importance, since when using an optimal combination of doping additives without introducing flux, the temperature stability of the dielectric permittivity (capacitance of the model capacitor) is lost. This fact is illustrated in Fig. 4.

In the presence of the melt formed during flux melting at sintering, it can be assumed that the doping additives are distributed more uniformly along the intergranular boundaries of the ceramic. This makes the ceramic's composition and properties more homogeneous and less susceptible to thermal effects.

Control measurements on six samples of ceramic discs made from a hollandite-like solid solution powder mixture based on the PPT/Mn, Al, Cr systems, as well as a zinc borate flux and a dopant complex (Nb_2O_5, Nd_2O_3, and LiF), showed that at an operating frequency of 1 kHz, the synthesized ceramic's dielectric permittivity is ε = (57,800 ± 600)

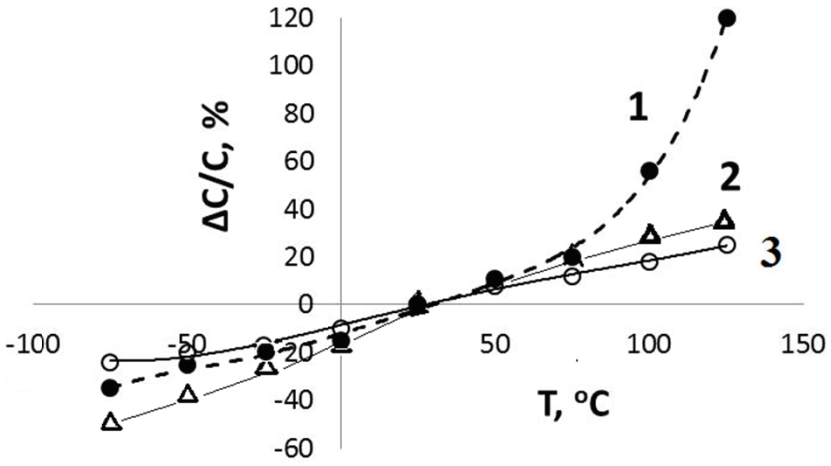

Fig. 4. Temperature stability of the capacitance of disc-shaped ceramic capacitor samples manufactured by sintering pressed blanks from a hollandite-like solid solution powder of PPT/Mn, Al, Cr (*1*), its mixture with dopants (*2*), as well as its mixture with dopants and flux (*3*)

and its dielectric loss is characterized by a tg(δ) value of (0.084 ± 0.002).

An important quantitative parameter that determines the potential for using ceramics in the production of ceramic capacitors is the relative change in dielectric constant across an operating temperature range of –55 to +125 °C.

Figure 4 shows how the capacitance of ceramic capacitors sintered from powders of the obtained hollandite-like solid solution of the K_2O-MnO-Al_2O_3-Cr_2O_3-TiO_2 system changes. The samples used contained: 1) no dopants or flux; 2) selected dopants with no flux; and 3) selected dopants with flux.

The results show that, for capacitors made from ceramic powder synthesized from a hollandite-like solid solution based on PPT/Mn, Al, Cr and containing no flux or doping additives, there is a significant deviation in the dielectric constant (capacitance) from the value measured at room temperature with changes in temperature, and this value exceeds the limits set by international standards, especially at temperatures above 70 °C (curve *1* in Fig. 4). However, if only a combination of doping additives is introduced into the ceramic composition without flux (curve *2* in Fig. 4), the dielectric constant stabilizes at high temperatures, but becomes unstable at sub-zero temperatures.

Concurrently, the incorporation of zinc borate (flux) and a combination of Nb_2O_5, Nd_2O_3, and LiF across the entire temperature range stipulated by international standards (from –55 to +125 °C) ensures adequate stability of the dielectric constant (+21 and –20 % of the value ascertained at room temperature).

The obtained results allow the synthesized ceramics based on a hollandite-like solid solution to be classified as category X7T, according to the EIA-198-1 international classification of capacitor materials. Within the temperature range of –55 to +125 °C, this category permits a capacitance deviation $\Delta C/C$ of +25 to –33 % of the value measured at room temperature. This class of materials is used in capacitor structures for smoothing, bypassing, connecting, and decoupling circuits in household appliances, control and power circuits, automotive electronics (ignition, diagnostic, and safety systems), and mobile communication devices and computers, where they are used for signal filtering, power stabilization, and improving microchip performance [20]. Additionally, the dielectric constant of ceramics based on hollandite-like solid solutions of the K_2O-MnO-Al_2O_3-Cr_2O_3-TiO_2 system is much higher than that of traditionally used $BaTiO_3$-based systems. This makes it possible to miniaturize multilayer ceramic capacitors (MLCCs) further, and MLCCs are important elements of electronic components [20].

The significant increase in the dielectric constant and temperature stabilization of ceramics synthesized using an intermediate containing a combination of MnO and two trivalent metals can be attributed to the accumulation of trivalent metals (Al and Cr) in the surface layer of the crystal during the crystallization of hollandite-like solid solutions [21]. These metals participate in forming the intergranular boundary structure. In this case, the mechanism by which Al and Cr participate in forming the intergranular boundary may differ.

Trivalent aluminum can form a dielectric layer (Al_2O_3) at the grain boundary of a hollandite-like solid solution. According to the generally accepted view, this increases the dielectric permittivity of the ceramic [3, 22]. This effect is known as the Maxwell-Wagner effect and is associated with different concentrations of charge carriers in contacting structures. Formation of an intergranular boundary between ferroelectric particles, which lack charge carriers, leads to their accumulation on the boundary in an electric field, causing an additional polarization effect.

At the same time, chromium (Cr), which is introduced into the composition of the intermediate, is a variable-valent metal. During heat treatment, it can assume various valence states ranging from +3 to +6. As a dopant that concentrates at the grain boundary, Cr can reduce dielectric losses and improve the temperature stability of the structure as well as the dielectric permittivity of the synthesized material [23, 24].

Further optimization of the dopant composition will reduce variation in the capacitance (dielectric permittivity) of ceramic materials based on solid solutions of the K_2O-MnO-Al_2O_3-Cr_2O_3-TiO_2 system, meeting the EIA-198-1 international standard for the highest X7R dielectric category (±15 % of the value measured at room temperature). It will also reduce dielectric loss from $tg(\delta) \approx 0.08$ at 1 kHz to less than 0.05.

4. Conclusion

Using potassium polytitanate, which is modified in an aqueous solution of a mixture of manganese, aluminum, and chromium sulfates (PPT/Mn, Al, and PPT/Mn, Al, Cr), as an intermediate allows for the production of single-phase powders of a hollandite-like solid solution of the K_2O-MnO-Al_2O_3-Cr_2O_3-TiO_2 system upon subsequent heat treatment. These powders can be used to make ceramic materials. In this context, chromium oxide in the structure of the resulting ceramic acts as a doping additive. It increases dielectric permittivity and reduces dielectric losses by decreasing the grain size of the ceramic material. It also presumably participates in forming intergranular boundaries.

Introducing a flux-forming additive (zinc borate, 2 %) into the ceramic composition does not positively affect the electrical properties of ceramics in the studied system. However, combining it with the doping additive Nb_2O_5, especially with a mixture of additives (Nb_2O_5, 0.5 %; Nd_2O_3, 0.3 %; and LiF, 0.8 %), significantly improves the electrical properties of ceramic samples. The dielectric permittivity increases from 1580 to (57,800 ± 600) at the operating frequency of 1 kHz and remains stable within the temperature range of –60 to +125 °C. The dielectric loss tangent decreases from 0.220 to (0.084 ± 0.02) due to the combined effect of the donor additive Nb_2O_5 and the acceptor additive Nd_2O_3, as well as the blocking of cation and oxygen vacancies at grain boundaries involving LiF.

5. Funding

The present study did not receive any external funding.

Финансирование

Настоящее исследование не получило внешнего финансирования.

6. Conflict of interests

The authors declare no conflict of interest.

Конфликт интересов

Авторы заявляют об отсутствии конфликта интересов.

References

1. Carter CB, Norton MG. *Ceramic materials: science and engineering*. New York: Springer; 2013. 766 p.

2. Humera N, Riaz S, Ahmad N, Arshad F, et al. Colossal dielectric constant and ferroelectric investigation of $BaTiO_3$ nano-ceramics. *Journal of Materials Science: Materials in Electronics*. 2020;31(7):5402-5415. DOI: 10.1007/s10854-020-03100-8

3. Lunkenheimer P, Krohns S, Riegg S, Ebbinghaus SG, et al. Colossal dielectric constants in transition-metal oxides. *The European Physical Journal Special Topics.* 2009;180(1):61-89. DOI:10.1140/epjst/e2010-01212-5

4. Ma C, Wang XH, Chen RZ, Li LT, Gui ZL. The structure and dielectric properties of low temperature sintering barium titanate based X7R ceramics. *Journal of Electroceramics.* 2008;21(1):242-245. DOI:10.1007/s10832-007-9139-x

5. Chen S, Ding Y, Mu H, Tian W, et al. Research progress on multilayer ceramic capacitors for energy storage: review. *Journal of Materials Science: Materials in Electronics.* 2025;36:77. DOI:10.1007/s10854-024-14004-2

6. Gorokhovsky AV, Tretyachenko EV, Goffman VG, Gorshkov NV, et al. Preparation and dielectric properties of ceramics based on mixed potassium titanates with the hollandite structure. *Inorganic Materials*. 2016;52(6):587-592. DOI:10.1134/S0020168516060042

7. Gorokhovsky AV, Saunina SI, Maximova LA, Tretyachenko EV, et al. Synthesis and electric properties of the high-k ceramic composites based on potassium polytitanate modified by manganese. *Research on Chemical Intermediates*. 2022;48(3):1227-1248. DOI: 10.1007/s11164-022-04669-x

8. Tsyganov AR, Gorokhovsky AV, Vikulova MA, Artyukhov DI, et al. Synthesis and dielectric properties of $K_{1.6}Fe_{1.6}Ti_{6.4}O_{16}$ ceramics produced by the Pechini method. *Journal of Advanced Materials and Technologies*. 2022;7(1):68-77. DOI:10.17277/jamt.2022.01.pp.068-077

9. Tumurugoti P, Betal S, Sundaram SK. Hollandites' crystal chemistry, properties, and processing: a review. *International Materials Reviews*. 2021;66(3):141-159. DOI:10.1080/09506608.2020.1743592

10. Besprozvannykh NV, Sinel'shchikova OY, Morozov NA., Kuchaeva SK, Galankina OL. Combustion synthesis and electrophysical properties of hollandites of the system K_2O–MeO–TiO_2 (Me = Mg, Ni, Cu). *Ceramics International.* 2022;48(17):24283-24289. DOI:10.1016/ j.ceramint.2022.04.048

11. Pearsall F, Farahmand N, Lombard, J, Dehipawala S, et al. Structure–property trends in a hollandite multiferroic by Fe doping: structural, magnetic and dielectric characterization of nanocrystalline $BaMn_{3-x}Fe_xTi_4O_{14+\delta}$. *Journal of Materials Chemistry C.* 2020;8(23):7916-7927. DOI:10.1039/D0TC00703J

12. Gorokhovsky AV, Tsyganov AR, Goffman VG, Gorshkov NV, et al. Synthesis and electrical properties of the ceramic materials based on $K_xMn_yR_zTi_{8-y-z}O_{16}$ (R = Al, Cr, Fe) hollandite-like solid solutions. *Journal of Advanced Materials and Technologies*. 2024;9(3):160-166. DOI: 10.17277/jamt.2024.03.pp.160-166

13. Burn I. Flux-sintered $BaTiO_3$ dielectrics. *Journal of Materials Science*. 1982;17(5):1398-1408. DOI: 10.1007/BF00752252

14. Rahman MA, Hasan Z, Islam J, Das DK, et al. Tailoring the properties of bulk $BaTiO_3$ based perovskites by heteroatom-doping towards multifunctional applications: a review. *ECS Journal of Solid State Science and Technology*. 2023;12(10):103015. DOI: 10.1149/2162-8777/ad00da

15. Sharma V, Pilania G, Rossetti GA, Slenes K, Ramprasad R. Comprehensive examination of dopants and defects in $BaTiO_3$ from first principles. *Physical Review B – Condensed Matter and Materials Physics*. 2013;87(13): 134109. DOI:10.1103/PhysRevB.87.134109

16. Freeman CL, Dawson JA, Chen HR, Ben L, et al. Energetics of donor-doping, metal vacancies, and oxygen-loss in A-site rare-earth-doped $BaTiO_3$. *Advanced Functional Materials*. 2013;23(31):3925-3928. DOI: 10.1002/adfm.201203147

17. Chen Z, Li Z, Ma M, Zhao T, et al. Effect of Nd_2O_3 doping on the electrical properties of $Ba_{0.96}Ca_{0.04}Ti_{0.90}Sn_{0.10}O_3$ ceramics. *Journal of Rare Earths.* 2018;36(7):745-749. DOI:10.1016/j.jre.2018.02.003

18. Li Z, Yu J, Hao S, Janolin PE. Enhancing properties of lead-free ferroelectric $BaTiO_3$ through doping. *Journal of the European Ceramic Society*. 2022;42(12):4693-4701. DOI:10.1016/j.jeurceramsoc. 2022.05.023

19. Tewatia K, Sharma A, Sharma M, Kumar A. Factors affecting morphological and electrical properties of Barium Titanate: A brief review. *Materials Today: Proceedings,* 2021;44:4548-4556. DOI:10.1016/j.matpr. 2020.10.813

20. Kim D, Lee G, Seo M, Cha B, et al. Experimental evaluation of saturation capacitance in aging phenomena in multi-layer ceramic capacitors (MLCCs). *Ceramics International.* 2024;50(6):9878-9883. DOI:10.1016/ j.ceramint.2023.12.313

21. Moetakef P, Larson AM, Hodges BC, Zavalij P, et al. Synthesis and crystal chemistry of microporous titanates $K_x(Ti,M)_8O_{16}$ where M=Sc–Ni. *Journal of Solid State Chemistry*. 2014;220:45-53. DOI:10.1016/j.jssc. 2014.08.012

22. Prodromakis T, Papavassiliou CJ. Engineering the Maxwell–Wagner polarization effect. *Applied Surface Science*, 2009;255(15):6989-6994. DOI:10.1016/j.apsusc. 2009.03.030

23. Xia X, Jiang X, Chen C, Jiang X, Tu N, Chen Y. Effects of Cr_2O_3 doping on the microstructure and electrical properties of $(Ba,Ca)(Zr,Ti)O_3$ lead-free ceramics. *Frontiers of Materials Science*. 2016;10(2):203-210. DOI:10.1007/s11706-016-0342-z

24. Zeb A, Milne SJ. High temperature dielectric ceramics: a review of temperature-stable high-permittivity perovskites. *Journal of Materials Science: Materials in Electronics.* 2015;26(12):9243-9255. DOI:10.1007/ s10854-015-3707-7

Information about the authors / Информация об авторах

Nikolay V. Gorshkov, Cand. Sc. (Eng.), Associate Professor, Yuri Gagarion State Technical University of Saratov (SSTU), Saratov, Russian Federation; ORCID 0000-0003-3248-3257; e-mail: gorshkov.sstu@gmail.com

Alexey R. Tsyganov, Cand. Sc. (Chem.), Associate Professor, SSTU, Saratov, Russian Federation; ORCID 0000-0002-5112-7939; e-mail: tsyganov.a.93@mail.ru

Горшков Николай Вячеславович, кандидат технических наук, доцент, Саратовский государственный технический университет имени Гагарина Ю. А. (СГТУ имени Гагарина Ю.А.), Саратов, Российская Федерация; ORCID 0000-0003-3248-3257; e-mail: gorshkov.sstu@gmail.com

Цыганов Алексей Русланович, кандидат химических наук, научный сотрудник, СГТУ имени Гагарина Ю.А., Саратов, Российская Федерация; ORCID 0000-0002-5112-7939; e-mail: tsyganov.a.93@mail.ru

Andrey V. Durakov, Postgraduate Student, SSTU, Saratov, Russian Federation; ORCID 0000-0003-1156-2028; e-mail: andrey.durakov@nanotec.pro

Alexey A. Makarov, Postgraduate Student, SSTU, Saratov, Russian Federation; ORCID 0009-0006-6650-1440; e-mail: aleksey.makw@gmail.com

Alexander V. Gorokhovsky, D. Sc. (Chem.), Professor, Head of the Department, SSTU, Saratov, Russian Federation; ORCID 0000-0002-4210-3169; e-mail: algo54@mail.ru

Дураков Андрей Владимирович, аспирант, СГТУ имени Гагарина Ю.А., Саратов, Российская Федерация; ORCID 0000-0003-1156-2028; e-mail: andrey.durakov@nanotec.pro

Макаров Алексей Алексеевич, аспирант, СГТУ имени Гагарина Ю.А., Саратов, Российская Федерация; ORCID 0009-0006-6650-1440; e-mail: aleksey.makw@mail.ru

Гороховский Александр Владиленович, доктор химических наук, профессор, заведующий кафедрой, СГТУ имени Гагарина Ю.А., Саратов, Российская Федерация; ORCID 0000-0002-4210-3169; e-mail: algo54@mail.ru

Received 15 March 2026; Revised 20 May 2026; Accepted 21 May 2026

Original papers
Materials for energy and environment, next-generation photovoltaics, and green technologies

УДК 661.666 DOI: 10.17277/jamt-2026-11-02-162-171

Synthesis and study of the porous structure of biochars obtained from crustacean waste

© Anastasia E. Memetova[a]✉, Andrey D. Zelenin[a], Viktor S. Yagubov[a], Nariman R. Memetov[a]

[a] *Tambov State Technical University, Bld. 2, 106/5, Sovetskaya St., Tambov, 392000, Russian Federation*

✉ anastasia.90k@mail.ru

Abstract. Biochar samples from crustacean processing waste were synthesized by carbonization followed by alkaline activation. The influence of synthesis parameters (time, temperature) on the porous structure of biochar was considered. The results showed that biomass carbonization conditions significantly affect the final porosity parameters. It was found that the biochar samples obtained by varying the synthesis parameters were micromesoporous. Temperature was shown to be the main influencing factor during biomass carbonization. At a three-hour carbonization duration and a temperature of 650 °C, the specific surface area (2708 $m^2 \cdot g^{-1}$) and pore volume (total pore – 1.58 $cm^3 \cdot g^{-1}$, micropore – 0.64 $cm^3 \cdot g^{-1}$, mesopore – 0.94 $cm^3 \cdot g^{-1}$) in the obtained biochar reached their maximum values. Methane adsorption on the obtained biochar was studied at ambient temperature and pressure up to 100 bar. Biochar obtained from crustacean waste was shown to exhibit a high methane adsorption capacity of ~18 $mmol \cdot g^{-1}$. Experimental adsorption data were analyzed using the Langmuir, Freundlich, and Dubinin-Radushkevich models. The influence of synthesis parameters on the pore structure of biochars, as well as the adsorption data evaluated in the study, are useful for designing adsorption systems.

Keywords: biochar; specific surface area; porosity; biomass carbonization; adsorption.

For citation: Memetova AE, Zelenin AD, Yagubov VS, Memetov NR. Synthesis and study of the porous structure of biochars obtained from crustacean waste. *Journal of Advanced Materials and Technologies*. 2026;11(2):162-171. DOI: 10.17277/jamt-2026-11-02-162-171

Синтез и исследование пористой структуры биоуглей, полученных из отходов ракообразных

© А. Е. Меметова[a]✉, А. Д. Зеленин[a], В. С. Ягубов[a], Н. Р. Меметов[a]

[a] *Тамбовский государственный технический университет, ул. Советская, 106/5, пом. 2, Тамбов, 392000, Российская Федерация*

✉ anastasia.90k@mail.ru

Аннотация. Образцы биоуглей из отходов переработки ракообразных синтезированы путем карбонизации с последующей щелочной активацией. Рассмотрено влияние параметров синтеза (время, температура) на пористую структуру биоугля. Результаты показали, что условия карбонизации биомассы существенно влияют на конечные параметры пористости. Установлено, что образцы биоугля, полученные путем варьирования параметров синтеза, микромезопористые. Показано, что температура является основным влияющим фактором при карбонизации биомассы. При трехчасовой продолжительности карбонизации и температуре 650 °С значения удельной поверхности (2708 $м^2/г$) и объемов пор (общий объем пор – 1,58 $см^3/г$, объем микропор – 0,64 $см^3/г$, объем мезопор – 0,94 $см^3/г$) в полученном биоугле достигали максимального значения. Изучена адсорбция метана на полученном биоугле при температуре окружающей среды и давлении до 100 бар. Показано, что биоуголь из отходов переработки ракообразных демонстрирует высокую адсорбционную способность по метану, равную 18 ммоль/г. Экспериментальные данные адсорбции проанализированы с использованием моделей Ленгмюра, Фрейндлиха и Дубинина-Радушкевича. Влияние параметров синтеза на пористую структуру биоуглей, а также данные адсорбции, оцененные в исследовании, полезны для проектирования адсорбционных систем.

Ключевые слова: биоуголь; площадь удельной поверхности; пористость; карбонизация биомассы; адсорбция.

Для цитирования: Memetova AE, Zelenin AD, Yagubov VS, Memetov NR. Synthesis and study of the porous structure of biochars obtained from crustacean waste. *Journal of Advanced Materials and Technologies*. 2026;11(2):162-171. DOI: 10.17277/jamt-2026-11-02-162-171

1. Introduction

The performance of biochar in various applications is mainly determined by its properties [1, 2]. The surface area and porosity of biochar are among the most important parameters that determine the quantity/quality of available active sites in biochar and, consequently, improve its properties such as cation exchange, water retention, and adsorption capacities [3]. Biochar consists of a wide range of pores, ranging from nanometers to tens of micrometers [4]. The pores can be divided into three groups according to the International Union of Pure and Applied Chemistry (IUPAC) standard: micropores (< 2 nm), mesopores (2–50 nm), and macropores (> 50 nm). In this work, the IUPAC pore standard is used to characterize the pore size distribution. The internal structure of biochar can be estimated from the pore distribution, which is based on the assumption that the complex porous structure in a real solid can be represented by a model with equivalent interactions and regularly shaped pores [5].

Pore size distribution is an important parameter in characterizing the heterogeneity of the biochar porous structure. The surface area is closely related to its porosity. The question of how to obtain biochar with a highly porous structure and large surface area is an active research topic [6].

Over the past ten years, many reviews devoted to biochar have been published. The topics of these reviews mainly focus on the applications of biochar in various fields [7], the relationship between process parameters and biochar characteristics [8], as well as additional modifications for the production of modified biochar [9], and so on. Recent studies have reported the use of shrimp shells to obtain biochars for use as a catalytic support [10], an alternative cathode in fuel cells, supercapacitors [11, 12], an adsorbent of heavy metal ions [13], dyes, and antibiotics [14]. It has also been reported that carbonization parameters have a significant effect on the porosity of the final product [15]. However, biochar obtained by carbonization without subsequent activation has a low specific surface area and porosity [16]. Furthermore, it is important to note that among all activating agents, alkaline activation with KOH is the most effective in producing carbon materials with extremely high specific surface area and pore volume, particularly micropores [17].

At the beginning of the last decade, research on biochar mainly focused on its characteristics in various application areas [18–21]. In the past few years, research has shifted towards studying surface area and porosity [2, 22, 23]. Thus, the efforts of many scientists are aimed at identifying general patterns in the formation of biochar porosity parameters. Various methods and synthesis parameters are used in the production of biochar. It is obvious that the porous structure of biochar changes depending on these parameters. However, the effect of synthesis parameters on the volume and pore size distribution of biochar remains unclear.

In this study, we synthesized biochars from crustacean waste, investigated the influence of synthesis parameters on the development of the porous structure of the resulting materials, and assessed the methane adsorption properties of the biochar with the highest porosity values. As far as we know, the conversion of shrimp waste into highly porous carbon using carbonization followed by KOH activation for methane adsorption has not been previously studied. Therefore, the results of this study offer a promising solution for converting biowaste into a high-tech product for environmental applications.

2. Materials and methods

2.1. Method for producing activated biochar

Shrimp shells were used as the biomass in this study. After removing the meat, the crustacean shells were washed repeatedly with deionized water. The resulting waste was then dried at 110 °C to a constant weight. The crustacean processing waste in the form of a powder with a particle size of < 0.5 mm was loaded into the pilot reactor. The biomass was heated in an argon flow to a predetermined temperature (550–750 °C) and held for various periods of time (2–4 h), and then cooled to room temperature under an argon atmosphere. Next, the resulting carbonizate in the form of a powder with a particle size of < 0.5 mm and granules of 85 % potassium hydroxide with a mass ratio of potassium hydroxide (calculated as 100 % KOH): carbonizate (w/w:2:1) were loaded into the pilot reactor. The reaction mixture was heated to 700°C under an argon flow and held for 2 hours, then cooled to room temperature. After the reactor cooled to room temperature, the reaction mixture was poured with

water, the precipitate was washed to remove alkali until neutral pH, then kept in a hydrochloric acid solution for 24 hours to dissolve metal impurities, after which it was washed again with water and dried at 110 °C to constant weight.

2.2. Analytic methods

To determine the specific surface area, total volume porosity, and micro- and mesoporosity of each sample obtained during the synthesis, an Autosorb-iQ automated adsorption system (Quantachrome, USA) was used. Samples (weighing 1–2 g) prepared for adsorption analysis were degassed at 350 °C for 5 hours under vacuum to remove air, free water, and other impurities before pore structure analysis. At 77 K, N_2 adsorption isotherms were obtained for relative pressures (P/P_0) (gas pressure/vapor pressure) ranging from 0.01 to 0.995. The specific surface area (S_{BET}) was calculated using the Brunauer-Emmett-Teller (BET) equation. The pore size distribution and micropore and mesopore volume were calculated using the Density Functional Theory (DFT) method under the assumption of slit-shaped/cylindrical pores (QSDFT model).

CH_4 adsorption isotherms on the sample at pressures up to 100 bar (at a temperature of 298.15 K) were recorded using an iSorbHP gas adsorption analyzer (Anton Paar GmbH, Graz, Austria). High-purity CH_4 (99.999 % purity; normal boiling point $T_{b.p} = 111.66$ K; critical temperature $T_{cr} = 190.77$ K; critical pressure $P_{cr} = 4.626$ MPa) was used for the measurement. Before the adsorption experiment, the sample was degassed at 350 °C for 5 h.

2.3. Theoretical justification of approaches to determining the specific surface area

Measuring the surface area and porosity of biochar (primarily micro- and mesopores) is typically accomplished using gas adsorption, which involves priming the sample with a given gas atmosphere, recording the adsorption isotherm, and analyzing it accordingly. The most commonly used gas is N_2 (77 K) due to its high availability and low cost.

Both the European Biochar Certificate (EBC) [24] and the International Biochar Initiative (IBI) [25], the most influential biochar organizations worldwide, recommend the BET method for analyzing nitrogen adsorption isotherms to determine surface area [26]. However, the BET method also has some problems. For example, the basic theory of the BET equation is based on a monolayer coating of gas molecules, whereas the primary adsorption mechanism in micropores is pore filling, which inevitably leads to errors in calculating the surface area of biochar. The BET equation is not applicable even for mesopores with widths from 2 to 4 nm due to an overestimation of the monolayer capacity. In the pressure range used in the calculation, not only the formation of monolayer-multilayer structures but also pore filling occurs [27]. Therefore, the BET surface area should be considered as an apparent rather than an absolute surface area, especially for porous materials with a large number of micropores. Despite this, it is still useful for evaluating sorbents for comparative purposes, and the BET surface area is considered a “fingerprint” of the sorbent [28].

For assessing the size distribution, it is advisable to use density functional theory (DFT). This method allows for a more accurate analysis of pore sizes, covering the entire range of mesopores and micropores, unlike other methods, such as the Barrett-Joyner-Halenda (BJH) [29, 30]. In recent years, particular attention has been paid to the DFT method for analyzing pore size distribution. The methane adsorption isotherm was analyzed using the Langmuir, Freundlich, and Dubinin–Radushkevich models [31–33]. An important characteristic of the Langmuir isotherm model is the presence of homogeneous active binding sites on the adsorbent surface, which have identical sorption energies [31]. In contrast, the Freundlich isotherm model assumes a heterogeneous adsorbent surface, namely, different sorption energies. In this case, active binding of adsorbate molecules occurs in areas with higher energy values [33]. The Dubinin–Radushkevich isotherm model is widely used to identify the nature of adsorbate adsorption on an adsorbent and to study the free energy and porosity characteristics of adsorbents [32].

3. Results and Discussion

Traditional technologies for producing highly porous biochars involve carbonization and activation stages, which form a porous structure. Control of the pore structure is possible by varying both the carbonization process conditions (duration, temperature) and the activation process (duration, temperature, and activating agent consumption).

3.1. Effect of carbonization duration on the porous structure of biochars

Process time is a factor that must be considered when conducting the carbonization process. Nitrogen adsorption-desorption isotherms and pore size

distribution curves for biochar samples, obtained at a fixed temperature (t = 550 °C) and variable carbonization time followed by alkaline activation (τ = 2 h; t = 700 °C; w/w: 2/1), are shown in Figs. 1 and 2.

All samples are characterized by similar reversible adsorption isotherms corresponding to combinations of types I and II according to the IUPAC classification (Fig. 1), which is inherent in materials with a wide range of pore size distributions. The hysteresis loops are somewhat similar to adsorption branches corresponding to type H4. This type of loop is often found in micromesoporous carbon materials. In addition to the IUPAC classification, one can refer to the work [34], in which the author identified and correlated five types of hysteresis loops with different pore shapes. Thus, the loop type in the obtained biochar samples (Fig. 1) corresponds to type B, indicating a large number of cylindrical and slit-shaped pores with all sides open.

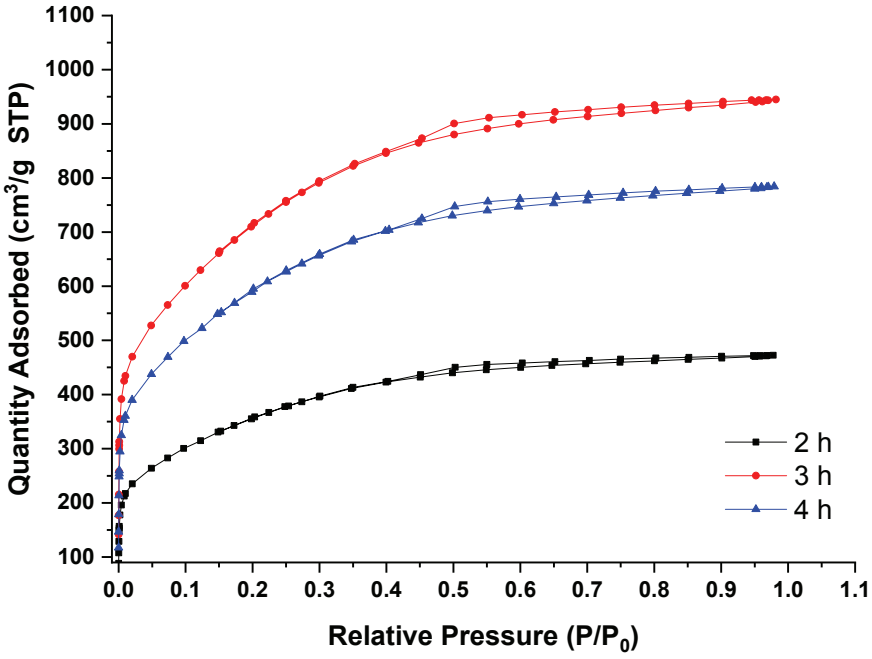

Fig. 1. Nitrogen adsorption-desorption for biochar samples obtained at different carbonization times

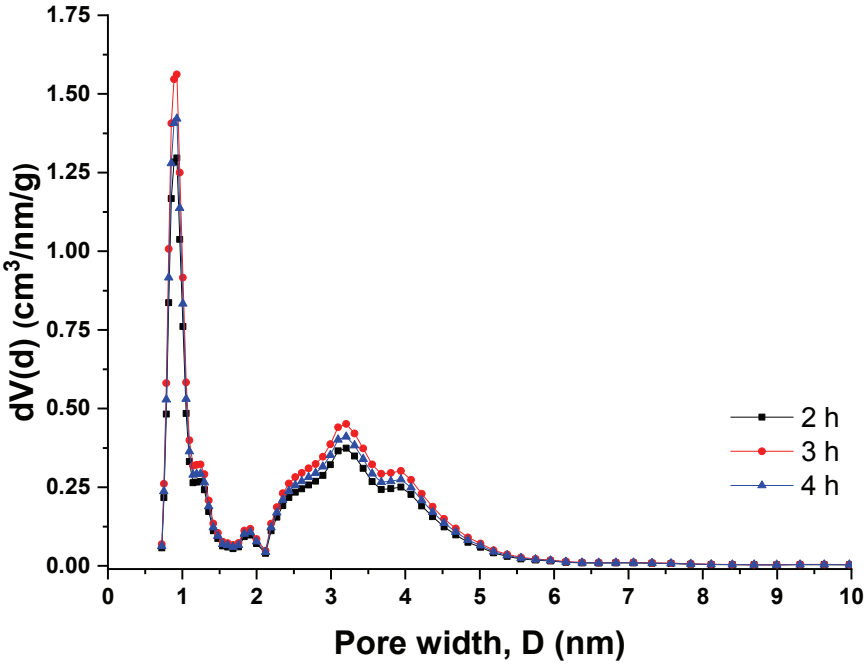

Fig. 2. Pore size distribution for biochar samples obtained at different carbonization times

The pore size distribution curves for the samples (Fig. 2) also exhibit a similar pattern. The results indicate that all of the samples studied exhibit a multimodal pore size distribution. For all samples, the predominant mesopore size ranges from 2 to 6 nm, with a main peak at approximately 3.2 nm. The microporous structure of all of the samples studied appears to be trimodal, with a main peak at 0.92 nm. Thus, the similar appearance of the nitrogen adsorption-desorption isotherm and pore size distributions for the obtained samples indicates that carbonization duration does not significantly influence the porosity type.

In this study, we used the BET and DFT methods to calculate the specific surface area, pore volume, and pore size. The data obtained indicate that sufficient carbonization time results in the complete release of volatiles, which promotes the development of a porous structure. However, excessively long exposure to high temperatures can destroy the pore structure. For example, the biochar surface area increased from 2016 to 2488 $m^2 \cdot g^{-1}$ (BET) and from 1731 to 2120 $m^2 \cdot g^{-1}$ (DFT) with an increase in residence time from 2 to 3 hours, and then decreased to 2121 $m^2 \cdot g^{-1}$ (BET) and 1852 $m^2 \cdot g^{-1}$ (DFT) with an increase in residence time for 4 hours.

Carbonation time also affected the total pore volume (V_p), as well as the micropore (V_{mic}) and mesopore (V_{mes}) volumes of the biochar samples. With increasing carbonation time to 3 h, micro- and mesopore volumes tended to increase, while with a further increase in carbonization duration ($\tau = 4$), they decreased. At a carbonization time of 3 h, the pore volumes in the resulting biochar reached their maximum values ($V_p = 1.37$ $cm^3 \cdot g^{-1}$, $V_{mic} = 0.53$ $cm^3 \cdot g^{-1}$, $V_{mes} = 0.84$ $cm^3 \cdot g^{-1}$).

Thus, the experimental studies demonstrated that carbonization for 3 h promotes the formation of biochars with the best porosity parameters.

3.2. Effect of carbonization temperature on the porous structure of biochars

Carbonization temperature is considered the main parameter influencing the surface area and porosity of biochar. Figures 3 and 4 illustrate this. The nitrogen adsorption-desorption isotherms and pore size distribution curves of biochar samples obtained at different carbonization process temperatures and holding times of 3 h followed by alkaline activation ($\tau = 2$ h; $t = 700$ °C; w/w:2/1) are shown.

All samples exhibit a combination of type I and II isotherms with an H4; B hysteresis loop, which are typical of micromesoporous materials. The maximum amount of nitrogen is adsorbed on the sample obtained at a carbonization temperature of 650 °C. According to the data presented in Fig. 4, micro- and mesopores with diameters less than 6 nm predominate in all samples. The pore structure of all the studied samples, except for the one obtained at 750 °C, is pentamodal, with the main peak at about 0.9 nm. The intensity of the peaks in the range from 0 to 2 nm (insert in Fig. 4) tends to increase.

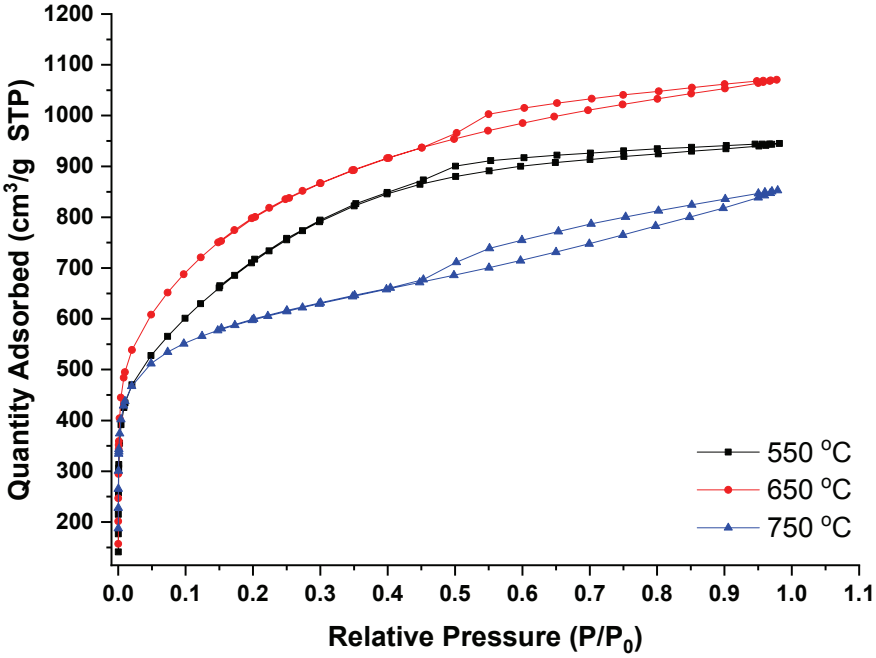

Fig. 3. Nitrogen adsorption-desorption isotherms for biochar samples obtained at different carbonization temperatures

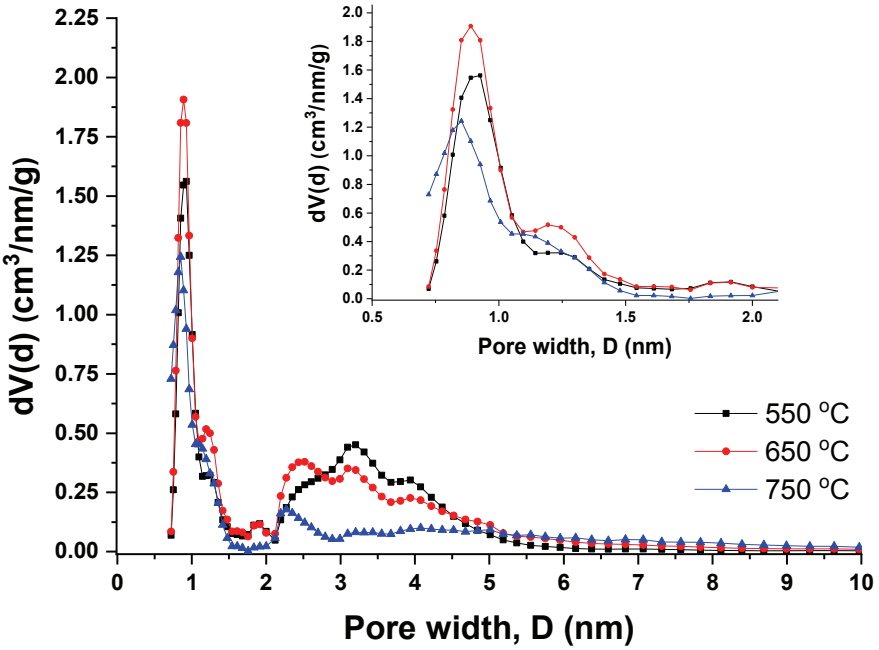

Fig. 4. Pore size distribution for biochar samples obtained at different carbonization temperatures

Table 1. Influence of carbonization temperature on the porosity parameters of biochar samples

Sample	550 °C	650 °C	750 °C
S_{BET}, $m^2 \cdot g^{-1}$	2488	2708	1924
S_{DFT}, $m^2 \cdot g^{-1}$	2102	2384	2158
V_{DFT}, $cm^3 \cdot g^{-1}$	1.37	1.58	1.23
V_{mic}, $cm^3 \cdot g^{-1}$	0.53	0.64	0.64
V_{mes}, $cm^3 \cdot g^{-1}$	0.84	0.94	0.59
V_{01}, $cm^3 \cdot g^{-1}$	0.41	0.46	0.36
V_{02}, $cm^3 \cdot g^{-1}$	0.09	0.17	0.27
V_{03}, $cm^3 \cdot g^{-1}$	0.03	0.27	0.11
V_{04}, $cm^3 \cdot g^{-1}$	0.51	0.23	–
V_{05}, $cm^3 \cdot g^{-1}$	0.33	0.42	0.49
D_{01}, nm	0.92	0.89	0.85
D_{02}, nm	1.24	1.19	1.09
D_{03}, nm	1.91	2.52	2.27
D_{04}, nm	3.20	3.09	–
D_{05}, nm	3.93	3.93	4.82

S_{BET} is the specific surface area for nitrogen calculated by the Brunauer–Emmett–Teller method; S_{DFT} is the specific surface area for nitrogen calculated using the density functional theory; V_{mic} is the specific volume of micropores; V_{mes} is the specific volume of mesopores; V_{01}–V_{05} is the specific volume of pores of the mode; D_{01}–D_{05} is the average diameter (width) of the pores of each mode.

A higher peak intensity value corresponds to a better adsorption capacity of biochar. In other words, on the micropore scale, the sample obtained at a carbonization temperature of 650 °C has the highest adsorption capacity, while the sample obtained at 750 °C has the lowest. These results are in good agreement with the results presented in Table 1.

The sample obtained at 650 °C had the highest specific surface area and pore volumes (S_{BET}= =2708 $m^2 \cdot g^{-1}$, V_p = 1.58 $cm^3 \cdot g^{-1}$, S_{DFT} = 2384 $cm^3 \cdot g^{-1}$, V_{mic} = 0.64 $cm^3 \cdot g^{-1}$, V_{mes}= 0.94 $cm^3 \cdot g^{-1}$).

3.3. Adsorption characteristics of biochar

The adsorption isotherm of excess methane content versus pressure, recorded at ambient temperature (298.15 K), for the biochar sample obtained by carbonization at 650 °C and a holding time of 3 h followed by alkaline activation (τ = 2 h; t = 700 °C; w/w:2/1) is shown in Fig. 5. The presented results show that methane adsorption increases sharply in the initial region (up to approximately 30 bar), then slows down and gradually increases with increasing pressure, showing no tendency to saturate even at 100 bar. The change in the adsorption capacity of the biochar sample as a function of pressure is also shown, approximated by the Langmuir, Freundlich, and Dubinin–Radushkevich models. Results from these models were processed using the equations presented in [31–33].

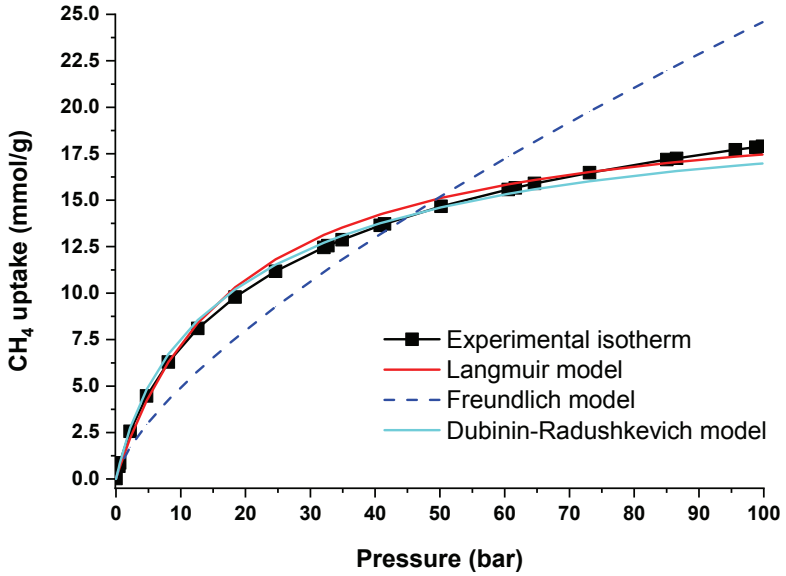

Fig. 5. Adsorption isotherm of CH_4 on a biochar sample obtained at 650 °C adapted to the Langmuir, Freundlich and Dubinin-Radushkevich models

Comparing the data obtained using the models, it can be concluded that they correlate well with the Langmuir ($R^2 = 0.9939$) and Dubinin–Radushkevich ($R^2 = 0.9975$) equations and best describe the process of methane adsorption on the biochar sample in the pressure range considered in this study. However, evaluating the reliability of the models used by the normalized standard deviation (Δa), defined as [35], it can be concluded that the Dubinin–Radushkevich equation (Δa = less than 5 %) describes the studied adsorption process on biochar more accurately than the Langmuir equation (Δa = less than 10 %). The results of processing the experimental data using the Langmuir, Freundlich, and Dubinin–Radushkevich models are presented in Table 2.

The deviation of the limiting methane sorption capacity for the Langmuir (a_L), and Dubinin–Radushkevich ($a_{D–R}$) models from the experimentally obtained value (a_{ekp}) did not exceed ~2 and ~5 %, respectively. The limiting values of micropore adsorption capacity (a_0), calculated using the Dubinin-Radushkevich equation, deviate from a_{ekp} by no more than 2%.

Table 2. Adsorption isotherm coefficients for the Langmuir, Freundlich and Dubinin–Radushkevich models

a_{ekp}, mmol·g^{-1}	Langmuir model constants				
	a_L, mmol·g^{-1}	A, mmol·g^{-1}	b	R^2	Δa, %
	17.5	20.7	0.0539	0.9939	9.93
	Freundlich model constants				
17.9	a_F, mmol·g^{-1}	k	$1/n$	R^2	Δa, %
	24.6	0.9915	0.6974	0.9654	31.02
	Constants of the Dubinin-Radushkevich model				
	$a_{D–R}$	a_0	E	R^2	Δa, %
	17.0	18.2	22.91	0.9975	4.61

S_{BET} – a_L, a_F, $a_{D–R}$ are theoretical values of equilibrium gas adsorption according to the Langmuir, Freundlich and Dubinin–Radushkevich models, respectively, mmol·g^{-1}; A and a_0 are the limiting values of gas adsorption according to the Langmuir and Dubinin–Radushkevich models, respectively, mmol·g^{-1}; b and k are the equilibrium constants according to the Langmuir–Freundlich models, respectively; n is an empirical parameter that characterizes the interaction energy in the adsorbent-adsorbate system; E is the characteristic adsorption energy of the gas under study, kJ·mol^{-1}.

The Dubinin–Radushkevich equation was used to establish the nature of the methane adsorption process on biochar. Based on the obtained values of the characteristic adsorption energy (E = ~23 kJ·mol^{-1}), it is clear that the mechanism is physical in nature [36].

4. Conclusion

Biochar samples were obtained from crustacean processing waste. The influence of carbonization parameters on the development of the porous structure of the biochars was studied. Carbonization temperature can modulate the pore structure of biochars. A three-hour biomass carbonization process at 650°C proved to be most favorable for the development of high specific surface area and pore volumes (S_{BET}= 2708 m^2·g^{-1}, V_p = 1.58 cm^3·g^{-1}, V_{mic} = 0.64 cm^3·g^{-1}, V_{mes}= 0.94 cm^3·g^{-1}). This sample is a micromesoporous material exhibiting high methane adsorption capacity, amounting to 18 mmol·g^{-1} at room temperature and 100 bar.

Thus, this study demonstrates that crustacean waste carbon material is a highly porous and promising biosorbent for methane adsorption.

5. Funding

This study was supported by grant No. 26-16-20053 from the Russian Science Foundation.

Финансирование

Исследование выполнено за счет средств гранта Российского научного фонда № 26-16-20053.

6. Conflict of interests

The authors declare no conflict of interest.

Конфликт интересов

Авторы заявляют об отсутствии конфликта интересов.

References

1. Mohanty AK, Vivekanandhan S, Das O, et al. Biocarbon materials. *Nature Reviews Methods Primers.* 2024;4(1):19. DOI:10.1038/s43586-024-00297-4

2. Zhang Z, Lei Y, Li D, et al. Sudden heating of H3PO4-loaded coconut shell in CO_2 flow to produce super activated carbon and its application for benzene adsorption. *Renewable Energy.* 2020;153:1091-1099. DOI:10.1016/j.renene.2020.02.059

3. Weber K, Quicker P. Properties of biochar. *Fuel.* 2018;217:240-261. DOI:10.1016/j.fuel.2017.12.054

4. Sing KSW. Reporting physisorption data for gas/solid systems with special reference to the determination of surface area and porosity (Recommendations 1984). *Pure and Applied Chemistr.* 1985;57(4):603-619. DOI:10.1351/pac198557040603

5. Hu S, Xiang J, Sun L, Xu M, Qiu J, Fu P. Characterization of char from rapid pyrolysis of rice husk. *Fuel Processing Technology*. 2008;89(11):1096-1105. DOI:10.1016/j.fuproc.2008.05.001

6. Memetova A, Tyagi I, Karri RR, et al. Synthesis of carbon energized materials with directed regulation of specific surface and pore structure as potential adsorbent for methane mitigation. *Journal of Environmental Chemical Engineering.* 2022;10(6):108929. DOI:10.1016/j.jece.2022.108929

7. Wan Z, Sun Y, Tsang DCW, et al. Customised fabrication of nitrogen-doped biochar for environmental and energy applications. *Chemical Engineering Journal.* 2020;401:126136. DOI:10.1016/j.cej.2020.126136

8. Panwar NL, Pawar A. Influence of activation conditions on the physicochemical properties of activated biochar: a review. *Biomass Conversion and Biorefiner.* 2022;12(3):925-947. DOI:10.1007/s13399-020-00870-3

9. Wan Z, Sun Y, Tsang DCW, et al. Sustainable remediation with an electroactive biochar system: mechanisms and perspectives. *Green Chemistry.* 2020;22(9):2688-2711. DOI:10.1039/D0GC00717J

10. Ni J, Li Q, Gong L, et al. Highly efficient chemoenzymatic cascade catalysis of biomass into furfurylamine by a heterogeneous shrimp shell-based chemocatalyst and an ω-transaminase biocatalyst in deep eutectic solvent-water. *ACS Sustainable Chemistry & Engineering*. 2021;9(38):13084-13095. DOI:10.1021/acssuschemeng.1c05109

11. Zhang H, Sun Q, He Q, et al. Single Cu atom dispersed on S,N-codoped nanocarbon derived from shrimp shells for highly-efficient oxygen reduction reaction. *Nano Research.* 2022;15(7):5995-6000. DOI:10.1007/s12274-022-4289-3

12. Zheng FY, Li R, Ge S, Xu WR, Zhang Y. Nitrogen and phosphorus co-doped carbon networks derived from shrimp shells as an efficient oxygen reduction catalyst for microbial fuel cells. *Journal of Power Sources.* 2020;446:227356. DOI:10.1016/j.jpowsour.2019.227356

13. Abomosallam M, Elalfy M, Zheng Z, Nagata K, Suzuki M. Adsorption kinetics and thermodynamics of toxic metal ions onto chitosan nanoparticles extracted from shrimp shells. *Nanotechnology for Environmental Engineering.* 2022;7(1):35-47. DOI:10.1007/s41204-021-00179-0

14. Chen S, Cai H, Du X, et al. Adsorption behavior of hierarchical porous biochar from shrimp shell for tris(2-chloroethyl) phosphate (TCEP): Sorption experiments and DFT calculations. *Environmental Research.* 2023;219:115128. DOI:10.1016/j.envres.2022.115128

15. Yu J, Tang L, Pang Y, et al. Hierarchical porous biochar from shrimp shell for persulfate activation: A two-electron transfer path and key impact factors. *Applied*

Catalysis B: Environmental. 2020;260:118160. DOI: 10.1016/j.apcatb.2019.118160

16. Oginni O, Singh K, Oporto G, Dawson-Andoh B, McDonald L, Sabolsky E. Effect of one-step and two-step H_3PO_4 activation on activated carbon characteristics. *Bioresource Technology Reports.* 2019;8:100307. DOI: 10.1016/j.biteb.2019.100307

17. Ludwinowicz J, Jaroniec M. Effect of activating agents on the development of microporosity in polymeric-based carbon for CO_2 adsorption. *Carbon.* 2015;94:673-679. DOI:10.1016/j.carbon.2015.07.052

18. Yang F, Wang J, Liu L, et al. Synthesis of porous carbons with high N-content from shrimp shells for efficient CO_2 – capture and gas separation. *ACS Sustainable Chemistry & Engineering.* 2018;6(11):15550-15559. DOI:10.1021/acssuschemeng.8b03995

19. Yuan X, Wang J, Deng S, et al. Sustainable food waste management: synthesizing engineered biochar for CO_2 capture. *ACS Sustainable Chemistry & Engineering.* 2022;10(39):13026-13036. DOI:10.1021/acssuschemeng.2c03029

20. Shao S, Wang Y, Ma L, Huang Z, Li X. Sustainable preparation of hierarchical porous carbon from discarded shells of crustaceans for efficient CO_2 capture. *Fuel.* 2024;355:129287. DOI:10.1016/j.fuel.2023.129287

21. Liu C, Huang L, Wei S, et al. Valorized shrimp shell-derived aerogel for trace enrofloxacin removal from aquaculture wastewater: adsorption performance and mechanisms exploration. *Gels.* 2026;12(3):247. DOI:10.3390/gels12030247

22. Zhang Y, Song X, Xu Y, Shen H, Kong X, Xu H. Utilization of wheat bran for producing activated carbon with high specific surface area via NaOH activation using industrial furnace. *Journal of Cleaner Production.* 2019;210:366-375. DOI:10.1016/j.jclepro.2018.11.041

23. Zhang Y, Song X, Zhang P, Gao H, Ou C, Kong X. Production of activated carbons from four wastes via one-step activation and their applications in Pb^{2+} adsorption: Insight of ash content. *Chemosphere.* 2020; 245:125587. DOI:10.1016/j.chemosphere.2019.125587

24. Schmidt HP. *European biochar certificate (EBC) – guidelines version 6.1.* Preprint posted online 2015. DOI:10.13140/RG.2.1.4658.7043

25. Gerlach FM, Szecsenyi J. Family doctor-centred care in Baden-Wuerttemberg: concept and results of a controlled evaluation study. *Zeitschrift für Evidenz, Fortbildung und Qualität im Gesundheitswesen.* 2013;107(6):365-371. DOI:10.1016/j.zefq.2013.07.002

26. Brunauer S, Emmett PH, Teller E. Adsorption of gases in multimolecular layers. *Journal of the American Chemical Society.* 1938;60(2):309-319. DOI:10.1021/ja01269a023

27. Cychosz KA, Guillet-Nicolas R, García-Martínez J, Thommes M. Recent advances in the textural characterization of hierarchically structured nanoporous materials. *Chemical Society Reviews.* 2017;46(2):389-414. DOI:10.1039/C6CS00391E

28. Sdanghi G, Canevesi RLS, Celzard A, Thommes M, Fierro V. Characterization of carbon materials for hydrogen storage and compression. *C.* 2020;6(3):46. DOI:10.3390/c6030046

29. Tarazona P. Free-energy density functional for hard spheres. *Physical Review A.* 1985;31(4):2672-2679. DOI:10.1103/PhysRevA.31.2672

30. Tarazona P, Evans R. A simple density functional theory for inhomogeneous liquids: Wetting by gas at a solid-liquid interface. *Molecular Physics.* 1984;52(4):847-857. DOI:10.1080/00268978400101601

31. Langmuir I. The adsorption of gases on plane surfaces of glass, mica and platinum. *Journal of the American Chemical Society.* 1918;40(9):1361-1403. DOI:10.1021/ja02242a004

32. Dubinin MM. Generalization of the theory of volume filling of micropores to nonhomogeneous microporous structures. *Carbon.* 1985;23(4):373-380. DOI:10.1016/0008-6223(85)90029-6

33. Hu W, Duan S, Chen Y, Zhang Y, Xie Y, Li G. Adsorption characteristics of methane on microporous carbon prepared from bitumite: Equilibrium, thermodynamics and site energy distribution studies. *Journal of Industrial and Engineering Chemistry.* 2025;148:701-723. DOI:10.1016/j.jiec.2025.01.028

34. De Boer JH. The structure and properties of porous materials. In: *Proceedings of the Tenth Symposium of the Colston Research Society Held in the University of Bristol*. London: Butterworths Scientific Publications; 1958. p. 68-94.

35. Tan IAW, Ahmad AL, Hameed BH. Adsorption isotherms, kinetics, thermodynamics and desorption studies of 2,4,6-trichlorophenol on oil palm empty fruit bunch-based activated carbon. *Journal of Hazardous Materials.* 2009;164(2-3):473-482. DOI:10.1016/j.jhazmat.2008.08.025

36. Chen S, Qin C, Wang T, et al. Study on the adsorption of dyestuffs with different properties by sludge-rice husk biochar: Adsorption capacity, isotherm, kinetic, thermodynamics and mechanism. *Journal of Molecular Liquids.* 2019;285:62-74. DOI:10.1016/j.molliq.2019.04.035

Information about the authors / Информация об авторах

Anastasia E. Memetova, Cand. Sc. (Eng.), Associate Professor, Tambov State Technical University (TSTU), Tambov, Russian Federation; ORCID 0000-0002-1036-7389; e-mail: Anastasia.90k@mail.ru

Меметова Анастасия Евгеньевна, кандидат технических наук, доцент, Тамбовский государственный технический университет (ТГТУ), Тамбов, Российская Федерация; ORCID 0000-0002-1036-7389; e-mail: Anastasia.90k@mail.ru

Andrey D. Zelenin, Cand. Sc. (Eng.), Junior Research, TSTU, Tambov, Russian Federation; ORCID 0000-0002-2399-9510; e-mail: zeleandrey@yandex.ru

Viktor S. Yagubov, Cand. Sc. (Eng.), Senior Researcher, TSTU, Tambov, Russian Federation; ORCID 0000-0003-4855-0530; e-mail: vitya-y@mail.ru

Nariman R. Memetov, Cand. Sc. (Eng.), Associate Professor, Head of the Department, TSTU, Tambov, Russian Federation; ORCID 0000-0002-7449-5208; e-mail: mnr979@gmail.com

Зеленин Андрей Дмитриевич, кандидат технических наук, младший научный сотрудник, ТГТУ, Тамбов, Российская Федерация; ORCID 0000-0002-2399-9510; e-mail: zeleandrey@yandex.ru

Ягубов Виктор Сахибович, кандидат технических наук, старший научный сотрудник, ТГТУ, Тамбов, Российская Федерация; ORCID 0000-0003-4855-0530; e-mail: vitya-y@mail.ru

Меметов Нариман Рустемович, кандидат технических наук, доцент, заведующий кафедрой, ТГТУ, Тамбов, Российская Федерация; ORCID 0000-0002-7449-5208; e-mail: mnr979@gmail.com

Received 15 May 2026; Revised 19 June 2026; Accepted 22 June 2026

Reviews
Nanostructured, nanoscale materials and nanodevices

УДК 679.871 DOI: 10.17277/jamt-2026-11-02-172-193

Application of detonation nanodiamonds in new technologies

© Valerii Yu. Dolmatov[a]✉, Alexander A. Merkin[a], Maxim N. Kiselev[b], Nataliya P. Satonkina[c], Natalia M. Lapchuk[d], Anna N. Oleshkevich[d], Kristina V. Lotnikova[a], Vladimir T. Senyut[e], Sergey D. Pisarevsky[f], Alla V. Nozhkina[g], Alexander P. Ershov[c]

[a] *Special Design and Technology Bureau "Tekhnolog", 33-a, Sovetsky Av., St. Petersburg, 192076, Russian Federation,*
[b] *JSC "Plant "Selmash", 66, Shchorsa St., Kirov, 610014, Russian Federation,*
[c] *Lavrentiev Institute of Hydrodynamics of Siberian Branch of RAS, 15, Lavrentieva Av., Novosibirsk, 630090, Russian Federation,*
[d] *Belarusian State University, 4, Nezavisimosti Av., Minsk, 220030, Belarus,*
[e] *The Joint Institute of Mechanical Engineering of the NAS of Belarus, 12, Akademicheskaya St., Minsk, 220072, Belarus,*
[f] *Geoinformation Systems of the NAS of Belarus, 6, Surganova St., Minsk, 220012, Belarus,*
[g] *JSC "Research Institute of Natural, Synthetic Diamonds and Tools", 65, Gilyarovsky St., Moscow, 107996, Russian Federation*

✉ diamondcentre@mail.ru

Abstract. This review summarizes the results of using detonation nanodiamonds (DNDs) over the past 10 years in emerging areas of science and technology. Oriented coalescence of nanodiamond crystallites (~ 4 nm) under high temperature and pressure leads to the formation of single crystals with multi-micron dimensions. New magnetic resonance imaging contrast agents have been proposed and studied in the form of aqueous suspensions containing DNDs doped with manganese and gadolinium ions. The potential use of DND crystallites as reflectors for very slow neutrons (~ 50 $m \cdot s^{-1}$) has been demonstrated. The feasibility of producing diamond coatings containing europium ions by the CVD-method has been shown. An electrorheological effect was observed when an electric field is applied to suspensions of nanodiamond crystallites in oils, with DND crystallites acting as nodes in a fractal conductive network. Mixing DNDs with tungsten (W) powder followed by sintering increases the Young's modulus of sintered tungsten by a factor of four and its hardness by 1.5–2.0 times. Replacing standard DNDs (derived from TNT/RDX mixtures) with boron-doped DNDs produced during detonation synthesis further increases the microhardness of sintered tungsten by up to four times. New types of pseud alloys were obtained for the first time: an aluminum-tungsten alloy containing 10 wt. % tungsten and 90 wt. % aluminum with a hardness of HB 60, and an aluminum-copper-tungsten alloy containing 15 wt. % Al, 50 wt. % Cu, 35 wt. % W, and 1.2 wt. % DNDs. The resulting compositions are readily machinable. The use of aqueous nanodiamond suspensions in photonics has been demonstrated for producing linear optical filters resistant to high-power radiation. Application of an intermediate product from DND synthesis – diamond charge – increased the germination rate of Chinese cabbage seeds by 70 % compared to normal rates. Adding diamond charge to space-grade lubricants reduced component wear by a factor of two. Modification of paste-like fuels with nanodiamonds increased their burning rate by up to 23%.

Keywords: detonation nanodiamonds; sintering; modification; electroplating; slow neutron reflectors; tungsten-containing alloys; fuel; space lubricants.

For citation: Dolmatov VYu, Merkin AA, Kiselev MN, Satonkina NP, Lapchuk NM, Oleshkevich AN, Lotnikova KV, Senyut VT, Pisarevsky SD, Nozhkina AV, Ershov AP. Application of detonation nanodiamonds in new technologies. *Journal of Advanced Materials and Technologies*. 2026;11(2):172-193. DOI: 10.17277/jamt-2026-11-02-172-193

Применение детонационных наноалмазов в новых технологиях

© В. Ю. Долматов[a]✉, А. А. Меркин[a], М. Н. Киселев[b], Н. П. Сатонкина[c], Н. М. Лапчук [d], А. Н. Олешкевич[d], К. В. Лотникова [a], В. Т. Сенють[e], С. Д. Писаревский[f], А. В. Ножкина[g], А. П. Ершов[c]

[a] *Специальное конструкторско-технологическое бюро «Технолог», Советский пр., 33-а, Санкт-Петербург, 192076, Российская Федерация,*
[b] *АО «Завод «Сельмаш», ул. Щорса, 66, Киров, 610014, Российская Федерация,*
[c] *Институт гидродинамики им. М. А. Лаврентьева СО РАН, пр. Лаврентьева, 15, Новосибирск, 630090, Российская Федерация,*
[d] *Белорусский государственный университет, пр. Независимости, 4, Минск, 220030, Республика Беларусь,*
[e] *Объединенный институт машиностроения НАН Беларуси, ул. Академическая, 12, Минск, 220072, Республика Беларусь,*
[f] *УП «Геоинформационные системы» НАН Беларуси, ул. Сурганова, 6, Минск, 220012, Республика Беларусь,*
[g] *ОАО «Научно-исследовательский институт природных, синтетических алмазов и инструмента», ул. Гиляровского, 65, Москва, 107996, Российская Федерация*

✉ diamondcentre@mail.ru

Аннотация. Обзор обобщает результаты использования детонационных наноалмазов (ДНА) за последние 10 лет для новых областей науки и техники. Ориентированное сращивание кристаллитов наноалмазов (~ 4 нм) при воздействии высоких температур и давлении способствует образованию монокристаллов многомикронных размеров. Предложены и изучены новые контрастные МРТ-вещества в виде водных суспензий с введенными в них ДНА, легированные ионами марганца и гадолиния. Показана возможность использования кристаллитов ДНА в качестве отражателей очень медленных нейтронов (~ 50 м/с). Показана возможность получения (CVD-метод) алмазных покрытий, содержащих ионы европия. Обнаружен электрореологический эффект при наложении электрического поля на суспензию кристаллитов наноалмазов в маслах, причем кристаллиты ДНА являются центром узлов фрактальной токопроводящей сетки. Смешивание ДНА с порошком вольфрама (W) при последующем спекании приводит к усилению модуля Юнга в 4 раза и твердость в 1,5–2,0 раза у спеченного W. Замена стандартных ДНА (из смеси тротила с гексогеном) на ДНА, легированных бором при детонационном синтезе, увеличивает микротвердость спеченного W дополнительно до четырех раз. Впервые получены новые виды псевдосплавов – алюмовольфрамовый, содержащий 10 мас. % вольфрама и 90 мас. % алюминия с твердостью НВ 60 и алюминиево-медно-вольфрамовый, содержащий 15 мас. % Al, 50 мас. % медь, 35 мас. % вольфрам и 1,2 мас. % ДНА. Полученные составы легко подвергаются механической обработке. Показана возможность использования водных суспензий наноалмазов в фотонике с целью получения линейно-оптических фильтров, устойчивых к мощному излучению. Применение полупродукта синтеза ДНА-алмазной шихты (АШ) привело к увеличению всхожести семян пекинской капусты на 70 % по сравнению с обычной всхожестью таких семян. Введение АШ в используемые космические смазки снизило износ деталей в 2 раза. Модификация пастообразных топлив наноалмазами позволила поднять скорость их горения до 23 %.

Ключевые слова: детонационные наноалмазы; спекание; модифицирование; гальваника; отражатели медленных нейтронов; вольфрамсодержащие сплавы; топливо; космические смазки.

Для цитирования: Dolmatov VYu, Merkin AA, Kiselev MN, Satonkina NP, Lapchuk NM, Oleshkevich AN, Lotnikova KV, Senyut VT, Pisarevsky SD, Nozhkina AV, Ershov AP. Application of detonation nanodiamonds in new technologies. *Journal of Advanced Materials and Technologies*. 2026;11(2):172-193. DOI: 10.17277/jamt-2026-11-02-172-193

List of Abbreviations

BTF – benzotrifuroxan (benzotris);
CEC – composite electrochemical coating;
CJ plane – Chapman–Jouguet plane;
CRZ – chemical reaction zone during explosive decomposition of HE;
DC – diamond detonation charge;
DND – detonation nanodiamond;
DP – detonation products;
EPR – electron paramagnetic resonance;
FL – fluorescence;
HE – high explosive;
HPHT – a widely used method for layer-by-layer diamond film growth at high temperatures and pressures;
MRI – magnetic resonance imaging;

NMR – nuclear magnetic resonance;
NV – nitrogen-vacancy center;
OB – oxygen balance of the explosive;
PA – picric acid;
PVP – poly(N-vinylpyrrolidone);
RDX – cyclotrimethylenetrinitramine (hexogen);
SEM – scanning electron microscopy;
TATB – 1,3,5-triamino-2,4,6-trinitrobenzene;
TEM – transmission electron microscopy;
TG – charge composed of TNT and RDX;
TNT – 2,4,6-trinitrotoluene.

1. Introduction

Detonation (ultradispersed) nanodiamonds (DNDs) were discovered by Russian scientists in 1963 [1]. Their synthesis uses carbon-containing high explosives (HEs) that have an insufficient amount of oxidizer (oxygen) in their molecular structure. As a result, only part of the carbon is oxidized into gaseous products, while the remaining carbon is released in solid form within the detonation products (DP). Under certain conditions (defined by 12 key control parameters), DNDs form and persist within these solid carbon products [2–5].

The resulting DNDs have a complex structure: inside each crystallite (~5 nm) there is a classical diamond cubic lattice, but closer to the surface the crystal structure gradually transforms – from "diamond-like" sp^3-hybridization to "graphite-like" sp^2-hybridization of carbon with each coordination shell [6]. The surface of DND particles predominantly contains oxygen-containing functional groups such as hydroxyl, carbonyl, carboxyl, ester groups, etc. [3].

Typically, nanodiamonds are produced using a mixture of TNT and RDX in proportions ranging from 60/40 to 40/60 [1, 3].

At present, there is a significant resurgence of interest in DNDs. New types of high explosives (HEs), including those derived from decommissioned materials, are being used. Research is underway on producing doped (modified) DNDs, improving various methods of nanodiamond functionalization, and developing relatively simple and environmentally acceptable purification technologies. Doping DNDs with silver, gold, and platinum opens up the possibility of creating superconducting materials in the near future and expands their potential applications in micro- and nanoelectronics. Achieving high concentrations of NV centers in nanodiamond crystallites contributes to the development of nanodiamond-based spintronics.

Industrial production (in Russia, Belarus, China, and Japan) is based on the use of mixtures of TNT (2,4,6-trinitrotoluene) and RDX (cyclotrimethylenetrinitramine). In Russia, a technology based on tetryl (N-methyl-N-2,4,6-tetranitroaniline) has also been developed. These explosives serve simultaneously as both an energy source and a carbon source. The use of DNDs across various industries is driven by the need to significantly improve the performance characteristics of composite materials.

The cost of DNDs is relatively affordable, industrial-scale production exists, and market expansion is expected. However, DNDs cannot yet be considered a fully well-characterized diamond material. This is due to variability in surface chemical composition, crystal structure, and therefore properties, which depend on differences in synthesis and purification technologies among manufacturers [1–5].

The aim of this review is to systematize empirical and theoretical knowledge on the application of detonation nanodiamonds in various fields of science and technology.

2. Oriented sintering of DNDs

Under high temperature (1300–1800 °C) and pressure of 5–7 GPa (~ 50,000–70,000 atm.), DNDs introduced into mono- or dihydric alcohols form single-crystal diamonds up to 50 μm in size with a highly perfect crystal structure [7].

Most likely, according to the theory of A. Barnard [8], at high temperatures nanodiamonds – temporarily existing as individual crystallites in liquid alcohols – become oriented relative to one another through oppositely charged crystal facets and "collapse" together in accordance with Coulomb's law. It is also possible that the carbon-containing alcohols, upon further decomposition at high temperature, act as an additional carbon source, which under high pressure becomes incorporated into the newly forming crystal structure of micron-sized diamonds.

Since the resulting diamonds are multi-micron in size and exhibit a highly perfect crystal structure, reconstruction also occurs in the carbon atoms of the defective near-surface regions of each DND crystallite. In addition, carbon generated from alcohol decomposition likely fills microdefects formed during oriented sintering due to the imperfect shape of the initial nanodiamond particles.

Prior to sintering, isopropyl or ethyl alcohol, ethylene glycol, glycerol, and other alcohols were added to DND powder. The influence of alcohol content in the range of 5–60 wt. % was investigated.

The yield of micron-sized diamond crystals from the initial DND mass was significant – up to 100 %. The resulting particle size range was broad, from 70 nm to 15 μm, with the majority consisting of microdiamond particles ≥ 4 μm.

As seen in Fig. 1, the authors [7] obtained faceted single-crystal diamonds during sintering, with sizes reaching up to 15 μm (average size ~ 1 μm). Figure 1a shows that a significant portion of microcrystals exhibit an octahedral shape.

Raman spectroscopy confirms the single-crystal nature of the sintered DNDs. The resulting product shows only a single narrow symmetric peak at 1332 cm^{-1}, corresponding to the diamond crystal lattice.

Further evidence of the high structural perfection of the obtained crystals is that the full width at half maximum (FWHM) of the 1332.3 cm^{-1} band is 2.9 cm^{-1}, compared to 3.0 cm^{-1} for natural diamond. The growth of defect-free microdiamonds from defective nanodiamond precursors most likely proceeds via an oriented attachment mechanism, which is only possible for particles with a truncated octahedral shape. This geometry enables the formation of void-free crystals.

In addition, it was established that the formation of high-quality microcrystals from defective nanocrystallites is only possible when a saturated acyclic hydrocarbon is added to the DNDs. No difference was observed between the sintering of agglomerated and deagglomerated nanodiamonds (Fig. 2).

In these micron-sized nanocrystals, an ensemble of point defects (in particular, NV centers) forms without the need for irradiation by high-energy particles.

3. Nanodiamonds functionalized with Gd and coated with PVP as a new and potentially safer MRI contrast agent

The aim of study [10] was to investigate the feasibility of using a saline suspension of DNDs coated with polyvinylpyrrolidone (PVP) and functionalized with gadolinium (Gd) as a new MRI contrast agent.

Stable saline suspensions of highly purified, deagglomerated Gd-functionalized DND particles coated with a protective PVP shell were prepared. Proton relaxivities T1 and T2 of suspensions with different gadolinium concentrations were measured at 8 Tesla. A series of *ex vivo* (phantom) and *in vivo* dynamic scans were obtained using 3 Tesla MRI, comparing PVP-coated Gd-functionalized DNDs with gadoterate meglumine at equal gadolinium concentrations. T1-weighted hyperintensity was then evaluated.

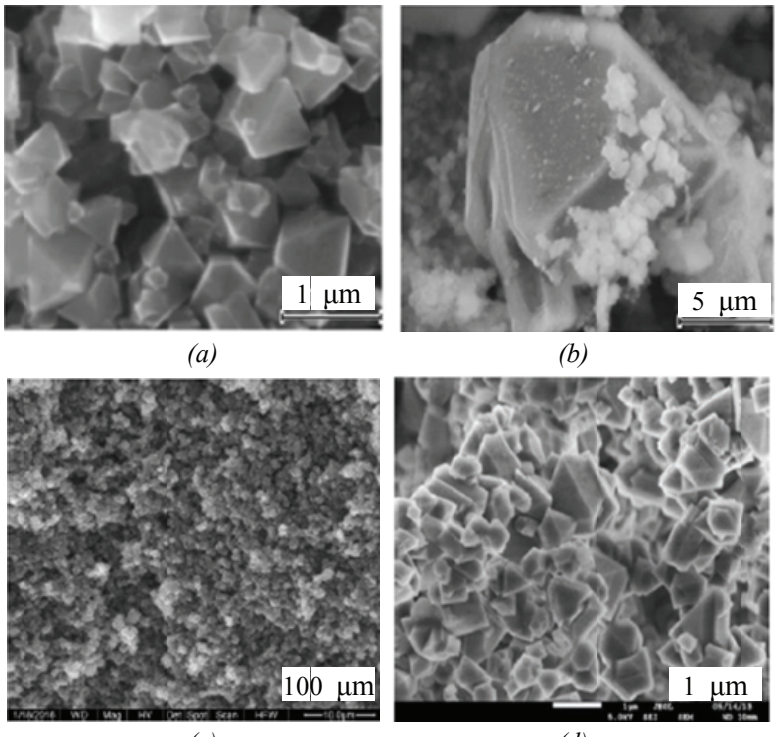

(a) *(b)* *(c)* *(d)*

Fig. 1. Appearance of oriented-sintered diamonds (scanning electron microscopy): *a* – scale 1 μm; *b* – scale 5 μm; *c* – scale 10 μm; *d* – scale 100 μm [7]

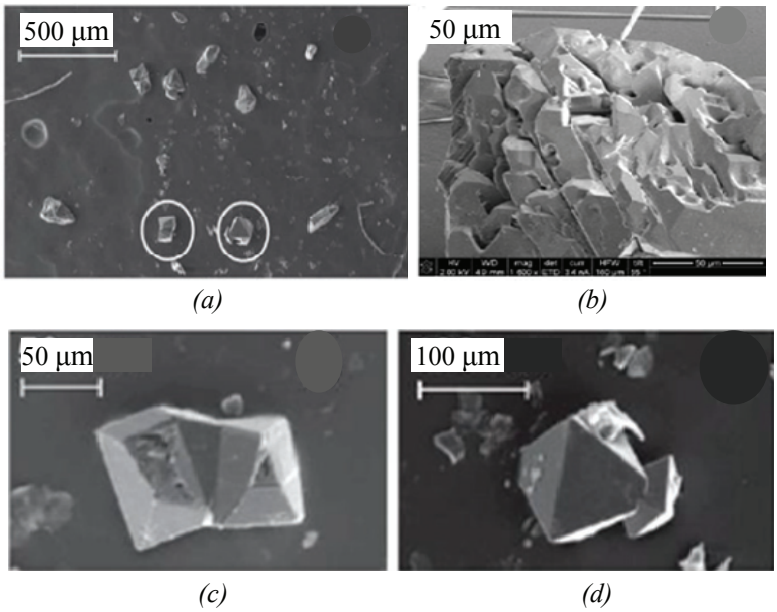

Fig. 2. *a* – Appearance of diamond single crystals after oriented attachment; *b* – surface morphology of a diamond crystal corresponding to the oriented attachment mechanism (scale 50 μm), scanning electron microscopy; *c*, *d* – obtained diamond single crystals (~100 μm) [9]

It was found that the proton relaxivity coefficients for PVP-coated Gd-functionalized DNDs were $r_1 = (33.4 \pm 0.8)$ $s^{-1} \cdot mM^{-1}$ and $r_2 =$ $= (332 \pm 15)$ $s^{-1} \cdot mM^{-1}$ [10], respectively. These values are slightly lower than those for uncoated Gd-functionalized DNDs, but still remain relatively high. MRI evaluation *ex vivo* demonstrated dose-dependent T1-weighted hyperintensity, with a significant advantage over gadoterate meglumine. Similar results were observed in *in vivo* testing of the two contrast agents.

Thus, the new MRI contrast agent-saline suspensions of PVP-coated Gd-functionalized DNDs – provides significantly higher signal intensity than the conventional agent gadoterate meglumine, increasing its potential for safer clinical use.

4. Manganese-functionalized detonation nanodiamonds as a new potential MRI contrast agent

In an effort to develop universal MRI contrast agents, the authors [11] report the synthesis and magnetic resonance study of DNDs with manganese ions directly grafted onto their surface. The sample was obtained by reacting an aqueous suspension of nanodiamonds with an aqueous solution of manganese sulfate. Evidence is presented for the chemical bonding of Mn^{2+} ions to the nanodiamond surface; these ions interact with the electronic and nuclear spins of the diamond nanoparticle, thereby accelerating spin-lattice relaxation. The distance between the Mn^{2+} ion and the diamond surface was estimated using ^{13}C NMR relaxation data. Comparison of Mn-DND interactions with previously studied Gd-functionalized DNDs [10] suggests that Mn-NDs may serve as promising MRI contrast agents.

Thus, highly purified nanodiamond particles with surfaces functionalized by paramagnetic manganese ions were obtained for the first time. The Mn grafting was achieved via ion exchange, where Mn^{2+} ions replaced hydrogen atoms of carboxyl groups during the reaction between an aqueous DND suspension and a manganese sulfate solution. NMR and EPR studies provide clear evidence that Mn^{2+} ions are chemically bound to the DND surface and interact with the electronic and nuclear spins of the diamond nanoparticles, leading to accelerated nuclear spin-lattice relaxation. The distance between Mn^{2+} ions and the DND surface, estimated from ^{13}C relaxation data, lies in the range of 0.25–0.36 nm. The authors showed that manganese functionalization reduces the ^{13}C spin-lattice relaxation time $Tln(^{13}C)$, with values comparable to those observed for Gd^{3+}-functionalized DNDs. They suggest [12] that Mn-functionalized nanodiamonds could be promising candidates for MRI contrast agents. Their safety and effectiveness will require further investigation, similar to studies conducted for Gd-functionalized DND suspensions [10].

In study [13], a new approach is reported that enables determination of spatially resolved nuclear spin–lattice relaxation times and NMR linewidths in nanomaterials. This method was applied to DNDs with manganese ions directly grafted onto their surface [11]. Interaction between carbon nuclear spins and paramagnetic Mn^{2+} ions leads to accelerated spin-lattice relaxation and broadening of the ^{13}C resonance line. Using spin dephasing experiments, the authors were able to determine the layer-by-layer contribution of Mn^{2+} ions to relaxation times and linewidths of carbon spins located at different depths from the diamond surface.

Although developed for nanodiamonds, this approach is more general and can be successfully applied to study distributions of nuclear relaxation rates and linewidth broadening, as well as to map magnetic interactions within various nanoparticles. This has practical applications in multiple nanotechnology fields. In particular, it enables investigation and tuning of magnetic interactions in DND particles functionalized with paramagnetic ions. The resulting insights are relevant for applications in spintronics, memory devices, magnetic data storage, sensors, and for studying the influence of paramagnetic ions on the relaxation of NV centers in diamonds.

5. Effect of particle size of fluorinated nanodiamonds on the efficiency of neutron reflectors

More than ten years ago, it was demonstrated that DND powders diffusely reflect very cold neutrons (VCNs) at any angle of incidence and reflect cold neutrons quasi-specularly at small angles of incidence [14]. This study investigated the neutron reflection efficiency of nanodiamonds as a function of their size. To do so, a fraction of smaller DND nanoparticles (referred to here as S-DNDs) was separated from the initially broad size distribution by centrifugation. The neutron reflector performance of these particles was then compared, both experimentally and theoretically, with that of deagglomerated fluorinated DNDs (DF-DNDs).

Typical commercially available DNDs with a size of ~ 4.3 nm are close to optimal for VCNs with a typical velocity of ~ 50 $m \cdot s^{-1}$. Smaller DNDs are more efficient for higher neutron velocities, while larger ones are more effective for slower VCNs.

Neutrons serve as both tools and subjects in many areas of research. Major global efforts are focused on increasing the intensity of neutron sources and improving neutron delivery efficiency for experimental facilities. In this context, neutron reflectors play a key role, as they can significantly enhance both efficiency and cost-effectiveness. For slow neutrons, DND powders exhibit exceptionally strong reflective properties due to a combination of enhanced coherent scattering and low neutron absorption.

The enhancement is maximized when the nanoparticle diameter is close to the neutron wavelength. Therefore, both the average particle size and the size distribution are critical factors. Additionally, DNDs tend to form clusters, which effectively increases their particle size. Study [14] reports on how the breakup of agglomerates influences DND clustering and overall reflector performance.

The authors [14] characterized DNDs using small-angle neutron scattering, X-ray diffraction, scanning and transmission electron microscopy, neutron activation analysis, dynamic light scattering, infrared spectroscopy, and other methods. Based on these results, they discuss the calculated particle size distribution of DNDs, absolute neutron scattering cross-sections, neutron albedo, and the neutron intensity gain coefficient for neutron traps with DND-based walls.

Fluorination of DNDs has little effect on the nanoparticle size distribution or the surface chemical composition.

Reducing the size of DND clusters increases neutron albedo and neutron storage time, especially in closed nanodiamond-based traps.

5. Eu-doped nanocrystalline diamond films (CVD)

Paper [15] presents experimental results on the formation of luminescent centers of europium ions in CVD diamond films. The new approach is based on using nanodiamond particles with surfaces modified by Eu ions as seed material for CVD growth. Europium-doped nanocrystalline diamond (NCD) films were grown from the gas phase on silicon substrates using microwave plasma CVD at a frequency of 2.45 GHz. Photoluminescence spectra clearly show several electronic transitions of Eu^{3+} ions, confirming their incorporation into the NCD film.

In study [15], DND particles functionalized with Eu^{3+} ions (DND–COO–{Eu}) were used to synthesize a europium-containing NCD layer. Eu-containing DND particles were attached to a 300 nm thick NCD film grown by CVD through ultrasonic treatment. Subsequent overgrowth of the

NCD film resulted in the formation of a europium-containing diamond layer. The europium ions were not etched away from the surface and remained embedded in the film. Photoluminescence analysis clearly revealed multiple electronic transitions of Eu^{3+} ions, confirming their incorporation into the NCD structure. Thus, by combining CVD growth with Eu^{3+}-functionalized DND particles, luminescent europium centers were successfully created in NCD films.

6. Electrorheological fluids with detonation nanodiamonds

Study [16] investigated the feasibility of using oils (mineral, olive, and silicone) filled with DND crystallites as electrorheological fluids. The introduced deagglomerated nanodiamonds were characterized by specific surface chemical groups, faceted shapes, and a narrow size distribution (2–10 nm, with the majority in the 3–7 nm range). The authors [16] used DND crystallites with sizes of 4 and 5 nm.

The resulting sols exhibited high sedimentation stability. An increase in viscosity was observed with increasing nanodiamond concentration, along with the emergence of a yield stress even at low nanoparticle concentrations.

A fractal structure formed by DND particles was proposed and confirmed by cryogenic tomography [16]. This method revealed differences in the fractal structure of sols depending on the type and quantity of functional groups on the nanodiamond surface. In particular, fractals formed by carboxylated DNDs are more compact than those formed by hydrogenated nanodiamonds (where a percolation network is formed, with a DND concentration of about 1 wt. %). In carboxylated nanodiamonds, the charge is localized near the functional groups.

For both hydrogenated and carboxylated nanodiamonds, the interactions between DND particles are governed by a balance between Coulomb forces and van der Waals forces. The observed differences in particle interaction depend on the nature of the liquid, particularly the dielectric properties of the solvent.

Particle size has a greater influence on the sedimentation stability of the sol than the nature of the solvent. For example, in hydrogenated DNDs, the sedimentation ratio is higher for suspensions with 5 nm particles than for those with 3 nm particles (0.95 and 0.74, respectively).

This difference in sedimentation stability may be attributed to variations in particle surface area and less pronounced charge distribution on the facets of 3 nm DND particles. These smaller particles exhibit less well-defined faceting and a higher density of structural defects.

Regardless of the type of oil used, sols of hydrogenated DNDs exhibit an electrorheological effect when an electric field is applied, whereas sols containing carboxylated nanodiamonds show electrophoresis. Thus, the nature of surface functional groups plays a decisive role in determining the behavior of DND suspensions under an electric field.

Small-angle X-ray scattering results demonstrate that 5 nm DND crystallites form significantly more branched, three-dimensional fractal structures, providing a greater number of conductive pathways in sols compared to similar structures formed by 3 nm particles. A portion of the smaller particles does not participate in fractal structure formation and remains isolated.

Carboxylation of the DND surface promotes electrophoretic motion of nanodiamond crystallites under an applied electric field in dielectric solvents. This is due to the dissociation of carboxyl groups facilitated by layers of adsorbed water on the DND surface, which generate surface charges upon dissociation.

7. Electroplating

The development of technologies for applying DND in electroplating has required further optimization both in terms of the quality of the resulting coatings and the quality and quantity of the diamond component used [3, 17]. In essence, solving this problem remained at the level of the 1980s in Russia, China, South Korea, India, Belarus, Finland, and other countries.

A striking and attractive feature of DND is the narrow range of crystal core sizes of the particles (4–5 nm). After chemical purification and removal of non-diamond (graphite-graphene) carbon-which partially hinders full aggregation of DND crystallites-agglomeration intensifies, and the size of DND agglomerates produced by industrial synthesis ranges from hundreds of nanometers to several microns.

The problem of agglomeration in dried DND powders is even worse: agglomerates range in size from single microns to tens of microns. Such particles are unsuitable for electroplating processes, as they lead to a deterioration of coating properties. However, even the use of ~ 4 nm DND nanoparticles obtained by the complex and expensive method of the Ioffe Institute does not provide any advantages over the use of DND-TAN produced by the method of the

FSUE "SKTB "Technolog," [18]. Empirically, it was established that for electroplating processes the optimal agglomerate size is 30–70 nm, which are essentially the first non-destructible agglomerates.

The solution to the problem lies in the ability to control the structure and its transformation during the creation of a new type of powder compositions based on DND, capable of disintegration in an aqueous medium into nanosized particles, and their effective use in the process of applying electrochemical metal–diamond coatings [18, 19].

To date, DND can be used for electroplating in the form of aqueous suspensions obtained immediately after chemical purification of the explosion intermediate product – ASh. After detonation of the explosive material, nanodiamond particles of various sizes are formed: crystallites of 3 to 8 nm dominate, a smaller amount in the range of 10 to 18 nm is present, and some individual particles in the range of 20 to 40 nm are also formed. The ratio of these groups strongly depends on the type of explosive and the parameters of detonation synthesis. However, due to the charge heterogeneity of the faces of a single DND particle, Coulomb interactions cause them to combine into aggregates: primary aggregates range from 10 to 50 nm (the most difficult to break down), secondary aggregates range from 70 to 250 nm, and tertiary aggregates range from 250 nm to several microns (the easiest to disintegrate). Even strong ultrasonic or mechanical disintegration cannot destroy primary aggregates and only weakly affects secondary ones.

In addition, partially disintegrated DND in suspension in strong electrolytes re-agglomerate due to the formation of multiple ion layers from the electrolyte on the surface of DND particles and their aggregates, which promotes further aggregation into rather "loose" structures that hinder the deposition of high-quality metal-diamond coatings. As a result, it becomes necessary to transport a relatively inefficient 5 % DND suspension over long distances (at higher concentrations the suspension becomes difficult to flow), meaning that 1 part of DND corresponds to approximately 20 parts of aqueous "ballast." Furthermore, such a suspension is sensitive to freezing, since this leads to irreversible agglomeration of DND particles.

It is necessary to develop dry compositions (DC) that are stable during long-term storage without changes in their properties and effective when used in aqueous solutions of strong electrolytes for the deposition of electrochemical and chemical metal-diamond coatings (chromium, nickel, copper, silver, gold).

This problem has been solved as follows: the native DND suspension obtained after chemical purification is treated with an aqueous solution of a surfactant (SAS) under simultaneous strong energy input (ultrasound, mechanical activation in a disintegrator, etc.). The surfactant penetrates the aggregated DND through macro-, micro-, and nanopores and adsorbs onto the surface of DND particles and their aggregates due to adsorption and van der Waals forces, as well as through compensation (neutralization) of electrical charges.

Next, an alkaline agent containing a carbonyl group is introduced into the suspension, and the suspension is again subjected to high-energy treatment, facilitating the penetration of metal or non-metal carbonates as deeply as possible into the DND aggregates. After this, the aqueous suspension of the primary composite is dried, crushed, and a calculated amount of dry acid (for example, citric acid) is added. The material is again ground and mixed, producing the final composite suitable for introduction into an aqueous electrolyte solution for the formation of metal–diamond coatings [19].

When the dry composite is introduced into water, soluble salts and the acid dissolve, and the carbonates react with the acid, releasing carbon dioxide gas, which disrupts the DND aggregates. The presence of the surfactant in the solution prevents re-agglomeration of the disaggregated DND particles and their primary aggregates.

In addition, due to the high disaggregation of DND and the activation of their surface, an increase in their activity is expected, along with the possibility of reducing their loading in electroplating baths. For example, if standard chromium plating requires a DND concentration of 10–15 $g \cdot L^{-1}$, the proposed product requires only 5 $g \cdot L^{-1}$, with an operating concentration range from 5 down to 1 $g \cdot L^{-1}$.

Thus, preliminary testing of various DND-containing compositions obtained under different conditions has so far identified only one formulation out of 17 that met the required quality criteria for wear-resistant chromium–diamond coatings (an increase in wear resistance of up to 4 times) at a DND concentration of 5.0 $g \cdot L^{-1}$ (Table 1). It is clear that reducing the DND loading in the electroplating bath by a factor of 2–3 significantly improves the economics of the process, especially at the initial, most cost-intensive stage.

Table 1. Comparative values of microhardness and wear resistance (wear-resistant chromium): Cr_3O – 250 g·L^{-1}, H_2SO_4 – 2.5 g·L^{-1}, SC (in terms of DND) – 5.0 g·L^{-1}. Deposition regime: current density – 50 A·dm^{-2}, electrolyte temperature – 55 °C. DND concentration – from 5.0 to 1.0 g·L^{-1} in the electrolyte [19]

Amount of additive calculated based on DND, g·L^{-1}	Microhardness H_μ, kgf·mm^{-2}. Coating thickness: 20 μm (40 min)							Wear, g
	Point 1 (center)	Point 1 (center)	Point 3 (top left)	Point 4 (bottom right)	Point 5 (bottom left)	Average	Difference between maximum and minimum values	
–	690	750	887	874	892	818	202	0.043
5.0	1050	1032	982	994	1057	1023	75	0.011

It is relevant to develop a universal diamond-containing dry powder capable of ensuring high-quality deposited coatings (chromium, nickel, copper, silver, gold) at low electrolyte concentrations. Such a powder should have a long shelf life (at least 5 years) without deterioration of properties, be resistant to freezing, be easily introduced into the electrolyte, and provide a wide range of working concentrations relative to the initially introduced amount (up to 80 %).

It should be noted that achieving a microhardness above 1050 kg/mm² for wear-resistant chromium leads to negative consequences – reduced wear resistance due to embrittlement and crack formation (numerous fine cracks appear), as well as decreased adhesion of the chromium-nanodiamond coating to the substrate surface.

In [20], the authors used a sulfuric acid electrolyte and an intermediate product (ASh) obtained from the detonation of a TNT–RDX mixture, containing 56 % DND, to produce an anodic coating. Under test conditions, the oxide layer containing ASh does not wear off. After 220 hours of exposure in a climate chamber, no signs of corrosion were detected on samples with ASh, whereas without ASh, corrosion traces appeared after 96 hours.

In this paper, for the first time, the influence of ASh on the anodizing process in a sulfate electrolyte was studied with the aim of eliminating the impregnation step from the technological chain. At an ASh concentration of 2 g·L^{-1}, a high microhardness of the oxide coating is achieved – up to 10 GPa·mm^{-2}. The corrosion resistance of the oxide layer obtained in an electrolyte with 3 g·L^{-1} ASh is at least 2.4 times higher than that of films produced under standard conditions with water impregnation. The porosity of films obtained in an electrolyte with 3 g·L^{-1} ASh is 2.5 times lower than that of films produced under standard conditions.

For obtaining anodized aluminum or aluminum alloy coatings with high performance characteristics, the following electrolyte composition is recommended:

– sulfuric acid – 200 g·L^{-1};
– diamond-containing charge – 2.0–3.0 g·L^{-1};
– remainder – water;
– process temperature – not higher than +12 °C.

8. Tungsten alloys with DND

Tungsten (W) has many unique properties, including resistance to very high temperatures, high density and hardness, and excellent wear resistance, which determine its use in tool manufacturing, mechanical engineering, and the aerospace industry. It has the highest melting point (3420 °C) and high thermal conductivity [21, 22]. A disadvantage of tungsten is its high brittleness. However, reducing the grain size of the powder improves ductility, machinability of tungsten compacts, and resistance to chipping [23]. In addition, the authors of [24–27] suppress possible grain growth of W at high temperatures by adding ultrafine particles such as ZrC, HfC, La_2O_3, Y_2O_3, CeO_2, or TiC.

In studies [25], fullerene C_{60} and DND were used as nanoscale carbon additives to tungsten, with primary sizes of a single molecule and 4–6 nm particles, respectively.

The sample preparation scheme consisted of four stages:

1) milling of the initial powders to a size of ≤ 50 nm;

Table 2. Parameters of sintered tungsten-containing samples [25]

Composition, wt. %	*P*, GPa	*T*, °C	OCR before sintering, nm	ρ, g·cm^{-3}	OCR after sintering, nm	Microhardness (Vickers), GPa	*E* (Young's modulus), GPa
W 100 %	5.3	1220	34	18.4	37–38	7.7	290
		1380	34	18.5	46–47	7.2	285
		1550	34	18.4	47–48	6	283
		1700	34	18.6	48–50	5.3	278
W 99.7 % – nanodiamond 0.3 %	5.3	1220	34	18.2	30	13.0	895
		1380	25	18.0	25	15.9	1281
		1550	25	18.2	40	13.0	805
W 99.7 % – C_{60} 0.3 %	5.3	1220	37	17.1	–	7.3	348
		1380	37	17.1	–	5.1	339
		1550	37	17.0	–	3.2	261

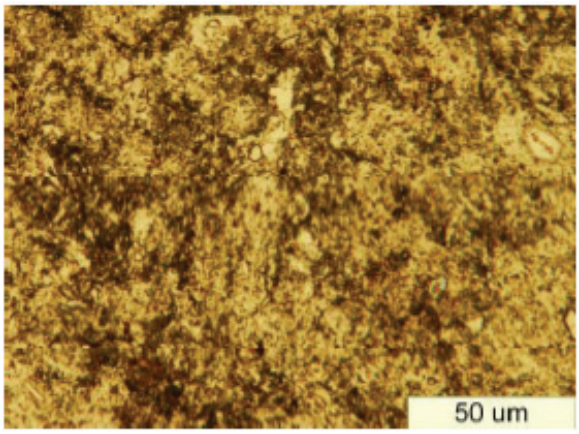

Fig. 3. Sintered W powder (polished section), light areas indicate reduced density of the compact [25]

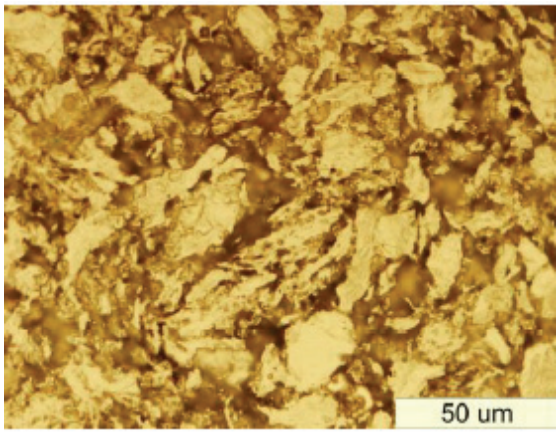

Fig. 4. Sintered tungsten powder with DND addition (0.3 wt. %), temperature 1200 °C; light areas correspond to W–DND conglomerates [25]

2) forming the specimen of the future compact from the milled powder;

3) sintering of the formed sample;

4) polishing and grinding of the obtained compact for surface characterization.

The initial powders were ground in a planetary mill. The formed samples were sintered at various temperatures under a pressure of 5.3 GPa. The resulting compacts were cylindrical, with a diameter of 4.5 mm and a height of up to 4.6 mm.

For the obtained samples (before and after sintering), the crystallite size, density, microhardness, and elastic modulus were determined (Table 2) [25].

Table 2 demonstrates a decrease in the hardness of sintered tungsten (W) with increasing sintering temperature.

Figure 3 shows a sample of pure tungsten (sintering temperature T_{sint} = 1200 °C); the light spots correspond to regions of reduced density.

With the addition of 0.3 wt. % DND, sintering had virtually no effect on grain size, and the density of the material also remained nearly unchanged. However, the microhardness of the compact increased significantly–by a factor of 1.7–2.2 (Fig. 4). At the same time, the stiffness (rigidity) of the compact increased by a factor of 2.8–4.5.

Since the size of nanodiamonds is smaller than the size of dislocations, they hinder crack propagation in the compact and reduce recrystallization of tungsten. The introduction of fullerenes (0.3 wt. %) into the composition of sintered tungsten powder leads to a reduction in tungsten grain size; however, at the same time the main properties of the compact deteriorate, namely hardness, strength, and density.

Thus, the authors of [25] showed that sintering tungsten with a small amount of nanodiamonds allowed an increase in the microhardness of the compacts by 1.5–2.0 times, while the Young's modulus increased by almost 4 times.

In [21], tungsten powder grade PVV (TU 48-19-72-92) with a particle size of 0.8–1.7 μm was used to obtain samples. DND produced by the FSUE "SKTB "Technolog", (St. Petersburg, Russia), obtained from tetryl in accordance with TU 3974-456-05121441-2008, were used as an additive. The DND had an average particle size of 3.5–6.5 nm and a specific surface area of (310 ± 10) $m^2 \cdot g^{-1}$. Highly purified DND with a non-combustible residue content of 0.6 wt. % was used, as well as DND doped during synthesis with amorphous boron in an amount of 2 wt. %.

The powder mixture consisting of tungsten powder and 0.3 wt. % DND additive (5 at. %) was activated with a power density of 3 $W \cdot g^{-1}$ in a planetary ball mill using steel balls 5 mm in diameter in a hardened steel drum. Based on the activated mixture, cylindrical compacts with a diameter of 4.5 mm and a height of 5–6 mm were produced by pressing. These were then sintered in a high-pressure apparatus at 4.5 GPa in the temperature range of 1200–1500 °C with a holding time of 10 s. For comparison, compacts from pure tungsten powder without DND addition were produced under the same sintering conditions.

The microhardness (H_μ) of the sintered compacts was measured using a PMT-3 microhardness tester by the Vickers method under a load of 200 g. The fracture toughness (K_{1c}) of the compacts was also evaluated using the indentation method.

It was found that the shrinkage of compacts sintered without DND additives is 5–10% higher compared to samples obtained from powder mixtures containing DND.

As a result of thermobaric sintering in the temperature range of 1300–1400°C, compacts based on "pure" tungsten were obtained with a microhardness H_μ in the range of 3.3–3.8 GPa. An increase in sintering temperature to 1500 °C contributed to a decrease in material porosity and an increase in microhardness up to 5.5–5.7 GPa, with fracture toughness at the level of 5.5–6.5 $MPa \cdot m^{1/2}$.

At the same time, the introduction of a 0.3 wt. % DND additive led to an increase in H_μ to 8–11 GPa, which is 2.5–3 times higher than the microhardness of compacts without DND addition (Table 3).

During indentation of compacts with DND additives, no cracks were observed on the polished surfaces, which may indicate relatively high fracture toughness of the sintered material.

X-ray diffraction studies confirmed the presence of tungsten and "traces" of DND in the sintered compacts, with no graphite phase detected (Fig. 5). Comparative studies of the fine structure of the compacts showed a reduction in tungsten crystallite size (L) in samples with DND compared to compacts of "pure" tungsten (57 nm and 103 nm, respectively). A decrease in the tungsten lattice parameter was also observed (a = 3.1648 Å for pure tungsten samples and a = 3.1635 Å for samples with DND), indicating the formation of a carbon solid solution in tungsten.

Analysis of the X-ray diffraction patterns showed that the sintered samples predominantly developed crystallographic planes in the {211} direction, which is consistent with atomic force microscopy data and indicates plastic deformation of tungsten grains (Fig. 6).

Table 3. Results of microhardness studies of compacts [21]

Composition of the composite, wt. %	Sintering pressure P, GPa	Cell temperature T, °C	Sintering time t, s	Microhardness H_μ, GPa
100 % W	4.5	1300	10	3.3
		1400		3.8
		1500		5.5–5.7
99.7 % W +0.3 % DND	4.5	1200	10	6–7
		1300		9–11
		1400		8–9.7
		1500		6.5–7.5
99.7 %W +0.3 % DND (boron)	4.5	1200	10	7–8
		1300		11.5–15.5
		1400		11.5–12.7
		1500		8.5–10

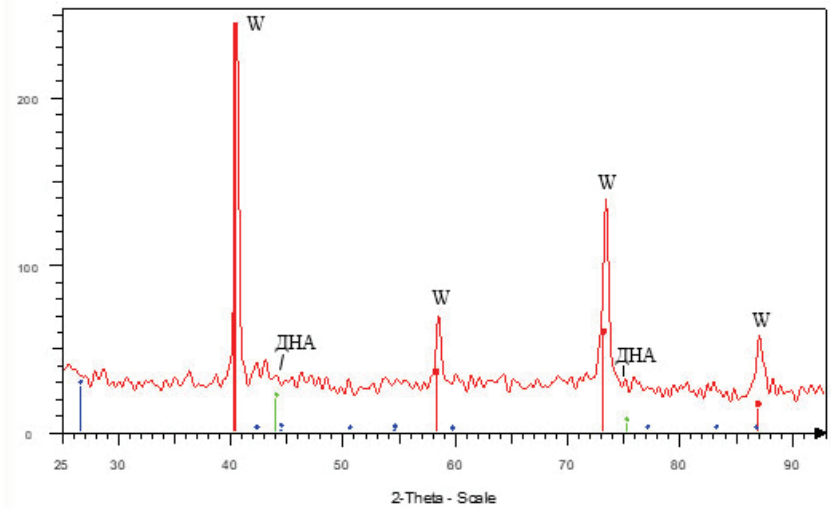

Fig. 5. Fragment of the diffraction pattern of a tungsten-based compact with 0.3 wt. % DND addition, obtained at a pressure of 4.5 GPa, temperature of 1300 °C, and holding time of 10 s

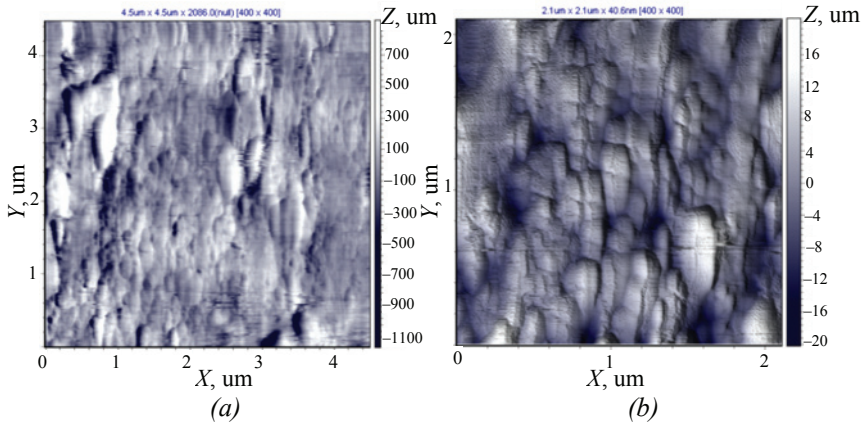

(a) *(b)*

Fig. 6. Microstructure of a tungsten-based compact with 0.3 wt. % DND addition, obtained at a pressure of 4.5 GPa, temperature of 1300 °C, and holding time of 10 s:
a – lateral contrast image; *b* – topography of the submicrocrystalline structure [21]

After deformation, tungsten grains predominantly acquire an elongated shape, with a size ranging from 100 to 500 nm (Fig. 6*a*, *b*). At the grain boundaries, inclusions are observed (presumably aggregates of DND particles) with a size of up to 30 nm (Fig. 6*a*).

Under isothermal holding of 10 s, an increase in sintering temperature leads to a decrease in the microhardness of the compacts (Table 3), which is attributed to grain growth of tungsten [25]. Further increase of isothermal holding time beyond 15 s in the temperature range of 1300–1400 °C also contributes to a reduction in microhardness to 5.8–6.5 GPa.

At 1300°C, increasing the isothermal holding time to 45–135 s, on the contrary, leads to an increase in H_μ to 8–10 GPa. As noted in [26–28], the increase in microhardness in this case occurs due to the formation of tungsten carbides. The tungsten lattice parameter decreases to 3.1625 Å, while tungsten crystallites grow to a size of 138 nm.

Higher H_μ values are exhibited by samples obtained with boron-doped DND additions (Table 3). In this case, the resulting material is characterized by pronounced structural heterogeneity, which manifests itself in a wider range of measured H_μ values (Fig. 7*c*).

An increase in the sintering temperature of compacts with boron-doped DND above 1400°C leads to their embrittlement, as evidenced by the appearance of cracks during sample indentation. Structural studies of the compacts revealed the presence on the polished surfaces of plate-like particles with a hexagonal shape (Fig. 7*c*), indicating the formation of refractory compounds based on the W–C–B system at these temperatures [29].

Thus, the use of high-pressure techniques in combination with DND enabled the production of tungsten-based compacts with a submicrocrystalline structure and microhardness levels of 10–11 GPa and

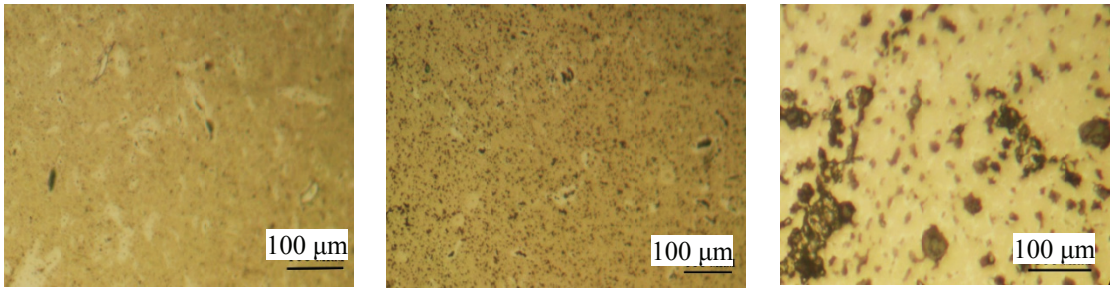

(a) *(b)* *(c)*

Fig. 7. Structure of compacts after sintering for 10 s:
a – addition of deeply purified DND, sintering temperature 1300 °C; *b* – boron-doped DND addition, sintering temperature 1300 °C; *c* – boron-doped DND addition, sintering temperature 1400 °C [21]

11.5–15.5 GPa for samples containing 0.3 wt. % deeply purified DND and samples containing 0.3 wt. % boron-doped DND, respectively. At the same time, deeply purified DND improves the ductility of the resulting material, whereas boron-doped DND increases its brittleness due to possible boride formation.

In [30], the possibility of producing lightweight pseudo-alloys based on tungsten was investigated. Tungsten pseudo-alloys with lighter metals such as Cu, Fe, and Ni are well known [31].

The resistance of tungsten pseudo-alloys to high-temperature creep and heat resistance is ensured by the fact that nanoparticles hinder dislocation motion and stabilize the sintered structure.

In [30], strengthening of pseudo-alloys was achieved by introducing powders of DND, ASh (produced by FSUE "SCTB "Tekhnolog"), and multi-walled carbon nanotubes (MWCNTs) (produced by JSC "ZAVKOM", Tambov) into mixtures of tungsten powder with copper and/or aluminum.

Analysis of the data in Table 4 shows that DND treated at 650°C in the absence of air partially de-agglomerates, and its introduction into aluminum powder at a level of 10 wt. % (experiment 1, Table 4) results in a non-pressable mixture (2000 atm); the sample disintegrates after removal of the pressing load. Thus, fully molten aluminum cannot wet the entire surface of the DND.

Table 4. Characteristics of tungsten/aluminum (DND) compacts, ∅ 25 mm [30]

Experiment No.	Pressed composition (ratio), wt. %, process conditions	Actual density, g·cm^{-3}	Porosity, vol. %	Hardness HB (pressed at room conditions)	Tablet annealing at 700 °C after pressing	Notes
1	Al + 10 % DND standard powder (650 °C), t = 750 °C					The sample disintegrated after pressing
2	W/Al (70/30), t = 750 °C + + 0.3 wt. % DC	5.11	24.7	21.5	Partially disintegrated after annealing	
3	Al/W (33/67), t = 750 °C + + 0.3 wt. % DND (Ioffe Institute)	3.29	51.5	27.9	Withstood annealing, HB = 27.1	Sent for annealing at 1220 °C
4	Al/W (90/10) +0.58 wt. % DND (Ioffe Institute), t = 630 °C	2.32	21.5	20.0	Did not settle, h = 20 mm, d_{av} = 25 mm	The powder composition breaks down after heating.
5	Al/W (90/10), +0.58 wt. % DND (Ioffe Institute) + + MWCNTs (0,6 wt. %), t = 630 °C	2.13	27.9		Cracked after holding at 700 °C	

The introduction into a tungsten–aluminum mixture (70/30, respectively) of another allotropic form of carbon–detonation diamond-containing charge (ASh) (experiment 2, Table 4) –at a low concentration of 0.3 wt. % (with ~70 % DND content in ASh) made it possible to obtain a sufficiently strong compact with a Brinell microhardness HB of 21.5, but with high porosity of 24.7 %. However, after annealing at 750 °C, the compact partially disintegrated.

In experiment 3 (Table 4), a sample consisting of a mixture of aluminum (33 wt. %), tungsten (67 wt. %), and 0.3 wt. % DND (above 100 %), modified using the Ioffe Institute technology (DND particle size ~4 nm in a 0.5 wt. % aqueous suspension), was pressed at 3000 atm. The resulting compact before annealing had a relatively high microhardness of 27.9 HB (and very high porosity of 51.5 %), and after annealing at 700 °C, the sample showed no visible changes and the microhardness remained almost unchanged at 27.1 HB.

In experiments 4 and 5 (Table 4), compositions with a significant predominance of Al over W (with only ~10 wt. % W) were studied under 2000 atm pressing. In experiment 4, the compact had a microhardness of 20 HB with relatively high porosity of 21.5 vol. %, using an addition of ~0.6 wt. % DND modified at the Ioffe Institute. However, after heating at 630 °C, the compact disintegrated. In experiment 5, multi-walled carbon nanotubes (MWCNTs) were additionally introduced in an amount of 0.6 wt. % into the composition of experiment 4, which further deteriorated the compact; after annealing, the sample cracked.

Table 5 presents the properties of three-component systems based on copper, tungsten, and aluminum with DND additions ranging from 0.3 to ~0.6 wt. %. For some samples, no pre-pressing thermal treatment of the powder mixture was used (experiments 1–3), while for others, thermal treatment at 630 °C in an argon atmosphere was applied. Considering the large difference in densities of the metals used (Al:Cu:W), where Al is 7.1 times and Cu is 2.1 times lighter than W, it is difficult to expect the formation of a sufficiently homogeneous pseudo-alloy with high intermetallic adhesion, although such a material would have broad application potential.

Table 5. Characteristics of compacts tungsten/copper/aluminum/nanodiamond, ∅ 25 mm, 2000 atm, aqueous DND suspension [30]

Experiment No.	Pressed composition (ratio), wt. %, process conditions	Theoretical density (non-porous), g·cm^{-3}	Actual density, g·cm^{-3}	Porosity, vol. %	Hardness HB, without heating after pressing	Annealing at 700 °C, after pressing
	Without heat treatment of the initial powder mixture					
1	W/Cu/Al = 75/5/20 + DND (Ioffe Institute); (0.58 %)	8.44	6.10	27.7	22.5 HB	After annealing, a small amount of golden-silver powder is present on the surface
2	W/Cu/Al=20/55/25 + DND (Ioffe Institute); (0.58 %)	6.08	5.62	7.6	24.0 HB	After 700 °C (argon, 1 h) the compact cracked
3	W/Cu/Al = 50/25/25 + DND (Ioffe Institute); (0.58 %)	6.83	5.14	24.7		After 700 °C (argon, 1 h) the compact partially disintegrated
	Heat treatment of the initial powder mixture (630 °C, argon, 1 h)					
4	W/Cu/Al = 35/50/15 + DND (Ioffe Institute); (0.58 %)	7.71	6.03	21.8		Sintered; did not fall apart, but the appearance is non-uniform subjected to annealing at 1220 °C
5	W/Cu/Al=35/50/15 + + Standard aqueous DNA suspension, (0.3 %)	7.71	5.89	23.6		Monolithic sintered body subsequent annealing (Table 6)

Experiment 1 (Table 5) showed relatively high microhardness of 22.5 HB and medium porosity of 27.7 vol. %. However, due to ambiguous results after annealing at 700 °C, the composition was not further used.

A reduction in tungsten content (almost fourfold) compared to experiment 1 (from 75 to 20 wt. %) in experiment 2 (Table 5) resulted in very low porosity of 7.6 vol. % and relatively high microhardness of 24.0 HB. However, after thermal treatment at 700°C in argon, the sample failed and cracked.

Experiment 3 (Table 5) also did not yield a strong compact; after thermal treatment at 700 °C, the compact partially cracked.

In experiments 4 and 5, aqueous DND suspensions were used to treat the metal powders separately rather than jointly, as in previous cases. After water removal, the powders were mixed. The porosity of the resulting compacts remained relatively high (22–24 vol. %), but after sintering at 700 °C, no disintegration or damage of the compacts was observed, and they were subsequently subjected to vacuum sintering at 1220 °C.

Next, the authors, having observed the low wettability of metal powders with aqueous DND suspensions, replaced water with isopropyl alcohol (IPA) and found high wettability for W, Cu, and Al. IPA containing DND readily penetrates into the pores of metal powders, delivering nanodiamonds into them, and is easily removed afterward. This makes it possible to ensure uniform distribution of nanodiamonds throughout all pores of the powders, which is important for subsequent pressing and thermal treatment at 1220 °C.

Before pressing, each metal was impregnated separately; after removal of IPA, each metal was thoroughly ground by mechanical rubbing. After mixing the metals with DND, the mixture was again carefully homogenized. Pressing was then carried out at 3000 atm.

From the data in Table 6 it can be seen that thermal treatment at 1220 °C in a vacuum furnace of binary and ternary systems (based on W, Al, and Cu) with DND additions preserved the integrity of the compacts and increased their microhardness by 2–3 times compared to previous experiments (Tables 4 and 5). However, the high porosity of the sample in experiment 4 (Table 6) led to embrittlement and failure of the specimen during microhardness testing.

Experiments showed that among the studied forms of carbon nanomaterial allotropy (DND, graphene, and nanotubes), the most effective additive was DND pre-treated at 650 °C. The stability of the samples (Table 6) to heat treatment at 1220 °C was not affected by their high porosity.

As a result, the authors of [30] obtained two new types of lightweight pseudo-alloys – binary and ternary systems containing tungsten. One of them contains 10 wt. % W, 90 wt. % Al, and 0.3 wt. % nanodiamond (above 100 %), and has a microhardness of 60.2 kg·mm^{-2}.

Table 6. Main parameters of W/Cu/Al/DND press-sintered compacts, ∅ 20 mm, annealing temperature 1220 °C [30]

Experiment No.	Pressed composition (ratio), wt. %, process conditions	Mass (table), g Diameter, mm	Theoretical density (non-porous), g·cm^{-3}	Actual density, g·cm^{-3}	Porosity, vol. %	Notes, HB
1	W/Al = 10/90, DND (650 °C), suspensions in IPA, ∑ DND 0.3 wt. %.	19.75 ∅25.06	2.95	2.55	13.6	∅25, *h* = 17 mm, the sample was preserved; HB 60.2
2	W/Cu/Al = 35/50/15, ∑ 1.2 % DND (650 °C) in IPA	20.10 ∅20.2	7.71	4.94	35.9	After annealing at 1220 °C, the sample was preserved; HB 94.1
3	W/Al = 10/90 DND (Ioffe Institute) 0.45 %	22.30 ∅20.10	2.95	2.28	22.7	The sample was preserved; HB 40.2
4	W/Cu = 65/35, DND (Ioffe Institute) 0.45 %	19.45 ∅20.20	13.73	7.78	43.3	The sample was preserved, but cracked during microhardness testing

The other contains 35 wt. % W, 50 wt. % Cu, 15 wt. % Al, and 1.2 wt. % DND, and has a microhardness of 94.1 $kg \cdot mm^{-2}$. These compositions are easily machinable and have smooth, glossy surfaces.

9. Possibility of using nanodiamonds in photonics

The authors of [32] aimed to test the possibility of using such a complex but promising product as DND crystallites as a nonlinear light scatterer in hydrosols. It was shown that the decrease in transmittance of nanodiamond hydrosols under optical limiting (OL) of pulsed laser radiation is caused by an increase in nonlinear scattering. At the same time, nanodiamond hydrosols exhibit high stability under high-power laser exposure. In addition, under prolonged and intense laser irradiation (~1 $GW \cdot cm^{-2}$), nanodiamond hydrosols demonstrate high optical stability – no aggregation of crystallites was observed.

In [33], it was found that the nonlinear transmittance coefficient of DND hydrosols is independent of polarization. The results of [32, 33] show that nanodiamond hydrosols are suitable for use as optical limiters of laser radiation.

In [34, 35], the authors demonstrated the possibility of producing films from nanodiamond hydrosols on glass substrates and laser recording of images on them. Under laser irradiation, the semi-transparent films darken, accompanied by a decrease in background luminescence.

In [36], nanodiamond hydrosols with aggregate sizes of 50, 110, and 320 nm were investigated. It was shown that the size of DND aggregates influences both the optical limiting (OL) characteristics and the stability of the hydrosol under laser irradiation. Nanodiamond aggregates in hydrosols with a size of 320 nm exhibit significantly better OL performance than DND aggregates with a size of 50 nm. In addition, such hydrosols can be used for smooth control of laser pulse duration.

In [37], nanodiamonds were introduced into heavy water (D_2O), and a nanodiamond colloidal sol was proposed as a nonlinear optical filter for the telecommunication range. The resulting nanodiamond sol in heavy water exhibits high beam and colloidal stability.

In [38], the authors studied the optical limiting behavior of nanodiamonds with surface-grafted amino and hydrogen functional groups under exposure to nanosecond Nd:YAG laser pulses. It was shown that nonlinear attenuation in DND-H is significantly greater than attenuation in DND-NH_2.

The authors of [32–38] demonstrated the strong potential of nanodiamonds for generating nonlinear optical effects.

10. Possible use of nanodiamonds in crop production

The problem of increasing crop yield and disease resistance in plant cultivation has always been and will remain a key issue in agriculture across all countries. In [39], in order to protect plant seeds from diseases and preserve nutrients, the authors developed a technology for applying a protective porous film (a silica shell) using aqueous sols based on tetraethoxysilane $Si(OEt)_4$. Based on tetraethoxysilane (TEOS), later in [40] the compositions were significantly expanded, and sol-gel systems were developed containing solutions of micro- and macroelements, as well as DND or ASh, where the latter was doped with amorphous boron during detonation synthesis (produced by FSUE "SCTB "Tekhnolog" St. Petersburg, Russia) [41].

Figure 8 shows SEM-images of barley seed surfaces (*a* – untreated, *b* and *c* – treated with silica using different TEOS concentrations), and Fig. 9 shows SEM-images of Chinese cabbage seeds treated with TEOS in the same proportions as in Fig. 8.

The most significant result was the use of boron-doped ASh for modifying silica sols, which led to the formation of plants with high biomass.

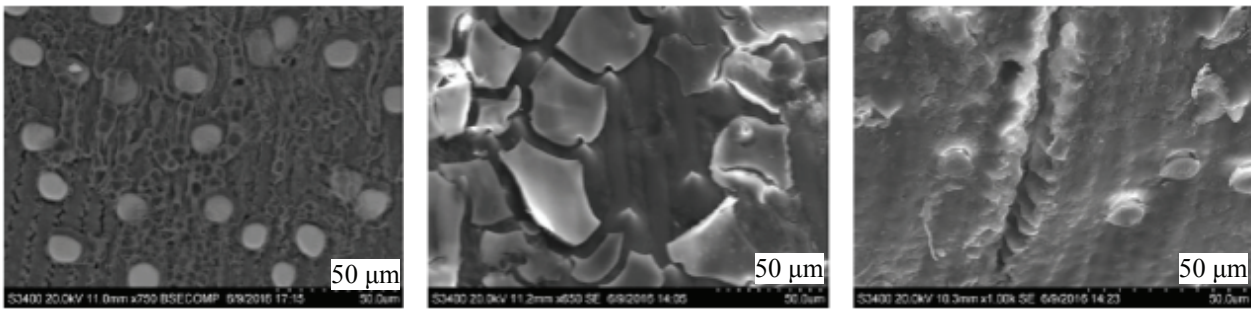

(a) *(b)* *(c)*

Fig. 8. SEM-images of spring barley seeds:
a – untreated; *b* and *c* – treated with silica sols containing 1 wt. % and 20 wt. % TEOS, respectively [40]

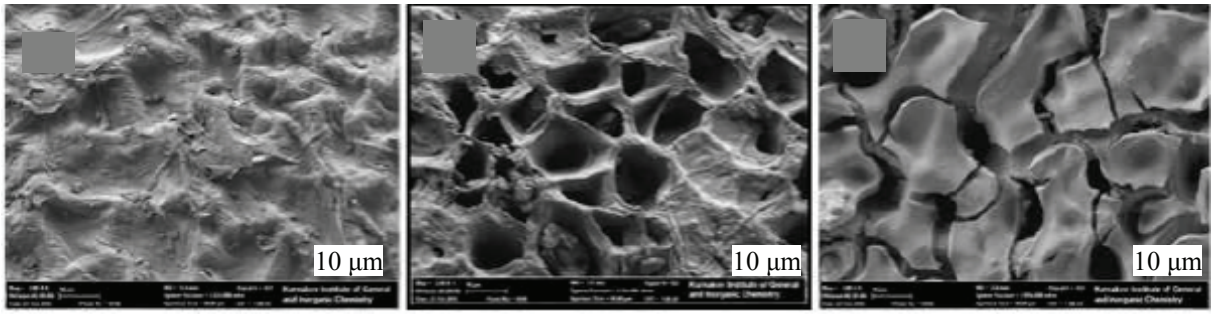

(a) *(b)* *(c)*

Fig. 9. SEM-images of Beijing cabbage seeds:
a – untreated; *b* and *c* – treated with silica sols containing 1 wt. % and 20 wt. % TEOS, respectively [40]

Thus, ASh (boron) was tested as a biologically active additive (0.05–0.1 wt. %) for pre-sowing treatment of Chinese cabbage seeds (variety Daqingkou, China, k – 56). As a result, a statistically significant positive effect of the aqueous suspension of ASh (boron) (0.05–0.1 wt. %) was observed on the following seedling characteristics (compared to the control): seed germination energy and germination rate of Chinese cabbage increased by approximately 50–70 % [42].

A significant positive effect of ASh (boron) on the morphological characteristics of Chinese cabbage plants at early growth stages was also observed when using ASh-boron for pre-sowing seed treatment in combination with silica (increase in shoot length by ~20 % and root length by ~50 % compared to the control), as well as an increase in plant biomass by ~100 % (20 days after planting treated seeds).

11. Oils and lubricants. Space lubricants with DND

Components and mechanisms of spacecraft operate under extreme space conditions, including high vacuum, radiation, and low and high temperatures [43, 44]. Space lubricants (SL) for friction units are formulated from thickened synthetic oils with various functional additives. However, under the influence of penetrating radiation and elevated temperatures (up to ~150 °C), undesirable chemical reactions may occur on tribological contact surfaces, including thermal degradation of the lubricant.

The introduction of ASh into SL (0.2–5.0 wt. %) according to [45] helps to suppress such destructive processes. Table 7 presents the studied lubricant compositions, while Table 8 shows the results of key

Table 7. Composition of main lubricant components [45]

Name	Content in composition, wt. %				
	1	2	3	4	5
Diamond-graphite nanopowder (NP)	0.20	0.75	1.50	3.00	5.00
Diamond NP	0.05	0.188	0.375	0.75	1.25
Graphite NP	0.15	0.562	1.125	2.25	3.75
Tin sulfate SnO_4	1.00	5.0	10.0	15.0	17.0
Soap-based plastic lubricant	98.80	94.25	88.50	82.00	78.0

Table 8. Main characteristics of tested lubricants on the SMT-1 friction testing machine [45]

Composition of lubricants	Maximum specific load, MPa	Friction coefficient	Wear rate, $10 \cdot 10^{-6}$ kg·m^{-3}
1	26.3	0.062	59.4
3	3.3	0.050	30.2
5	21.4	0.063	57.5
Lubricant VNIINP-232 Russian Standart 14068-79	23.5	0.059	66.0

performance characteristics of the proposed lubricants. It was shown that the coefficient of friction decreases by 12–15 %, and wear of mating steel components is reduced by a factor of 2.

DND nanoparticles remove micro-asperities from steel contact surfaces, increasing the real contact area. At the same time, nanodiamond crystallites also penetrate microcracks on the surfaces of contacting parts, strengthening them. The non-diamond graphite-like carbon also contributes to reducing friction by filling the oil film.

12. Application of nanodiamonds for improving internal combustion engine lifetime

Improving the service life of machines and mechanisms strongly depends on enhancing the quality of lubricants and oils, including the introduction of various additives into them [46, 47]. To eliminate metallic contact between mating components and to form a reliable boundary lubrication layer, additives of ultrafine solid particles are often used in oils and greases, providing high anti-friction and anti-wear properties to the lubricating composition [48]. At the recommended minimum concentrations of such additives (0.01–0.5 wt. %), the physico-chemical properties of lubricants and oils remain practically unchanged, and the operating temperature range of such lubricants is wide. These additives exhibit a pronounced positive effect both on the contact surfaces and on the characteristics of the boundary and lubricating layers [49]. The use of ultradisperse additives makes it possible to eliminate oil-soluble additives.

Layered fillers have often been used, such as molybdenum disulfide, graphite, soot, and sometimes metal powders and their compounds; however, the particle size of these additives is relatively large (1–20 μm) [50]. In this context, the use of DND with individual crystallite sizes of 4–8 nm is a logical development. DND are characterized by low chemical reactivity, a high specific surface area (300–400 m²/g), and an almost spherical shape [46]. In addition, due to their high surface energy, DND exhibit a strong structuring effect in lubricating compositions. They significantly enhance the physico-mechanical properties of lubricant films.

The running-in process of mating surfaces under the influence of diamond-containing oil additives is completed when the contact area reaches a hydrodynamic lubrication regime. In this case, closed liquid-crystalline structures are formed, which contribute to an increase in the load-bearing capacity of the contact.

In plastic lubricants, nanodiamonds, due to their strong structuring ability, form a load-bearing framework structure.

13. Fuel. Influence of detonation nanodiamonds on the combustion process of model composite solid rocket propellants

In [51], the authors evaluated the combustion of various fuel compositions containing nanodiamonds. A total of 14 formulations were prepared, and the laws of burning rates were determined; five of the compositions are presented in Table 9.

Among 14 formulations, different forms of carbon nanomaterial allotropy were tested, including: standard DND powder (DND-STP); DND-STP treated at various temperatures without air access (450, 650, 900 °C); nanocrystalline DND (4 nm) produced by the Ioffe Institute method; charcoal; graphite nanopowder; oxidized few-layer graphene; and ground adamantane powder.

It was found that DND increases the burning rate of the fuel compositions, with the highest increase of 23 % achieved when modified nanodiamond is introduced. At the same time, the combustion temperature decreases by approximately 200 °C, which has a positive effect on engine lifetime. It is assumed that DND particles do not fully oxidize to carbon dioxide during combustion, but are instead partially converted only to low-molecular-weight CO.

The introduction of DND into the fuel promotes the formation of a fractal carbon system, with a carbon framework emerging at the combustion surface, thereby providing high thermal conductivity of the composition.

14. Conclusion

It was shown that oriented sintering of DND (~5 nm) makes it possible to obtain monocrystallites of significant size (~80 μm). New, safer contrast agents based on DND grafted with gadolinium and manganese for MRI were developed. The effectiveness of DND as a material for diffuse reflection of very cold neutrons was demonstrated. The results of creating europium luminescent centers in CVD diamond films using DND precursors with europium deposited on their surface were described.

It was established that DND nanoparticles in liquid media form branched fractal structures with a dimensionality of d_m = 1.7–2.2 (in water and oils). A universal powder additive based on DND for electroplating processes was developed, providing coating quality significantly superior to previously achieved results.

Table 9. Investigated compositions of fuel formulations [51]

Composition number	Composition, %		Dependence $U(p)$, mm·s^{-1}	U_{40}, mm·s^{-1}	U_{100}, mm·s^{-1}	U_{150}, mm·s^{-1}
1	Binder Oxidizer Plasticizer	28 70 2	$615p^{0.315}$	19.7	26.2	29.8
2	Binder Oxidizer Modified DND Plasticizer	26 70 2 2	$2.585p^{0.549}$	19.6	32.4	40.5
3	Binder Oxidizer DND (650 °C)	28 70 2	$2.676p^{0.529}$	18.9	30.6	37.8
4	Binder Oxidizer DND (4 nm)	28 70 2	$3.031p^{0.508}$	19.8	31.4	38.5
5	Binder Oxidizer DND (900 °C)	28 70 2	$2.844p^{0.505}$	18.4	29.1	35.6

U – Burning rate of fuel compositions at different pressures in the combustion chamber.

Based on tungsten powder and DND, new high-quality sintered compacts were developed, and the use of DND in lightweight tungsten-based pseudo-alloys made it possible to obtain new high-quality lightweight tungsten–aluminum and tungsten-copper-aluminum alloys.

The nonlinear optical properties of nanodiamonds in aqueous suspension were demonstrated, enabling their use as optical power limiters. The application of an aqueous suspension of boron-doped diamond-containing charge for pre-sowing treatment of Chinese cabbage resulted in an approximately 100 % increase in plant biomass.

The effectiveness of diamond-containing charge as an additive in plastic space lubricants was demonstrated, reducing wear of mating parts by a factor of 2, and by a factor of 2.2 for ground transport components. DND additives in model paste-like fuels increase the combustion rate by 23 %, while the temperature of combustion products decreases by approximately 200 °C.

15. Funding

The present study did not receive any external funding.

Финансирование

Настоящее исследование не получило внешнего финансирования.

16. Conflict of interests

The authors declare no conflict of interest.

Конфликт интересов

Авторы заявляют об отсутствии конфликта интересов.

References

1. Volkov KV, Danilenko VV, Elin VI. Synthesis of diamond from the carbon in the detonation products of explosives. *Combustion, Explosion and Shock Waves*. 1990;26(3):366-368. DOI:10.1007/BF00751383

2. Danilenko VV. *Explosion: physics, engineering, technology*. Moscow: Energoatomizdat; 2010. 784 p. (In Russ.)

3. Dolmatov VYu. *Detonation nanodiamonds. Preparation, properties, application*. Saint Petersburg: Professional; 2011. 536 p. (In Russ.)

4. Titov VM, Anisichkin VF, Mal'kov IYu. Synthesis of ultradispersed diamond in detonation waves. *Combustion, Explosion and Shock Waves*. 1989;25(3):372-379. DOI:10.1007/BF00788819

5. Ershov AP, Satonkina NP, Dibirov OA, Tsykin SV, et al. A study of the interaction between the components of heterogeneous explosives by the electrical-conductivity method. *Combustion, Explosion and Shock Waves*. 2000;36(5):639-649. DOI:10.1007/BF02699528

6. Yur'ev GS, Dolmatov VYu. X-ray diffraction analysis of detonation nanodiamonds. *Journal of Superhard Materials*. 2010;32(5):311-328. DOI:10.3103/S1063457610050035

7. Kidalov SV, Shahov FM, Shvidchenko AV, Smirnov AN, et al. Growth of diamond microcrystals by the mechanism of oriented attachment at high pressure and temperature. *Pis'ma v zhurnal tehnicheskoj fiziki = Technical Physics Letters*. 2017;43(1):21-29. DOI:10.21883/PJTF.2017.01.44085.16417 (In Russ.)

8. Barnard AS. Self-assembly in nanodiamond agglutinates. *Journal of Materials Chemistry*. 2008;18(34):4038-4041. DOI:10.1039/b809188a

9. Kidalov SV. *Phase transitions graphite-diamond in carbon nanostructures at high pressures and temperatures*. Available from: https://www.ioffe.ru/serve/theses/avtoref/Thes_0578.pdf [Accessed 15 January 2026] (In Russ.)

10. Panich AM, Salti M, Goren SD, Yudina EB, et al. Gd(III)-grafted detonation nanodiamonds for MRI contrast enhancement. *The Journal of Physical Chemistry C*. 2019;123(4):2627-2631. DOI:10.1021/acs.jpcc.8b11655

11. Panich AM, Shames AI, Aleksenskii AE, Yudina EB, et al. Manganese-grafted detonation nanodiamond, a novel potential MRI contrast agent. *Diamond and Related Materials*. 2021;119:108590. DOI:10.1016/j.diamond.2021.108590

12. Panich AM, Aleksenskii AE, Yudina EB, Vul' AYa. Spatially resolved spin–lattice relaxation times and line widths in manganese-grafted detonation nanodiamonds. *The Journal of Physical Chemistry C*. 2022;126(3):1489-1495. DOI:10.1021/acs.jpcc.1c09026

13. Aleksenskii A, Bleuel M, Bosak A, Chumakova A, et al. Effect of particle sizes on the efficiency of fluorinated nanodiamond neutron reflectors. *Nanomaterials*. 2021;11(11):3067. DOI:10.3390/nano11113067

14. Aleksenskii A, Bleuel M, Bosak A, Chumakova A, et al. Clustering of diamond nanoparticles, fluorination and efficiency of slow neutron reflectors. *Nanomaterials.* 2021;11(8):1945. DOI:10.3390/nano11081945

15. Yudina EB, Aleksenskii AE, Bogdanov SA, Bukalov SS, et al. CVD nanocrystalline diamond film doped with Eu. *Materials*. 2022;15(16):5788. DOI:10.3390/ma15165788

16. Kuznetsov NM, Belousov SI, Kamyshinsky RA, Vasiliev AL, et al. Detonation nanodiamonds dispersed in polydimethylsiloxane as a novel electrorheological fluid: Effect of nanodiamonds surface. *Carbon*. 2021;174:138-147. DOI:10.1016/j.carbon.2020.12.014

17. Dolmatov VY. Detonation-synthesis nanodiamonds: synthesis, structure, properties and applications. *Russian Chemical Reviews*. 2007;76(4):339-360. DOI:10.1070/RC2007v076n04ABEH003643

18. Dolmatov VYu, Rudenko DV, Burkat GK, Aleksandrova AS, et al. A study of the process of gold plating from citrate and phosphate electrolytes in the presence of modified detonation nanodiamonds. *Journal of Superhard Materials*. 2019;41(3):169-177. DOI:10.3103/S1063457619030043

19. Dolmatov VYu. Bogdanov SP, Marchukov VA, Vehanen A, et al. A powder composition containing detonation nanodiamonds (DNDs) is an effective additive to the electrolyte of wear–resistant chrome plating. *XXXIV Symposium "Modern Chemical Physics". Collection of reports. September 16-25.* Tuapse; *2022*, p. 191-192. (In Russ.)

20. Myllymäki V, Vehanen A, Dolmatov VYu, Burkat GK, et al. Electrochemical anode oxidation of aluminum in the presence of detonation diamond-containing carbon. *Book of abstracts of 4th International scientific-practical conference "Graphene and related structures: synthesis, production, and application". October 6-8.* Tambov; *2021*, p. 95-97. (In Russ.)

21. Senyut' VT, Kovaleva SA, Dolmatov VYu, Vityaz' PA, Grigor'ev IE. Investigation of the effect of nanodiamond additives on the structure and microhardness of a sintered tungsten-based composite. *New materials and technologies: powder metallurgy, composite materials, protective coatings, welding: materials of the 16th International Scientific and Technical Conference (Minsk, May 22-24, 2024), National Academy of Sciences of Belarus.* Minsk: Belarusskaya Nauka; 2024. p. 291-293. (In Russ.)

22. Rieth M, Boutard JL, Dudarev SL, Ahlgren T, et al. Review on the EFDA programme on tungsten materials technology and science. *Journal of Nuclear Materials*. 2011;417(1-3):463-467. DOI:10.1016/j.jnucmat.2011.01.075

23. Levin ZS, Hartwig KT. Strong ductile bulk tungsten. *Materials Science and Engineering: A*. 2017;707:602-611. DOI:10.1016/j.msea.2017.09.100

24. Dine S, Bernard E, Herlin N, Grisolia C, et al. SHS synthesis, SPS densification and mechanical properties of nanometric tungsten. *Metals*. 2021;11(2):252. DOI:10.3390/met11020252

25. Zharchenkova MI, Perfilov SA, Lomakin RL. Investigation of the physico-mechanical properties of nanostructured tungsten modified with carbon nanoclusters. *ChemChemTech.* 2014;57(5):74-76. (In Russ.)

26. Chernozatonskii LA, Sorokin PB, Kuzubov AA, Sorokin BP, et al. Influence of size effect on the electronic and elastic properties of diamond films with nanometer thickness. *The Journal of Physical Chemistry C*. 2011;115(1):132-136. DOI:10.1021/jp1080687

27. Kuznetsov VL, Butenko YV. Nanodiamond graphitization and properties of onion-like carbon. *NATO Science Series II: Mathematics, Physics and Chemistry*. 2005;192:199-216. DOI:10.1007/1-4020-3322-2_15

28. Zhang P, Wang J, Wang L, Li J, et al. Dense tungsten carbide bulks by self-densification reaction sintering of nanodiamond with tungsten at 1700 °C. *Ceramics International*. 2023;49(6):9287-9297. DOI:10.1016/j.ceramint.2022.11.095

29. Kvashnin AG, Rybkovskiy DV, Filonenko VP, Bugakov VI, et al. WB_{5-x}: synthesis, properties, and crystal structure – new insights into the long-debated compound. *Advanced Science*. 2020;7(16):2000775. DOI:10.1002/|advs.202000775

30. Dolmatov VYu, Kiselev MN, Senyut' VT, Bazanov OV, et al. Development of lightweight, durable tungsten pseudo-alloys with aluminum and copper in the presence of nanodiamonds. *New materials and*

technologies: powder metallurgy, composite materials, protective coatings, welding: materials of the 16th International Scientific and Technical Conference (Minsk, May 22-24, 2024), National Academy of Sciences of Belarus. Minsk: Belarusskaya Nauka; 2024. p. 344-347. (In Russ.)

31. Peskova AS, Vinogradova TS, Farmakovskij BV, Ulin IV, et al. *Alloy on the basis of the "iron-aluminum-copper-tungsten carbide" system*. Russian Federation patent 2,434,077 C1. 20 November 2011. (In Russ.)

32. Mikheev GM, Puzyr' AP, Vanyukov VV, Purtov KV, et al. Nonlinear scattering of light in nanodiamond hydrosol. *Technical Physics Letters*. 2010;36(4):358-361. DOI:10.1134/S1063785010040206

33. Vanyukov VV, Mikheev GM, Mogileva TN, Puzyr AP, et al. Polarization-sensitive nonlinear light scattering and optical limiting in aqueous suspension of detonation nanodiamonds. *Journal of the Optical Society of America B*. 2014;31(12):2990. DOI:10.1364/JOSAB.31.002990

34. Mikheev GM, Mikheev KG, Mogileva TN, Puzyr AP, Bondar VS. Basic of images laser recording technology on the detonation nanodiamond films. *Himicheskaya fizika i mezoskopiya*. 2013;15(4):638-644. (In Russ.)

35. Mikheev GM, Mikheev KG, Mogileva TN, Puzyr AP, Bondar VS. Laser image recording on detonation nanodiamond films. *Quantum Electronics*. 2014;44(1):1-3. DOI:10.1070/QE2014v044n01ABEH015299

36. Vanyukov V, Mogileva T, Mikheev G, Puzir A, et al. Size effect on the optical limiting in suspensions of detonation nanodiamond clusters. *Applied Optics*. 2013;52(18):4123-4130. DOI:10.1364/AO.52.004123

37. Vanyukov VV, Mikheev GM, Mogileva TN, Puzyr AP, et al. Near-IR nonlinear optical filter for optical communication window. *Applied Optics*. 2015;54(11): 3290. DOI:10.1364/AO.54.003290

38. Muller O, Pichot V, Merlat L, Spitzer D. Optical limiting properties of surface functionalized nanodiamonds probed by the Z-scan method. *Scientific Reports*. 2019;9(1):519. DOI:10.1038/s41598-018-36838-7

39. Shilova OA, Hamova TV, Panova GG, Anikina LM. *Method for pre-sowing treatment of barley seeds*. Russian Federation patent 2,618,143 C1. 2 May 2017. (In Russ.)

40. Panova GG, Shilova OA, Hamova TV, Anikina LM, et al. The effect of nanocomposite silica shell on the surface of seeds on the initial stages of plant development. *Agrofizika*. 2017;2:30-39. (In Russ.)

41. Shilova OA, Panova GG, Hamova TV, Nikolaeva AM, et al. Selection and application of nanoparticles as biologically active additives in agricultural technologies. *In the collection of abstracts "The Second International Symposium Chemistry for Biology, Medicine, Ecology and Agriculture", Russian Federation, Saint Petersburg, December 6-8;* 2021. p. 30-31. (In Russ.)

42. Shilova O, Dolmatov V, Panova G, Khamova T, et al. Nanodiamond batch enriched with boron: properties and prospects for use in agriculture. *Biointerface Research in Applied Chemistry*. 2022;12(5):6134-6147. DOI:10.33263/BRIAC125.61346147

43. Mishin AA, Krushenko GG. Plastic lubricants containing nanodiamond powders. *Aktual'nyye problemy aviatsii i kosmonavtiki*. 2012;1(8):122-123. (In Russ.)

44. Nusinov MD. *Space vacuum and the reliability of space technology*. Moscow: Znanie; 1986. 63 p. (In Russ.)

45. Shchelkanov SI, Red'kin VE, Dokshanin SG, Terent'ev VF, Lyamkin AI. *Plastic grease*. Russian Federation patent 2,163,921 C. 10 March 2001. (In Russ.)

46. Artymuk TN, Potapov VM. The use of nanodiamonds in increasing the life of the ICE. The state and innovations of technical service of machinery and equipment. *Proceedings of the VIII Regional Scientific and practical Conference of students and postgraduates, 10-11 November, Novosibirsk, Russian Federation.* Novosibirsk: Zolotoy kolos; 2016. p. 93-95. (In Russ.)

47. Novakov IA, Rahimova NA, Krasnov AP, Zheltobryuhov VF, et al. Features of using nanocomposites Na^+ – montmorillonite – polyfluorinated alcohol as an antifriction solid lubricant. *Izvestiya Volgogradskogo gosudarstvennogo tehnicheskogo universiteta*. 2012;5(92):174-178. (In Russ.)

48. Rahimova NA, Kudashev SV. Hydrophobization of bentonite with polyfluorinated alcohols. *Izvestiya Volgogradskogo gosudarstvennogo tehnicheskogo universiteta*. 2010;2(62):49-53. (In Russ.)

49. Musaeva RA. *On the interaction of nanoscale particles with lubricants in ICE.* Available from: https://science-bsea.narod.ru/2011/mol_2011/musaeva_vz.htm [Accessed 15 January 2026]. (In Russ.)

50. Vereshchagin AL. *Properties of detonation nanodiamonds*. Biysk: Altai State Technical University Publ. House; 2005. 134 p. (In Russ.)

51. Naryzhnyj SYu, Dolmatov VYu, Kozlov AS, Fomenko VV, et al. Influence of modified carbon allotropes on the combustion process of model composite rocket fuels. *In: All-Russian conference 'Physics of explosion: theory, experiment, applications', September 18-21, 2023, Novosibirsk, Russia.* Novosibirsk: Sibirskoye otdeleniye Rossiyskoy akademii nauk; 2023. p. 88. DOI: 10.53954/9785604990025_88 (In Russ.)

Information about the authors / Информация об авторах

Valerii Yu. Dolmatov, D. Sc. (Eng.), Head of research laboratory, Special Construction and Technology Bureau "Technolog", St. Petersburg, Russian Federation; ORCID 0000-0001-8643-0404; e-mail: diamondcentre@mail.ru

Долматов Валерий Юрьевич, доктор технических наук, начальник научно-исследовательской лаборатории, Специальное конструкторско-технологическое бюро «Технолог», Санкт-Петербург, Российская Федерация; ORCID 0000-0001-8643-0404; e-mail: diamondcentre@mail.ru

Alexander A. Merkin, D. Sc. (Eng.), Director-Chief Designer, Special Construction and Technology Bureau "Technolog", St. Petersburg, Russian Federation; e-mail: merkin@sktb-technolog.ru

Maxim N. Kiselev, General Director, JSC "Plant "Selmash", Kirov, Russian Federation; e-mail: maksimel1977-77@mail.ru

Nataliya P. Satonkina, D. Sc. (Phys. and Math.), Senior Researcher, Lavrentiev Institute of Hydrodynamics, Siberian Branch of RAS, Novosibirsk; Russian Federation; ORCID 0000-0002-5894-7497; e-mail: n.satonkina@g.nsu.ru

Natalia M. Lapchuk, Cand. Sc. (Phys. and Math.), Associate Professor, Belarusian State University, Minsk, Belarus; Scopus ID 6506141523; e-mail: lapchuk@bsu.by

Anna N. Oleshkevich, Engineer of the first category, Belarusian State University, Minsk, Belarus; e-mail: oleshkevich@bsu.by

Kristina V. Lotnikova, Research Engineer, Special Construction and Technology Bureau "Technolog", St. Petersburg, Russian Federation; ORCID 0009-0008-3331-4272; e-mail: lotnikova.k@bk.ru

Vladimir T. Senyut, Cand. Sc. (Eng.), Leading Researcher, The Joint Institute of Mechanical Engineering of the NAS of Belarus, Minsk, Belarus; ORCID 0000-0002-1595-8516; e-mail: vsenyut@tut.by

Sergey D. Pisarevsky, Cand. Sc. (Eng.), Chief Researcher, Geoinformation Systems of the NAS of Belarus, Minsk, Belarus; e-mail: pi_sar@mail.ru

Alla V. Nozhkina, D. Sc. (Chem.), Scientific Supervisor, JSC "Research Institute of Natural, Synthetic Diamonds and Tools", Moscow, Russian Federation; ORCID 0000-0003-4750-2625; e-mail: nojkina@inbox.ru

Alexander P. Ershov, D. Sc. (Phys. and Math.), Senior Researcher, Lavrentiev Institute of Hydrodynamics, Siberian Branch of RAS, Novosibirsk, Russian Federation; ORCID 0000-0003-2306-1837; e-mail: ers@hydro.nsc.ru

Меркин Александр Александрович, доктор технических наук, директор-главный конструктор, Специальное конструкторско-технологическое бюро «Технолог», Санкт-Петербург, Российская Федерация; e-mail: merkin@sktb-technolog.ru

Киселев Максим Николаевич, генеральный директор, АО «Завод «Сельмаш», Киров, Российская Федерация; e-mail: maksimel1977-77@mail.ru

Сатонкина Наталья Петровна, доктор физико-математических наук, ведущий научный сотрудник, Институт гидродинамики им. М. А. Лаврентьева СО РАН, Новосибирск, Российская Федерация; ORCID 0000-0002-5894-7497; e-mail: n.satonkina@g.nsu.ru

Лапчук Наталья Михайловна, кандидат физико-математических наук, доцент, Белорусский государственный университет, Минск, Республика Беларусь; Scopus ID 6506141523; e-mail: lapchuk@bsu.by

Олешкевич Анна Николаевна, инженер первой категории, Белорусский государственный университет, Минск, Беларусь; e-mail: oleshkevich@bsu.by

Лотникова Кристина Витальевна, инженер-исследователь третьей категории, Специальное конструкторско-технологическое бюро «Технолог», Санкт-Петербург, Российская Федерация; ORCID 0009-0008-3331-4272; e-mail: lotnikova.k@bk.ru

Сенють Владимир Тадеушевич, кандидат технических наук, ведущий научный сотрудник, Объединенный институт машиностроения НАН Беларуси, Минск, Республика Беларусь; ORCID 0000-0002-1595-8516; e-mail: vsenyut@tut.by

Писаревский Сергей Дмитриевич, кандидат технических наук, главный научный сотрудник, УП «Геоинформационные системы» НАН Беларуси, Минск, Республика Беларусь; e-mail: pi_sar@mail.ru

Ножкина Алла Викторовна, доктор химических наук, научный руководитель, ОАО «Научно-исследовательский институт природных, синтетических алмазов и инструмента», Москва, Российская Федерация; ORCID 0000-0003-4750-2625; e-mail: nojkina@inbox.ru

Ершов Александр Петрович, доктор физико-математических наук, главный научный сотрудник, Институт гидродинамики имени М. А. Лаврентьева СО РАН, Новосибирск, Российская Федерация; ORCID 0000-0003-2306-1837; e-mail: ers@hydro.nsc.ru

Received 15 January 2026; Revised 24 February 2026; Accepted 27 February 2026

Review
Nanostructured, nanoscale materials and nanodevices

УДК 538.9 DOI: 10.17277/jamt-2026-11-02-194-204

Modified carbon nanotubes in polymethylmethacrylate and polypropylene matrices: DFT modeling of electronic energy structure, creation technologies and application prospects (review)

© Lusine S. Elbakyan[a]✉

[a] *Volgograd State University, 100, Universitetskiy Av., Volgograd, 400062, Russian Federation*

✉ lusniak-e@yandex.ru

Abstract. This article presents a review of contemporary studies on the production of composite materials based on polymethyl methacrylate (PMMA) and polypropylene (PP) with improved properties. The formation of a coherent scientific understanding of the processes involved in producing nanocomposites underpins the development of next-generation materials. In such systems, conventional polymers serve as the matrix, while carbon nanotubes act as the conductive filler. The study of effects that arise from the introduction of ultra-small quantities of carbon nanoparticles is of key importance here: it is precisely these effects that enable a dramatic change in a wide range of polymer properties without significantly increasing material costs. Alongside experiments aimed at improving conductive polymers, multiscale modeling is playing an increasingly priority role. Computational experiments reduce development costs and predict the stability of materials under load, transforming modeling into a key driver of technological progress in the field of organic electronics. Confirming the effectiveness of computational methods, the authors of this article present the findings of their own research on the interaction mechanisms between the aforementioned polymers and single- and double-walled carbon nanotubes, which led to the creation of a composite polymer system. This research was conducted using a modern quantum-chemical method – density functional theory (DFT). Thus, the presented review not only summarizes existing achievements in the field of CNT/PMMA and CNT/PP composites, but also establishes a new methodological vector in which computational methods (particularly DFT) become an equal and, at early stages, a priority tool for designing nanocomposites with predictable properties.

Keywords: polymethylmethacrylate; polypropylene; carbon nanotubes; polymer nanocomposites; density functional theory; adsorption interaction; conductive properties.

For citation: Elbakyan LS. Modified carbon nanotubes in polymethylmethacrylate and polypropylene matrices: DFT modeling of electronic energy structure, creation technologies and application prospects (review). *Journal of Advanced Materials and Technologies*. 2026;11(2):194-204. DOI: 10.17277/jamt-2026-11-02-194-204

Модифицированные углеродные нанотрубки в матрицах полиметилметакрилата и полипропилена: DFT-моделирование электронно-энергетической структуры, технологии создания и перспективы применения (обзор)

© Л. С. Элбакян[a]✉

[a] *Волгоградский государственный университет, пр. Университетский, 100, Волгоград, 400062, Российская Федерация*

✉ lusniak-e@yandex.ru

Аннотация. Статья содержит обзор современных работ, посвященных получению композиционных материалов на основе полиметилметакрилата (ПММА), полипропилена (ПП) с улучшенными характеристиками. Формирование целостных научных представлений о процессах получения нанокомпозитов лежит в основе создания материалов нового поколения. В таких системах матрицей служат традиционные полимеры, а функцию проводящего наполнителя выполняют углеродные нанотрубки. Ключевое значение здесь приобретает изучение

эффектов, возникающих при введении сверхмалых количеств углеродных наночастиц: именно они позволяют кардинально изменить широкий спектр свойств полимеров без значительного удорожания материала. Наряду с экспериментами по улучшению проводящих полимеров все более приоритетную роль играет многомасштабное моделирование. Вычислительные эксперименты сокращают затраты на разработку и прогнозируют стабильность материалов при нагрузках, что превращает моделирование в ключевой драйвер технологического прогресса в области органической электроники. Подтверждая эффективность вычислительных методов, авторы приводят результаты собственных исследований механизмов взаимодействия перечисленных полимеров с одно- и двуслойными УНТ, приведших к созданию композитной полимерной системы, выполненных с использованием современного квантово-химического метода – теории функционала плотности DFT. Таким образом, представленный обзор не только обобщает существующие достижения в области композитов УНТ/ПММА и УНТ/ПП, но и задает новый методологический вектор, в котором вычислительные методы (в частности, DFT) становятся равноправным, а на начальных этапах – приоритетным инструментом проектирования нанокомпозитов с прогнозируемыми свойствами.

Ключевые слова: полиметилметакрилат; полипропилен; углеродные нанотрубки; полимерные нанокомпозиты; метод теории функционала плотности; адсорбционное взаимодействие; электропроводящие свойства.

Для цитирования: Elbakyan LS. Modified carbon nanotubes in polymethylmethacrylate and polypropylene matrices: DFT modeling of electronic energy structure, creation technologies and application prospects (review). *Journal of Advanced Materials and Technologies*. 2026;11(2):194-204. DOI: 10.17277/jamt-2026-11-02-194-204

1. Introduction

Over the past decades, interest in nanostructures based on conductive polymers has steadily increased in both fundamental science and applied industries. This field has seen particularly rapid development in the last ten years, driven by the discovery of unique properties in nanoscale forms of these materials and significant increases in the efficiency of devices based on them [1].

Market growth is driven by the automotive and diesel industries, as well as the general demand for lightweight, high-performance, and affordable electronic components. However, to reach the mass market, it is necessary to dramatically improve the processability of these polymers. The main challenges relate to their sensitivity to temperature and time fluctuations, as well as the nonlinear nature of their physicochemical properties.

The focus of modern research is on the creation of polymer composite materials reinforced with nanoscale fillers, including carbon nanotubes (CNTs) [2–6]. As evidenced by an analysis of the extensive scientific literature [7–9], CNTs occupy a key position in the field of composites due to their unique combination of thermal, mechanical, electrical, and optical properties. Growing interest in integrating CNTs into various polymer matrices is stimulating the development of CNT-based polymer nanocomposites, as well as hybrid polymer/fiber composites, which boast exceptional performance characteristics [10]. Advances in the technologies for producing such materials are considered among the most significant advances in nanoscience, as well as for biomedical, aerospace, construction, and other industries [11–15].

Along with in-depth experimental research aimed at improving the stability and processability of conductive polymers, the development of theoretical and computational foundations for their behavior under real-world operating conditions is of fundamental importance.

The development of multiscale modeling of conductive polymers will be able to link quantum-chemical calculations of binding energies, molecular dynamics descriptions of charge transfer, and continuum models of mechanical relaxation into a unified picture. Computational experiments should precede synthesis, minimizing development costs, and accompany production, allowing for the prediction of long-term material stability under cyclic loads and temperature fluctuations. This approach transforms modeling from an academic tool into a key driver of technological progress in organic electronics and “smart” materials.

A promising approach to assessing the effectiveness of nanofillers involves quantifying the interaction between the nanofiller and the polymer matrix by studying the electron-energy parameters of the process. This not only improves efficiency but also minimizes the need for practical testing. The quality of the adsorption interaction determines the stability of the resulting polymer-CNT complex. Given the difficulties associated with directly measuring the interaction energy of the studied complexes experimentally, computational methods offer a good alternative. Density functional theory calculations for solid-state systems yield results that are in good agreement with experimental data. Therefore, this method allows for studying the interaction between different types of nanofillers and polymers.

The aim of this study is to review modern approaches to producing polymethyl methacrylate and polypropylene-based composite materials with improved properties, as well as to develop and validate a computational approach (based on density functional theory (DFT)) for quantitatively assessing adsorption interactions in a polymer-carbon nanotube complex, ensuring the best balance between the accuracy of describing the electron-energy parameters and computational costs.

Determining the optimal functional and basis set for density functional theory calculations is a prerequisite for achieving computational reliability and depends on a number of factors, such as the purpose of the study, the size and complexity of the system, the type of interactions, computational resources, etc. For large systems (e.g., biomolecules or materials), a tradeoff between accuracy and computational costs may be required. Thus, the optimal choice of functional and basis set is a balance between the required accuracy and available computational resources.

We investigated the effectiveness of functionals in studying nanoparticles with semiconductor-like conductivity using GaAs quantum dots and 5CB (4-pentyl-4-cyanobiphenyl) liquid crystals [16]. Theoretical calculations showed that the B3LYP functional is the most preferable for such systems, as the obtained results are in good agreement with experimental results and theoretical calculations by other authors [17–19]. In [20], we tested the choice of functionals and basis sets for the quantum-mechanical DFT calculation method for TiO_2 nanotubes. There are also works by other authors in which the B3LYP functional in combination with the 3-21G basis set, known as B3LYP/3-21G, has demonstrated accurate results for a number of chemical systems, including complex organic molecules such as natural resins or polymers [21, 22].

2. PMMA-CNT polymer composite materials

Polymethyl methacrylate (PMMA) is a lightweight, non-toxic synthetic polymer with high transparency, weather resistance, and good physical, mechanical, and electrical insulating properties (Fig. 1). It is characterized by high impact strength, light transmittance, processability, and biocompatibility [23]. Due to this, PMMA is widely used in lighting engineering, medicine, aviation, and mechanical engineering. However, its thermal and mechanical stability are insufficient to meet modern industrial requirements, making modification of the material a pressing issue. The creation of new PMMA-based composites with predictable physical and mechanical properties will significantly expand its applications.

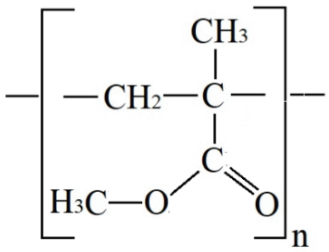

Fig. 1. The structural formula of polymethylmethacrylate

2.1. Experimental study of PMMA-CNT composite materials

The introduction of carbon nanotubes into polymer matrices plays a key role in expanding the potential application of composites, providing an increase in the elastic modulus and strength. To achieve the desired result, the method of producing the composite material plays a significant role. For example, in [24], using the 3D mixing method, various concentrations of multiwalled CNTs (MWCNTs) were introduced into PMMA to create polymer nanocomposites, followed by injection molding. Properties such as permittivity, conductivity, dielectric loss tangent, and electric modulus at intermediate frequencies were studied. The authors state that the findings have significant potential for application in electronics, sensors, and advanced materials, which emphasizes the novelty and practical significance of the study.

In [25], PMMA/MWCNT composites with concentrations of 2.5, 5, and 10 wt. % were obtained by mixing solutions. It was found that at 5 wt. % with the addition of 5 wt. % MWCNTs, the elastic modulus and hardness increase by 44 and 27 %, respectively, relative to pure PMMA. A further increase in the nanotube content to 10 wt. % leads to a decrease in these parameters by 23 and 28 %, respectively, compared to the sample containing 5 wt.%. Dynamic mechanical analysis in the frequency range of 50–210 Hz showed that the composite with 5 wt. % MWCNTs outperforms pure PMMA in elastic modulus across the entire studied range. Thus, the authors of [24] confirmed the feasibility of using low MWCNT concentrations in PMMA composites for operation under low- and medium-frequency loads.

Studies [26, 27] have shown that an increase in the CNT content leads to an increase in the elastic modulus and a decrease in fracture strain. In [28], the effect of process parameters (pressure, holding time, melt temperature) and the CNT concentration on the mechanical properties of composites was studied using the injection molding method. It has been found that with an increase in the nanotube content from

0 to 1.5 wt. %, tensile strength and elongation at failure decrease by approximately 30 and 40 %, respectively, while hardness increases slightly.

A significant amount of research has been devoted to the development of highly effective PMMA/CNT-based materials for electromagnetic shielding [29, 30].

In [29], the absorption characteristics of electromagnetic radiation by PMMA/CNT nanocomposite foam with a laminated configuration were studied. The layered structure ensured an absorption band extension to 3.5 GHz (8.9–12.4 GHz), which is 0.8 GHz wider than that of a single-layer 2 mm thick foam, as well as a reduction in reflection losses over a wide frequency range. This was achieved by reducing reflectivity in the upper layer and increasing absorption in the lower layer.

In the review paper [31], various methods for synthesizing foamed carbon materials (3D printing, supercritical foaming, carbonization, etc.) were considered, and the electromagnetic interference shielding properties of polymer composites reinforced with CNTs were analyzed, including existing problems and prospects for their solution.

The optimization of structural solutions for improving absorption characteristics is of particular interest. In [32], a foam plastic design with alternating layers of pure PMMA and PMMA/CNTs, forming a gradient structure, was proposed. The absorption band was 3.2 GHz (8.8–12.0 GHz), and the minimum reflection loss reached − 30.2 dB at 8 wt. % CNTs.

In [33], the possibility of producing PMMA/CNT composite granules combining high electrical conductivity and optical transparency was demonstrated. Using the electrostatic assembly method, homogeneous decoration of PMMA particles with nanotubes was achieved at their content of only 0.0068–0.068 vol. %, which ensured the formation of conductive channels.

In [34], composites based on PMMA granules with a coating of MWCNTs dispersed in a thermoplastic polyurethane (TPU) matrix were studied as sensing elements for pressure measurements. As the load increases, the granules converge, forming three-dimensional conductive networks across the interphase boundaries, ensuring early contact even at low pressures. An additional advantage is the increased thermal conductivity of the material. The authors recommend these composites for use in pressure measurement systems. In [35], the possibility of controlling the electrical conductivity of PMMA/MWCNT nanocomposites through halogenation was demonstrated, enabling the formation of a stable percolation network and achieving high conductivity.

In [36], a technology for producing flexible monopole antennas from PMMA films filled with single-walled carbon nanotubes (SWCNTs) was presented. The characteristics (reflection coefficient, radiation patterns, and gain) were evaluated in the unbent and bent states, confirming the potential for using such films. In [37], rectangular and circular polymer antennas were developed in which carbon nanotubes completely replace copper in the conductive elements and grounding. The achieved balance between dimensions, gain and efficiency demonstrated the practical suitability of such designs.

2.2. Theoretical modeling of the PMMA-CNT composite system

The reviewed studies were devoted to the strengthening of a polymer matrix by carbon nanomaterials, as well as imparting conductive properties to it. A comparison of the mechanical properties before and after the introduction of the filler showed that carbon nanotubes are capable of reinforcing the matrix. Furthermore, it was established that their addition to a polymer dielectric can lead to the emergence of electrical conductivity. The contribution of researchers to the development of nanocomposites is outstanding. Nevertheless, the mechanisms of strengthening the same matrix by different types of nanotubes are of particular interest; this aspect requires further study. The DFT method has proven itself as one of the most accurate approaches for atomic analysis of the structure, stability, mechanical and electronic properties of new materials [38]. Modern DFT modeling also allows for the prediction of the characteristics of carbon nanocomposites [39]. In [40], extended tight binding (xTB), DFT, symmetry-adapted perturbation theory (SAPT), and molecular dynamics (MD) simulations were used to understand the interaction of PMMA polymer with industrial gases (H_2, O_2, N_2, and H_2O). A theoretical experiment allows us to investigate the behavior of gas molecules in the presence of PMMA, which is important for understanding their adsorption and solubility in the polymer matrix.

In [41], molecular dynamics was used to analyze the interaction of β-blockers with PMMA in a pure matrix and in water, providing reliable information on the potential role of PMMA at the molecular level in the environment when in contact with pharmaceutical pollutants.

In [42], theoretical modeling of PMMA composites with SWCNTs was performed.

The CNT diameters (0.54–1.08 nm), volume fractions (8.1–16.5 %), and temperatures (100–700 K) were studied. The results showed a significant improvement in mechanical properties at low SWCNT contents. Furthermore, double-walled carbon nanotubes (DWCNTs) were twice as strong as single-walled carbon nanotubes (DWCNTs) at the same simulation cell dimensions.

We conducted quantum-chemical modeling of the interaction of polymethyl methacrylate with carbon nanotubes of various types, diameters, and layer counts. Theoretical studies revealed the high sorption activity of polymethyl methacrylate with carbon nanotubes of varying layer counts. Figure 2 shows a model of the interaction between a PMMA fragment $[C_5H_8O_2]_{15}$ and DWCNTs. We also studied the electron-energy structure of polymer nanocomposites based on polymethyl methacrylate, an analysis of which revealed that the complexes in question are narrow-bandgap semiconductors [43–48].

In [49], the effect of boron (16–50 %) on the adsorption of methyl methacrylate by boron-carbon nanotubes was studied. Quantum-chemical calculations showed that boron modification increases the adsorption energy by 45–50 % compared to pure tubes due to donor-acceptor interactions and electron density redistribution. The stability of the complex is ensured by physical adsorption with a Coulomb contribution. Boron-carbon nanotubes (p-semiconductors) improve the electrical conductivity of the composite and its mechanical properties (strength, elastic modulus), which is promising for flexible electronics and sensors.

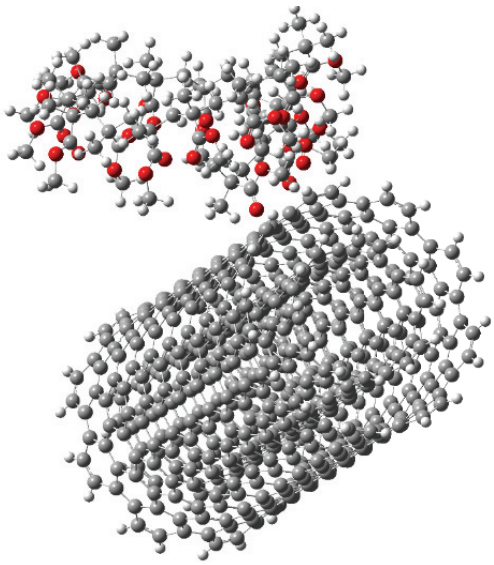

Fig. 2. Model of the interaction of the PMMA $[C_5H_8O_2]_{15}$ and DWCNT [46] fragment

The results obtained through quantum-chemical modeling are of direct practical significance, as they allow us to predict the effectiveness of using polymethyl methacrylate nanocomposites with carbon nanotubes as semiconductor materials for micro- and nanoelectronics. The theoretical data presented in this paper provide the basis for the targeted creation of such composites with tailored performance properties, promising for use in solar energy, microelectronics, optical materials, and polymer-based photoelectronic engineering.

3. Polypropylene-CNT polymer composite materials

Polypropylene is one of the most sought-after thermoplastics due to its high chemical resistance to acids, alkalis, and solvents, although it is unstable to non-polar liquids (Fig. 3). The material is characterized by low vapor permeability, good insulating properties, high air permeability, and water repellency. This explains its application in a variety of fields: from packaging and fibers to automotive, medical equipment, and household appliances.

Today, polypropylene is one of the most sought-after thermoplastics. This growth is driven by both increasing plastic consumption and improved processing technologies. However, the demands of modern industry are already exceeding the capabilities of traditional polymers [50].

The introduction of CNTs into a polymer matrix opens up the possibility of creating composites with improved electromagnetic shielding properties, which is relevant for electrical engineering, telecommunications, and the defense industry.

3.1. Experimental study of PP-CNT composite materials

The authors of [51] studied polypropylene composites reinforced with MWCNTs (0.4–1.5 wt. %), produced by compression molding. The introduction of MWCNTs increased the tensile strength to 62.80 % (at 1.2 wt. %), as well as the impact strength (by 82.14 %) and hardness (by 12.44 %) at the maximum filler concentration.

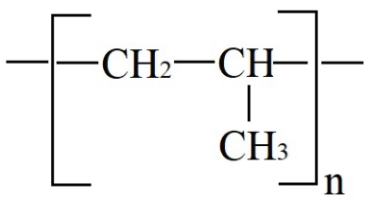

Fig. 3. Structural formula of the polypropylene molecule

In [52], it was shown that the addition of 5 wt. % carbon nanotubes to polypropylene improves the mechanical properties: the tensile strength increases by 11 %, Young's modulus by 33 %. Furthermore, the thermal stability of the composite increases by more than 30 °C compared to the original polymer.

The authors of [53] used microwave treatment to improve the mechanical properties of PP/MWCNT nanocomposites with a 10 % volume fraction of filler. This method promotes uniform volumetric hardening and increased strength. A strain rate sensitivity study showed that the tensile strength varied from 5.74 to 15.7 MPa depending on the loading rate. The highest flexural strength (21.91 MPa) and flexural modulus (2.69 GPa) were recorded at a rate of 1.25 mm·min^{-1}. In [54], the effect of MWCNTs on the mechanical properties of polypropylene fiber concrete (PPFC) was studied. MWCNTs were dispersed in water using ultrasound and added in three dosages (0.05–0.15 % of the cement mass) with varying polypropylene fiber content (0.5–1.5 % of the mixture volume). The tests included compressive strength, flexural strength, tensile strength, elastic modulus, rebound number, and ultrasound velocity. Optimal results were obtained with 0.10 % MWCNTs and 1.0 % PPF: compression – 49.4 MPa, bending – 6.4 MPa, tension – 4.9 MPa, elastic modulus – 42257 MPa, rebound number – 47.0, ultrasound velocity – 5567 m·s^{-1}. The addition of MWCNTs significantly improved the properties of PPFC, especially with this combination.

A number of studies [55, 56] are devoted to the study of creep and recovery of polypropylene with the introduction of carbon nanotubes. In [56], using coarse-grained MD modeling, it was shown that doping with CNTs increases the creep resistance of the nanocomposite. In [57], M. Sabet studied the effect of SWCNTs and MWCNTs on the thermal behavior and crystallization of isotactic polypropylene. It was found that the addition of nanotubes increases the crystallization temperature and the critical cooling rate without significantly changing the melting temperature. A percolation threshold of 0.5 wt. % was found for MWCNTs, at which the physical properties improved without the use of a compatibilizer. The increased interfacial surface area promotes increased thermal stability of the polymer, which opens up opportunities for the creation of high-performance nanocomposites based on PP. The authors of [58] also observed an improvement in the thermal stability of PP/CNT polymer composite materials.

The potential of using carbon nanotubes to impart high electrical conductivity to materials has long been confirmed [59–62]. Researchers worldwide are particularly interested in the development of conductive polymers and studying the potential for their practical use. In recent years, such polymers have found application in the creation of electronic devices, batteries, artificial muscles, solar energy conversion systems, and various types of sensors [63, 64].

In [65], it was shown that with an increase in the MWCNT content, the electrical conductivity of PP/MWCNT composites changes from insulating to semiconducting. Up to 3 wt. % of the material is non-conductive, but when this threshold is exceeded, a conductive network forms, and the conductivity increases sharply from 10^{-12} to 10^{-1} S·m^{-1}, which corresponds to a percolation transition. Moreover, the conductivity is independent of the injection molding temperature.

In [66], statistical percolation theory methods were used to establish the electrical percolation threshold for PP/SWCNT composites at 1.4 wt. % (critical value $t = 2.05$). An optimized melt mixing process enabled the formation of a conductive network with an SWCNT content of approximately 1.28 wt. %. However, given the superior properties of SWCNTs compared to MWCNTs, such a low percolation threshold may not meet expectations.

In a number of studies [67–69], special nanocomposite production modes are used in addition to the introduction of CNTs to achieve conductive properties in polymeric materials. In [68], the effect of injection molding parameters on the crystalline structure and electrical resistance of PP/MWCNT composites was studied. The materials were produced by twin-screw melt extrusion followed by injection molding. With the same MWCNT content, increasing the mold temperature and injection speed resulted in a decrease in specific electrical resistance.

3.2. Theoretical modeling of the PP-CNT composite system

In parallel with the experimental work, a number of theoretical studies were conducted to explore the potential for improving the properties of polypropylene. In [70], the construction of seven models of PP-based composite materials was presented, and molecular dynamics (MD) simulations were conducted to determine the thermodynamic properties of these composite models. This study aimed to elucidate the microstructural mechanisms underlying the improved mechanical properties observed in functionalized MWCNT/PP composites. Furthermore, the study compared the effects of grafting different numbers of functional groups on improving the mechanical properties of PP composites.

Molecular models of CNT/PP nanocomposites containing randomly dispersed bundles of carbon nanotubes were also investigated in [71]. The modeling results showed that the properties of the modeled nanocomposite continuously improve with increasing nanotube content due to the effective CNT/PP interphase boundary and the reinforcing effect of the CNTs themselves.

In [72, 73] theoretical studies of the interaction processes of polypropylene (PP) polymer with carbon nanotubes of various types, diameters and layer density are presented. The adsorption process of one monomer unit (C_3H_6) of polypropylene, as well as a PP fragment $[–CH_2CH(CH_3)–]_n$ consisting of 15 structural units, was modeled. The E_{ad} values revealed the fact of physical adsorption of the polymer fragment with the CNT cluster. Thus, our results allowed us to predict the possibility of creating stable complexes of a composite polymer material based on nanotube-reinforced polypropylene. In this case, the adsorption energy value is fundamentally independent of the CNT layer density. We also analyzed the electron-energy structure of complexes formed by SWCNTs and DWCNTs and a polypropylene fragment [74]. The analysis of the band gap width ΔE_g of the complexes revealed that the system has a semiconductor conductivity type (Figs. 4, 5).

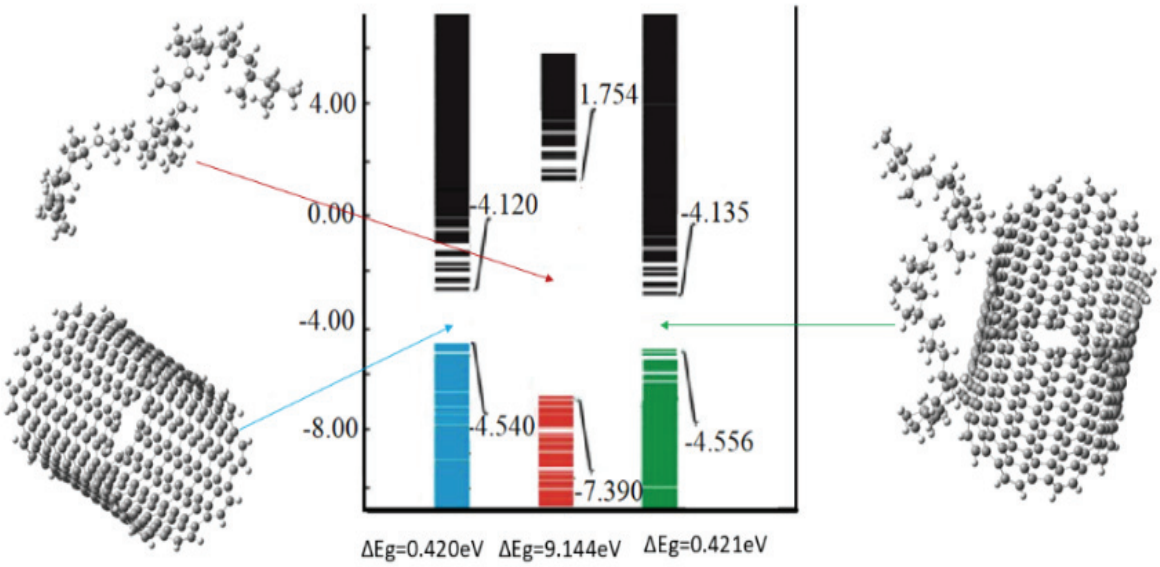

Fig. 4. Visualization of single-electron energy spectra of clusters of single-layer CNTs, a fragment of PP and interacting PP + CNTs modeling the structure of a composite polymer material [74]

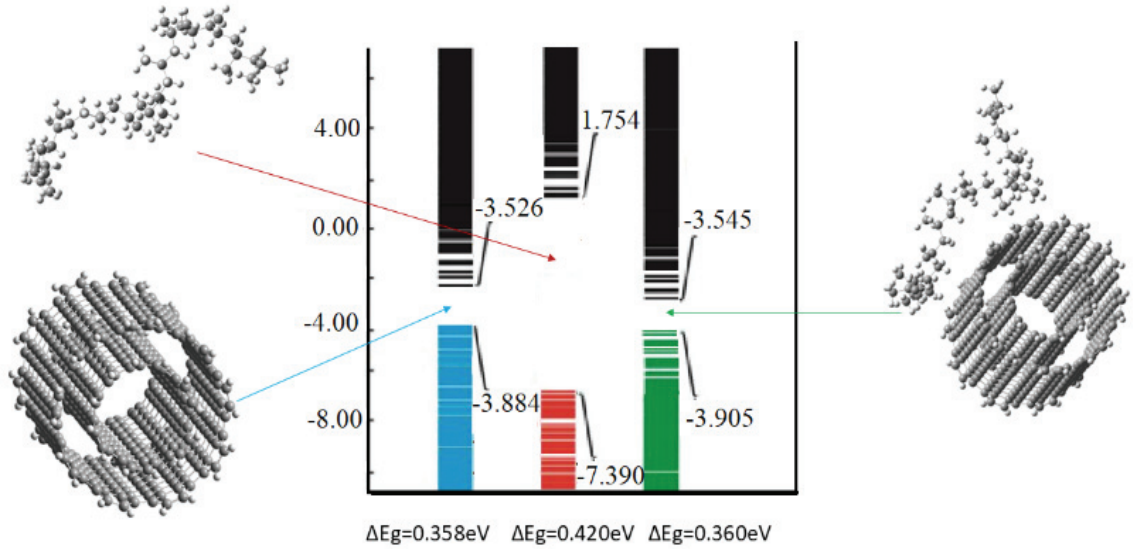

Fig. 5. Visualization of single-electron energy spectra of clusters of two-layer CNTs, a fragment of PP, and interacting PP + CNTs modeling the structure of a composite polymer material [74]

Thus, the introduction of the nanotubes under consideration into the polymer matrix of polypropylene, which is a dielectric by conductivity type, leads to the appearance of semiconducting properties in the resulting polymer nanocomposite.

4. Conclusion

The analysis of experimental studies on polymer composites based on polypropylene and polymethyl methacrylate with added carbon nanotubes demonstrates the wide range of applications for such materials. According to current data, PP/CNT and PMMA/CNT composites represent a promising area for further research and practical application. Improving production technologies opens up opportunities for creating new physical objects with both fundamental and applied significance. This review examines not only the unique physicochemical properties of polymers but also the effects arising from their modification with nanofillers. The composites obtained in this way exhibit enhanced mechanical, electrical, and radio-absorbing properties, opening up broad prospects for their application in various industries.

Ab initio calculations (DFT) reliably establish that the introduction of modified MWCNTs into PMMA and PP matrices leads to a restructuring of the electron-energy structure. Modifying carbon nanotubes in a polypropylene and polymethyl methacrylate matrix creates additional energy levels in the polymer's band gap, facilitating more efficient charge transfer at the interface.

Thus, the synthesis of DFT modeling data and fabrication technologies opens up prospects for creating polymer composites with tailored properties, defining a strategy for the further development of functional materials.

5. Funding

The present study did not receive any external funding.

Финансирование

Настоящее исследование не получило внешнего финансирования.

6. Conflict of interests

The authors declare no conflict of interest.

Конфликт интересов

Авторы заявляют об отсутствии конфликта интересов.

References

1. Mishra AK. Conducting polymers: concepts and applications. *Journal of Atomic, Molecular, Condensate and Nano Physics*. 2018;5(2):159-193. DOI:10.26713/jamcnp.v5i2.842

2. Shadrov SP, Butt HA, Vildanova AR, Agafonova EE, et al. Carbon nanotube fibers as high-fidelity sensors for carbon nanotube/polymer nanocomposites. *iScience*. 2026;29(4):115498. DOI: 10.1016/j.isci.2026.115498

3. Ze Y, Liu Y, Wang B, Yin H, et al. Carbon nanotube materials for future integrated circuit applications. *Materials Today*. 2024;79:97-111. DOI: 10.1016/j.mattod.2024.07.008

4. Malaya EV, Savvin AI. Composite materials in modern aviation. *Aktual'nye issledovaniya*. 2022; 49(128):6-9. (In Russ.)

5. Chen J, Liu B, Gao X, Xu D. A review of the interfacial characteristics of polymer nanocomposites containing carbon nanotubes. *RSC Advances*. 2018;8(49):28048-28085. DOI:10.1039/C8RA04205E

6. Pour GB, Ashourifar H, Aval LF, Solaymani S. CNTs-supercapacitors: a review of electrode nanocomposites based on CNTs, graphene, metals, and polymers. *Symmetry*. 2023;15(6):1179. DOI:10.3390/sym15061179

7. Soni SK, Thomas B, Kar VR. A comprehensive review on CNTs and CNT-reinforced composites: syntheses, characteristics and applications. *Materials Today Communications*. 2020;25:101546. DOI:10.1016/j.mtcomm.2020.101546

8. Green MJ, Behabtu N, Pasquali M, Adams WW. Nanotubes as polymers. *Polymer*. 2009;50(21):4979-4997. DOI:10.1016/j.polymer.2009.07.044

9. Grady BP. *Carbon nanotube-polymer composites: manufacture, properties and applications*. New Jersey: Ballet; 2011. 352 p. DOI:10.1002/9781118084380

10. Yesil S, Bayram G. Poly(ethylene terephthalate)/carbon nanotube composites prepared with chemically treated carbon nanotubes. *Polymer Engineering & Science*. 2011;51(7):1286-1300. DOI:10.1002/pen.21938

11. Ribeiro B, Botelho EC, Costa ML, Bandeira CF. Carbon nanotube buckypaper reinforced polymer composites: a review. *Polímeros*. 2017;27(3):247-255. DOI:10.1590/0104-1428.03916

12. Koch W, Holthausen MC. *A chemist's guide to density functional theory*. Wiley; 2001. DOI:10.1002/3527600043

13. Rahman MdM, Mustakim S, Ullah MH, Islam MR, et al. Carbon nanotube and conducting polymer reinforced biomaterials for flexible supercapacitor electrodes toward sustainable energy storage. *Journal of Energy Storage*. 2026;162:122060. DOI:10.1016/j.est.2026.122060

14. Ali A, Rahimian Koloor SS, Alshehri AH, Arockiarajan A. Carbon nanotube characteristics and enhancement effects on the mechanical features of polymer-based materials and structures – a review. *Journal*

of Materials Research and Technology. 2023;24:6495-6521. DOI:10.1016/j.jmrt.2023.04.072

15. Ullah A, Hussain J, Waqar M, Humayun M, et al. Optimizing oxygen reduction efficiency with a robust nickel nitrogen-doped carbon nanotube catalyst for polymer electrolyte membrane fuel cells. *Results in Chemistry*. 2026;19:102918. DOI:10.1016/j.rechem.2025.102918

16. Elbakyan LS, Hayrapetyan DB, Mantashyan PA. DFT study of GaAs quantum dot and 5CB liquid crystal molecule interaction. *Journal of Molecular Graphics and Modelling*. 2025;136:108953. DOI:10.1016/j.jmgm.2025.108953

17. Chen Z, Nagase S, Hirsch A, Haddon RC, et al. Side-Wall opening of single-walled carbon nanotubes (SWCNTs) by chemical modification: a critical theoretical study. *Angewandte Chemie International Edition*. 2004;43(12):1552-1554. DOI:10.1002/anie.200353087

18. Dinadayalane TC, Leszczynski J. Stone-Wales defects with two different orientations in (5, 5) single-walled carbon nanotubes: a theoretical study. *Chemical Physics Letters*. 2007;434(1-3):86-91. DOI:10.1016/j.cplett.2006.11.099

19. Budyka MF, Zyubina TS, Ryabenko AG, Lin SH, et al. Bond lengths and diameters of armchair single wall carbon nanotubes. *Chemical Physics Letters*. 2005;407(4-6):266-271. DOI:10.1016/j.cplett.2005.03.088

20. Zaporotskova IV, Vilkeeva DE, Elbakyan LS. Sensor activity of titanium dioxide nanotubes in relation to acetone molecules. *Journal of Physics: Conference Series*. 2021;1967(1):012048. DOI:10.1088/1742-6596/1967/1/012048

21. Kumar S, Sharma A, Cherwoo L, Thombare N, et al. DFT study on the polymerization mechanism of aleuritic acid and jalaric acid in shellac molecule. *Kuwait Journal of Science*. 2024;51(1):100138. DOI:10.1016/j.kjs.2023.10.005

22. Akman F, Çankaya N. A study of experimental and theoretical analysis of N-cyclohexylmethacrylamide monomer based on DFT and HF computations. *Pigment & Resin Technology*. 2016;45(5):301-307. DOI:10.1108/PRT-04-2015-0039

23. Gao Y, Zhang J, Liang J, Yuan D, et al. Research progress of poly(methyl methacrylate) microspheres: preparation, functionalization and application. *European Polymer Journal*. 2022;175:111379. DOI:10.1016/j.eurpolymj.2022.111379

24. Jain P, Thakor S, Joshi A, Chauhan KV, et al. Machine learning-driven analysis of dielectric response in polymethyl methacrylate nanocomposites reinforced with multi-walled carbon nanotubes. *Journal of Materials Science: Materials in Electronics*. 2024;35(20):1419. DOI:10.1007/s10854-024-13188-x

25. Jindal P, Sain M, Kumar N. Mechanical characterization of PMMA/MWCNT composites under static and dynamic loading conditions. *Materials Today: Proceedings*. 2015;2(4-5):1364-1372. DOI:10.1016/j.matpr.2015.07.055

26. Mohamadian N, Ramhormozi MZ, Wood DA, Ashena R. Reinforcement of oil and gas wellbore cements with a methyl methacrylate/carbon-nanotube polymer nanocomposite additive. *Cement and Concrete Composites*. 2020;114:103763. DOI:10.1016/j.cemconcomp.2020.103763

27. David OB, Banks-Sills L, Aboudi J, Fourman V, et al. Evaluation of the mechanical properties of PMMA reinforced with carbon nanotubes – experiments and modeling. *Experimental Mechanics*. 2014;54(2):175-186. DOI:10.1007/s11340-013-9792-8

28. Navidfar A, Azdast T, Karimzad Ghavidel A. Influence of processing condition and carbon nanotube on mechanical properties of injection molded multi-walled carbon nanotube/poly(methyl methacrylate) nanocomposites. *Journal of Applied Polymer Science*. 2016;133(31):43738. DOI:10.1002/app.43738

29. Yuan H, Xiong Y, Shen Q, Luo G, et al. Synthesis and electromagnetic absorbing performances of CNTs/PMMA laminated nanocomposite foams in X-band. *Composites Part A: Applied Science and Manufacturing*. 2018;107:334-341. DOI:10.1016/j.compositesa.2018.01.024

30. Zhou D, Yu Z, Yuan H, Luo G, et al. Achieving wideband electromagnetic wave absorbing performance for PMMA-based composites foam by designing the alternating directional (Ad) microporous structure. *Materials Today Advances*. 2023;19:100395. DOI:10.1016/j.mtadv.2023.100395

31. Liu H, Yang Y, Tian N, You C, et al. Foam-structured carbon materials and composites for electromagnetic interference shielding: design principles and structural evolution. *Carbon*. 2024;217:118608. DOI:10.1016/j.carbon.2023.118608

32. Zhou D, Yuan H, Yu Z, Guo W, et al. Broadband electromagnetic absorbing performance by constructing alternate gradient structure (AGS) for PMMA-based foams. *Composites Part A: Applied Science and Manufacturing*. 2021;149:106578. DOI:10.1016/j.compositesa.2021.106557

33. Tan WK, Matsubara Y, Yokoi A, Kawamura G, et al. Transparent conductive polymer composites obtained via electrostatically assembled carbon nanotubes-poly (methyl methacrylate) composite particles. *Advanced Powder Technology*. 2022;33(4):103528. DOI:10.1016/j.apt.2022.103528

34. Muhammad Imran S, Go GM, Hussain M, Al-Harthi MA. Multiwalled carbon nanotube-coated poly-methyl methacrylate dispersed thermoplastic polyurethane composites for pressure-sensitive applications. *Macromol*. 2022;2(2):211-224. DOI:10.3390/macromol2020014

35. Blokhin A, Stolyarov R, Burmistrov I, Gorshkov N, et al. Increasing electrical conductivity of PMMA-MWCNT composites by gas phase iodination. *Composites Science and Technology*. 2021;214:108972. DOI:10.1016/j.compscitech.2021.108972

36. Kuromatsu S, Watanabe T, Nonoguchi Y, Suga R, et al. Single-wall carbon nanotube-based flexible monopole antenna fabricated using poly (methyl methacrylate)-supported transfer technique. In: *2022 Asia-*

Pacific Microwave Conference (APMC). Yokohama, Japan: IEEE; 2022. p. 866-868. DOI:10.23919/APMC55665.2022.9999853

37. Ziani D, Belkheir M, Rouissat M, Mokaddem A. Design optimization for microstrip antennas based on polymethyl methacrylate (PMMA) substrate and carbon nanotube (CNT) conductive material in sub-6 Ghz band. *Beni-Suef University Journal of Basic and Applied Sciences*. 2024;13(1):26. DOI:10.1186/s43088-024-00486-w

38. Patrignani M, Juan J, Nagel O, Reimers W, et al. The adsorption of CO and NO on (8,0) SWCNT decorated with transition metals: a DFT study as a possible gas sensor. *Powder Technology*. 2024;438:119691. DOI: 10.1016/j.powtec.2024.119691

39. Islam MdA, Hossain N, Ahsan Z, Rana M, et al. DFT insights into the mechanical properties of NMs. *Results in Surfaces and Interfaces*. 2025;18:100417. DOI: 10.1016/j.rsurfi.2025.100417

40. Krunić D, Armaković S, Bilić A, Armaković SJ, et al. Understanding the interactions between PMMA polymer and common industrial gasses: a computational xTB, DFT, SAPT and MD study. *Molecular Physics*. 2025;123(17):e2456108. DOI: 10.1080/00268976.2025.2456108

41. Krunić D, Armaković S, Yang Y, Bilić A, et al. Multiscale atomistic insights into interactions between PMMA and environmentally relevant β-blockers in an aqueous environment. *Molecular Simulation*. 2026; 52(8):646-661. DOI:10.1080/08927022.2026.2659203

42. Raj A, Alvi SMAA, Islam K, Motalab M, et al. An atomistic study of the tensile deformation of carbon nanotube-polymethylmethacrylate composites. *Polymers*. 2023;15(13):2956. DOI:10.3390/polym15132956

43. Zaporotskova IV, Elbakyan LS. Obtaining new dental materials reinforced with carbon nanotubes. In: *Advanced Technologies, Equipment, and Analytical Systems for Materials Science and Nanomaterials: Proceedings of the XI International Conference, Kursk, May 13-15, 2014*. Kursk: Southwestern State University; 2014. p. 325–326.

44. Zaporotskova IV, Elbakyan LS. New dental materials reinforced by carbon nanotubes: the technology of obtaining and the study of properties. *Vestnik Volgogradskogo gosudarstvennogo universiteta. Innovatsionnaya deyatel'nost'*. 2014;6(15):87-94. DOI: 10.15688/jvolsu10.2014.6.8 (In Russ.)

45. Zaporotskova IV, Elbakyan LS. The possibility of creating polymer nanocomposites based on methacrylic acid by reinforcing them with carbon nanotubes. *Yevraziyskiy Soyuz Uchenykh. Seriya: Tekhnicheskiye i fiziko-matematicheskiye nauki.* 2014:39-42. (In Russ.)

46. Elbakyan L, Zaporotskova I. Experimental and DFT study of the conductive properties of PMMA composite material by doping with carbon nanotubes. *Nano-Structures & Nano-Objects*. 2025;44:101568. DOI: 10.1016/j.nanoso.2025.101568

47. Zaporotskova IV, Elbakyan LS. The mechanism of interaction of esters of methacrylic acid with carbon nanotubes to create a new polymer composite material. *Journal of Nano- and Electronic Physics*. 2016; 8(3):03047-1-03047-3. DOI:10.21272/jnep.8(3).03047

48. Elbakyan LS, Zaporotskova IV, Vilkeeva DE. The mechanism of getting new composite polymer materials with improved hardness properties. *Key Engineering Materials.* 2021;887:85-90. DOI:10.4028/www.scientific.net/KEM.887.85

49. Elbakyan LS, Zaporotskova IV. Investigation of the effect of boron substitution impurities in carbon nanotubes on the interaction of polymethylmethacrylate with borocarbon nanotubes. *Fiziko-khimicheskiye aspekty izucheniya klasterov, nanostruktur i nanomaterialov.* 2025;17:906-915. DOI:10.26456/pcascnn/2025.17.906 (In Russ).

50. Hossain MdT, Shahid MdA, Mahmud N, Habib A, et al. Research and application of polypropylene: a review. *Discover Nano*. 2024;19(1):2. DOI:10.1186/s11671-023-03952-z

51. Patil J, Patil H, Sankpal R, Rathod D, et al. Studies on mechanical and thermal performance of carbon nanotubes/polypropylene nanocomposites. *Materials Today: Proceedings*. 2021;46:7182-7186. DOI:10.1016/j.matpr.2020.11.452

52. Sahli M, Barrière T, Roazard X, Assoul M. Investigating mechanical, thermal and rheological properties of polypropylene/carbon nanotubes composites. *Microsystem Technologies*. 2020;26(9):3023-3027. DOI: 10.1007/s00542-020-04833-6

53. Bisht PS, Arora G, Pathak H. Strain-rate sensitivity analysis of microwave processed polypropylene-carbon nanotube composites. *Journal of Engineering Research*. 2026;14(1):237-245. DOI:10.1016/j.jer.2024.04.022

54. Thangavel S, Rajkumar D S, Jagadesh P. The impact of multi walled carbon nanotubes on the mechanical properties of polypropylene fibre reinforced concrete. *Case Studies in Construction Materials*. 2026;24:e05949. DOI:10.1016/j.cscm.2026.e05949

55. Hassanzadeh-Aghdam MK, Mahmoodi MJ, Ansari R. Creep performance of CNT polymer nanocomposites -An emphasis on viscoelastic interphase and CNT agglomeration. *Composites Part B: Engineering*. 2019;168:274-281. DOI:10.1016/j.compositesb.2018.12.093

56. Wu C, Wu R, Tam L ho. The creep behavior of semicrystalline carbon nanotube/polypropylene nanocomposite: a coarse-grained molecular study. *Polymer Degradation and Stability*. 2022;196:109834. DOI: 10.1016/j.polymdegradstab.2022.109834

57. Sabet M. Enhancing the thermal and crystallization properties of polypropylene through carbon nanotube integration: a comprehensive investigation. *Iranian Polymer Journal*. 2024;33(6):727-741. DOI: 10.1007/s13726-024-01278-w

58. Li Y, Lin J, Gao Y, Su Y. Regulation mechanism of hard-elastic behavior of polypropylene fibers by multiwalled carbon nanotubes. *Journal of Applied Polymer Science.* 2025;142(47):e57825. DOI:10.1002/app.57825

59. Ameli A, Nofar M, Park CB, Pötschke P, et al. Polypropylene/carbon nanotube nano/microcellular

structures with high dielectric permittivity, low dielectric loss, and low percolation threshold. *Carbon*. 2014;71:206-217. DOI:10.1016/j.carbon.2014.01.031

60. Gulrez SKH, Ali Mohsin ME, Shaikh H, Anis A, et al. A review on electrically conductive polypropylene and polyethylene. *Polymer Composites*. 2014;35(5):900-914. DOI:10.1002/pc.22734

61. Zhao K, Li S, Huang M, Shi X, et al. Remarkably anisotropic conductive MWCNTs/polypropylene nanocomposites with alternating microlayers. *Chemical Engineering Journal*. 2019;358:924-935. DOI:10.1016/j.cej.2018.10.078

62. Li C, Jiao Z, Xiong L, Yang W. Electrical conductivity of carbon nanotube/polypropylene composites prepared through microlayer extrusion technology. *Journal of Polymer Engineering*. 2017;37(8):795-804. DOI: 10.1515/polyeng-2016-0040

63. Bauhofer W, Kovacs JZ. A review and analysis of electrical percolation in carbon nanotube polymer composites. *Composites Science and Technology*. 2009; 69(10):14861498. DOI:10.1016/j.compscitech.2008.06.018

64. Tiwari SKr, Mishra J, Hatui G, Nayak GC. Conductive polymer composites based on carbon nanomaterials. In: Kumar V, Kalia S, Swart HC. (eds). *Conducting Polymer Hybrids*. Cham: Springer International Publishing; 2017. p. 117-142. DOI: 10.1007/978-3-319-46458-9_4

65. Stanciu NV, Stan F, Sandu IL, Fetecau C, et al. Thermal, rheological, mechanical, and electrical properties of polypropylene/multi-walled carbon nanotube nanocomposites. *Polymers*. 2021;13(2):187. DOI:10.3390/polym13020187

66. Kang D, Hwang S, Jung B, Shim J. Characterizations of polypropylene/single-walled carbon nanotube nanocomposites prepared by the novel melt processing technique with a controlled residence time. *Processes.* 2021;9(8):1395. DOI:10.3390/pr9081395

67. Wang J, Kazemi Y, Wang S, Hamidinejad M, et al. Enhancing the electrical conductivity of PP/CNT nanocomposites through crystal-induced volume exclusion effect with a slow cooling rate. *Composites Part B: Engineering*. 2020;183:107663. DOI:10.1016/j.compositesb.2019.107663

68. Zaccone M, Armentano I, Cesano F, Scarano D, et al. Effect of injection molding conditions on crystalline structure and electrical resistivity of PP/MWCNT nanocomposites. *Polymers*. 2020;12(8):1685. DOI: 10.3390/polym12081685

69. Alimoradi Y, Nourisefat M, Farzaneh A, Nazokdast H. Concurrent effect of shear flow and CNT presence on crystallization behavior and electrical properties of polypropylene based nanocomposites: a comprehensive structure-property investigation. *Journal of Composite Materials*. 2024;58(13):1589-1604. DOI: 10.1177/00219983241245998

70. Guo Y, Zhang D, Zhang X, Wu Y. Thermal properties and mechanical behavior of functionalized carbon nanotube-filled polypropylene composites using molecular dynamics simulation. *Materials Today Communications*. 2023;37:107510. DOI:10.1016/j.mtcomm.2023.107510

71. Wu C, Wu R, Tam L ho. Coarse-grained molecular simulation of the effects of carbon nanotube dispersion on the mechanics of semicrystalline polymer nanocomposites. *Nanotechnology.* 2021;32(32):325705. DOI:10.1088/1361-6528/abf458

72. Zaporotskova IV, Elbakyan LS, Vilkeeva DE. Strengthening of polymer ropes based on polypropylene with carbon nanotubes. *Journal of Physics: Conference Series*. 2021;1967(1):012047. DOI:10.1088/1742-6596/1967/1/012047

73. Elbakyan LS, Zaporotskova IV. Polypropylene modified with carbon nanomaterials: structure, properties and application (a review). *Polymers*. 2025;17(4):517. DOI:10.3390/polym17040517

74. Elbakyan LS, Zaporotskova IV. Mechanism for creating a composite based on polypropylene modified with carbon nanotubes of various layer degree. *Izvestiya vysshikh uchebnykh zavedeniy. Materialy elektronnoy tekhniki*. 2025;28(1):15-24. DOI:10.17073/1609-3577j.met202501.646 (In Russ.)

Information about the authors / Информация об авторах

Lusine S. Elbakyan, Cand. Sc. (Phys. and Math.), Associate Professor, Volgograd State University, Volgograd, Russian Federation; ORCID 0009-0006-1014-240X; e-mail: lusniak-e@yandex.ru

Элбакян Лусине Самвеловна, кандидат физико-математических наук, доцент, Волгоградский государственный университет, Волгоград, Российская Федерация; ORCID 0009-0006-1014-240X; e-mail: lusniak-e@yandex.ru

Received 06 April 2026; Revised 11 May 2026; Accepted 18 May 2026

Территория распространения – Российская Федерация, зарубежные страны
Distributed is the Russian Federation and foreign countries

Computer layout: Olga V. Mochalina, TSTU, Tambov, Russian Federation
Компьютерный дизайн и верстка: Мочалина О. В., ТГТУ, Тамбов, Россия

Оригинал-макет подготовлен в Издательском центре ФГБОУ ВО «ТГТУ»,
392032, Тамбовская обл., г. Тамбов, ул. Мичуринская, д. 112А

Подписано в печать 23.06.2026. Дата выхода в свет 30.06.2026.
Формат 60×90/8. Усл. печ. л. 14,25. Уч.-изд. л. 14,05. Тираж 100 экз. Цена свободная. Заказ № 022.
СМИ журнал “Journal of Advanced Materials and Technologies”
(Журнал современных материалов и технологий) выпуск 2026. Том 11, № 2


ISSN 2782-2192
9 772782 219000 >